

© 2010 Shin Ae Jang.

STRUCTURAL HEALTH MONITORING FOR BRIDGE STRUCTURES
USING WIRELESS SMART SENSORS

BY

SHIN AE JANG

DISSERTATION

Submitted in partial fulfillment of the requirements
for the degree of Doctor of Philosophy in Civil Engineering
in the Graduate College of the
University of Illinois at Urbana-Champaign, 2010

Urbana, Illinois

Doctoral Committee:

Professor B. F. Spencer, Jr., Chair
Professor Gul A. Agha
Professor Amr S. Elnashai
Professor Lawrence A. Bergman

ABSTRACT

Structural health monitoring (SHM) has drawn significant attention in recent decades because of its potential to reduce maintenance costs and increase the reliability of structures. An important class of structures that can potentially benefit from SHM are bridges, many of which are structurally deficient due to lack of adequate maintenance. Through condition assessment of these bridges, an effective plan of maintenance can be determined, offering the possibility to prolong service life, as well as to prevent catastrophic disasters due to sudden collapse. To date, numerous damage detection algorithms have been proposed. Still, challenges remain in applying such algorithms to monitor bridges in the field. In reality, the extent of an SHM system is limited by available budgets, which define the number of sensors that can be deployed.

This dissertation first presents a damage detection algorithm using static strain developed for efficient structural condition assessment with a few sensor nodes. A laboratory moving vehicle experiment has been developed for validation of the approach. However, just a few sensor nodes in SHM system cannot provide detailed information on damage location.

A solution to include many sensors within a limited budget with increased efficiency is to use a Wireless Smart Sensor Network (WSSN) because of the merits of low cost, easy installation, and effective data management. An acceleration-based SHM algorithm for WSSN has been developed with a decentralized network topology. This approach has been implemented into a modularized damage detection service. The SHM application is designed to leverage the on-board computation capability of the WSSN, reducing the transmitted data size by distributing the computation burden. The SHM application for WSSN has been validated in lab-scale experiments on a truss bridge model.

Nonetheless, the real challenge of SHM is in the deployment on full-scale bridges for continuous monitoring. The usability and stability of WSSN has been validated on an architectural staircase in the Siebel Center. Based on the usability investigation, the deployment of the world's largest WSSN on the Jindo Bridge, a cable-stayed bridge has been achieved in South Korea. The main purpose of the deployment was to validate the bridge monitoring system using WSSN and energy harvesting devices in a long-term manner.

The ultimate goal of this dissertation is to deploy the developed on-board decentralized damage identification application using WSSN on a historic truss bridge. As a first step, a series of dynamic tests were conducted for modal analysis using both wired and wireless sensor systems. During the tests, the functionality of the wireless sensor system with ISHMP Services Toolsuite was confirmed. For model-based damage identification approach developed herein, a finite element (FE) model was created. The initial FE model was updated based on a visual estimate of the corrosion. The updated model was used to generate baseline information for damage detection. Finally, the WSSN-based autonomous SHM system using the decentralized damage detection application was deployed on the historic bridge. The permanent SHM system was installed on the bridge, and the damage detection application was successfully run on the bridge. The damage detection results using the decentralized comprehensive application will be compared with those from the centralized approach using WSSN. The performance of WSSN and energy harvesting devices will be evaluated. In summary, this dissertation provides a robust SHM system for bridge structures in use of WSSN.

ACKNOWLEDGMENTS

I would like to thank my advisor, Professor B. F. Spencer, Jr., for his endless support and guidance of my research throughout my PhD studies. He is my ultimate role model as researcher, advisor, lecturer, and mentor. His dedication to teaching is sincerely appreciated.

I would also like to thank my committee professors, Professor Gul Agha, Professor Amr Elnashai, and Professor Lawrence Bergman. Their advice and comments on my research were invaluable in honing my thesis. Their support is greatly appreciated.

My research and work on the Jindo bridge monitoring project would not have been possible without the support of my B.S. and M.S. advisor, Professor Chung-Bang Yun. His endless help and input are truly appreciated. I also thank Professor Hyung-Jo Jung for supporting me on the Jindo bridge project. Professor Shirley Dyke and Doctor Michael McFarland helped me on running experimental equipments for the lab and full-scale tests. I also thank Professor Bernhard for valuable advice on antenna technology for full-scale deployment.

My research is based on the foundation of pioneer research by the senior members of the Smart Structures Technology Laboratory. Thanks are owed to Doctors Yong Gao and Tomonori Nagayama with great dissertations on SHM with WSSN. I would like to thank Doctors Guangqiang Yang and Narutoshi Nakata for their kind guidance on experimental equipments in SSTL.

I specially thank my colleagues in Computer Science, Kirill Mechitov for his help on programming and general advices on computer science and Parya Moinzarde for multihop communication. I also thank Edward Lee in Electrical Engineering for helping me with various technical issues.

I thank my colleagues and sincere friends in the Sensor group for helping me with various aspects of my research, Jennifer Rice, Honki Jo, Jian Li, Sung-Han Sim, Robin Kim, Lauren Linderman, Ryan Giles, Chris Hsiao, Timothy Miller. I would like to thank all other SSTL members during my PhD study, Doctor Young-Suk Kim, Doctor Juan Carrion, John Glatt, Ty Stokes, Alan Mullenix, Stephen Schmitt Jr., Michael Davieau, Takehiko Asai, David Bennier, Chia-Ming Chang, Doctor Liang Chang, Kenneth Mitchell, Brian Phillips, Brian Schertz, Nicholas Wierschem, Soon Sim Goh. The entire experience at UIUC would not have been the same without them.

Many visiting scholars and friends in SSTL helped me to conduct field experiments. I appreciate their help and supports: Professor Yuxin Zhang, Taotao Zhang, Min Zhang, Professor Quansheng Yan, Professor Daisuke Iba, Chun-Chung Jingo Chen, Professor Hao Wang, Zhihao Wang, Doctor Mariella De Fino, Professor Jingzhou Lu, and Professor Jin Bo. I thank Doctors Yoshihiro Nitta, In-Ho Hwang, Heon-Jae Lee, Ou Yang, Emiliano Matta, Professors Zhifei Shi, Yasunori Miyamori, Zuoya Sun, Xun Guo, Kangsheng Ye for their advices in various research aspects and friendship.

I thank colleagues at KAIST for their help on the Jindo bridge monitoring project, Soojin Cho, Jongwoong Park, Seung Sub Jin and Dong Doo Jang. I thank Tim Prunkard and his staffs in machine shop at UIUC for his leadership to help the research project.

The study in this dissertation is sponsored and supported by the Samsung Scholarship, the National Science Foundation Grant Number CMS 06-00433 (Dr. S.C. Liu, Program Manager), and the Global Research Network program from the Natural Research Foundation in Korea (NRF-2008-220-D00117). Their financial supports are greatly appreciated.

I thank my brother, Se Hyun Jang, for his great support on my study as a civil engineer himself. Finally, I thank my parents for their encouragement for continuing my study and support during all of challenges I have faced. My strength to complete this task through to the end is from them.

TABLE OF CONTENTS

CHAPTER 1 INTRODUCTION	1
1.1 IMPORTANCE OF BRIDGE HEALTH MONITORING	1
1.2 HISTORIC BRIDGE MONITORING USING MODEL UPDATING.....	3
1.3 CHALLENGES OF APPLYING EXISTING SHM METHOD TO BRIDGE STRUCTURES.....	4
1.4 OVERVIEW OF DISSERTATION	6
CHAPTER 2 BACKGROUND.....	11
2.1 STRUCTURAL HEALTH MONITORING.....	11
2.2 FULL-SCALE BRIDGE MONITORING APPLICATIONS.....	23
2.3 WIRELESS SMART SENSORS	28
2.4 SOFTWARE DEVELOPMENT FOR WSSN.....	34
2.5 SUMMARY	41
CHAPTER 3 STRAIN DAMAGE LOCATING VECTOR METHOD	43
3.1 THEORETICAL DEVELOPMENT OF STRAIN DLV.....	43
3.2 DAMAGE IDENTIFICATION USING STRAIN DLV	46
3.3 NUMERICAL VALIDATIONS.....	47
3.4 EXPERIMENTAL VERIFICATION OF STRAIN DLV METHOD	49
3.5 CONCLUSION.....	54
CHAPTER 4 DECENTRALIZED SDDL V METHOD FOR WSSN	55
4.1 BACKGROUND	55
4.2 DEVELOPMENT OF DAMAGE DETECTION CRITERIA	61
4.3 DECENTRALIZED SDDL V METHOD.....	65
4.4 EXPERIMENTAL VALIDATION.....	68
4.5 IMPLEMENTATION OF DECENTRALIZED DAMAGE DETECTION METHOD ON WSSN	74
4.6 CONCLUSION.....	84
CHAPTER 5 FULL-SCALE VALIDATION OF WSSN ON SIEBEL STAIRCASE.....	85
5.1 DESCRIPTION OF TESTBED.....	85
5.2 HARDWARE SETUP.....	87
5.3 COMMUNICATION OPTIMIZATION	92
5.4 SOFTWARE SETUP	94
5.5 PERFORMANCE EVALUATION.....	95
5.6 CONCLUSION.....	103
CHAPTER 6 FULL-SCALE SHM USING WSSN FOR JINDO BRIDGE.....	104
6.1 BRIDGE DESCRIPTION.....	104

6.2	BRIDGE MONITORING SYSTEM	107
6.3	ENVIRONMENTAL HARDENING	114
6.4	DEPLOYMENT OF SHM SYSTEM	116
6.5	COMMUNICATION PARAMETER OPTIMIZATION	122
6.6	EVALUATION OF THE SHM SYSTEM	126
6.7	CONCLUSION.....	134
CHAPTER 7 FULL-SCALE SHM OF A HISTORIC BRIDGE.....		135
7.1	BRIDGE DESCRIPTION.....	135
7.2	VISUAL INVESTIGATION.....	139
7.3	FULL-SCALE MODAL ANALYSIS USING WIRED SYSTEM.....	146
7.4	MODAL SURVEY USING WSSN.....	161
7.5	CORROSION ASSESSMENT USING MODEL UPDATING.....	171
7.6	CONCLUSION.....	181
CHAPTER 8 FULL-SCALE SHM OF A HISTORIC BRIDGE USING WSSN		182
8.1	LONG-TERM BRIDGE MONITORING SYSTEM.....	182
8.2	FIELD DEPLOYMENT	191
8.3	COMMUNICATION OPTIMIZATION	194
8.4	BRIDGE HEALTH MONITORING.....	200
8.5	LONG-TERM PERFORMANCE OF SHM SYSTEM	214
8.6	CONCLUSION.....	220
CHAPTER 9 CONCLUSIONS AND FUTURE WORK		221
9.1	CONCLUSIONS.....	221
9.2	NEAR-TERM FUTURE STUDIES	224
9.3	BROADER FUTURE STUDIES	226
REFERENCES		230
APPENDIX A: DECENTRALIZED DAMAGE IDENTIFICATION		246
A.1.	PARAMETER SETTING	246
A.2.	SYNCHRONIZED SENSING.....	249
A.3.	CORRELATION FUNCTION ESTIMATION.....	250
A.4.	DAMAGE DETECTION.....	251

CHAPTER 1 INTRODUCTION

1.1 Importance of Bridge Health Monitoring

Civil infrastructure systems such as bridges, buildings, pipelines, and offshore structures are valuable national assets that must be maintained to ensure public safety. In a modern society, these structures facilitate our transportation networks, industrial activities, and everyday life. The annual expenditure of the United States on transportation infrastructure was \$66.7 billion in 2004 (Orszag, 2008). Currently, much of this infrastructure is reaching its design life and will need to be replaced or retrofitted to remain in service.

Bridge structures are one class of civil infrastructure that is particularly problematic. More than 148,000 bridges, mostly short and medium sizes, are structurally deficient or functionally obsolete, according to the 2009 report from the Federal Highway Administration (FHWA, 2009). One notable and highly publicized bridge from this list was the I-35W Bridge in Minnesota. The bridge had been given a “structurally deficient” rating from the federal government since 1990 due to severe corrosion in its bearings. This bridge collapsed in 2007, due to under-designed gusset plates. Indeed, a 2001 report from the Minnesota DOT (MnDOT, 2001) suggested instrumentation of this bridge using strain gages and a continuous SHM system to monitor some of the fracture critical members. Continuous evaluation of structural condition and timely maintenance of infrastructure might have offered the opportunity to prevent this catastrophic collapse.

In addition, such continuous monitoring systems could allow for structural monitoring immediately after natural hazards (earthquake, flood and tornado) and man-made disasters (arson and terrorist bombing) reducing the impact of such disaster both economically and socially.

To date, bridge maintenance has relied on schedule driven and unreliable visual inspection. Visual inspections are highly variable, lack resolution, and fail to detect damage unless it is visible (Chase, 2005). As a result, structurally deficient and even dangerous bridges may be left undiscovered, potentially putting the public at risk. The collapse of the I-35W bridge resulted in 13 deaths, 98 injuries, and significant economic loss. Therefore, an effective way to monitor the structural integrity of our nation's bridges is necessary.

1.2 Historic Bridge Monitoring using Model Updating

Metal truss bridges were a common type built from the 1870s and 1930s in the United States. However, most metal truss bridges are non-redundant fracture-critical structures; therefore, different types of the bridges such as slab or multi-girder bridges gained popularity. After about 100 years of operation, many old truss bridges have been demolished or replaced by these simpler structures because of consideration structural degradation. For examples, the Shanley Road Bridge in Elk county, PA, built in 1891 had been demolished in 2004 after a century of liability and the Hickory Bridge in Forest County, PA, built in 1896 had been demolished in 2007 (<http://www.historicbridge.org>). However, more than 2% of the whole nation's bridges are this type and they are still in use even though 79% of them are structural deficient or functionally obsolete. Therefore, preservation of these bridges is of growing concern because they are traditional historic bridges, improving regional landscapes as well as important assets.

Recently, finite element modeling of historic structures and its updating has been drawn attention in context of preservation of national historic assets (De Stefano, 2003; Ren *et al.*, 2004; Gentile and Gallino, 2008). However, not many examples of the model updating of the old metal truss bridge have been reported possibly because of lack of information and severe bridge condition. The design drawing or construction material is usually difficult to find; therefore, the model should rely only on the on-site measurement and inspection. Also, steel members have been corroded for a century losing significant portions of axial stiffness. The corrosion is especially distributed and varied member by member due to various environmental excitations. Therefore, these caused difficulties in the model updating of the metal truss bridges.

1.3 Challenges of Applying Existing SHM Method to Bridge Structures

Numerous SHM methods have been proposed in recent years; detailed reviews are provided by Doebling *et al.* (1996) and Sohn *et al.* (2003). However, challenges remain before such methods can be applied routinely to bridge structures in the field. While most SHM algorithms require both input and output measurements, measuring input excitation is quite difficult in general due to the distributed and random nature of the bridge loading. Thus, research on SHM algorithms has emphasized the use of ambient vibration data.

The number of sensors is another challenge to be considered in employing SHM methods. In reality, the number of the sensors in an installation is limited; the cost of the sensors, data acquisition systems, and system installation is significant, and the available budget is always limited. Traditionally, algorithms which can achieve adequate performance with a limited number of sensors are desirable. Unfortunately, such algorithms that are effective have been elusive. Considering that damage is an intrinsically local phenomenon, deployment of more sensors throughout the structure has the potential to lead to more accurate damage detection results.

One potential approach to overcoming the problems associated with a limited number of sensors is using wireless smart sensors (WSS). Wireless smart sensors offer a solution for long-term, scalable SHM of civil infrastructure by providing easier installation and efficient data management at a lower cost than traditional wired monitoring systems. Specifically, the wireless sensor unit used for the monitoring systems discussed herein possesses multiple sensor channels and costs less than \$500 USD each, including solar power harvesting devices. Moreover, installation time and effort is significantly less than the wired counterpart. Also, smart sensors have on-board computation capability that can help to mitigate the problem of data inundation

that is intrinsic to densely instrumented structures. These features of wireless smart sensors help to ensure the scalability of the SHM system to a large network necessary for long-span bridges.

Several researchers have employed wireless sensors to monitor bridge structures (Lynch *et al.*, 2006; Nagayama, 2007; Kim *et al.*, 2007; Pakzad, 2009; Jang *et al.*, 2010), providing important insight into the opportunities and challenges for WSSN technology for long-term monitoring. Critical issues identified include: (i) power management, (ii) energy harvesting, (iii) fault tolerance, (iv) autonomous operation, and (v) environmental hardening.

In addition, excitation methods for bridge structures need to be considered. The two main categories of excitation methods are ambient vibration and forced vibration. Ambient vibration tests are used for a long span bridge due to the difficulty in applying sufficient forces to a large bridge, while forced vibration tests are often used for a small or middle size bridges because the responses from the ambient vibration may be too small. Therefore, effective excitation schemes should be considered according to bridge size.

1.4 Overview of Dissertation

This research focuses on the development and implementation of SHM algorithms for bridge structures using wireless smart sensor technology. The contributions of the research are in the development of damage detection algorithms, implementation of an algorithm on WSSN, deployment of SHM system with a dense array of WSSN on a cable-stayed bridge, and condition assessment of a full-scale bridge using the developed framework. This section summarizes the overview of the dissertation on each chapter.

Chapter 2 presents the background for this research, including reviews of structural health monitoring (SHM), wireless smart sensors, software development for WSSNs, and full-scale bridge monitoring applications. Following a definition of damage employed for this work, an overview of vibration-based damage detection algorithms is presented. Among numerous algorithms, flexibility-based methods have shown to be robust in high frequency noise. One of the flexibility matrix based methods, the damage locating vector (DLV) method, is employed as a bases for the SHM framework developed in this research. Additionally, selective model updating technologies and their applications are presented. Because the main focus of this research is the use of WSSN, a brief summary of the hardware components of wireless smart sensor and the platform selection are provided, along with the associated software components. The last section of this chapter reviews full-scale bridge monitoring applications using traditional wired sensor systems. This background information provides the foundation for the research in this dissertation.

Chapter 3 and Chapter 4 describe the damage detection algorithm development. The basis for the algorithms is the flexibility-based DLV method. For bridge monitoring, static strain measurements are the most common measurement, because they are cost effective and can be

used for load rating and fatigue life estimation. Chapter 3 provides development of a static strain-based DLV method and its validation in lab scale experiments. The strain flexibility matrix based on the static strain measurement is defined, which can be obtained from moving truck load tests in the field. Damage location can be identified from the differences in the strain flexibility matrices before and after damage. A series of laboratory moving load tests were conducted for the validation of this method.

However, damage is intrinsically a local phenomenon; therefore, a dense network of sensors is desirable. One of the solutions to involving many sensors with cost constraints is the use of the wireless smart sensors. Most deployments of wireless smart sensors to date have assumed centralized data collection and processing (*i.e.*, emulated wired sensor networks). Such centralized approaches are not scalable due to limitations in wireless communication bandwidth. As described in section 2.4.3, the decentralized computing strategy is shown to be suitable for efficient network communication as well as damage identification.

In Chapter 4, a decentralized damage identification approach based on the stochastic dynamic DLV method is developed. New damage indices are proposed for robust damage identification. This approach is validated in lab-scale experiments on a truss bridge model using a wired sensor system that emulates a WSSN. This approach is then implemented as a damage detection service for the Imote2 and integrated as part of a new autonomous SHM framework in ISHMP Services Toolsuite.

Chapter 5 to Chapter 8 describes the field deployment of WSSN on various structures. For full-scale bridge monitoring, the feasibility of WSSN in hardware and software perspectives needs to be confirmed. In Chapter 5, the software performance of the ISHMP Services Toolsuite on the Imote2 system is validated on an architectural staircase in Siebel Center at University of

Illinois campus. A brief description of the Testbed and the components of structural monitoring system are provided. In this deployment, the network parameters for the radio communication and power consumption have been optimized. This Testbed allowed for debugging and refining the ISHMP Services Toolsuite for subsequent deployment on a cable-stayed bridge in South Korea.

Chapter 6 presents full-scale structural monitoring of the Jindo Bridge in South Korea. This project is a multi-national bridge monitoring project with institutions from the United States, Korea and Japan. The ISHMP Services Toolsuite, updated based on the Siebel staircase deployment, was loaded on the Imote2. Two types of sensor boards were utilized in this deployment for acceleration and wind measurement. In total, 427 sensor channels were installed in 71 sensor nodes. To supply long-term power to the Imote2, solar panels were installed for 8 nodes. The procedure to optimize the antenna direction, communication range, and network parameters is described in detail. After optimization of the system, the acceleration data was successfully measured. The performance of the hardware, software, power consumption, and the solar energy harvesting devices are discussed. The purpose of the Jindo bridge deployment is centrally collecting data from all leaf nodes, which emulates the wired monitoring system.

To take full advantage of on-board computation capability of wireless smart sensors, a high-level structural health monitoring framework should be developed to synthesize the raw data measurement. To this end, a 100-year-old historic truss bridge has taken as a Testbed for structural condition assessment in Chapter 7. First of all, full-scale vibration tests were conducted using a wired sensing system; while more complex to setup, the traditional wired system provides a high-quality baseline for evaluation of the WSSN approaches. Subsequently, the performance of wireless sensor system was compared with the wired system in terms of

modal analysis. The modal analysis results from the forced vibration tests matched well when the vibration is at least 20 mg due to coarse resolution of the basic sensor board. A FE model was built for future damage detection application development. However, the modal properties from the initial model and those from the measured data were significantly different. The main source of the difference was from severe corrosion distributed in the whole bridge. To incorporate the degrees of corrosion of various elements, the sectional area and mass density of a group of elements were updated using a multi-step optimization strategy. After updating, the modal properties from the model agreed with those of the measured data within 10 %. This updated FE model is used as a baseline of the bridge and for generating the input file for the decentralized damage identification application.

Finally, Chapter 8 provides the validation of a *DecentralizedDamageIdentification* application on a full-scale historic bridge with WSSN.. This damage localization application has been combined with an autonomous continuous monitoring application, *AutoMonitor*, in the ISHMP Services Toolsuite to enable on-demand damage identification as well as continuous raw data measurement. For higher resolution acceleration measurement, the SHM-A sensor board was employed for this deployment. Various deployment issues were resolved in the enclosure configuration, environmental protection, and wireless communication optimization for stable long-term measurement in the field. This deployment showed the potential of the developed SHM framework and practical deployment issues.

The conclusions of the dissertation and a discussion of future work are provided in Chapter 9. This research provides the showcase of a structural health monitoring system for bridge structures using WSSN. A decentralized damage detection strategy is developed, implemented for WSSN and validated experimentally. A dense array of wireless smart sensors have been

deployed on a cable-stayed bridge after a series of performance investigation and addressing the deployment issues. The developed bridge health monitoring application has been also validated on a historic bridge. The future work includes the issues for upgrading the SHM framework developed in this dissertation, as well as the potentials to extend the research for various applications on our civil infrastructure. The appendix provides a brief user guide for the developed *DecentralizedDamageIdentification* application.

CHAPTER 2 BACKGROUND

This chapter presents the background and motivation for this research. First, the definition of damage in structural health monitoring (SHM) and review on the vibration-based SHM algorithms are given, followed by the overview of bridge health monitoring efforts using traditional wired sensor system. Subsequently, the basic knowledge on wireless smart sensors is summarized, including a description of the components of wireless sensors, wireless sensor platform selection, and sensing using smart sensors. Software development for WSSN using TinyOS, the Illinois SHM Services Toolsuite, and decentralized data aggregation are provided.

2.1 Structural Health Monitoring

2.1.1 Damage definition in civil infrastructure

In general terms, damage can be defined as changes introduced into a system that adversely affects its current or future performance (Sohn *et al.*, 2003). Such damage can be induced either by aging or by catastrophic events. Damage is typically categorized as either linear or nonlinear. A linear damage is defined as the case when the initially linear-elastic structure remains linear-elastic after damage, while nonlinear damage corresponds to the situation when the initially linear-elastic structure behaves in a nonlinear manner after the damage has been introduced (Doebbling *et al.*, 1996). For example, linear damage is often associated with stiffness reduction due to steel and/or concrete corrosion, while nonlinear damage is associated with crack opening and closing, frozen bearings, loose connections, *etc.* The focus of this study is linear damage.

Before discussing damage detection methods, the theoretical formulation and physical examples of linear damage will be presented.

Damage resulting in a stiffness reduction can be modeled using Continuum Damage Mechanics concepts. Damage is defined as the creation of microvoids or microcracks in structures (Lemaitre and Desmorat, 2005). The basic hypothesis is isotropic damage; *i.e.*, microcracks and voids are equally distributed in all directions.

Kachanov (1958) introduced a damage measure D as the ratio of the area before and after damage to characterize this internal degradation of a uniaxial bar, *i.e.*,

$$D = \frac{A}{A_0}, \quad 0 \leq D \leq 1 \quad (2.1)$$

where, A_0 is the cross-sectional area of the undamaged bar, and A is the cross-sectional area of the damaged bar (see Figure 2.1). This damage measure also can be applied to estimate isotropic damage in three-dimensional structures with the assumption that the damage measure is identical for all cross section of the volume. Thus, damage resulting from stiffness reduction can be expressed as a percent reduction of the cross-sectional area.

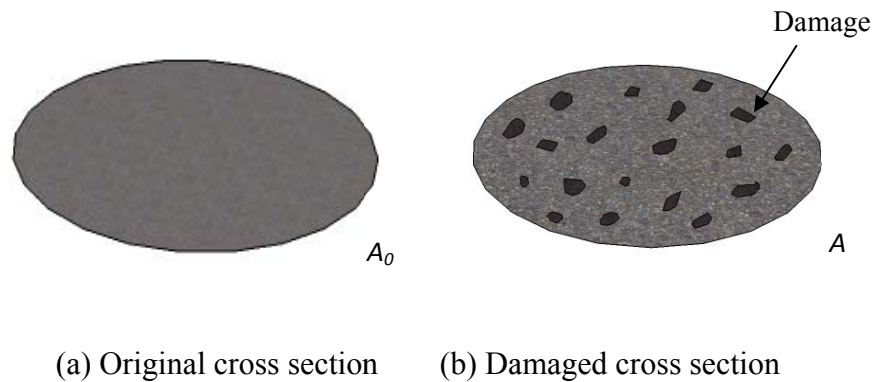


Figure 2.1. Damage representation

Stiffness reduction is common in aging construction materials, *e.g.*, steel, concrete, reinforced concrete, *etc.* Steel corrosion generally results in a reduction in the stiffness of structural elements. As can be seen in Figure 2.2, corrosion results in reduction in the cross section of the bridge members and therefore the stiffness of the element. The corrosion of re-bars in reinforced concrete is also included in this category. Therefore, damage caused by stiffness reduction is worth studying in the context of SHM.



Figure 2.2. Corroded truss elements of the Mahomet Bridge.

2.1.2 Vibration-based SHM algorithms

Doebbling *et al.* (1996) and Sohn *et al.* (2003) provided careful reviews of over 700 papers on structural health monitoring (SHM). Various damage identification methods and their application to bridges, offshore platforms, aerospace structures, and composites are presented in their reports. SHM methods are often classified based on type of structural responses measured, such as static strain, curvature, natural frequency changes, mode shape changes, flexibility, or damage detection techniques, such as matrix updating methods, neural networks, nonlinear methods, *etc.* Most of these approaches are based on vibration measurement. In this section, the vibration-based SHM algorithms for bridge structures are reviewed.

Damage detection methods using natural frequency changes have been applied by many researchers. Cawley and Adams (1979) employed the ratio of the natural frequency changes to detect the location of local stiffness reduction and the rough extent of damage. The main assumption was that the natural frequency is a function of only the location of damage. This method was not widely used because many pairs of modes before and after damage were required. Several researchers also proposed damage localization algorithms using natural frequencies (Chen *et al.*, 1995; Patil *et al.*, 2002). However, SHM methods using only natural frequency changes have intrinsic limitations, because many environmental and structural factors are related. For example, temperature can cause the natural frequency of a structure to vary significantly within a single day (Sohn, 2006). In addition, natural frequency shift represents the global behavior of a structure, so that it can represent the existence of damage, but is insufficient to determine the location. Therefore, natural frequency shift has often been used in conjunction with other SHM methods for damage localization.

SHM algorithms utilizing both natural frequencies and mode shapes have been subsequently considered. Lee *et al.* (2002) presented a damage detection method using both natural frequencies and mode shapes. A laboratory bridge was built and vertical accelerations were measured during a vehicle passing over the bridge. The modal properties were calculated using the random decrement method. The ratio of the natural frequencies before and after damage and the estimated mode shapes are fed into a neural network to identify the damage location and severity. Kim *et al.* (2002) proposed two damage detection algorithms using the correlation between stiffness reduction and changes in natural frequencies and mode shapes. A pre-stressed concrete beam model was employed for numerical studies for both methods. Stiffness reduction was used as the damage. The natural frequency was found to decrease as damage severity

increased. The mode shape-based method can also detect approximate damage location using a damage index and estimate damage severity using a stiffness ratio. Similar studies to correlate the structural stiffness parameters, as well as natural frequencies and mode shapes have been studied by other researchers (Ge *et al.*, 2005; Rahai *et al.*, 2007).

Modal strain energy also has been employed for the purpose of damage detection. Carrasco *et al.* (1997) located and quantified damage extent for a truss structure using the change in modal strain energy before and after damage. By characterizing the damage as a scalar quantity of the undamaged stiffness matrix, an expression was obtained for element damage factors that quantify the magnitude of the damage for each mode shape. Three types of damage were investigated: a 180° saw-cut of the cross-section of the elements, 50% reduction of area over one-third of the element length, and a complete cut through the element section. Among many experiments, this method was shown to detect area reduction and complete cut damage. However, only one of four cases of the 180° saw-cut damage was detected, because of errors in acceleration readings or modal analysis. Shi *et al.* (2000) introduced a method utilizing the ratio of change in modal strain energy. The sensitivity of the modal strain energy to damage is derived. The sensitivity is a function of the analytical mode shape changes and the stiffness matrix. Incomplete measured mode shapes and analytical system matrices are required for damage localization and quantification. A fixed-fixed beam is used for numerical verification. Multiple damage locations can be found with this method; however, the results were sensitive to measurement noise. Shi *et al.* (2002) improved their algorithm by using only the first few modes and verified the results using numerical simulation.

Parameter estimation methods have been developed by Shin and Hjelmstad (1994). By employing an adaptive element-grouping scheme, this method can localize a single damage

location with noisy and limited measurements. Errors occur in the case of multiple damage locations. Pothisiri and Hjelmstad (2003) improved the method proposed in 1994 using a new element-group updating scheme. In this method, errors in the estimated parameters are reduced by selecting a near-optimal measurement set to resolve non-unique solutions.

The flexibility matrix has been regarded as an effective structural measure for stiffness reduction. Stiffness matrices are dominated by higher modes; flexibility matrices are dominated by lower modes (Gao and Spencer, 2008). Because noise is usually of high frequency, flexibility-based methods are robust to noise (Mottershead *et al.*, 1993). The earliest study in the literature is perhaps the damage detection approach using the changes of modal flexibility reported by Pandey and Biswas (1994). A few lower modes were shown to be able to estimate the flexibility matrix easily, because it converges rapidly with increasing frequency. The column entries in the flexibility matrix with the largest absolute changes coincided with the location of damage. A drawback is that a full modal analysis is time-consuming.

Huth *et al.* (2005) investigated the performance of several damage identification methods on experimental data, including the flexibility matrix based method developed by Pandey and Biswas. In this study, the natural frequency changes corresponding to the damage were found to be negligible. The mode shape change increased with the level of damage, but the modal assurance criterion, which uses the mode shapes, showed low sensitivity to damage. On the other hand, the flexibility approach was able to localize damage at an earlier stage. In using all modal-based methods, the sensitivity of damage detection decreased as environmental factors increased.

Doebeling *et al.* (1998) presented a method based on modal flexibility disassembly. The measured incomplete flexibility matrix is decomposed into the individual stiffness parameters of

an assumed set of super elements within the structure. The boundaries of the super element are defined by the measurement sensors. This method was verified with a two degree-of-freedom (DOF) system and a cantilever beam. Parjawit *et al.* (2005) developed a global flexibility index-based method for highway bridges. This index is the square root of the largest eigenvalue of the norm of the modal flexibility matrix: $\sqrt{\lambda_{\max}(F^T F)}$, which is shown to increase as the damage extent increases. The algorithm was verified using impact tests of a RC highway bridge. Because the highway bridge is not supposed to be artificially damaged in use, the AASHTO load rating was provided based on a finite element model. According to the load rating results, the bridge was considered to be safe.

Among the many types of vibration-based damage detection algorithms, the flexibility-based damage detection algorithms have been found to be efficient for damage resulting in stiffness reduction. Although vibration-based algorithms show limited field applications due to various uncertainties (*e.g.*, environmental factors, measurement noise, *etc.*) affecting modal properties, they show potential for being employed for SHM.

2.1.3 DLV family methods

The damage locating vector (DLV) method was proposed by Bernal (2002), which employed the change of the modal flexibility matrices before and after damage. The DLVs are a series of load vectors which induce zero stress at the damaged elements (Bernal, 2002). The DLVs are calculated by singular value decomposition of the change in the flexibility matrix. Several DLVs are obtained and applied to the undamaged structural model one by one. The stress from structural analysis for each DLV is normalized, and added together and normalized again to

obtain normalized accumulated stress (NAS). Zero NAS indicates a damaged element. The DLV method had been experimentally validated by Gao *et al.* (2004) with laboratory tests on a 3D steel truss model. The DLV method has some limitations for practical applications such as the requirement of input measurement and false positive damage detection. To overcome these drawbacks, the several extensions to the original DLV method have been proposed, which herein are designated the DLV family methods.

The stochastic DLV method was developed using output-only data to overcome the requirement of measuring the input excitation. A surrogate matrix, Q , is employed for damage detection by employing state space representation and its derivatives (Bernal, 2004). The validity of DLV method remains because the surrogate matrix spans the same null space as the transfer function matrix. Nagayama (2007) implemented the stochastic DLV method in a smart sensor network and validated the performance of this method in the lab-scale experiments using a steel truss model.

The DLV method intrinsically has false positive damage identification issues. False damage indication can be categorized into two types: false positive indication is the report of damage when none is present; false negative indication is no report of damage when damage is present. Because the DLV induces zero NAS at the damaged element, adjacent elements may also have zero or low stress, particularly in statically determinant structures. False positive detection for nearby elements is not as critical an issue as false negative detection; however, excessive false positive detection can cause lack of confidence in the damage detection strategy. Sim *et al.* (2009) addressed the false positive detection problem by employing multi-metric sensing of acceleration and dynamic strain.

The dynamic DLV (DDLV) method was proposed, employing a transfer function matrix, also known as the receptance matrix, instead of a flexibility matrix to provide richer information on damage detection (Bernal, 2006). Note that the flexibility matrix is the transfer function matrix evaluated at $s = i\omega = 0$, which disregards dynamic information. By employing dynamic information contained in the receptance matrices, more than one set of DLV are obtained, which can help to reduce the positive detection problem. Therefore, DDLV method has robustness and the possibility to reduce the false positive detection. However, the DDLV method still requires the input measurements.

The stochastic DDLV method (SDDL) was developed to combine the merits of both stochastic and DDLV methods (Bernal, 2005). This method employs a surrogate of the receptance matrices over various frequency values obtained from output-only data. The dynamic information can reduce the false positive detection possibility. Therefore, the SDDL method has the potential for widespread application in terms of reliability and practicality.

2.1.4 Model updating for SHM

Model updating is the correction process of finite element models by processing experimental data from dynamic tests. For this research, such an updated model will be used in model-based damage detection strategies. Three commonly encountered model errors which may affect the model prediction accuracy are: (1) model structure errors from nonlinear behavior, (2) model parameter errors from the uncertainties in boundary condition and material properties, and (3) model order errors from inaccuracy in the analytical model discretization (Mottershead, 1993). To update the possible parameters above, the rule of thumb is to match the first three eigenvalues

of a finite element model. Mottershead (1993) recommended the preliminary elimination of unnecessary parameters and employment of multiple test results for model updating.

Two approaches for updating the finite-element models are system matrix updating and structural parameter updating. Because the system matrix updating method is not applicable for models in which the changes in mass and stiffness matrices are coupled, structural parameter updating has been widely used. The parameter updating method is based on the sensitivity analysis of the parameters in terms of physical changes of structures.

To date, many researchers have reported the application of the parameter updating method based on sensitivity of structural parameters. As an early example, Brownjohn and Xia (2000) applied the parameter updating method on the Safti Link Bridge in Singapore (see Figure 2.3). The parameters to be updated were the Young's modulus and the mass density. The differences in the natural frequencies of the data and the model were within 10% at maximum. They noted that an intrinsic limitation of model updating resides in structural complexity and simplifications in modeling.

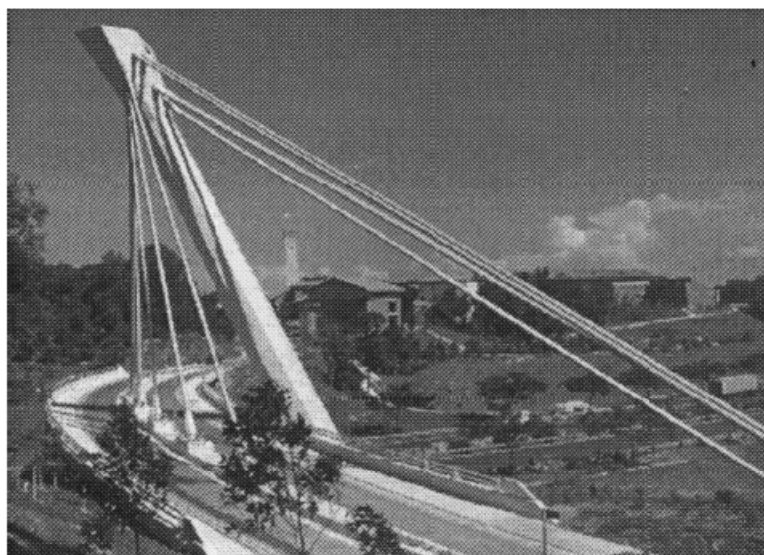


Figure 2.3. Safti Link Bridge (Courtesy of Brownjohn, 2000).

Zhang *et al* (2001) applied an improved sensitivity-based updating algorithm for the 710m Kap Shui Mun Bridge in Hong Kong. The updating parameters are selected using the sensitivity analysis for different structural systems: composite deck, box girder deck, tower, and connections. For example, for the composite deck, the Young's modulus, mass density, cross-sectional area, moment of inertia were been selected as parameters to be updated. The lowest 17 modes between 0 and 2.2 Hz are matched with experimental data after updating the total of 31 parameters.

Chang *et al.* (2000) applied the sensitivity-based parameter updating method to a 1/150 scale suspension bridge model. The changes of the updating parameters are found by solving a quadratic programming problem. The contribution of this paper is the use an objective function that is the sum of a weighted frequency error norm and a weighted perturbation norm of the parameters. This objective function can avoid ill-conditioning of the optimization.

Some researchers have focused on the way to prevent the ill-conditioning for the parameter updating method. Zapico *et al* (2003) suggested the rules for updating a small-scale irregular bridge model subjected to earthquake excitations. The first rule is that only parameters that the response is sensitive to and have physical meaning should be selected. The next rule is that when the parameters corresponding to several elements are expected to have similar values, one super-element parameter should be selected rather than individual element parameters.

Jaishi and Ren (2005) combined new objective function to improve the performance of the sensitivity-based parameter updating method. Because the modal flexibility is more sensitive to the local changes of structures, the proposed objective function is a function of the eigenvalue residuals, the mode shape-related functions, and the modal flexibility residuals. For the simple beam model, the maximum error after model updating was achieved within 1.29% using the

least-square algorithm. However, for a concrete-filled steel tubular arch bridge, the first three natural frequencies were matched to within 15.42%. Subsequently, Jaishi and Ren (2007) employed another objective function and new optimization technique for further improvement. An objective function combining the eigenvalues and strain energy residuals was used. For optimization, an iterative method using the Sequential Quadratic Programming (SQP) method was employed. After updating the numerical model of the Hongtang Bridge (Figure 2.4), the first 5 vertical bending natural frequencies are matched with the experimental data to within 5% for 1st and 2nd modes; however, is the error in the other modes ranged from 10% to 23 %. The field of model updating is mature but still actively studied to improve the objective function and optimization algorithms.



Figure 2.4. Photograph of Hongtang Bridge (Courtesy of Jaishi, 2007).

2.2 Full-scale Bridge Monitoring Applications

Bridges are an important class of infrastructure for our everyday lives; thus, researchers have spent their efforts to monitor bridges. The earliest bridge health monitoring applications using modern structural engineering knowledge are perhaps the Golden Gate Bridge and the Bay Bridge in San Francisco (Carder, 1937). The vibration from the towers and mid-span were measured by a photographic seismograph during construction. The changes of the amplitude and period of the motion were tabulated. The addition of cables decreases the amplitude of the vibration to 10-50 percent of the former value. The period of vibration of the tower increased by the addition of the cables and decking. The main purpose was to study the possibility of damage due to a strong earthquake, but the goal was not fulfilled because of uncertainty in potential earthquake ground motions. Compared to the 1930s when these tests were carried out, technology for measuring data and SHM algorithms have been substantially improved. In this section, examples of bridge health monitoring systems implemented in the last two decades are summarized.

Many researchers have monitored bridges to measure dynamic bridge responses such as acceleration. Doebling *et al.* (1997) measured the vertical acceleration of the Alamosa Canyon Bridge in New Mexico from ambient vibration and impact hammer tests. The modal properties calculated from both tests were compared. One of the modes identified from the hammer tests was not identified in the ambient vibration tests. A possible reason for this inconsistency was some vibration modes may not be well excited by ambient vibration. Abe *et al.* (2000) measured ambient vibration of the Hakucho Bridge in Japan to track modal property variations caused by wind loads. The dynamic properties of the bridge, natural frequencies, mode shapes, and modal damping ratios were calculated using the Ibrahim Time Domain method.

Some researchers measured the dynamic strain of bridges. Todd *et al.* (1999) monitored the I-10 Bridge in Southern New Mexico using fiber Bragg grating (FBG) strain sensors. A 64-channel strain sensor array was placed on the Bridge to monitor traffic loads, vibration responses, and real-time girder deflection. The bridge deflection was calculated by double integration of the strain data. The average deflection of the girder was 30 mm as a truck passes the mid-span. Giacosa *et al.* (2008) installed FBG sensors, accelerometers and inclinometers at the cables of the Pedestrian Olympic Bridge in Torino, Italy to monitor the behavior of the bridge.

To take advantage of the rich low-frequency content in displacement measurements, many researchers have proposed optical-based sensors for bridge health monitoring. Macdonald *et al.* (1998) employed a 3D computer vision system to measure dynamic displacement of a cable-stayed bridge, the Second Severn Crossing in UK. Black and white CCD cameras have been used for recording targets on the bridge. The position of the target is predicted based on the known locations. The camera views are calibrated by locating the reference points in each view, and the 2D image coordinates are transformed to 3D real world coordinates by reference to the calibrated data. Experimental verification both on laboratory shake table and on the bridge were provided. A measurement accuracy of 0.5 mm at a distance of over 200 m has been achieved. Lee *et al.* (2006) proposed a vision-based damage detection platform using digital image processing techniques with the development of optical technology and wireless communication technology. Dynamic displacements of a shake table were measured and compared with those from linear variable differential transformers. Ando *et al.* (2007) developed the correlation-based magneto-optic imager sensing for 6-axis displacement measurement. The system has the potential to be used for bridge health monitoring in the future because the accuracy of this imaging sensor is within micro-meters, and continuous displacement monitoring is possible. A

drawback of these vision-based displacement monitoring systems is that fixed points are required to install cameras, which is unfavorable for SHM of long span bridges.

Global positioning systems (GPS) have been tried to measure the displacement of some long-span bridges. Wong *et al.* (2004) introduced a GPS-based bridge monitoring system for three bridges in Hong Kong: the Tsing Ma Bridge, Kap Shui Bridge, and Ting Kau Bridge. A Navigation System and Ranging GPS using a constellation of 24 satellites was employed for positioning these bridges. A corresponding software package for real-time monitoring was developed. The GPS receivers were installed in the main tower and cables to measure bridge displacements. The displacement influence line at mid-span using the GPS system has been compared with those from the level sensors and accelerometers. They matched well for the Tsing Ma Bridge. The displacements from the GPS system had higher noise contents than those from the traditional system. The possible SHM applications using GPS data are to estimate the bridge response due to traffic, wind, and temperature loads, as well as to obtain the cable force and strain/stress of the bridge.

Cosser *et al.* (2004) employed a GPS system to measure the transverse and vertical displacements of the Wilford Bridge in Nottingham and the Humber Bridge in Hull in the UK. The Wilford Bridge is a small pedestrian suspension bridge, while the Humber Bridge is a long-span cable-stayed bridge. For the Wilford Bridge, the dynamic displacements due to ambient loads were indistinguishable from the noise due to environmental factors. In the case of the Humber Bridge, the maximum displacements were approximately 20-25 cm. Though GPS measurements still has many technical drawbacks (*e.g.*, resolution, noise, *etc.*), it has great potential as a displacement measurement system in the future.

Full-scale applications for the purpose of damage detection have also been employed by some researchers. Farrar *et al.* (1994, 1998) monitored a decommissioned bridge, the I-40 Bridge in Albuquerque, New Mexico, measuring the vertical accelerations from ambient and forced vibration tests. Various degrees of damage using torch cuts were made in the web and flange in the plate-girder to simulate fatigue damage. Natural frequencies and the mode shapes are compared before and after damage. The natural frequency dropped 7.6% and 4.4% for the 1st and the 2nd modes, respectively, due to a 50% sectional area loss. The modal assurance criteria before and after damage were also obtained using the mode shapes. The changes of the MAC values were detectable at the final damage stage. Lee *et al.* (2006) also considered vertical accelerations of a decommissioned bridge, the old Han-Nam Grand Bridge in Seoul, Korea. Similar torch-cut damage was induced in the bridge girders. Neural networks were employed to localize the damage. The location and approximate severity were estimated. These tests are on-demand or campaign-type bridge tests, meaning that the tests were conducted during specific time duration, for damage detection.

Long-term SHM system has been implemented in several full-scale bridges around the world. The most extensively instrumented examples of long-term monitoring system are three bridges in Hong Kong: the Ting Kau Bridge, Kap Shui Mun Bridge, and Tsing Ma Bridge. These bridges are monitored by the Wind and Structural Health Monitoring System (WASHMS). For example, the Tsing Ma Bridge system consists of approximately 350 sensors and the relevant interfacing units, including the GPS system. The huge amount of data collected from many sensors may result in data inundation. Wang *et al.* (2007) installed a long term SHM system in the Kishwaukee River Bridge in Rockport, Illinois. Static responses from the bridge were measured using strain gages and LVDTs. Measured acceleration data was transferred to a computer

through an internet connection. The correlation between natural frequency shift and temperature change was calculated by a linear regression analysis. Other examples of the long-term SHM systems are the Commodore Barry Bridge Monitoring System (USA), the Jindo Grand Bridge Monitoring System (Korea), the Akashi Kaikyo Bridge Monitoring System (Japan), the Alamillo Bridge Monitoring System (Spain), the Hummer Bridge Monitoring System (UK), and the Zhanjiang Bay Bridge Monitoring System (China), *etc.* Mainly these systems measure only structural responses; effective damage detection algorithms are necessary to be implemented for efficient SHM.

2.3 Wireless Smart Sensors

Recent advancement in wireless sensor technology has enabled efficient measurement and data processing for SHM. Lynch and Loh (2006) provide a comprehensive literature review on wireless sensor technology for SHM applications. For completeness, this section summarizes the descriptions of the components of a wireless smart sensor (WSS), and selection of platform for SHM application from Rice and Spencer (2009).

2.3.1 Components of a wireless smart sensor

Radio component

The wireless data transmission using radio frequency (RF) communication is an essential characteristic of wireless smart sensors. Most WSS platforms operate on the 900 MHz, 2.4 GHz or the 5 GHz frequencies because they are unlicensed. Based on the operation frequencies, an adequate radio component should be selected among various wireless transceiver options according to the target power consumption. The intrinsic nature of the RF transmission is unreliable because of many uncertainties in communication range, physical interference, multi-path effects, and noise (Shankar, 2002).

Microprocessor component

The microprocessor is the computational core for the on-board data processing. The critical specifications of a microprocessor are bus size, clock speed, memory, and power consumption. The bus size options are 8-, 16-, 32-bit defining the internal data bus of the microcontroller. Among these, the larger bus size is desirable. Because the clock speed defines the data processing rate, the faster processor is desirable. The tradeoff of higher clock rate is increased

power consumption. Large size of memory is important to run SHM applications that involve intensive on-board calculation.

Power component

A WSS requires a local power source. Low power consumption is a desirable characteristic of smart sensors if battery-powered. The power consumption depends on radio strength, clock speed of microprocessor, memory types, sensing and processing intensity. In each case, the power consumption should be optimized in terms of the monitoring purposes.

2.3.2 Platform selection

Because one of the first WSS platforms including LWIM-III was proposed in 1996 (Estrin, 2006), a variety of WSS platforms have been developed. Spencer *et al.* (2004) gives an overview of smart sensor technology development and their merits to improve SHM applications. In addition, the summary provided by Lynch and Loh (2006) cites over 150 papers on the topic of wireless sensors for SHM, and specifically examines 24 wireless platforms that have been proposed for SHM including academic prototypes and commercial-off-the shelf (COTS) units.

One of famous ancestor of the academic prototypes is the Berkeley family of Motes. These are open source hardware and software platforms with generic sensing interface. These platforms allow users to customize the sensors and the software to their application. The Berkeley family of Motes include Rene Mote (1999), Mica2 (Crossbow 2007a), MicaZ (Mainwaring, *et al.*, 2002), Telos (Polastre, 2005), iMote (Kling, 2003), and Imote2 (Kling *et al.*, 2005; Adler *et al.* 2005). Table 2.1 shows the comparison of several of the commercially available smart sensor platforms.

Table 2.1. Comparison of commercially available smart sensor platforms (Rice, 2009).

	Mica2 (Crossbow)	MicaZ (Crossbow)	Telos(B)/Tmote Sky (MoteIV*)	Imote2 (Crossbow)
Processor	ATmega128L	ATmega128L	TIMSP430	XScalePXA271
Bus Size (bits)	8	8	16	32
Processor Speed (MHz)	7.373	7.373	8	13 - 416
Program Flash (bytes)	128 K	128 K	48 K	32 M
EEPROM (bytes)	512 K	512 K	n/a	n/a
RAM (bytes)	4 K	4 K	1024 K	256 K SRAM 32 M SDRAM
Radio Chip	CC1000	CC2420	CC2420	CC2420
ADC resolution (bits)	10	10	12	n/a
ADC channels	8	8	8	n/a
Digital Interface	DIO, I2C, SPI	DIO, I2C, SPI	I2C, SPI, UART, USART	I2C, SPI, GPIO, UART, PWM, SDIO, USB
Active Power (mW)	24	24	10	44 @ 13 MHz 116 @ 104 MHz 570 @ 416 MHz
Sleep Power (μ W)	75	75	8	100
Primary Battery	2 x AA	2 x AA	2 x AA	3 x AAA

* Now Sentilla

After the development of the Berkeley family Motes, many proprietary wireless sensor platforms have been also proposed. Some of commercially available microprocessor platforms have been proprietary, emulating wired sensors in the sense that the users cannot embed on-board processing algorithms (Ember, 2008; MicroStrain, 2008; Millennial Net, 2008; Sensicast, 2008, Bridge Diagnostics, Inc. 2008). These are less desirable for SHM purposes which involve heavy custom-developed computation on board.

As opposed to the previous platforms which do not allow embedding on-board processing algorithms, MEMSIC's Imote2, has drawn attention mainly due to its high processor speed and large RAM size. The large RAM enables longer data measurement for accurate modal analysis, and the high processor speed facilitates computationally demanding SHM application on the WSS. Additionally, the Imote2 is equipped with Intel's low-power X-scale processor (PXA27x), in which the processor speed can be scaled based on application needs without a significant increase in overall power consumption. Because of these features, the Imote2 is open source WSS platform that is suitable for SHM applications.

2.3.3 Wireless sensor board for Imote2

Crossbow produced the wireless sensor board for Imote2, ITS400CA (Crossbow, 2007), which is also called as basic sensor board. The basic sensor board is designed to interface with the Imote2 platform to have three-axis accelerometer, temperature/humidity sensor, a light sensor, and a 4 channel A/D converter. The accelerometer chip is ST Microelectronic's LISL02DQ, which has $\pm 2g$ range and 12-bit resolution, resulting in a resolution of approximately 1 mg. This board provides four different sampling rates: 280, 560, 1120, and 4480 Hz. The temperature/humidity sensor is Sensirion's SHT15, and additional digital temperature sensor, TI TMP175. The light sensor is Taos's TSL2651. The basic sensor board has been the only available wireless sensor board for Imote2 until 2009. However, the basic sensor board had the limitations in coarse resolution and un-programmable sampling frequency, which are essential for SHM practice.

The SHM-A sensor board has been designed to overcome the limitations of the basic sensor board for monitoring civil infrastructure. The SHM-A sensor board is a partial achievement of the Illinois SHM Project (ISHMP), an interdisciplinary collaborative effort by researchers in

civil engineering and computer science at the University of Illinois at Urbana-Champaign (Rice *et al.* 2010). The SHM-A sensor board has all components the basic sensor board has: three axes accelerometers, temperature/humidity sensors, and a light sensor. The components of the SHM-A sensor board are identified in Figure 2.5.

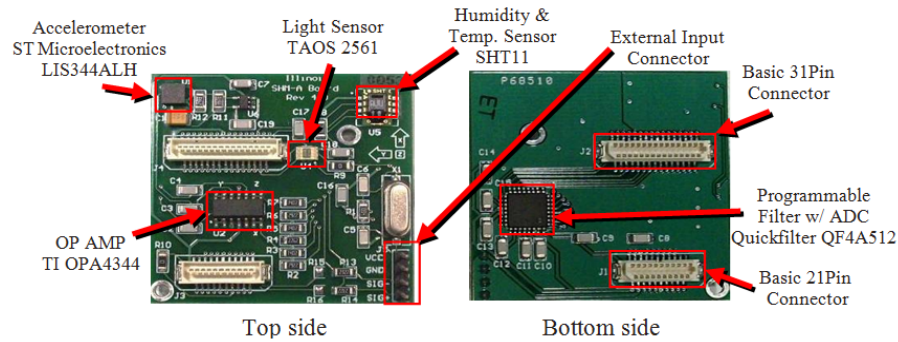


Figure 2.5. SHM-A sensor board (Rice, *et al.*, 2010).

The tri-axial accelerometer employed is the ST Microelectronic’s LIS344ALH capacity-type MEM accelerometer, which has a range of ± 2 g. The analog acceleration signals from this accelerometer are digitized by the Quickfilter QF4A512. The Quickfilter chip has a 4-channel, 16-bit Analog to Digital Converter (ADC) and programmable signal conditioner with user-selectable sampling rates and programmable digital filters. Therefore, the resolution of the accelerometer with the ADC is improved to 0.143 mg, and the noise floors are 0.3 mg for the x and y axes and 0.7 mg for the z axis. Additional temperature/humidity sensor is Sensirion’s SHT11, and the light sensor is Taos’s TSL2561. Noticeable feature of the SHM-A sensor board is an additional analog input which allows measuring data from many other types of sensors such as anemometers and strain gages.

The sampling frequency of the SHM-A sensor board is programmable. Four sampling frequencies (10, 25, 50, 100 Hz) have been pre-programmed on the SHM-A board for bridge monitoring applications. The lowest sampling rate, 10Hz, will be employed for monitoring the Jindo Bridge, of which the several first natural frequencies are smaller than 1Hz in chapter 6. The highest sampling rate, 100Hz, will be employed for monitoring the mid-size historic truss bridge in chapter 8. The sampling rate can be chosen nearly arbitrarily by designing appropriate filters for the QF4A512. More details on sensor board verification and comprehensive user guide can be found in Rice and Spencer (2010).

2.4 Software Development for WSSN

Another enabler of the WSSN for SHM applications is the development of programming languages and network communication strategies. This section provides an overview of TinyOS, the ISHMP Services Toolsuite, and the decentralized SHM strategy (Rice, 2009; Rice *et al*, 2009; Sim and Spencer, 2009).

2.4.1 TinyOS

TinyOS (www.tinyos.net) is the open-source operating system used on many smart sensors (Levis, *et al.* 2005). It utilizes a component-based architecture that makes it well suited to the WSS with memory constraints. For this reason, there is a large TinyOS user community and many successful implementations of sensor networks employing TinyOS. TinyOS applications are written in nesC, a C-like language. Numerical sub-functions can be written entirely in C and included with applications. Although TinyOS is widely used for WSSN applications, it is challenging to develop network control and application software for casual programmers. The potential complexity of software and the unique programming environment have limited the use of smart sensors for SHM applications.

2.4.2 ISHMP Services Toolsuite

ISHMP has developed service-based architecture (SOA) to support WSSN for SHM applications, named ISHMP Services Toolsuite. The main categories of the ISHMP Services Toolsuite include foundation services, application services, tools and utilities, and computational services and applications (Rice *et al.* 2009).

Foundation services

Services are defined as high level, self-describing building blocks for applications, and applications are stand-alone software which employ services or other applications as their components. The foundation services support the application and other services, including gathering synchronized sensor data, reliably communicating data, and providing accurate timestamps. For example, these foundation services can be used by applications to achieve synchronized sensing from multiple sensors.

Four main foundation services are the unified sensing, time synchronization, resampling, and reliable communication services. The unified sensing service provides a general-purpose sensing application interface. This service includes precise time-stamping of the data and supports various sensor boards. Sensor data is stored in 16-bit integers representing raw ADC values with 32-bit timestamps. A time synchronization service provides consistent global timestamps for measured data collected from a network of sensors. The resampling application service takes the sensor data and resamples them to a specified fixed sampling rate. Finally, the reliable communication (*ReliableComm*) service eliminates data loss when sending commands and data between sensor nodes.

Application services

The application services provide the numerical algorithms necessary to implement SHM applications on the Imote2s and can also be used independently. The application services include *SyncSensing*, Correlation Function Estimation (CFE), Eigensystem Realization Algorithm (ERA), Stochastic Subspace Identification Algorithm, and Stochastic DLV services,

etc. Among these, CFE and ERA services will be employed for development of an on-board modular SHM application in this research.

CFE: calculates the correlation functions of the accelerations between a cluster head and leaf nodes in a local community.

ERA: determines the modal properties – natural frequencies, mode shapes, damping ratio, and system matrices - from the correlation functions.

Tools and utilities

The application tools are necessary in large-scale long-term WSSN deployments to evaluate the conditions of the structure, to determine appropriate system parameters, and the utilities are necessary for maintaining the network to assess power consumption and wireless network communication quality, *etc.* The application tools are categorized as those operating on a single node and those operating on multiple nodes. The single node application tools used in this research are:

autocomm: An updated terminal program based on imote2comm for interfacing with the Imote2 through the Imote2 Interface Board's USB port. It uses the serial port UART interface to open a telnet-like connection with the mote. This enables automatic timestamping of file name of debugging log and the output file.

SnoozeAlarm: energy saving strategy using a sleeping mode, and frequent wake up for maintaining network functionality as described in Figure 2.6, which consists of cycles of deep sleep and wake up.

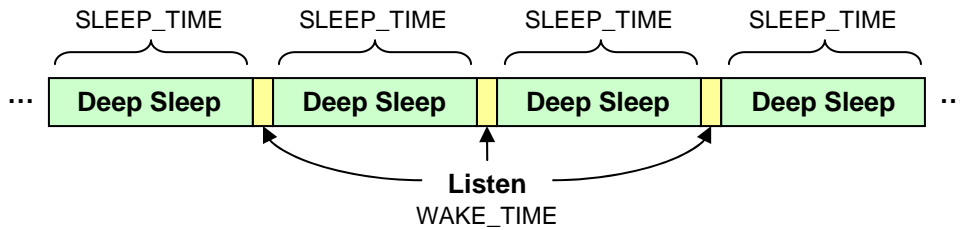


Figure 2.6. *SnoozeAlarm* timing (Rice and Spencer, 2009)

The application tools that involve multiple nodes in higher level network operation, used in this research are:

RemoteSensing: a network-wide distributed application, this tool is used to collect data from multiple sensors. *RemoteSensing* provides a high level of flexibility in the choice of network and sensing parameters. The network is synchronized prior to sensing, and timestamped data is collected. If the resampling option is selected, *i.e.*, the *RemoteSyncSensing* option is selected, the data is resampled using the *SyncSensing* service to account for any jitter or non-uniform time.

DecentralizedDataAggregation: A network-wide modal identification application from data acquisition to processing based on a decentralized hierarchical sensor network. This application supports multiple sensor clusters, in which data processing is conducted independently to other clusters. The outputs of the application are sensor data and their correlation functions in each local group.

Utility applications which are employed in this research are:

WakeUp: wakes up the remote leaf nodes from *SnoozeAlarm* mode. After wake up, they are ready to start measurement using *RemoteSensing*.

RemoteCommand Reset: reset the leaf nodes remotely.

RemoteCommand Vbat: measures the battery level of the leaf node remotely.

TestRadio: Tests the raw bi-directional communication quality between a sender node and a group of receiving nodes.

2.4.3 Decentralized SHM strategy

The use of WSS for SHM applications requires special attention in the design and selection of the associate SHM algorithms. Many SHM strategies require a dense array of sensors deployed throughout the structure. To this end, the adopted SHM scheme must be scalable to a large number of sensors. Scalability refers to the ability to increase the number of nodes in a network while maintaining proportional increases in cost and preserving data communication and processing efficiency (Rice *et al*, 2009). As shown in Figure 2.7, three primary approaches to data processing using wireless sensors have been employed to monitor civil structures, all of which impose limitations on network scalability and efficiency. Data processing refers to applying SHM algorithms such as modal analysis, system identification, damage detection, *etc*.

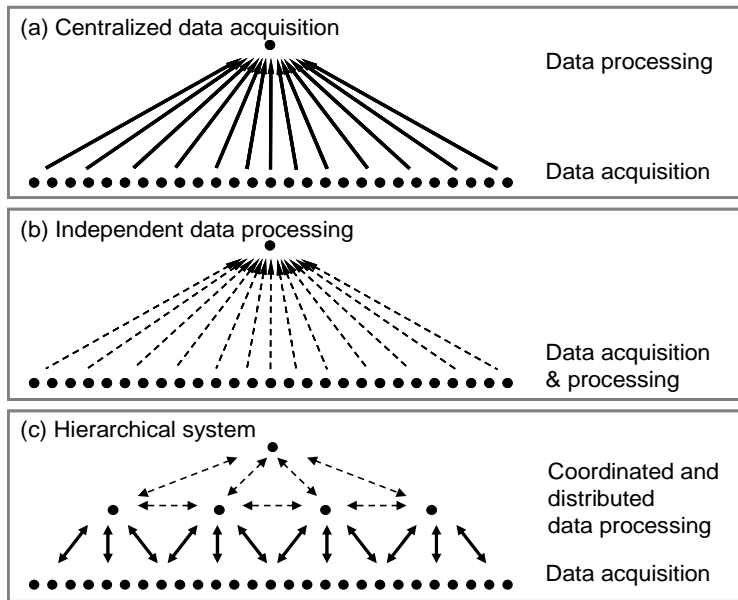


Figure 2.7. Network topologies (Nagayama and Spencer, 2007).

The first approach is to use a wireless smart sensor network as a direct substitute for a traditional monitoring system in a centralized data processing approach. To achieve results similar to that of a wired system using wireless sensors, the problems in accurate synchronization of the sensed data and effective power management must be addressed for stable long-term monitoring. In terms of the data management for this approach, the wireless system emulates a wired system by sending all of the recorded data to a central processing station for post-processing. Once the data has been centrally deposited and assuming adequate data quality that is sufficiently synchronized, traditional system identification and SHM algorithms can be applied. The primary limitation to this approach is that as the network size increases, the amount of data to be wirelessly communicated becomes unmanageable. This communication may take many times the amount of time it took to sense the data and will rapidly deplete limited network

resources. The approach does not take advantage of the local processing capabilities available on many smart sensor platforms and is a barrier to realizing a scalable wireless SHM system.

The second approach is to use the wireless smart sensor as an independent computation unit. Once data have been measured, the data are processed on each node for system identification and SHM algorithms without any data sharing before sending the results to the central base station. For example, single-node auto-regressive, wavelet transform and FFT are suitable to use in this approach (Sohn *et al*, 2002). Though the independent processing can reduce the amount of data transmitted, the spatial data between sensor nodes are lost. The lack of spatial information does not allow this strategy to be applied for SHM algorithms requiring mode shapes.

Gao and Spencer (2008) proposed a hierarchical approach to data processing to resolve the issues associated with the above approaches. In the Decentralized Computing Strategy (DCS), local sensor communities are formed in which data is shared and processed. This hierarchical approach takes advantage of the computational capacity of the smart sensors by pushing the computational burden out into the network while without sacrificing spatial information. This distributed approach significantly reduces the amount of required RF communication and is well suited for use with a scalable smart sensor network.

2.5 Summary

This chapter summarized the comprehensive background of this dissertation on structural health monitoring, bridge health monitoring applications, wireless smart sensors, and software development. The scope of damage in SHM was defined as linear isotropic damage, which can represent the stiffness reduction in metal or concrete. The vibration-based SHM algorithms were reviewed. Among numerous vibration-based damage detection methods, flexibility matrix based methods were shown stable performance. One of the promising flexibility-based methods was the DLV method. This method was evolved to overcome the limitation of each method into the latest version, the stochastic DDLV (SDDL V) method. This method is the basis of the modularized damage detection application for WSSN in this research. Additionally, SHM algorithms using model updating were reviewed in emphasis on the sensitivity-based parameter model updating. This model updating strategy will be used for condition assessment of historic truss bridge later.

As the emphasis of this research is on full-scale bridge health monitoring, various bridge monitoring efforts were reviewed. Several bridges were monitored to check the maximum structural responses in vibration, strain, and displacement. Full-scale damage detection tests were conducted on I-40 and Han-Nam bridges. Long-term continuous monitoring system was permanently installed on Hong Kong's bridges. However, the traditional wired sensor based SHM system is expensive and difficult to monitor such large bridges, which results in not many examples in full-scale bridge monitoring practices.

One of the solutions to overcome the cost problem while remaining the versatile functionality is wireless smart sensors (WSS). In this research, a SHM system using WSS will be developed. Therefore, the basic knowledge of components of wireless sensors, how to select the wireless

sensor platform for SHM application, and appropriate wireless sensor board for data measurement is given.

Along with the knowledge of hardware, the background of software framework for WSS is also given. The brief explanation of the TinyOS, a dedicated operating system for WSS, is followed by brief summary of ISHMP Services Toolsuite. The necessary services from the ISHMP Services Toolsuites were reviewed in terms of its three categories: foundation services, application services, and tools and utilities. Finally, three network topologies for WSS are reviewed and the pros and cons are reviewed. Among centralized data acquisition, independent data processing, and hierarchical system, the latter topology is suitable for the SHM application using WSS. Thus, the summarized background lays the foundation of the SHM system which will be described in this dissertation.

CHAPTER 3 STRAIN DAMAGE LOCATING VECTOR METHOD

Static strain measurements are common and reliable for SHM in practice. In this chapter, a strain-based DLV method is proposed combining the DLV method with static strain measurements. This method is based on the strain flexibility matrix, which is a mapping matrix between strain and force. The strain DLV method can use a limited number of sensors near the damage locations. For statically indeterminate structures, this method can detect the damage without the strain measurement at the damaged element (Jang *et al.*, 2007). Simple post processing and reasonable damage detection performance with incomplete measurements enable expedited bridge condition monitoring for practical applications. This chapter summarizes the theoretical development, numerical validation, and lab-scale experimental verification.

3.1 Theoretical Development of Strain DLV

Consider a discretized structure subjected to m loads in the vector $L = \{f_1, f_2, \dots, f_m\}$ and having n strain sensors near the damaged region as shown in Figure 3.1.

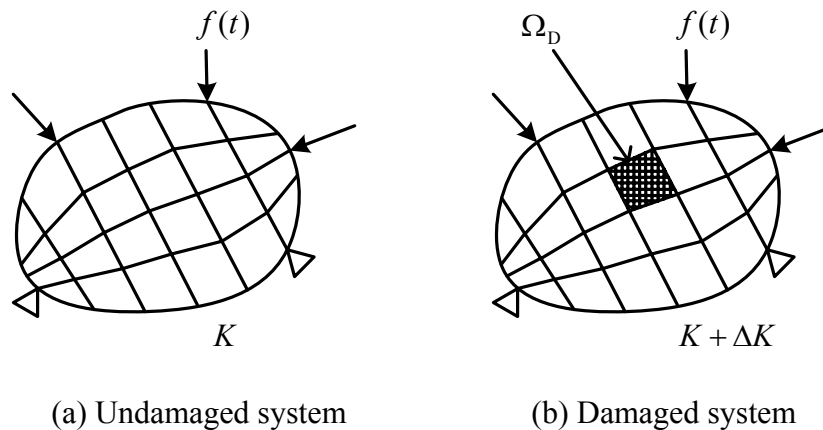


Figure 3.1. Generic description of undamaged and damaged structures.

A linear mapping between the load and strain is herein defined as the strain flexibility matrix, F^* ,

$$\varepsilon_{n \times 1} = F_{n \times m}^* L_{m \times 1} \quad (3.1)$$

Denoting the transformation matrix between displacement and strain, T , such that $\varepsilon = T d$, and $d = F L$, where d is displacement, and F is standard flexibility matrix,

$$F_{n \times m}^* = T_{n \times m} F_{m \times m} \quad (3.2)$$

The damaged and undamaged strain flexibility matrices for the system are given by F_d^* and F_u^* , respectively. Assume that a set of load vectors, L , exist that produce identical strains in the undamaged and damaged systems such that,

$$\varepsilon_u = \varepsilon_d \quad (3.3)$$

Substituting Eq. (3.1) into Eq. (3.3), one can write,

$$F_u^* L = F_d^* L \text{ or } (F_u^* - F_d^*) L = \Delta F^* L = 0 \quad (3.4)$$

Singular value decomposition of the change of the flexibility matrix, $\Delta F = U S V^T$ yields

$$\Delta F^* = T \Delta F = T (U S V^T) = T U \begin{bmatrix} S_1 & 0 \\ 0 & S_2 \approx 0 \end{bmatrix} V^T \quad (3.5)$$

where, U and V are unitary matrices, and S is a singular value matrix. S_2 consists of the singular values associated with the null space. Post-multiplying both sides of (3.5) by V yields:

$$\Delta F^* V = T U \begin{bmatrix} S_1 & 0 \\ 0 & S_2 \approx 0 \end{bmatrix} V^T V = T U \begin{bmatrix} S_1 & 0 \\ 0 & S_2 \approx 0 \end{bmatrix} I = T [US_1 \ 0] \quad (3.6)$$

$$\Delta F^* [V_1 \ V_2] = T [US_1 \ 0] \quad (3.7)$$

Comparing the second sub-matrix,

$$\Delta F^* V_2 = 0 \quad (3.8)$$

Here, V_2 is the set of strain DLVs spanning the null space of the change in the strain flexibility matrix. When the undamaged model is subjected to the strain DLVs, the elements having zero stress are candidate damage locations.

3.2 Damage Identification using Strain DLV

In practice, the stress at damaged elements may not be zero due to experimental noise and model uncertainties. Therefore, a threshold value to determine the existence of damage is employed. The candidate damage element is the j -th element, of which normalized accumulated stress is equal or less than a specific threshold such that

$$\text{Candidate damage element} \in \{\forall EL_j | \bar{\sigma}_j \leq tol\} \quad (3.9)$$

where, $\bar{\sigma}_j$ is the normalized accumulated stress (NAS) of each member such that,

$$\bar{\sigma}_j = \frac{\sigma_j}{\max_k(\sigma_j)} \quad \text{where} \quad \sigma_j = \sum_{i=1}^n \left(\frac{\sigma_j}{\max_k(\sigma_j)} \right) \quad (3.10)$$

and σ_j is stress of j -th element, k is the number of all elements, n is the number of DLV.

3.3 Numerical Validations

The performance of the strain DLV method is validated using a 53 DOF statically indeterminate truss model in Figure 3.2. The length of each bay is 0.4 m on each side. The supports are pinned on the left and roller on the right. The cross sectional area is $1.122 \times 10^{-4} \text{ m}^2$, Young's modulus is $1.999 \times 10^{11} \text{ MPa}$. Damage is simulated as 40% stiffness reduction at element 20.

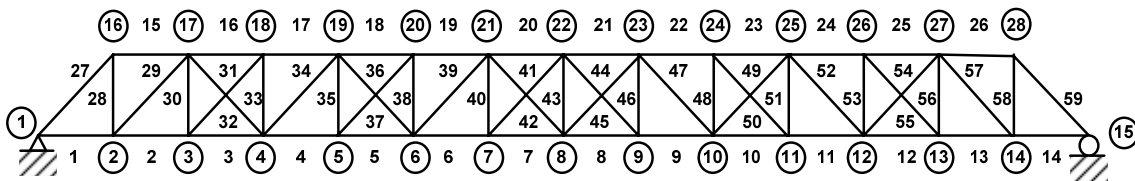


Figure 3.2. 2D planar truss model.

Measurement of all elements is practically intractable. To simulate an incomplete set of data are measured, and the static strains at the 13 lower chords are recorded when a static load is applied at node 2 to node 14, one by one. When the static load is applied at a node, each column of the strain flexibility is calculated by normalizing the measurements with the magnitude of applied load. After applying the strain DLV procedure as described previously, the NAS are calculated.

The calculated damage index, NAS, is shown in Figure 3.3. Though the strain is not measured at the damaged element 20, the NAS at element 20 is zero indicating the location of potential damage. Therefore, the performance of the strain DLV method is verified by this simulation.

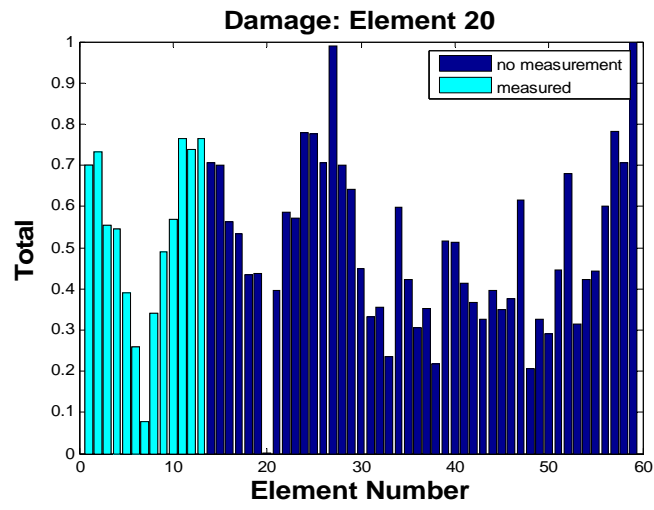
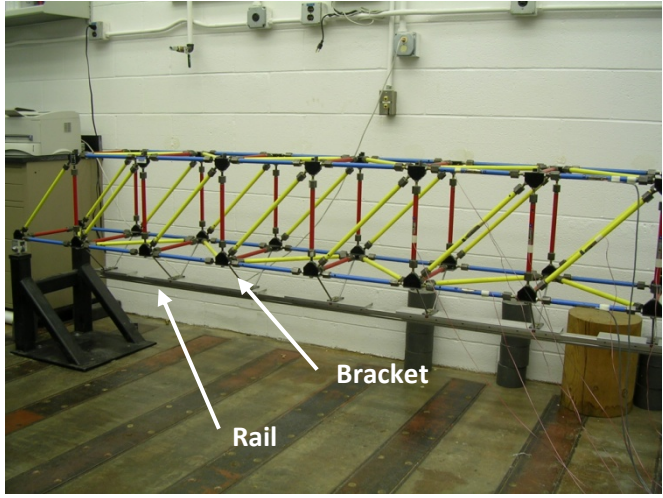
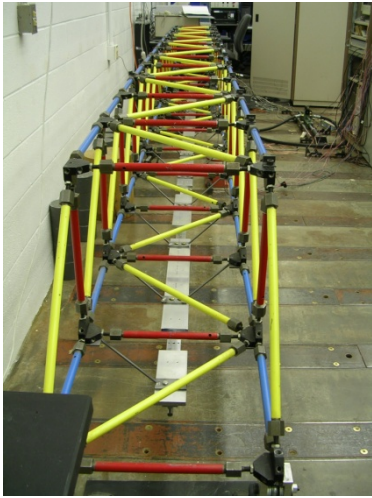


Figure 3.3. NAS: Damage at Element 20.

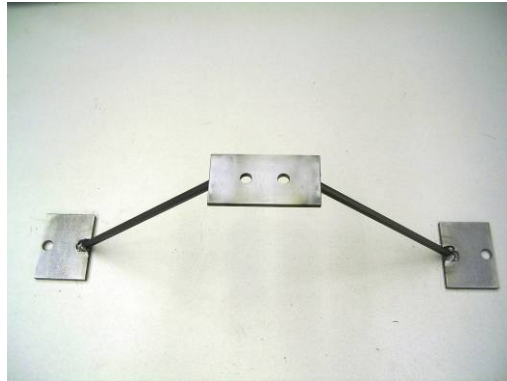
3.4 Experimental Verification of Strain DLV Method

The strain DLV method is experimentally verified using a truss bridge model. The truss has 14 bays, each of which is 0.4 m in length. The supports of the truss are a pin at the left end, and a roller at the right end. Each element has a tubular cross section with inner diameter of 1.09 cm and an outer diameter of 1.71 cm. More detailed description of this bridge is shown in Gao (2005).

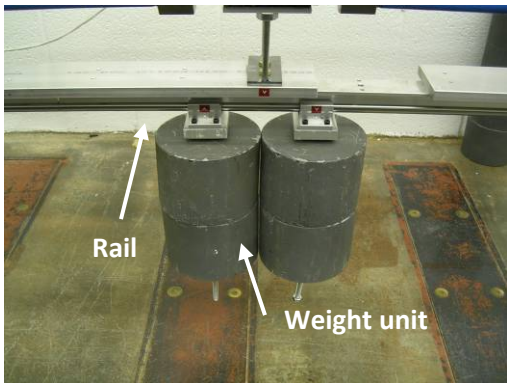
A moving load system is designed to simulate moving truck tests in the field. This loading system is a linear rail (Thomson® 60 linear shafts and support rails) bolted at 13 lower joints of the truss model with steel brackets (see Figure 3.4 (a)-(b)). A total of 36.29 kg (= 80 lb) steel weights are connected to the rail by a Thomson® linear bearing as shown in Figure 3.4 (c), so that the weights can travel smoothly along the shaft very slowly. Therefore, this system accurately simulates the moving load, which is required to experimentally measure the strain flexibility matrix.



(a) 3-D truss model with moving load system (UIUC, SSTL).



(b) Brackets.



(c) Moving weights.

Figure 3.4. 3D Truss model and Moving load system.

Foil strain gages are installed on thirteen bars 6~8, 19~21, 36~42, *i.e.*, which correspond to the elements in the box in Figure 3.5. The static strain responses of the elements are measured with a National Instrument® data acquisition system comprised of SCXI 1520 strain measurement modules and SCXI 1314 boxes. The resolution of the static strain is ~1 micro-strain for the system, which limits the quality of strain data.

The pseudo-static moving load tests have been conducted to calculate the strain flexibility matrices of the undamaged and damaged states. Two damage scenarios are considered: (1) damage in a horizontal element – element 6, and (2) damage in a diagonal element – element 39.

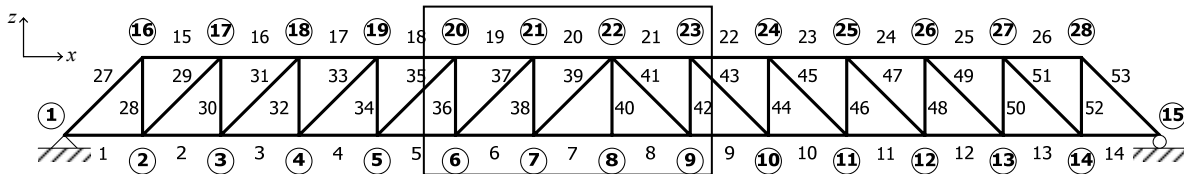


Figure 3.5. x - z plane of the truss model.

3.4.1 Case 1: damage to element 6

In the first case, damage on element 6 is simulated by replacing the healthy element with an element with 40% reduced cross-section. To simulate the situation when the strain measurement on the damage element is not available, strain data from the element 6 is not used in the damage localization process. After the moving load experiment, the measured strains are normalized by the magnitude of applied load to calculate the strain flexibility matrices. The strain DLVs are calculated from the change in the strain flexibility matrix. Each strain DLV was applied to a finite element model of the undamaged structure to obtain the stress level of the elements. The stress level from each strain DLV is summed up and normalized to calculate the normalized accumulated stresses (NAS).

Figure 3.6 shows the NAS of all elements. In this plot, elements 6 and 20 show low NAS levels. Note that the stress at a damaged element may not be exactly zero because of measurement noise, limited resolution, model uncertainty, *etc.* To accommodate these anomalies, a threshold of stress is set at 0.2; *i.e.*, the elements with stress less than 0.2 are regarded as candidate damaged elements. Using the threshold of 0.2, elements 6 and 20 are determined to be candidate damaged elements; the actual damaged element is element 6, and the low stress of element 20 is due to the truss geometry and force equilibrium. Therefore, the strain DLV method is seen to identify the damage.

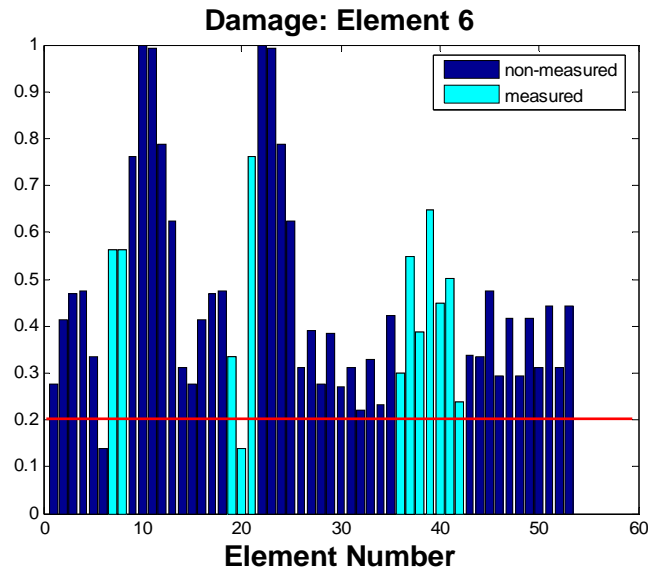


Figure 3.6. Normalized accumulated stress: damage at element 6.

3.4.2 Case 2: damage to element 39

The second damage scenario considers diagonal element 39. Because the diagonal elements carry a smaller part of the static load, the change in the strain flexibility is small; as a result, the signal to noise ratio is lower than that of Case 1. Again, an element with 40% reduced sectional

area is replaced with the health element at element 39. Here, the strain at the damaged element was not used for damage detection.

The NAS of all elements are shown in Figure 3.7. In this case, the element 39 has smaller NAS than the threshold, showing candidate damaged element. Element 41 has low NAS because of force balance with element 39 at node 22. Therefore, the performance of strain DLV method has been successfully validated without measuring damaged element.

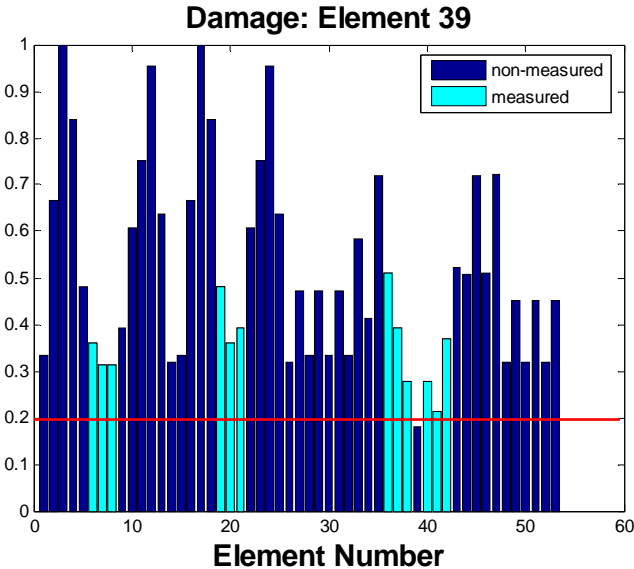


Figure 3.7. Normalized accumulated stress: damage at element 39.

3.5 Conclusion

The strain DLV has been developed by combining the DLV method to use of static strain data. The performance of this method has been verified through both numerical simulations and laboratory experiments using truss bridge structure. From these results, the damaged elements are successfully localized using a limited number of strain sensors, and in particular, without measurements at the damaged element. Despite of the limited resolution of strain measurement equipment, the potential of the strain DLV method for practical application to statically indeterminate bridges is successfully demonstrated.

CHAPTER 4 DECENTRALIZED SDDL V METHOD FOR WSSN

Various SHM strategies have been proposed recently that can be possibly implemented in the decentralized computing environment to WSSN. Some methods are based on changes in the experimentally determined flexibility matrix for the structure under consideration. However, the flexibility matrix contains only static information; much richer information is available by considering the dynamic flexibility, or receptance, of the structure. Recently, the stochastic DDLV (SDDL V) method has been proposed based on changes of dynamic flexibility matrices employing centrally collected output-only measurements.

This chapter proposes an implementation of the SDDL V method that is suitable for deployment on a decentralized network of smart sensors. Following a brief overview of the SDDL V method, new damage indices are derived that help to distill the wealth of information available through the SDDL V. The performance of the proposed approach is experimentally demonstrated using wired sensors that emulate a smart sensor network on a model truss structure. A comprehensive SHM application for WSS has been implemented based on the developed approach. The efficacy of the developed software has been experimentally validated using WSS.

4.1 Background

For completeness, the development of Dynamic DLV (DDL V) and SDDL V methods are summarized and illustrated in this section.

4.1.1 Dynamic DLV method

The DDLV method (Bernal, 2006) is a receptance-based damage identification method based on measured acceleration data. As was the case in Chapter 3, the applicability of this method is limited to linear damage (Lemaitre and Desmorat, 2005). This section provides the interpretation of the DDLV method from the application point of view and a brief illustration of the performance of the DDLV method, which is compared to the original DLV method.

The receptance matrix G , or transfer function matrix is a mapping matrix from force to displacement for a linear, time-invariant system, *i.e.*,

$$X = G \cdot U \quad (4.1)$$

where, X and U are the displacement and force, respectively, in the Fourier domain. A state-space representation of a linear system in continuous time for such a system can be represented as

$$\dot{z} = A z + B u \quad (4.2)$$

$$y = C_d z + D_d u \quad (4.3)$$

where the following time-dependent variables can be defined: $z = [z_1^T \quad z_2^T]^T = [x^T \quad \dot{x}^T]^T$ is the state vector, x is the displacement, \dot{x} is the velocity, u is the input vector, and y is the output vector. The following time-invariant matrices can also be defined: A is the state matrix, B is the input matrix, C_d is the output matrix for displacement, D_d is the feedforward matrix for displacement. By taking the Fourier Transform of Eqs. (4.2) and (4.3), the receptance matrix for this state space representation can be expressed as

$$G = C_d (I \cdot i\omega - A)^{-1} B + D_d. \quad (4.4)$$

Consider a discrete linear structure in two states as shown in Figure 3.1: one has a stiffness matrix of K , and the other has a stiffness matrix $K+\Delta K$, where ΔK denotes the reductions in some stiffness parameters due to damage. Here, $l(t)$ is the time history of load, and σ_D is the associated stress field over Ω_D . Let G_u and G_d be the experimentally estimated receptance matrices associated with the undamaged and damaged states, respectively, of this system; then, define the difference matrix, $\Delta G = G_u - G_d$.

The proposed method assumes the existence of a set of steady-state complex harmonic load vectors that induces identical steady-state displacement fields in the structure before and after damage. These load vectors can be written as

$$l(t) = l_k \exp(i\omega_k t) \quad (4.5)$$

where, l_k is a magnitude of the harmonic load as a function of the frequency, ω_k . The steady-state displacement fields for the undamaged and damaged structures are given respectively by

$$\begin{aligned} x_u(t) &= G_u(\omega_k) l_k \exp(i\omega_k t) \\ x_d(t) &= G_d(\omega_k) l_k \exp(i\omega_k t) \end{aligned} \quad (4.6)$$

Taking the difference between these two expressions yields

$$\{G_u(\omega_k) - G_d(\omega_k)\} l_k \exp(i\omega_k t) = \Delta G(\omega_k) l_k \exp(i\omega_k t) = 0 \quad (4.7)$$

Because (4.7) must be satisfied for all time, either $\Delta G(\omega_k) = 0$ or the matrix $\Delta G(\omega_k)$ is not full rank, and the vector l_k spans the null space of $\Delta G(\omega_k)$. Because $\Delta G(\omega_k) = 0$ implies no damage, the latter case provides the main focus. The vectors, l_k , spanning the null space of $\Delta G(\omega_k)$ are the DDLVs, for which the associated stress field is zero in the damaged region.

In practice, the DDLV can be computed from the null space of the experimentally determined receptance matrices for each frequency such that

$$l_k = l(\omega_k) = \text{Null}(\Delta G(\omega_k)) \quad (4.8)$$

Evaluating the receptance matrix at $\omega=0$ (*i.e.*, the static case) yields the flexibility matrix. Therefore, the DDLVs corresponding to this static case are the DLVs.

4.1.2 Illustration of the DDLV method

This section provides an illustration of the potential of the DDLV method. Consider a simple 3 DOF system, where each mass is 1000 kg, the stiffness of the first and second springs are 200 kN/m, the stiffness of the third spring is 150 kN/m, and the damping is 1 % of critical. Damage is assumed as a 25 % stiffness reduction in the second spring. Two DOFs, x_1 and x_3 , are measured to calculate the flexibility and receptance matrices for this structure.

The DDLV, the associated deflection shape, and the resulting normalized accumulated stress (NAS) plot for the static and dynamic cases evaluated at $\omega = 4\pi$ rad/sec = 2 Hz are compared in Figure 4.1. As can be seen, the NAS for the DLV case shown in Figure 4.1 (a) is zero for both spring 2 and 3, although spring 3 is undamaged. This false positive damage indication is because the adjacent element to the damaged element also has zero NAS. For the DDLV case shown in Figure 4.1 (b), only spring 2 shows zero dynamic NAS (DNAS). The DDLV is a complex vector that is a function of frequency that can induce a nonzero stress in element 3. Therefore, the damaged element has been accurately located without indications of false damage indication using the DDLV method.

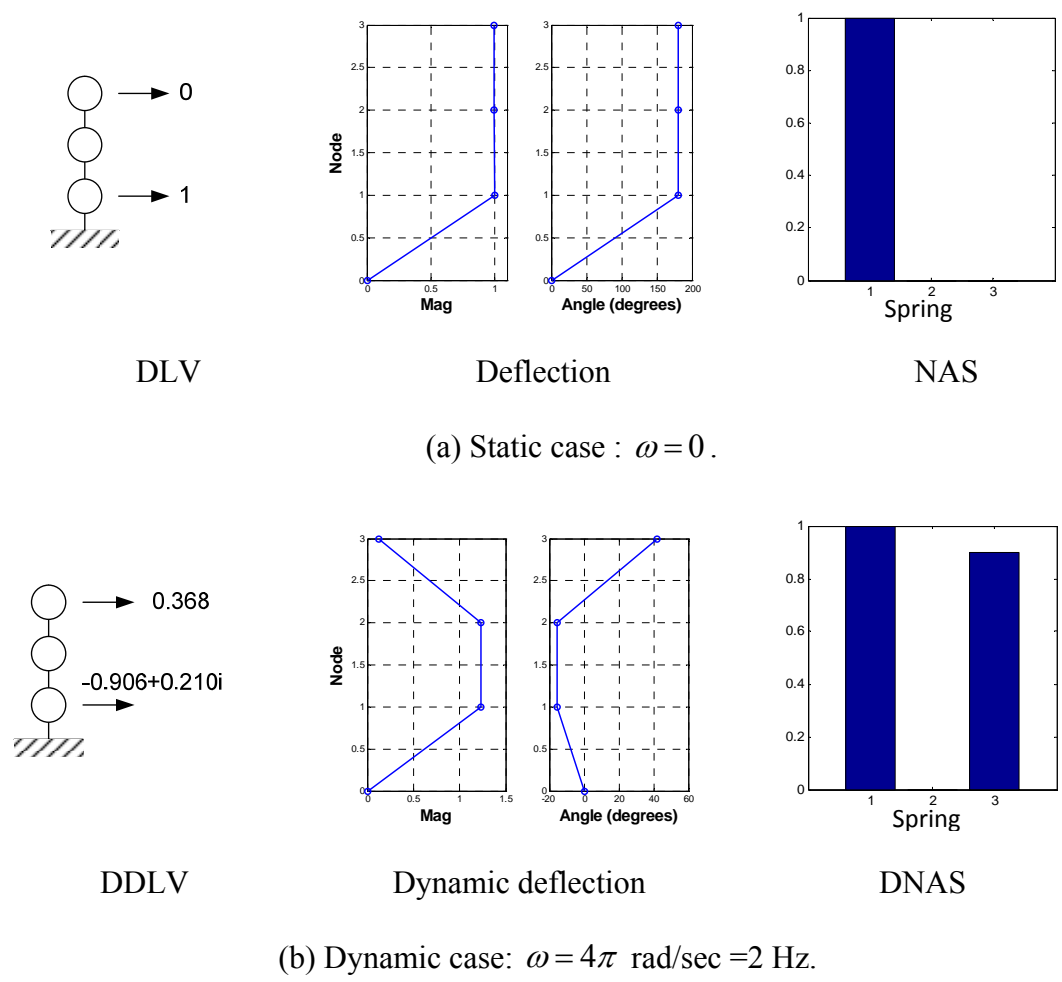


Figure 4.1. Comparison between DLV method and DDLV method.

4.1.3 Stochastic DDLV (SDDL) method

The SDDL method was proposed to extend the DDLV method to the case without input measurements (Bernal, 2005). For output-only implementation of the DDLV method, a surrogate matrix for the receptance matrix has been derived.

The surrogate for the receptance matrix can be obtained by defining a relationship between the system matrices such that

$$H_p B = L D_a \quad (4.9)$$

where H_p and L are given by

$$H_p = \begin{bmatrix} C_d A^1 \\ C_d \end{bmatrix} \text{ and } L = \begin{bmatrix} 1 \\ 0 \end{bmatrix} \quad (4.10)$$

Assuming that H_p is of full rank, B can be obtained from Eq. (4.9) as

$$B = H_p^\dagger L D_a \quad (4.11)$$

where H_p^\dagger is the pseudo-inverse of H_p because it is not a square matrix. Substituting Eq. (4.11)

into Eq. (4.2) yields

$$G = R D_a, \text{ where } R = C_a \{(I \cdot i\omega - A) A^2\}^{-1} H_p L \quad (4.12)$$

The change in the receptance matrix is

$$\Delta G \approx (R_d - R_u) D_a \quad (4.13)$$

Because D_a is of full rank, and ΔG is symmetric due to reciprocity, the null space of ΔG is the same as the null space of $\Delta R = R_d - R_u$. Therefore, the DDLVs are also in the null space of the difference in the surrogate matrices before and after damage, ΔR . These results allow the SDDL V to be used to localize damage when the input is not measured.

4.2 Development of Damage Detection Criteria

The application of the DDLV method is relatively straightforward for the simple 3DOF structure; however, interpreting the DDLV method may not be so easy for complex structures such as bridges. In this section, a numerical simulation on a 53 DOF truss is conducted to determine effective frequency region for damage detection. Based on the results, new damage indices for DDLV and SDDL methods will be proposed for robust damage detection.

4.2.1 Numerical simulation

Consider the 53 DOF truss structure as shown in Figure 4.2. Element 42 (see the dotted element in Figure 4.2) is assumed as 25% stiffness reduction. The accelerations of the nodes 2 to 14 along the lower chords were measured. 5% RMS noise has been added to the generated acceleration data to simulate the measurement noise.

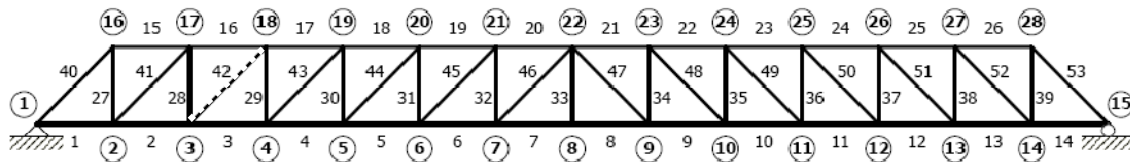


Figure 4.2. 53 DOF truss structure

Figures 4.3 show the DNAS of all elements for the frequency range of 0 – 200 Hz. Though the DDLV method gives much richer information, determining which elements correspond to candidate damage locations is challenging. Figure 4.4 shows the contour of the Figure 4.4. The NAS at element 42 is consistently low, but the NAS at some other elements change in terms of frequency.

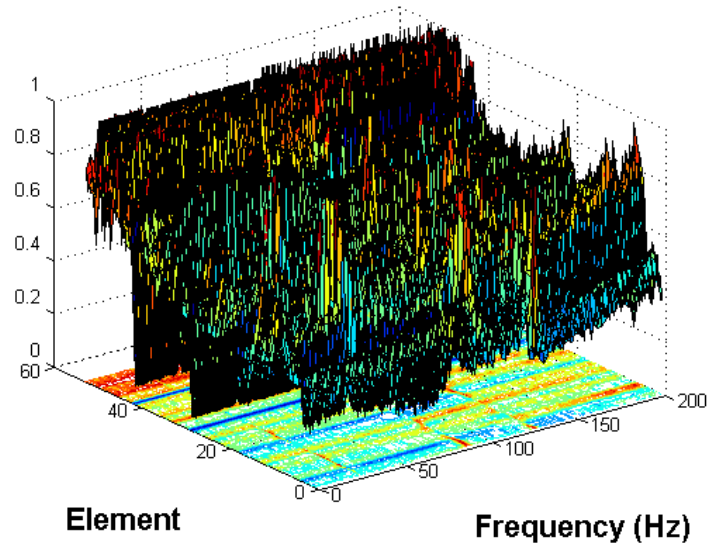


Figure 4.3. DNAS plot.

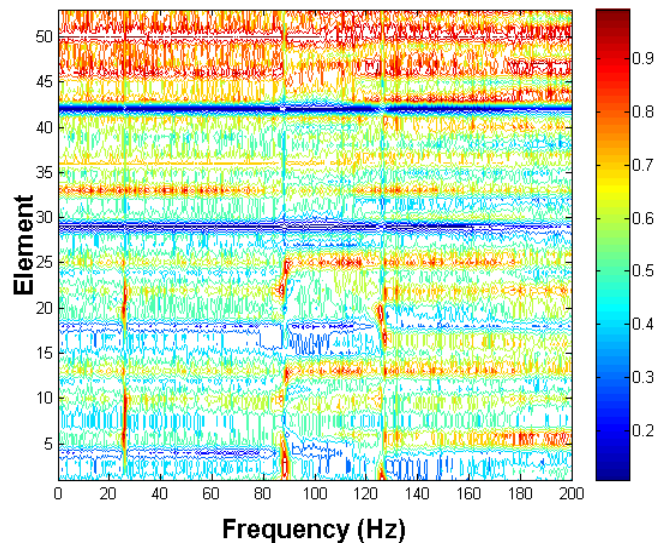


Figure 4.4. DNAS plot: contour

To find effective frequency regions, the NAS level at the damaged element is investigated. In Figure 4.5, the DNAS at the damaged element is less than 0.1 at most frequencies, while it is higher than 0.2 at some of the zeros of the receptance plot. At zeros, the dynamic responses

around the damaged element are small. If the data are measured in a noisy environment, the damage detection results may not be desirable because of decreased signal to noise ratio. Though the DNAS is not always higher at zeros, the DNAS at zeros are undesirable and should not be included in damage detection.

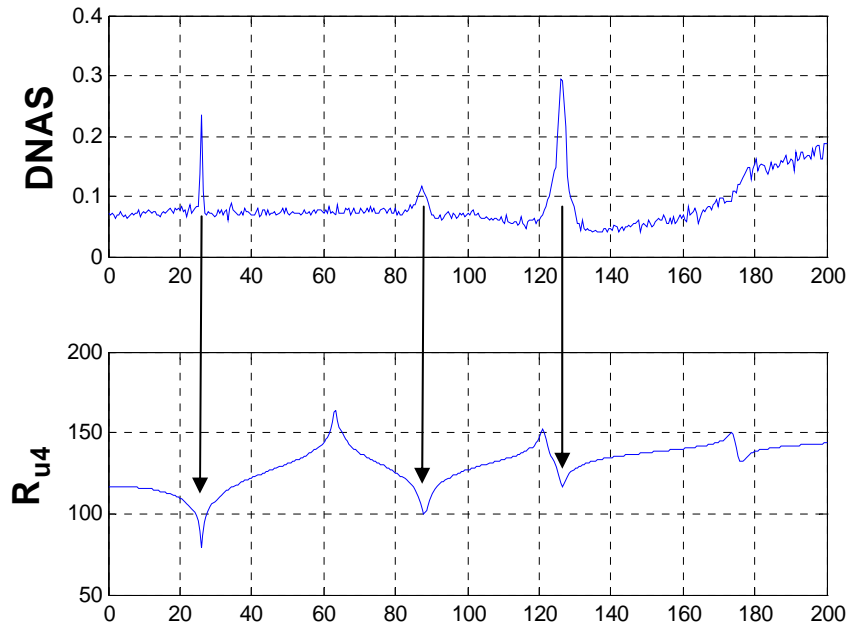


Figure 4.5. DNAS and Receptance

4.2.2 Damage Detection Criteria

The DDLV method provides much richer information on damage than the DLV method; however, the interpretation for complex structures was challenging as shown in section 4.2.1. For effective damage detection, new damage indices have been proposed based on the numerical simulation. The main idea is to calculate the DNAS at several frequencies and to manipulate them to have two damage indices.

The first damage index is the maximum stress index (MSI), which is defined as

$$\sigma_{j,\max} = \max_{\omega_i} \{ \sigma_{NA,j} |_{\omega_1}, \sigma_{NA,j} |_{\omega_2}, \dots, \sigma_{NA,j} |_{\omega_m} \} \quad (4.14)$$

where, $\sigma_{NA,j} |_{\omega_i}$ is a DNAS of the j -th element at $\omega = \omega_i$, tol is a tolerance level to determine the damage existence, and ns is the number of frequencies involved for DDLV calculation. The MSI is based on the fact that DNAS of the damaged element is always low.

By taking the maximum of the DNAS, the lower DNAS at undamaged elements can be delineated. For example, in Figure 4.4, element 18 has a varying level of DNAS in the 0-200Hz range. The DNAS of element 18 is as low as 0.2, but the maximum is 0.8 which cannot be falsely reported as a candidate damage element. However, one possible limitation of this index is that the DNAS at the damaged element may be higher than the DNAS at the undamaged element due to noise or measurement errors; *e.g.*, when the receptance matrix is calculated at the zeros of noisy data.

To avoid possible misleading decisions from the MSI when using noisy data, the average stress index (ASI) is also proposed, which is the average of DNASs at several frequencies,

$$\text{ASI (Average stress index): } \bar{\sigma}_j = \frac{1}{ns} \sum_{i=1}^{ns} \bar{\sigma}_j |_{\omega_i} \quad (4.15)$$

where, $\bar{\sigma}_j |_{\omega_i}$ is the DNAS at j -th element of i -th frequency. Because the DNAS at the damaged element are lower than undamaged ones in most cases, a few higher DNAS at the damaged element can be averaged out. By obtaining two damage indices, MSI and ASI, a more informed decision on damage location is feasible.

With two damage indices, the candidate damage element (CDE) criterion is defined as

$$\text{CDE} \in \{ \forall X_j | \sigma_j \leq tol \} \quad (4.16)$$

where σ_j is either ASI or MSI, X_j is j -th element. Therefore, the elements having the DNAS smaller than a threshold are the possible damaged elements. Therefore, the application issues of the SDDL method on complex structure have been addressed by providing efficient damage indices.

4.3 Decentralized SDDL Method

4.3.1 Decentralized damage detection approach

To implement the modified SDDL for WSSN, the network topology should be considered. Among the various network topologies introduced in section 2.4.3, the hierarchical system is suitable for damage detection algorithm because of its efficiency in network communication and capability to share the spatial information within a local community.

The decentralized damage detection employs the hierarchical system topology to divide a structure into a series of local communicates, where measured data is shared and processed. After processing, only cluster heads involve the communication with the gateway node. Because the bandwidth of communication is limited, the reduced number of nodes can prevent network overload.

Furthermore, the decentralized strategy is effective for damage detection, which is experimentally validated using the DLV method by Gao and Spencer (2008). Damage is a local phenomenon so that information far from the damage is not critical for damage detection. In a local community which potentially has damaged elements, the information in vicinity of damaged elements can only be used for damage detection. By overlapping some element in between local communities, the candidate damaged elements can be confirmed. Therefore, the

decentralized computing strategy has been applied to the extended SDDL method with new damage indices.

4.3.2 Decentralized SDDL method

The procedure of the decentralized SDDL method in each local community is shown. The first step is extracting the receptance matrices from the measured data before and after damage. The structure is assumed to be subjected to a stationary broadband random excitation; the acceleration responses are measured of the structure before and after damage. The system matrices are identified using output-only data based on the Natural Excitation Technique (NExT) in conjunction of the Eigensystem Realization Algorithm (ERA) (Farrar and James, 1997). The surrogate matrices are calculated from the identified system matrices at several specific frequencies. After the output-only modal analysis, the frequencies can be chosen except the zeros of the receptance.

The next step is damage detection using the SDDL method for each community. Various sets of SDDLs, $l(\omega_k)$, are determined from the singular value decomposition of the difference in the identified surrogate matrices before and after damage. The damage elements can be identified from the DNAS by applying $l(\omega_k)$ to a finite element model of the undamaged structure. The DNAS can be used to calculate the MSI and ASI, which indicates the candidate damaged area when they are lower than a threshold. A flow chart of the damage detection procedure using the SDDL method is shown in Figure 4.6.

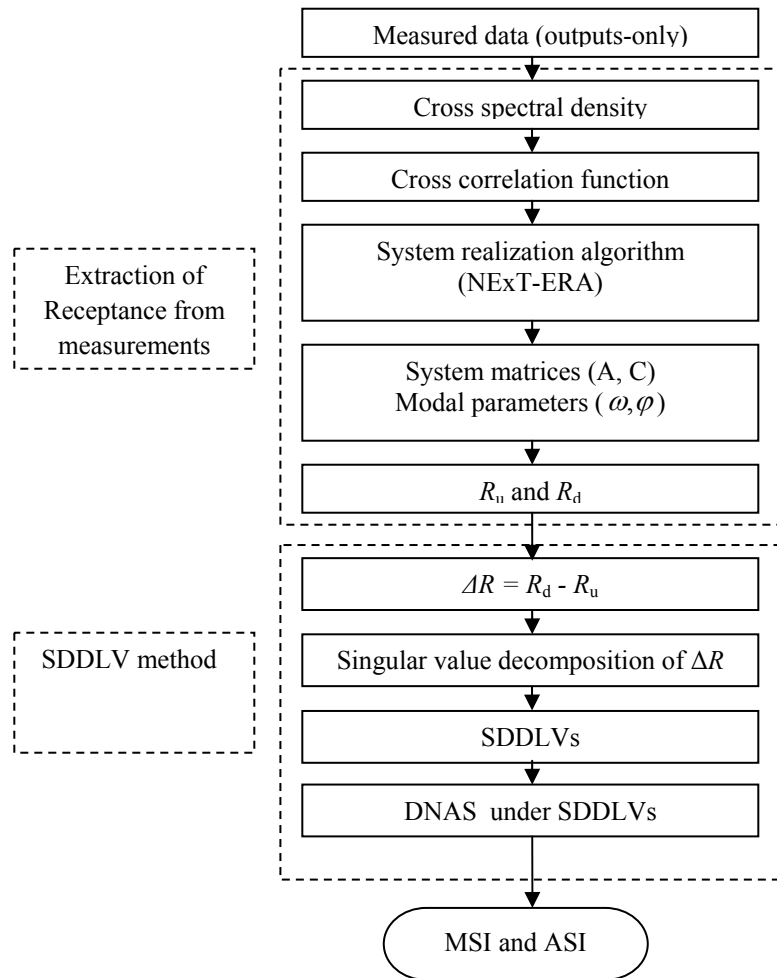


Figure 4.6. Damage detection procedure.

4.4 Experimental Validation

4.4.1 Experimental setup

The decentralized SDDL method has been validated on a lab-scale truss structure, which was used in section 3.4. Testing equipment included a shaker, spectrum analyzer, data acquisition system, and sensors. A Ling Dynamic Systems permanent magnetic V408 shaker is used to excite the model truss bridge. The maximum capacity of this shaker is 9.07 kgf, and the excitation frequency range is 5 ~ 9,000 Hz. A band-limited white noise was generated by a virtual function generator in the Siglab SL20-42. The National Instrument (NI)'s SCXI-1141, an 8-pole elliptic filter for anti-aliasing, and SCXI 1305 are connected to NI DAQpad 6052E, which performs analog to digital conversion of the acceleration signals with 16 bit resolution. A Labview program was written to control this data acquisition system.

The wired sensor system is used for this experiment to emulate the smart sensor network to demonstrate the potential of the proposed method. PCB 353B33 sensors are installed to measure acceleration. The nominal sensitivity of the sensors is 100 mV/g, the range is 1- 4,000 Hz, and a peak amplitude range is ± 50 g. For the input measurement, PCB 208C02 load cell is installed at the tip of connecting bar between the shaker and the structure.

The decentralized computing strategy is applied for damage detection of the truss bridge. The structure is divided into 11 local communities as shown in Figure 4.7. The local communities are aligned in linear manner. Between two adjacent communities, 4 nodes are overlapped for robust damage identification endowing redundancy. The candidate damage location can be identified the repeated alarm from those adjacent groups.

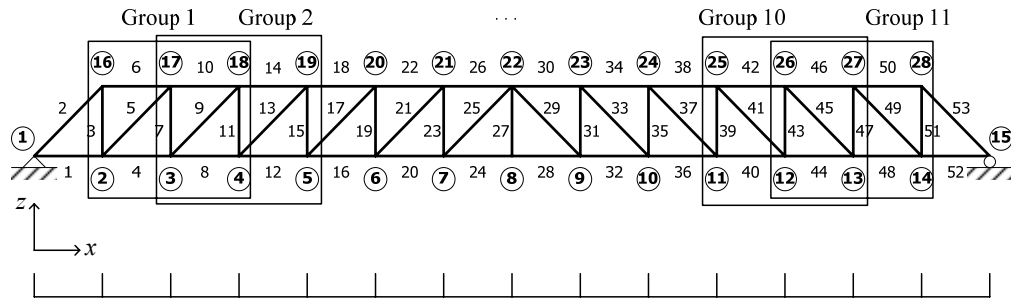
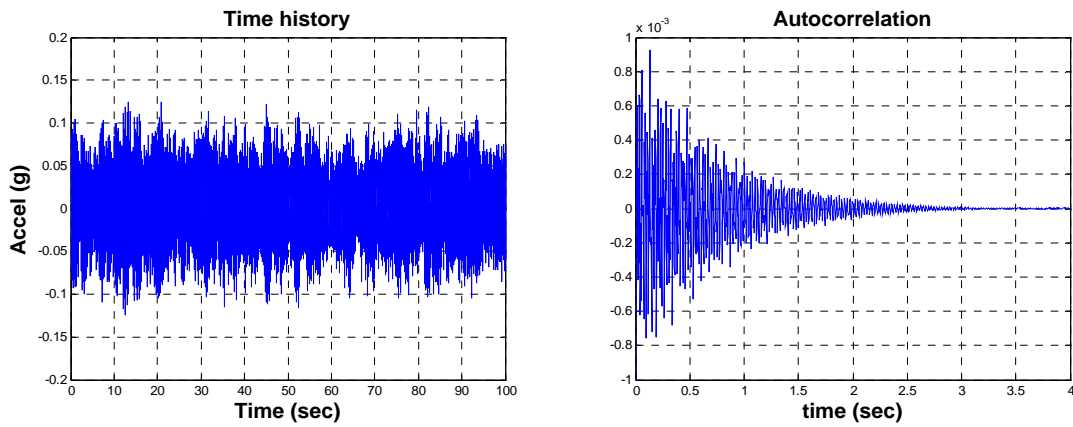


Figure 4.7. Side view of truss structure.

In each group, 12 accelerations are measured at 6 nodes: 6 transverse and 6 vertical directions. Damage is simulated as a 40% stiffness reduction. The tolerance value for the damage detection is 0.3. Two damage scenarios are considered; single damage at element 8, and damage at elements 9 and 20.

4.4.2 Single damage case: element 8

For the single damage case, the damage detection procedure using measurements are summarized. The acceleration time history and the auto-correlation function in the vertical direction at node 2 in group 1 are shown as an example of time histories in Figure 4.8. The system matrices are calculated using the NExT-ERA method. Because the SDDL method employs output responses only, the cross-correlation of each sensor location and the reference sensor is used as input for the ERA method. The surrogate receptance matrices before and after damage are obtained from the system matrices. The SDDL are obtained by singular value decomposition of the change of the surrogate receptance matrices. The SDDLs are applied into a 3D FE model, and the DNAs are calculated by structural analysis.



(a) Time history

(b) Autocorrelation function.

Figure 4.8. Vertical direction data at node 2

To find the frequencies of averaging, a cross spectrum of node 2 to the input point is plotted in Figure 4.9. To avoid zeros, 4 frequencies from 0 to 60 Hz in 20 Hz intervals have chosen to determine damage indices.

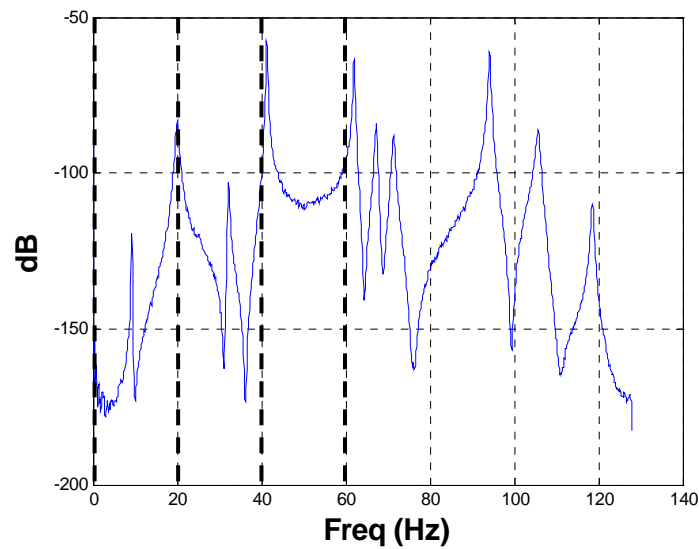


Figure 4.9. Cross Spectrum at node 2

The MSI and ASI for group 1 and 2, which include the damaged element are shown along with NAS in Figure 4.10. The first row is the NAS of the SDLV method when the flexibility matrices are used. The second and third rows are the MSI, taking the maximum of DNAS, and ASI, average of the DNAS of each element. The threshold is chosen as 0.3, as used in Gao and Spencer (2009).

In group 1 and 2, the MSI and ASI of element 8 is less than 0.3, indicating possible damage locations. The NAS of group 2 is lower than 0.3 at element 14 additionally, which is false positive damage indication. Also, the groups 5, 8, 9 show a false positive damage indication when the SDLV method is used, while the MSI and ASI did not show (see Figure 4.11). Therefore, the modified SDDL method using MSI and ASI has shown robust performance than the SDLV method.

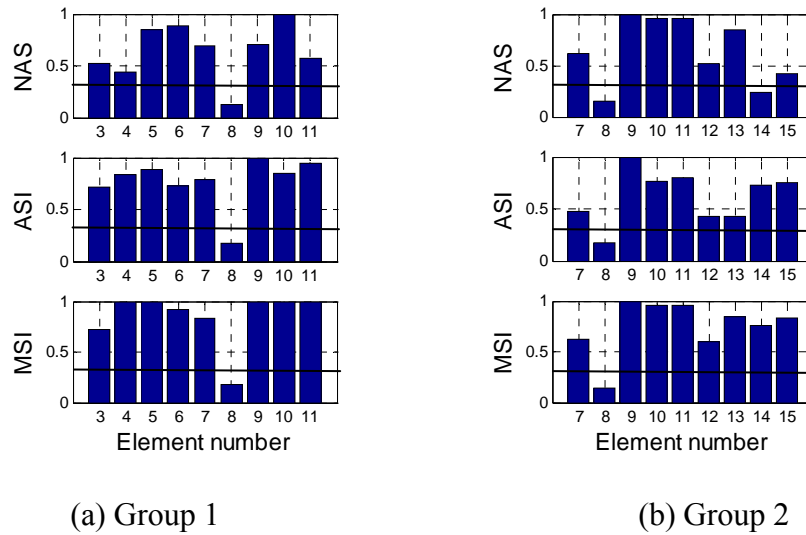
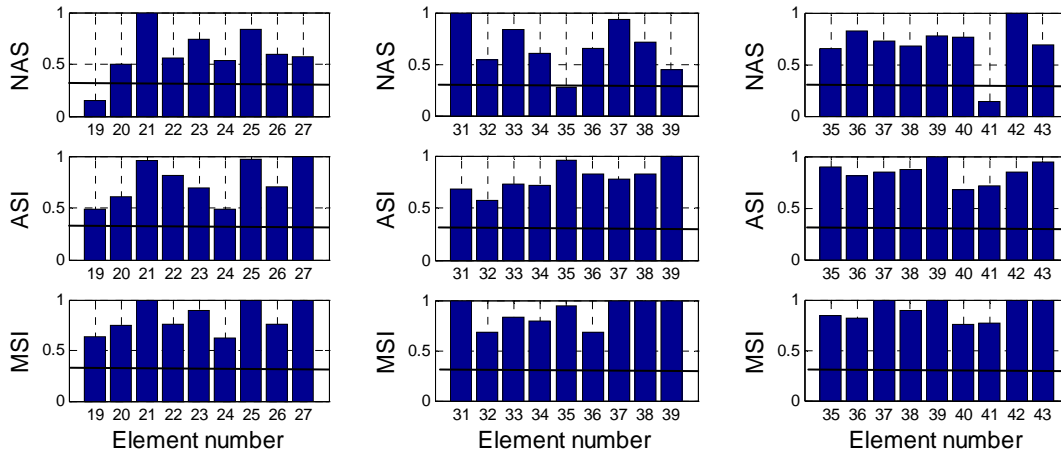


Figure 4.10. Comparison for Group 1 and Group 2: damage at element 8.



(a) Group 5 (b) Group 8 (c) Group 9

Figure 4.11. NAS of groups 5, 8, and 9: damage at element 8.

4.4.3 Multiple damage case: elements 9 and 20

The multiple damage case at element 9 and 20 is also considered. The decentralized SDDL method has been conducted using the measured acceleration data with the same parameters. The damage indices for the SDLV and SDDL methods are shown in Figure 4.12 for group 1, 2, and 4, which contains the damaged elements. For these groups, no false positive indication is seen. However, for other groups 3 and 7, the SDLV method reports false positive detection (see Figure 4.13). This shows that the MSI and ASI can delineate the true potential damaged elements from the low DNAS from force equilibrium. Therefore, the performance of the decentralized SDDL method has been experimentally demonstrated for the multiple damage case showing more accurate damage indication.

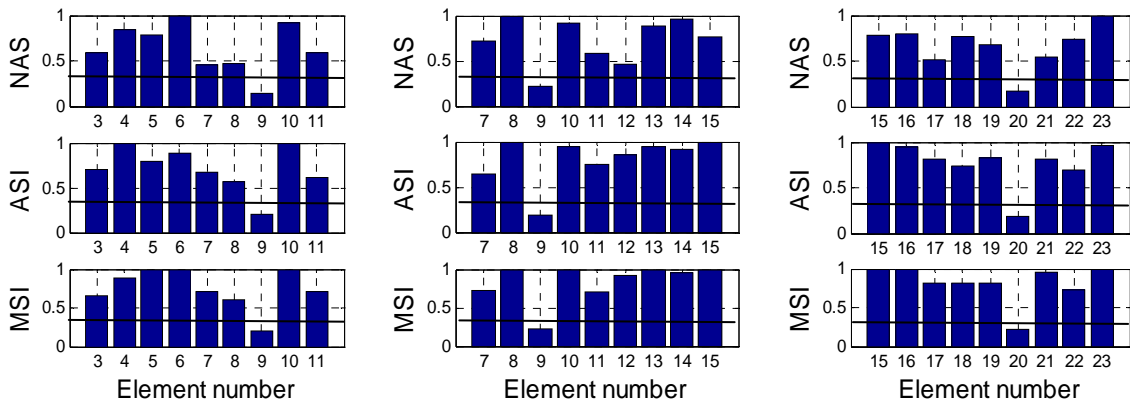


Figure 4.12. Comparison for Group 1, 2, and 4: damage at elements 9 and 20.

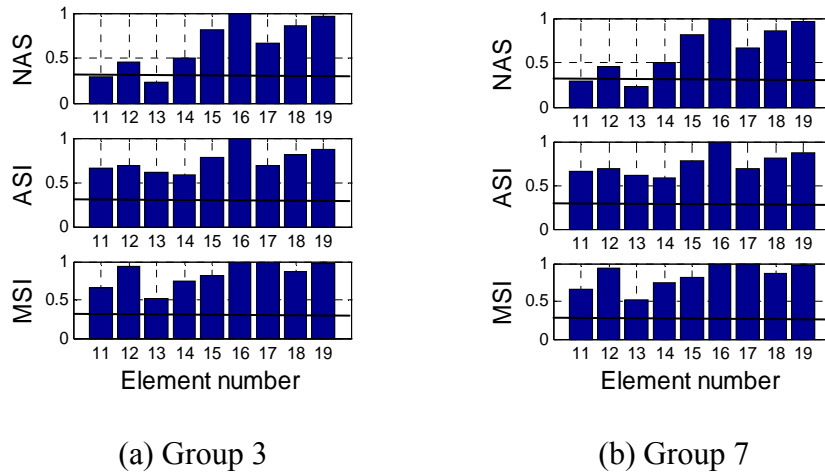


Figure 4.13. NAS of groups 3 and 7: damage at elements 9 and 20.

4.5 Implementation of Decentralized Damage Detection Method on WSSN

This section discusses implementation of the decentralized receptance-based damage detection strategy on the Imote2 sensor platform. The development is developed based on the ISHMP Services Toolsuite, combining *DecentralizedDataAggregation*, system identification using NExT-ERA, and the decentralized SDDL V method. A laboratory experiment using the three-dimensional truss structure, which was also used for the validation of the approach using the wired sensor system in 3.4, with a network of Imote2 sensors for decentralized damage identification.

4.5.1 Decentralized SDDL V service

The receptance-based damage identification method is implemented as a damage detection service based on nesC (Gay *et al*, 2003). First, the input file including the state space realization matrices (system matrix, A , and output matrix, C) and modal parameters of undamaged and damaged states of a target structure is prepared. Using the input information, the receptance matrices of the intact and damaged states are calculated in the second step. By this point, structural information is ready for damage detection process.

Next, the damage location is to be determined by the decentralized SDDL V method. In step 3, the SDDL V is calculated by singular value decomposition of the ΔR matrix ($=R_u - R_d$). In step 4, this SDDL V is applied to the undamaged FE model to obtain the DNAS of all elements. However, it is time consuming and computationally costly to run a structural analysis to obtain the DNAS of all elements on the wireless sensor node. To simplify the structural analysis, a force-to-stress (F2S) matrix is pre-defined as

$$H_{s f(m \times n)} = T_{(m \times n)} \cdot R_u(\omega_i)_{(n \times n)} \quad (4.16)$$

where, T is the transformation matrix from displacement to stress. $R_u(\omega_i)$ is the receptance matrix of the undamaged state at each frequency ω_i , while m is the number elements, and n is the number of degrees of freedom of the discretized FE model. The DNAS can be computed by multiplying the F2S matrix with the DDLV.

The final step is obtaining the damage indices, MSI and ASI from Eqs. (4.15) and (4.17), based on the DNAS. The MSI and ASI are stored in a text file in this process. The decentralized SDDL service is a module to run the damage detection so that the service can be utilized to make a comprehensive software package for WSSN with other foundation and numerical services. The flow chart of this service is shown in Figure 4.14.

The richer dynamic information calculated in the SDDL service provided better spatial resolution; in turn, the complexity of the SDDL service is considerable. The complexity of the SDDL service can be expressed as,

$$C_{\text{SDDL}} = N_{\text{freq}} \cdot N_{\text{out}}^2 \cdot N_{\text{mode}} \quad (4.17)$$

where, N_{freq} is the number of selected frequencies, N_{out} is the number of output measurements, and N_{mode} is the number of identified modes. This calculation takes place when calculating the surrogate receptance matrix using the output-only modal information.

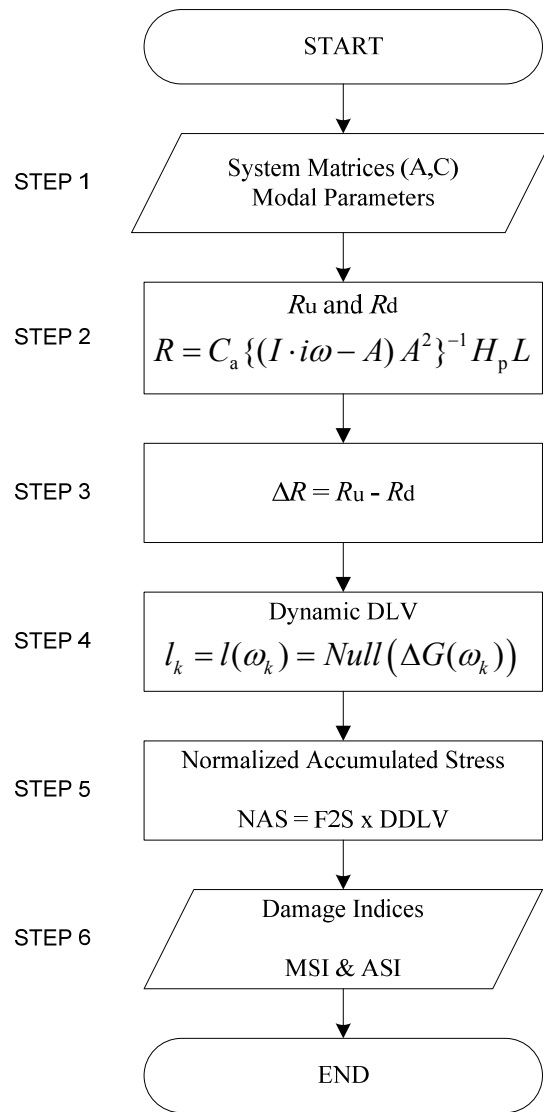


Figure 4.14. Flow chart of SDDL V service.

4.5.2 Decentralized damage identification

Using the decentralized SDDL V service, a high-level comprehensive decentralized damage detection application for WSSNs, *DecentralizedDamageIdentification* (DDI), has been developed. An input file contains state space matrices (A and C), modal parameters of the undamaged state of the target structure, as well as the F2S matrix and other runtime parameters in the first step.

The second step is the *DecentralizedDataAggregation* (DDA) (Sim and Spencer, 2009), which conducts the synchronized sensing, and estimates correlation functions in each local sensor community. The cluster-heads retain the correlation functions for further analysis, while all leaf nodes go to deep sleep to conserve power.

The step 3 is the system identification service using NEXT-ERA. On the cluster head in each group, the correlation functions are used to determine the modal properties including natural frequencies, mode shapes, and state space matrices (A and C) of the damaged state. Note that only local modal properties can be obtained because each cluster-head only collects local information.

The next step is conducting the decentralized SDDL V method based on the calculated modal parameters of undamaged and damaged states. After calculation, cluster heads send the damage indices to the gateway node in the last step. The final output is transferred to the base station. The flowchart the application is shown in Figure 4.15.

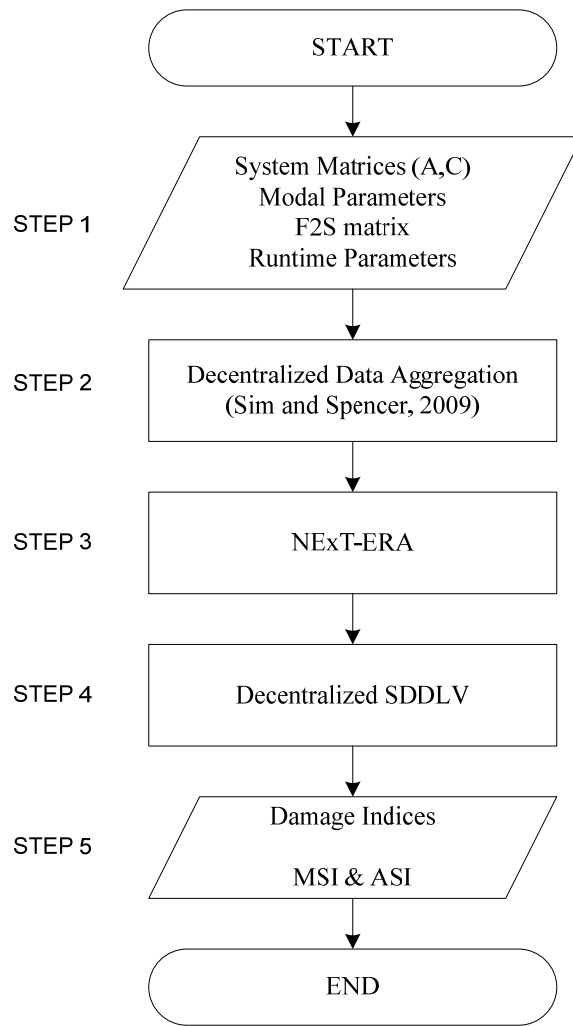


Figure 4.15. Flow chart of DDI application.

To run the application, three types of wireless smart sensors are employed: a gateway node, a cluster-head, and a leaf node (see Figure 4.16). The gateway node is connected to the base station computer to communicate with the leaf nodes. The cluster-head is a manager of a local community, which coordinates the in-group communication during system identification. After obtaining the data from leaf nodes, the cluster head is computing the modal properties. The main tasks of the leaf nodes are sensing and on-board computation.

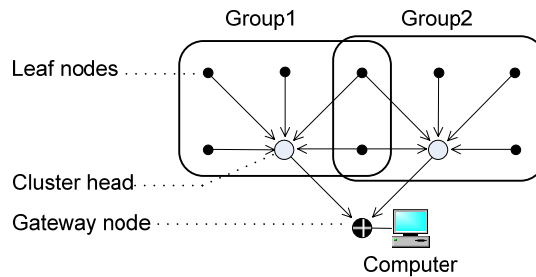


Figure 4.16. Types of wireless smart sensors.

The flow of software is controlled by a state machine as shown in Figure 4.17. The state is a series of short flags representing each step of an application in nesC. The default states for all nodes are initially set to ‘DISABLE’. Next, the DDA is executed in sensing and correlation function estimation. The detailed state machine of the DDA is found in Sim and Spencer (2009). After DDA is done, the state of the gateway node is set to ‘SENDDCSMSG’ to send the necessary parameters for the subsequent system identification and damage detection steps to the cluster heads. The states of the cluster heads become ‘CALCERA’ for system identification, then ‘CALCSDDL’V’ for the damage detection. When the on-board computations are completed, the state of each cluster head changes to ‘SENDDATA’, and the cluster head sends the damage detection results to the gateway node. When the data transfer is completed, the state of the gateway node is set to ‘PRINTDATA’ to transfer the data to the base station.

A comprehensive damage detection application was developed based on nesC. Detailed flow chart and the state machine of the application were also shown. The DDI application is the first comprehensive SHM application using modular services in ISHMP Services Toolsuite.

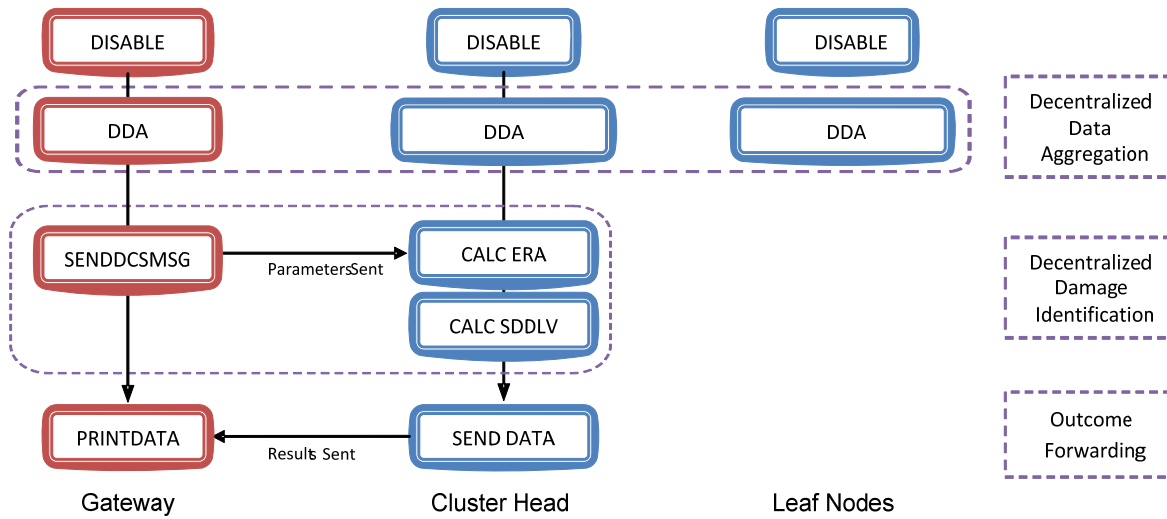
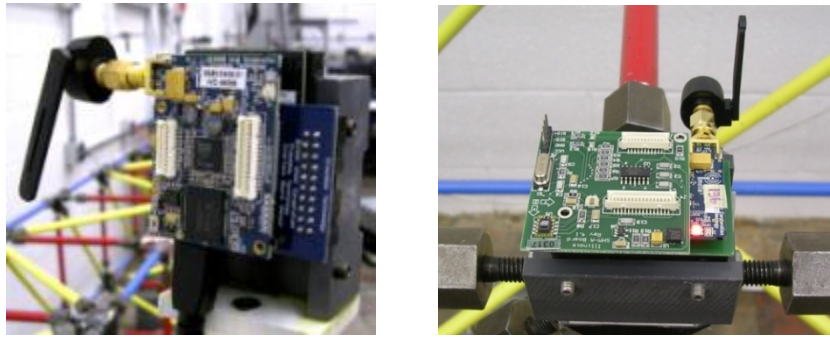


Figure 4.17. State machine in DDI.

4.5.3 Experimental validation

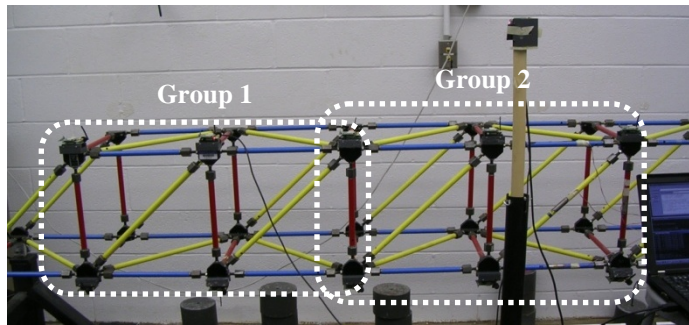
In this section, the efficacy and performance of the DDI is validated using the previously discussed lab-scale truss structure. MEMSIC’s Imote2 (Crossbow, 2009) is employed as the wireless sensor platform, and SHM-A sensor board (Rice and Spencer, 2009) is stacked on the Imote2 to measure the acceleration. The detailed information on the specification and functionality of the wireless sensor components was shown in Section 2.3. The gateway node consists of an Imote2 on the IIB interface board as shown in Figure 4.18 (a). The cluster-head and leaf nodes consist of a battery board, an Imote2 platform, and an SHM-A sensor board (see Figure 4.18 (b)). A local group consists of one cluster-head and five leaf nodes. All nodes have been loaded with the DDI application.

In total, 10 leaf nodes are installed at the nodal points. Each group includes 6 leaf nodes, and 2 leaf nodes are overlapped. Among all groups, two local groups adjacent to damaged element are examined (see Figure 4.19 (a)). The damage is simulated a 40% reduced section as shown in a dotted area of Figure 4.19 (b).

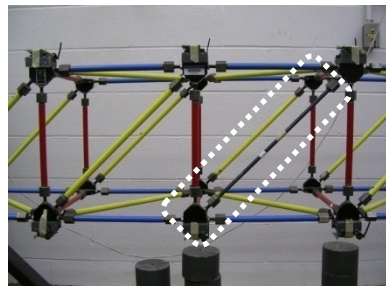


(a) Gateway node. (b) Cluster-head and leaf node.

Figure 4.18. Wireless smart sensor types.



(a) Testing setup.



(b) Damaged element

Figure 4.19. Testing setup.

The parameters for the DDI are set for measurement, modal analysis, and damage identification. For the synchronized acceleration measurement, a total of 22,528 data points in

the horizontal and vertical directions have been measured at 560 Hz with cutoff frequency of 140 Hz. This cutoff frequency captures four major lower natural frequencies of this truss model. For system identification using NExT-ERA, the size of the Hankel matrix is 50×50 and the number of FFT points chosen to be 2048. The lower 4 modes are employed for calculating the receptance matrices. The receptance matrix is determined at 0 and 20 Hz to obtain the damage indices. The threshold value to determine damage existence is set at 0.3 as the previous experiment using the wired sensor system in section 4.4.

The damage detection results for Groups 1 and 2 are shown in Figure 4.20. The top figure is the NAS from the SDLV method, and the center and bottom figures are the results from the SDDL-V-ASI and SDDL-V-MSI methods. Element 9 has lower damage indices than the threshold value, 0.3; therefore, the damaged element has been successfully identified using the developed method. In the results for group 2, the NAS and ASI at element 11 are less than the threshold value, while the MSI at element 11 are higher than 0.3. The element 11 is cannot confirmed as damaged element, because the damage indices of element 11 in group 1 are higher than the threshold. The small NAS of element 11 can be explained by force balance of the truss structure at the vertical direction at node 18, because the current sensor configuration indicates the SDDL-Vs are only applied in the vertical directions at the lower chords. The similar example was shown in Gao and Spencer (2009). The dynamic information at 20 Hz assisted to delineate the low damage index due to force equilibrium, from candidate damage. Therefore, the element 9 is confirmed as candidate damage element for this experiment.

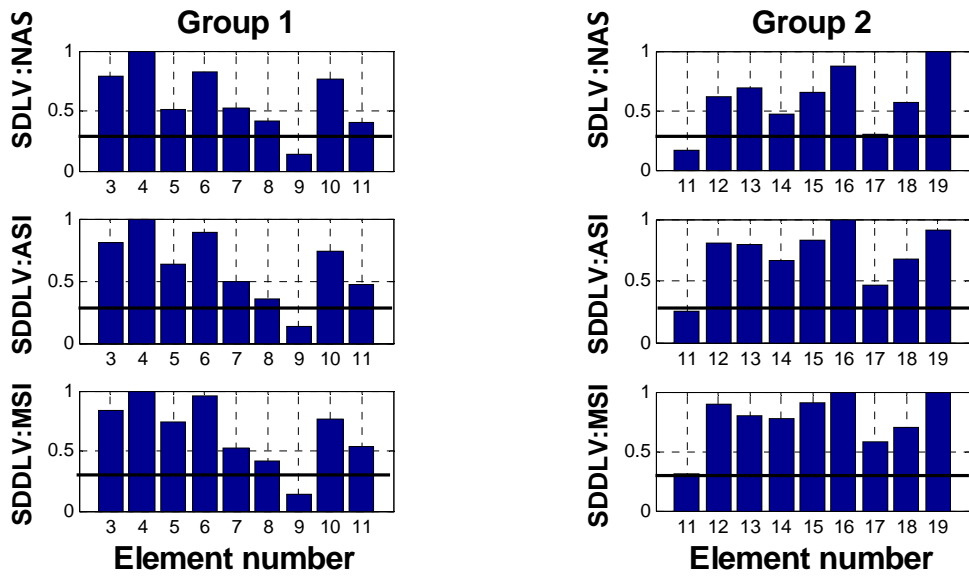


Figure 4.20. Damage indices.

4.6 Conclusion

A decentralized receptance-based damage identification method has been developed by combining the SDDL_V method and a new damage index for robust SHM using WSSN. The approach has been validated first on a lab-scale truss bridge model using a wired sensing system to demonstrate the performance. The results showed that the proposed strategy may reduce the false positive damage indication problem showing higher DNAS for undamaged elements than the NAS of undamaged elements; therefore, localized damage can be achieved more accurately than with the SDL_V method. The decentralized SDDL_V method has been implemented as a damage detection service for WSSN. Subsequently, the damage detection service has been combined into a comprehensive damage detection application. The DDI application has also been validated on the lab-scale truss bridge using Imote2-based WSSN.

CHAPTER 5 FULL-SCALE VALIDATION OF WSSN ON SIEBEL STAIRCASE

Before deployment of any SHM system on full-scale bridge structure, the usability of the wireless smart sensor network in large-scale structure should be determined. A separate base station should be prepared for remote monitoring in long-term. The wireless sensors should be protected from environmental excitation. The long-term stability of software should be evaluated. The power supply and consumption issues on wireless smart sensors should be addressed. The wireless communication should be enhanced because long distance communication is involved in the field. This chapter presents the long-term deployment of WSSN on a staircase in the Siebel Center to address the hardware feasibility, software stability, energy consumption, and communication optimization. The goal of this deployment is to evaluate the performance of the developed SHM system, as well as to provide future direction of the wireless SHM system.

5.1 Description of Testbed

Thomas M. Siebel Center for Computer Science at UIUC is a state-of-the-art building that opened in 2004 (Figure 5.1). The target structure is the central staircase reaching from the ground level to the top level as shown in Figure 5.2. The staircase is made of steel with mixed sections of I-beams and channel sections. The Testbed is the staircase connecting the 2nd floor and the 3rd floor, which has a longer span than the 1st floor staircase and has better accessibility from the ground floor than the 3rd floor to install the wireless sensors.



(a) North exterior



(b) South exterior

Figure 5.1. Thomas M. Siebel Center for Computer Science



(a) Top view



(b) 3rd floor front view

Figure 5.2. Staircase structure in Siebel Center

5.2 Hardware Setup

5.2.1 Wireless smart sensors

The components of wireless sensor node are MEMSIC's Imote2 with IBB2400CA battery board, IIB2400 Interface board and ITS400CA sensor board. The detailed specification is summarized in section 2.3.

Two configurations for the wireless smart sensors have been employed. The gateway node is the Imote2 stacked on IIB2400 Interface board, and the leaf node is the ITS400CA sensor board, Imote2, and a battery board.

The wireless sensor node has been protected and modified for long-term deployment as shown in Figure 5.3. Because the deployment is to prepare the full-scale deployment outside, the environmental protection has aimed protection from harsh exterior environment. The wireless sensor parts are housed in a PVC enclosure is a waterproof to protect the delicate electrical parts from temperature and humidity. The size of the enclosure mainly depends on the size of the battery holder and the sensor node. For this deployment, the D-cell battery is chosen because it has the highest capacity (20,000 mAh) and the size is reasonably small for installation. To use three D-cell batteries instead of three AAA batteries, the battery board is modified.

Furthermore, an external antenna has been employed to increase the communication range: Antenova® giganet® Titanus 2.4 GHz swivel antenna. Using this antenna, the range of radio communication has been ensured up to 200-m in the free field range test (Linderman and Spencer, 2010).



(a) Inside enclosure



(b) outside enclosure

Figure 5.3. Enclosure

In total, six leaf nodes have been installed at the quarter spans and the mid span of each side of the staircase as shown in Figure 5.4. The enclosure has been attached on top of the side girders of the staircase with two cantilever clamps (see in the dotted box of Figure 5.4).

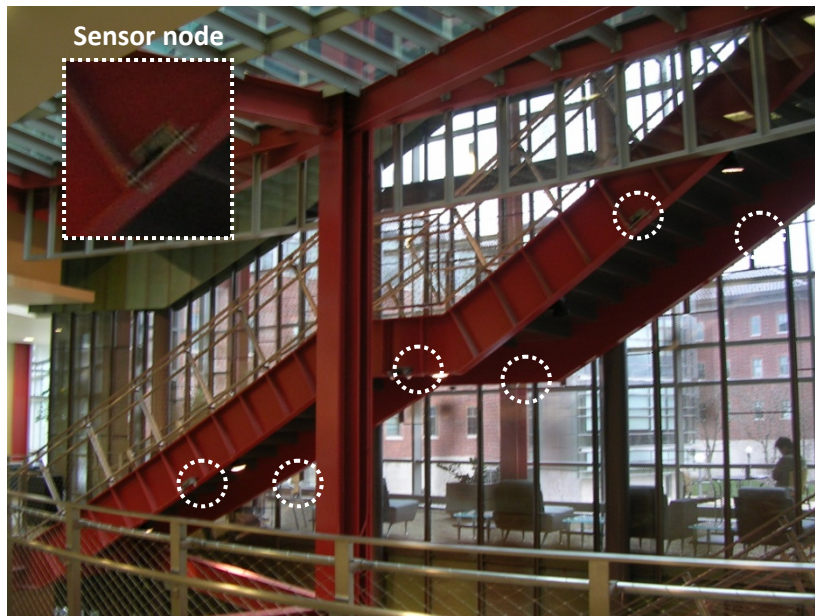
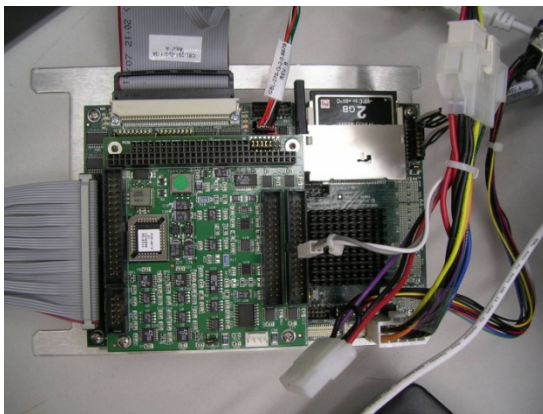


Figure 5.4. Siebel Center staircase.

5.2.2 Base station

The base station is a PC to manage and control structural monitoring, and to provide the measured data to users over the internet. For the stable performance, an industrial-grade single board computer Winsystems EPX-GX500 is employed in Figure 5.5. The temperature range of this computer is -40°C to $+85^{\circ}\text{C}$. The computer is AC-powered because the power is easily accessible within the building. A wired internet connection with a fixed IP address is used for stable remote monitoring and fast data transfer. In this PC, necessary software is installed: Cygwin, a Linux-like environment for Windows, and *imote2comm*, a communication protocol between the receiver Imote2 and the PC. The *imote2comm* is the previous version of *autocomm* which was introduced in section 2.4.2. Therefore, the base station for the deployment has been prepared.



(a) EPX-GX500 single board computer



(b) Enclosure for the computer

Figure 5.5. Base station PC

5.2.3 Webcam and the website

To initiate the network sensing when people pass, a webcam has been installed in front of the staircase. The webcam is an Axis® 207W wireless network camera, which is equipped with a 4.0mm F2.0 fixed iris lens, and of which the range is 0.5 m to infinity. The camera has a wireless network card (IEEE 802.11g 6- 54Mbps), so that the streaming visual data can be available on the internet. The captured motion image has been intentionally blurred to protect privacy as is required by University policy, as shown in Figure 5.6. The real-time staircase view was available in Figure 5.7 and the vibration data measured were updated during the measurement period.



Figure 5.6. View of webcam

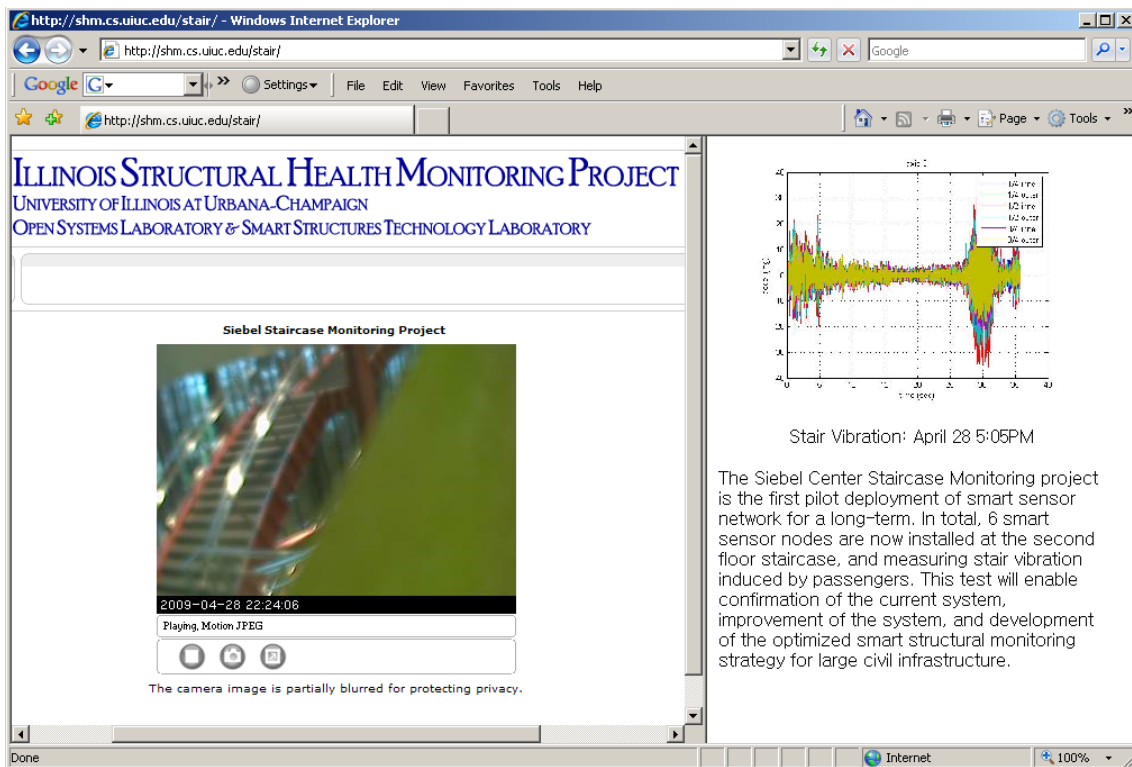


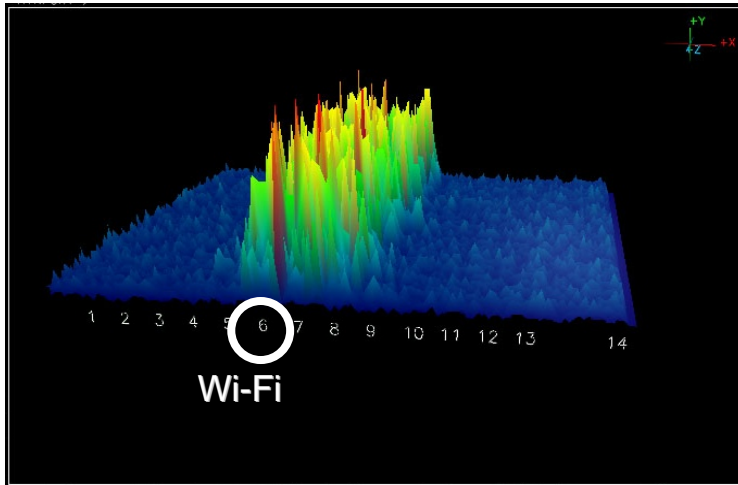
Figure 5.7. Staircase monitoring website

5.3 Communication Optimization

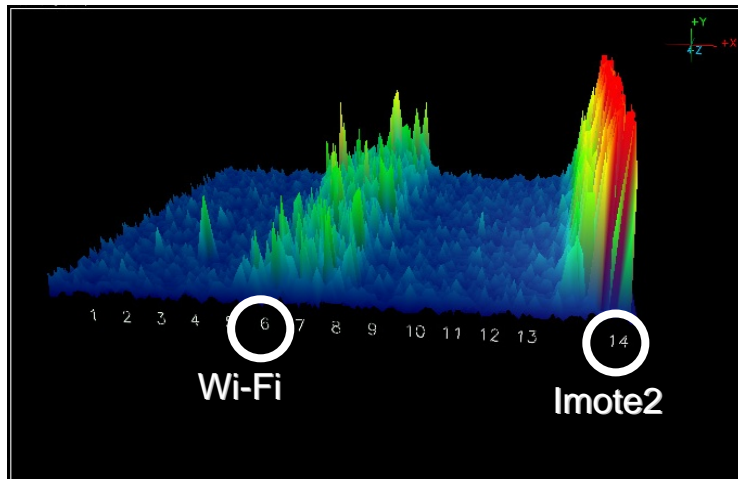
For successful deployment of WSSN, the communication channel has been selected considering ambient spectrum in the Siebel Center. The operating radio frequency should be selected not to conflict with the building's Wi-Fi frequency or common interfering spectrum around 2.4 GHz for efficient network communication. The ambient radio spectrum in the Siebel center has been recorded and compared with the radio spectrum during Imote2's operation (see Figure 5.8). Metageek® Wi-Spy 2.4i was employed to track the spectrum from Wi-Fi, Cordless phones, Microwave ovens, Zigbee, Bluetooth, or any other types of 2.4 GHz devices.

Figure 5.8 (a) shows the ambient spectrum in the Siebel center without any wireless sensor communication. As shown in this spectrum, the channel 6~8 was occupied, possibly by the building's Wi-Fi. To avoid this range of the spectrum, the Imote2 communication channel has been set as 26, which corresponds to channel 14 for the Wi-Fi channel. When two Imote2s are communicating, the radio spectrum showed additional peak at channel 14 in Figure 5.8 (b). Two peaks in the spectrum are well separated ensuring independent wireless communication.

In addition, the antenna orientation has been vertically aligned. The electric field component in the desired orientation is referred to as the co-polarized field, meaning the antennas should be co-linear (Linderman, *et al.* 2009). The radio power of the Imote2 is 31, which is a maximum power level. Therefore, the wireless communication has been optimized for the deployment with independent radio channel and external antenna which are aligned co-linearly.



(a) Ambient frequency in Siebel center



(b) Wi-Fi and the Imote2

Figure 5.8. Radio frequency spectrum

5.4 Software Setup

The *RemoteSensing* application with *SnoozeAlarm* from ISHMP Services Toolsuite is uploaded on Imote2 for this deployment. As introduced in section 2.4.2, the *RemoteSensing* is synchronized data measurement application from multiple sensor nodes and *SnoozeAlarm* is the energy saving mode.

The parameters for the network sensing have been selected as shown in Table 5.1. The sensing has been done once per day from all 6 nodes during the whole operation period. The sampling frequency is 280 Hz, the cut off frequency is 70 Hz which can cover several interesting natural frequencies of the structure. 10,000 data points in 3 directions have been measured. For the *SnoozeAlarm*, wake/listen time is 500 milliseconds and the sleeping time is 10 seconds, so that the duty cycle is 4.76%.

Table 5.1. Network and sensing parameters for Siebel Center Staircase tests.

Parameter	Value
Network size	6
Number of RemoteSensing events per day	1
Sampling rate	280 Hz
Channels sampled	3
Number of data points	10,000
<i>SnoozeAlarm</i> wake/listen time	500 ms
<i>SnoozeAlarm</i> sleep time	10 sec
<i>SnoozeAlarm</i> Duty cycle	4.76%

5.5 Performance Evaluation

5.5.1 Wireless SHM system

The acceleration of the staircase has been measured using the deployment wireless SHM system. Without any pedestrian passage, the vibration of the staircase is within 2 mg as shown in Figure 5.9. Because of low resolution of the ITS400CA sensor board (~1 mg), accurate ambient vibration was not measured. Here lays the necessity of a dedicated sensor board with higher resolution or higher sensitivity for SHM.

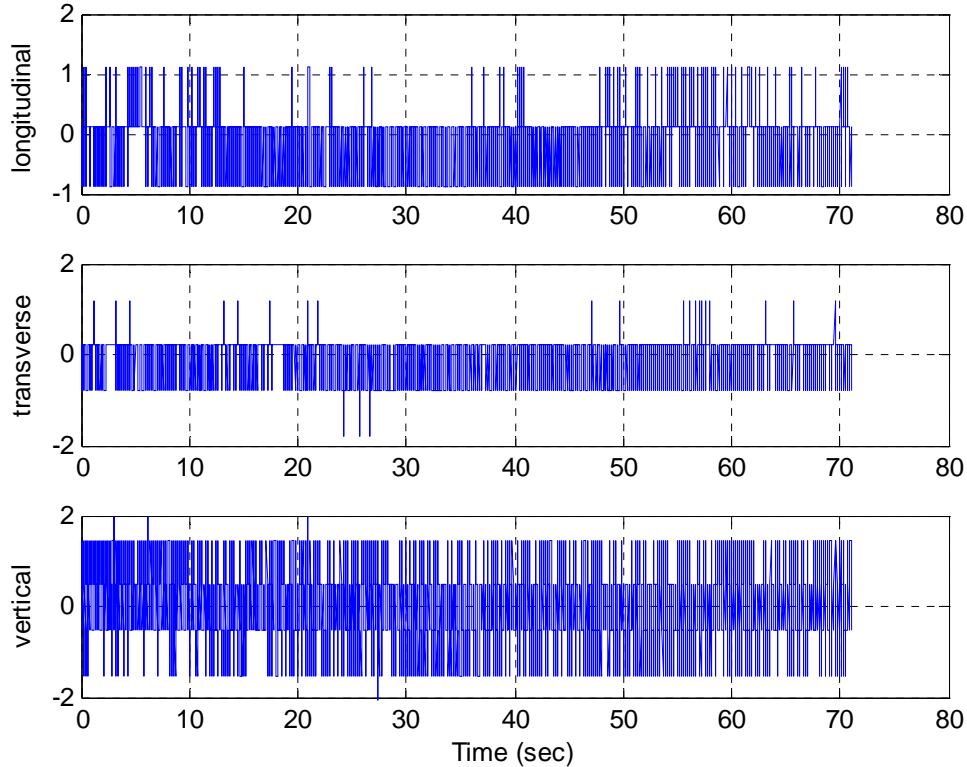


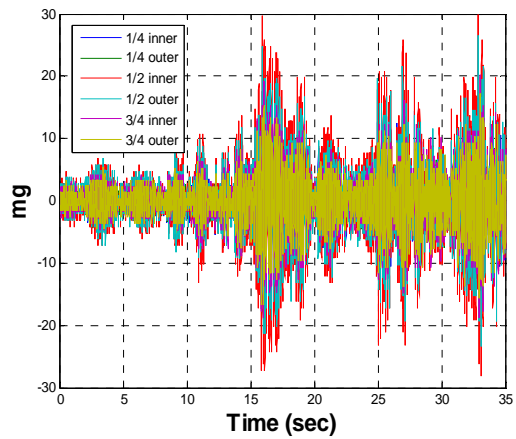
Figure 5.9. Ambient vibration

With the installed webcam, the vibration data during pedestrian passage were successfully measured as shown in Figure 5.10. The image of the webcam provided the brief number of the

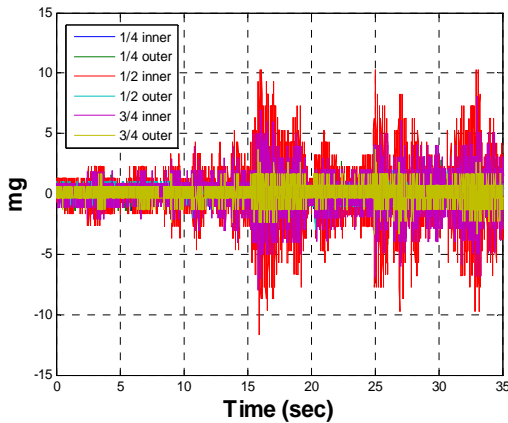
passengers. During this measurement, two people walked down after which another person walked down subsequently. The measurement parameters are in Table 5.1. The vertical vibration is most significant among three directions, up to 30mg. The vibrations of the longitudinal and transverse directions are mostly within 10mg. Still, the acceleration data have been quantized due to low resolution. Therefore, the basic sensor board is not adequate for monitoring low vibration structure.



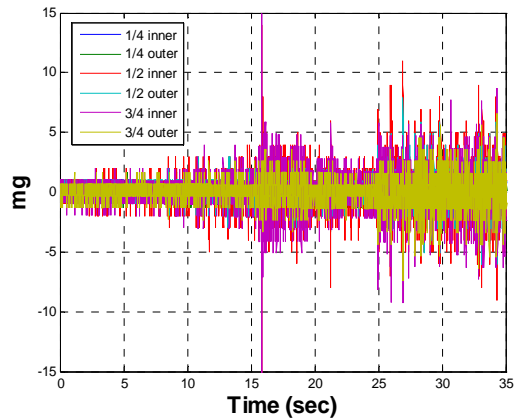
(a) Visual data



(b) Vertical vibration



(c) Longitudinal vibration



(d) Transverse vibration

Figure 5.10. Vibration correlated with the visual data.

In addition, the power spectral density of the vertical vibration has been calculated in Figure 5.11. The number of FFT is 2048, 50% overlap is used. Figure 5.11 (a) is the power spectral density up to the Nyquist frequency ($= fs/2$). Most frequency-domain contents are concentrated in the frequency range of 0 Hz to 22 Hz, showing low frequency vibration characteristic of the staircase. By reducing the sampling frequency, or by increasing the number of samples, the data quality can be significantly improved. For the basic sensor board, 280 Hz is the lowest sampling rate it can provide. Nominally, several first natural frequencies of long-span bridges can be even within 1 Hz. Therefore, a dedicated sensor board for SHM should be able to use a lower sampling rate to monitor civil infrastructure.

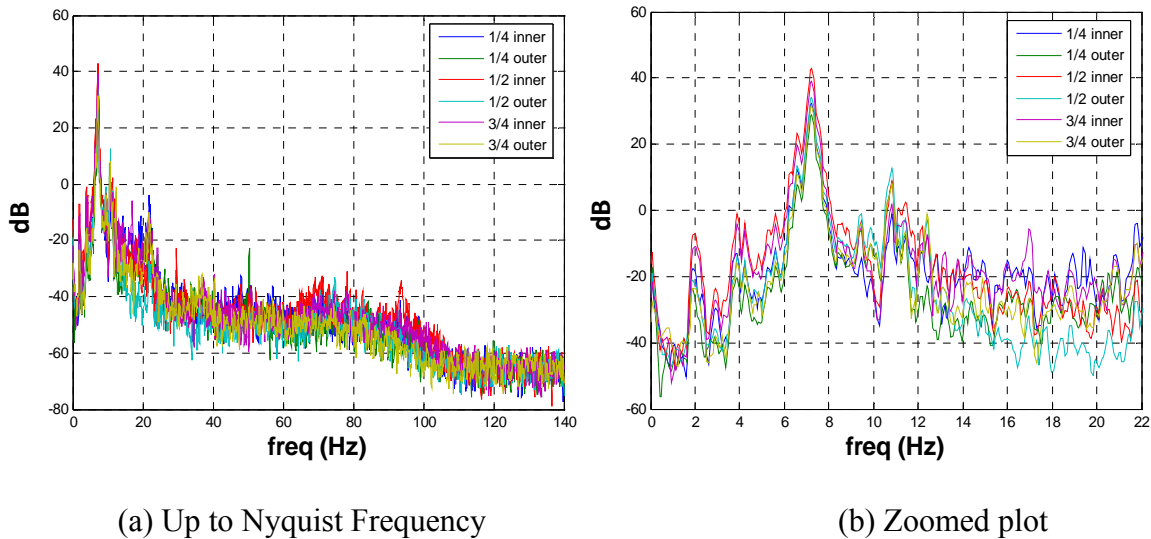


Figure 5.11. Power spectral density

5.5.2 Long-term software stability

This deployment of the SHM system shows the long-term performance of the developed software. Without using the *SnoozeAlarm*, the network life was only 12 days during laboratory tests because of high power consumption of the Imote2 processor during idle state. However,

the network life significantly increased up to 52 days by employing the *SnoozeAlarm* function. During the whole period of time, the software showed stable performance so that the leaf nodes never required a hardware reset during deployment.

Every day, the acceleration responses from the staircase have been measured for accurate network evaluation. Table 5.2 shows the duration of each step for the network sensing to measure 10,000 data in 3 directions from all 6 leaf nodes. First step is waking up the nodes from the *SnoozeAlarm* mode. The wake up duration nominally takes less than 30 seconds. The next step is sending the sensing command to the leaf nodes, which takes 1~2 seconds. After time synchronization among the leaf nodes, the acceleration data are measured. This step took about 1 min for the synchronized network sensing. After sending, the measured data are sent back to the base station. The measured data are stored in a text file, which can also be shown on the screen if the option is enabled. Total network operating time is approximately 7 minutes to measure one set of data. In this deployment, the lowest UART speed has been utilized for reliable data transfer, which results in slower communication speed. After this deployment, the performance of software has improved to have faster communication and printing. All steps of network sensing have initiated by the network operator; however, autonomous network operation is desirable for permanent SHM system. The used software herein is the first version of ISHMP Services Toolsuite of which stable long-term performance has been verified on a full-scale testbed.

Table 5.2. Time for RemoteSensing application

State of RemoteSensing application	Time (seconds)
WakeUp	30
Sensing parameters to leaf nodes	1-2
Time Synchronization	20
Data measurement	37
Extra wait time	10
Communication and printing	300

5.5.3 Communication quality

The gateway node was placed with the base station PC inside the wooden box located in an office near the staircase. The staircase and the office is approximately 10 m apart and a concrete wall, a steel mesh wall and a glass door are between the two. Despite the physical interference present and that the gateway and the leaf nodes are not line-of-sight, communication between the gateway node and the leaf nodes on the staircase was stable during 52 days of operation. Therefore, the network communication is successfully optimized by the uninterrupted radio channel, antenna orientation optimization.

5.5.4 Power consumption

The power consumption of Imote2s has been investigated during the monitoring. Imote2 is running with the battery voltage of 3.0 – 4.5 V. The initial battery voltage levels of 6 sensors are 4.5V in average as shown in Table 5.3. Among 6 sensors, the nodes, 73, 89, 133 are using the battery board manufactured by Intel, and the nodes, 67, 85, 87 are using the one manufactured by Crossbow.

Table 5.3. Initial voltage.

Node ID	67	85	87	89	133	73
Voltage	4.495	4.551	4.521	4.518	4.559	4.541

The on-board voltage can be measured using *RemoteCommand Vbat* command. As shown in Figure 5.12, Intel's battery board supplies a constant voltage on to the Imote2 because of on-board voltage regulator; therefore, the battery voltage readings are constant. The Crossbow battery board does not have the on-board regulator, so that the battery can supply its current voltage to the board. The voltage of the Crossbow sensor board decreased linearly during the specified operation. A voltage drop, in average of 0.4V, is shown between the on-board voltage reading and the actual voltage, when the battery board is turned on. This voltage difference is due to the diode used to prevent the voltage surges and outages. When the on board voltage decreases less than 3.2 V, the *RemoteSensing* application failed during sensing stage even though the Imote2 is turned on. Therefore, the voltage on the sensor board should be higher than 3.2V for stable sensing, which corresponds to 3.6V of actual battery voltage.

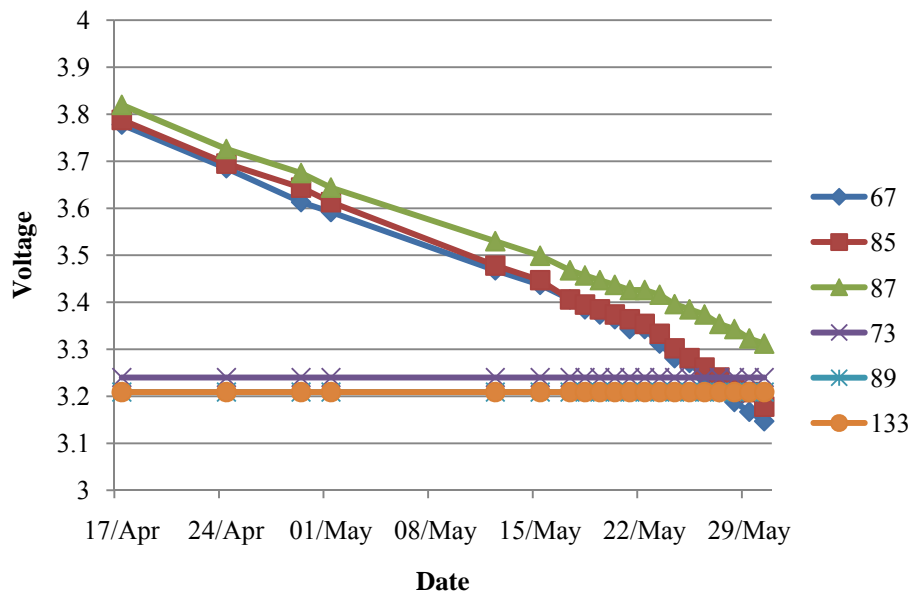


Figure 5.12. On-board voltage

Rice and Spencer (2009) calculated the estimated power consumption for the various hardware and software configuration and corresponding service life for 3 D-cell batteries (see Figure 5.13 and Table 5.4). Based on the consumption model, the battery life for the ITS400CA sensor board is 63 days for the Intel battery board, 59 days for the Crossbow battery board (Rice and Spencer, 2009). Actual network life for this deployment was 52 days. The power consumption can be greater than theoretical calculation because the operator can wait for the people who are passing on the staircase before starting network sensing. Therefore, the power consumption of the system using the basic sensor board agrees well with the calculation.

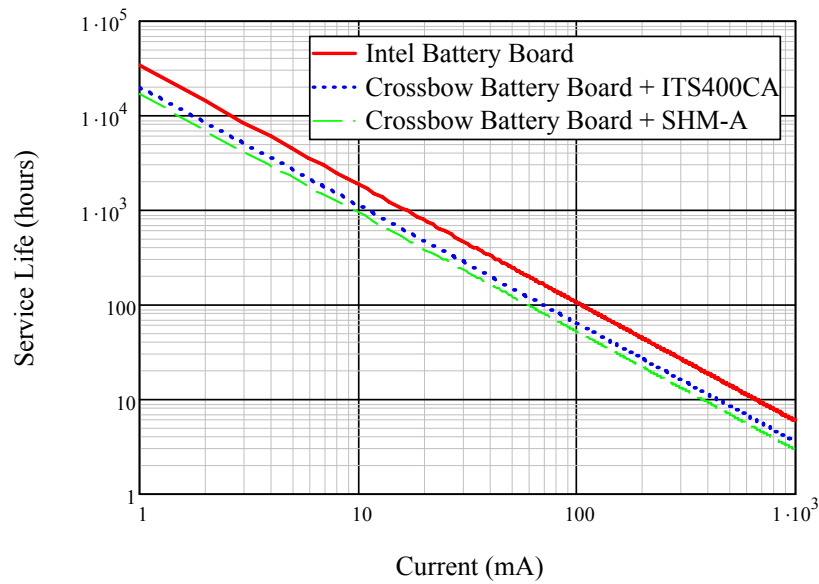


Figure 5.13. Estimated constant current service life (Rice and Spencer, 2009).

Table 5.4. Estimated service life (days) for 3 D-cell batteries with various hardware combinations (Rice and Spencer, 2009).

Battery Board	Sensor Board			
	SHM-A		ITS400CA	
	Sentry	Non-Sentry	Sentry	Non-Sentry
Intel	63	66	62	63
Crossbow	49	52	57	59

Though the *SnoozeAlarm* and D-cell batteries increased the network life up to 52 days, the batteries should be replaced regularly for long-term continuous monitoring. To address this problem, energy harvesting for the wireless sensor platform should be desirable such as solar panel.

5.6 Conclusion

The performance of a SHM system using WSSN has been validated on a Siebel staircase deployment for debugging and future development. The base station and the wireless smart sensors were working stably during the whole monitoring period. The *RemoteSensing* application in the ISHMP Services Toolsuite has shown reliable performance to measure acceleration during the operation. The network communication between the gateway node and leaf nodes were stable with vertically aligned external antenna. With 3-D cell batteries and *SnoozeAlarm* protocol, the network life is 52 days, which agreed well with theoretical calculation using power consumption model. The visual data was optional but helpful in correlating with the measured acceleration data. However, the basic sensor board is not adequate to monitor low vibration civil infrastructure because of the low resolution and higher sampling rate. For long-term SHM system, energy harvesting system is recommended to power wireless sensor platform. Therefore, the developed SHM system using WSSN has shown stable performance during the long-term deployment providing the potential for the SHM of large-scale full-scale civil infrastructure in the future.

CHAPTER 6 FULL-SCALE SHM USING WSSN FOR JINDO BRIDGE

Based on the lessons and experience from the Siebel staircase deployment, the software and hardware framework were updated for long-term full-scale deployment on the Jindo Bridge (Rice *et al*, 2010). This effort is part of a trilateral collaboration between the USA (University of Illinois at Urbana-Champaign), South Korea (Korean Advanced Institute of Science and Technology, KAIST), and Japan (University of Tokyo). The Testbed cable-stayed bridge connects the southern tip of the Korean peninsula with the Jindo Island. This chapter reports on the deployment and evaluation of this state-of-the-art WSSN in terms of hardware durability, software stability, power consumption, and energy harvesting capabilities. The Jindo Bridge SHM system constitutes the largest deployment of wireless smart sensors for civil infrastructure monitoring to date.

6.1 Bridge Description

The Jindo Bridges are twin cable-stayed bridges connecting Haenam on the mainland with the Jindo Island (see Figure 6.1). Each of these bridges consists of a 344-m central main span and two 70-m side spans.

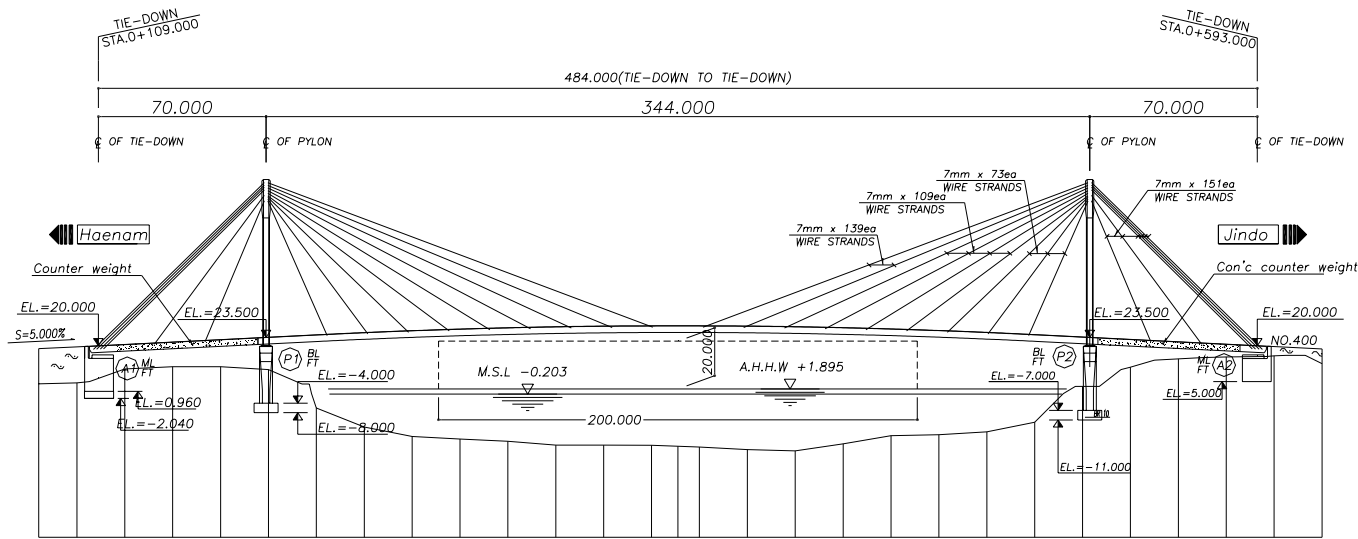
The original Jindo Bridge, constructed in 1984 by Hyundai Engineering & Construction Co., Ltd., was the first cable-stayed bridge in South Korea. The width of the bridge is 11.7 m, the design traffic velocity is 60 km/hr, and the design live load is based on AASHTO HS-20-44 (DB-18). The second Jindo Bridge was constructed in 2006 by Hyundai Engineering & Construction Co., Ltd., Daelim Industrial Co., Ltd., and Namhei Co., Ltd. The width of the second bridge is 12.55 m, the traffic design velocity is 70 km/hr, and the design live load is

based on AASHTO HS-20-44 (DB-24, DL-24). The streamlined steel box girder is supported by 60 high-strength steel cables connected to two pylons. A structural drawing of the bridge is shown in Figure 6.2.

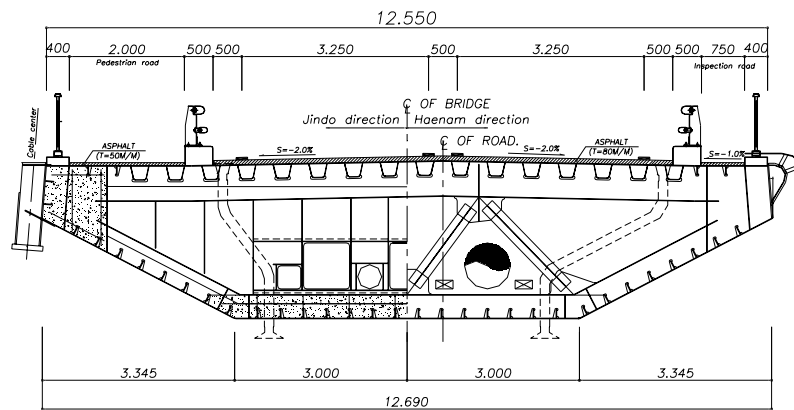


Figure 6.1. 1st (right) and 2nd (left) Jindo Bridges.

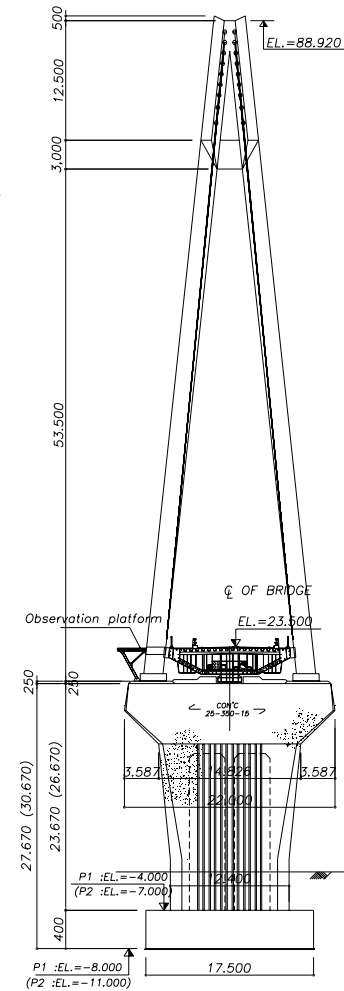
Both bridges have existing SHM systems based on wired sensors. The first Jindo Bridge has 38 strain gages, four inclinometers, two anemometers, two seismic accelerometers, five uniaxial capacitive accelerometers, and 15 uniaxial piezoelectric accelerometers. The second Jindo Bridge has 15 thermometers, 15 strain gages, four biaxial inclinometers, two string pots, two laser displacement meters, 24 Fiber Bragg Grating sensors, 20 uniaxial capacitive accelerometers, two biaxial force balance type accelerometers, and three triaxial seismic accelerometers. Among two bridges, the second Jindo Bridge is selected as the Testbed for this research, for two primary reasons: (i) the existing SHM system is quite versatile, including accelerometers and fiber optic sensors, and (ii) the design and construction documents are more complete.



(a) Elevation



(b) Typical Girder Section



(c) Pylon

Figure 6.2. Bridge drawings (2nd Jindo Bridge).

6.2 Bridge Monitoring System

The components of the bridge monitoring system have provided. The main components are the wireless smart sensor nodes. To monitor the bridge vibration correlated with strong wind excitation, an ultrasonic anemometer has also been installed with acceleration measuring sensor nodes. For remote monitoring of the bridge, a base station has been configured so that it can control and manage the network of wireless smart sensors. As a first step, most sensors are powered by D-cell batteries. For permanent deployment in near future, the solar panel has also been employed for some nodes where the battery replacement is difficult. Finally, the software framework for autonomous vibration monitoring is described.

6.2.1 Wireless smart sensor nodes

Each smart sensor unit consists of MEMSIC's Imote2, an IBB2400CA battery board, and the SHM-A multi-scale sensor board (Rice and Spencer, 2009). A detailed explanation of these components is given in section 2.3. Similar to the Siebel staircase, two types of smart sensor nodes are employed in the Jindo Bridge deployment: gateway nodes and leaf nodes. To increase the communication range, all nodes are equipped with an Antenova® Giganova Titanis 2.4 GHz external antenna (Antenova, 2009).

6.2.2 Wind monitoring system

The Jindo Island is located in Haenam, one of the windiest regions in South Korea with several typhoons each year. A cable-stayed bridge like the Jindo Bridge is sensitive to such strong wind; thus, an important objective of this study is monitoring the wind, in addition to the dynamic responses of the bridge.

A 3-D ultra-sonic anemometer has been incorporated into the WSSN for reliable wind monitoring of the Jindo Bridge. Because of its high resolution (wind speed: 0.01m/s, wind direction: 0.1 degree) and good accuracy (wind speed: $\pm 1\%$, wind direction: ± 2 degrees), the RM Young Model 81000 anemometer was chosen (see Figure 6.3 (a)). The durability of ultra-sonic anemometer makes them well-suited for long-term operation in harsh environments. Moreover, the anemometer's analog voltage outputs, ranging from 0 to 5V, can be easily accommodated by the SHM-A board with small modifications.

The SHM-W board is developed by modifying the SHM-A board to have three external 0–5V input channels and one acceleration channel. The wind speed (channel 1), horizontal and vertical wind directions (channels 2 and 3) are measured through analog input interface connectors on the SHM-W board as shown in Figure 6.3 (c). Because the SHM-W board also uses the QFA512-based sensor board, it uses the same drivers as the SHM-A board; as a result, the wind data acquired is precisely synchronized with the acceleration data from the SHM-A board. The SHM-W board is designed such that it uses the full 0-5V range for the inputs, resulting in better resolution for the wind data.

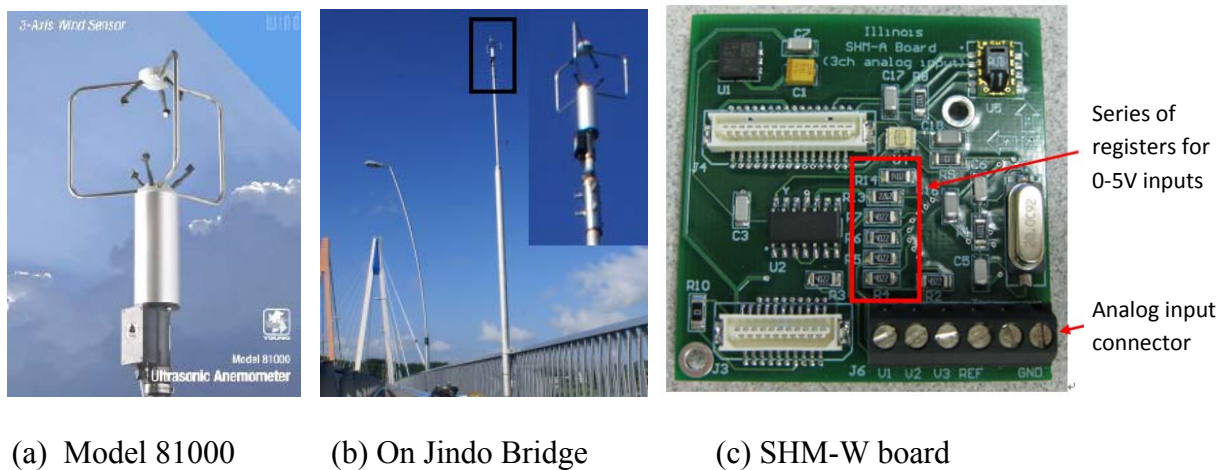


Figure 6.3. 3D ultra-sonic anemometer (Model 81000, RM Young) and SHM-W board.

6.2.3 Base station

Because the base station provides access to the WSSN and is therefore critical to the performance of the entire network. The base station controls the network by (1) sending messages to the leaf nodes through the gateway node, (2) storing the transmitted data from the WSSN, (3) processing received data, and (4) transferring the data to the remote server via the internet. To achieve these functions, the base station is built upon an industrial-grade PC running Windows XP Professional OS, an uninterruptible power supply (UPS) backup, a gateway node, and an environmentally hardened enclosure, as shown in Figure 6.4.

An industrial-grade PC AAEON AEC-6905 was adopted as base station because of its fanless architecture, protecting it from dust and moisture. The APC ES550 UPS backup protects the base station components from unexpected electric surges and outages. The gateway node consists of an Imote2 stacked on an interface board for interactive serial communication, an SHM-A sensor board, and a 2.4 GHz 5 dBi dipole antenna as shown in Figure 6.5. Though the gateway node is not involved in acceleration measurement, the attached SHM-A sensor board enables automatic rebooting of Imote2 after the base station PC is rebooted in some reason. A wired internet line was installed to the PC using an ADSL internet modem, providing remote access to base station, to control the WSSN, and to download the measured data.

Software for remote control and data download is installed on the base station. On the top of basic OS and anti-virus software, the key components of the software are the Cygwin and *autocomm* executable applications for interfacing with the gateway node, the VNC (Virtual Network Computing) server for remote desktop control, and an FTP (File Transfer Protocol) server to remotely download the measured data.

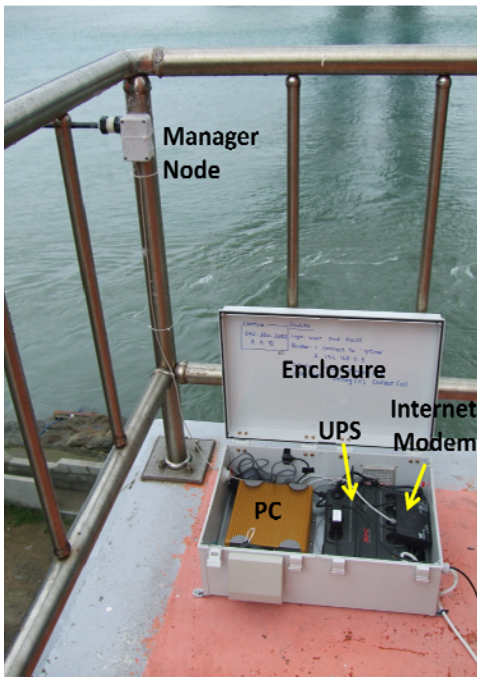


Figure 6.4. Base station

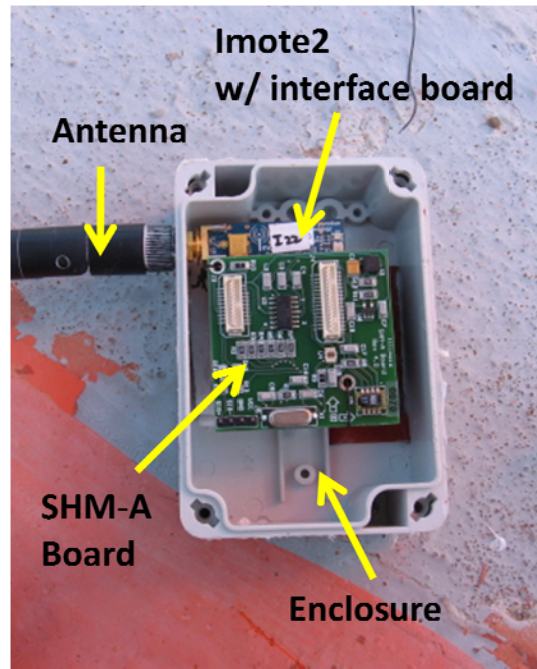


Figure 6.5. Gateway node

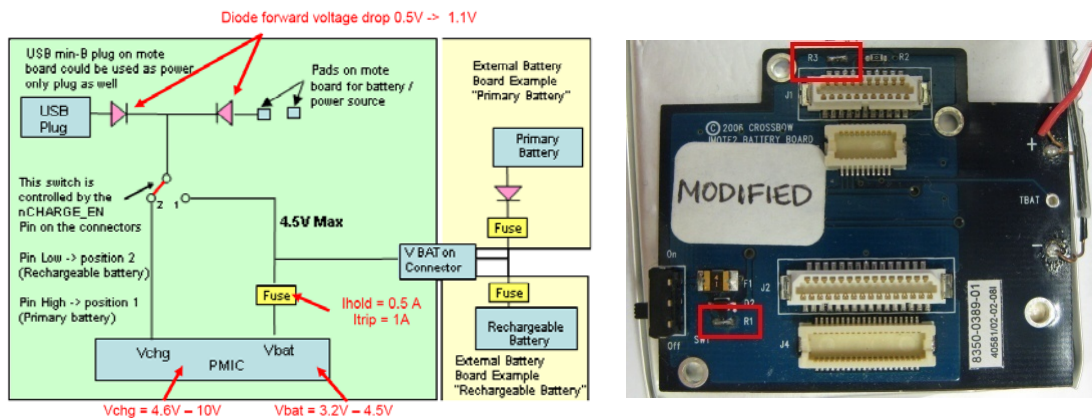
6.2.4 Energy harvesting with solar panel

While battery power provides a convenient and readily-available solution for WSSNs, the drawback is that regular battery replacements are required for long-term deployments. From this perspective, energy harvesting is important for long-term operation of the wireless SHM systems (Miller *et al*, 2010). Roundy *et al* (2004) compared the power densities of available harvesting sources such as sunlight, thermal gradient, human motion, vibration, and acoustic noise, *etc.* As shown in Table 6.1, the power density of the solar cells is the largest, showing the potential to increase the network lifetime to longer than one year. Therefore, solar panels and rechargeable batteries have been chosen as the energy the harvesting/power system and installed on several leaf nodes at locations where battery replacement is difficult.

Table 6.1. Power Densities of Harvesting Technologies (Roundy *et al.* 2004).

Harvesting Technology	Power density
Solar cells (outdoors at noon)	15 mW/cm ²
Piezoelectric (shoe inserts)	330μW/cm ³
Vibration (small microwave oven)	116μW/cm ³
Thermoelectric (10oC gradient)	40μW/cm ³
Acoustic noise (100dB)	960nW/cm ³

The Imote2 can be powered by rechargeable batteries using the Power Management Integrated Circuit (PMIC) (Crossbow, 2007). The PMIC can be connected directly to the Lithium-Ion or Lithium-Polymer batteries without a protection diode; the diode can be bypassed with an additional 0-ohm resistor (R1). To allow the current from solar panel to flow into the battery, the nCHARGE-EN pin, which is a control switch to decide battery options, should be pulled low with the another 0-ohm resistor (R3) on the battery board (see Figure 6.6).



(a) Power supply options for Imote2 (Crossbow, 2007) (b) Battery board modifications

Figure 6.6. Power supply options for Imote2 and battery board modification for recharging.

Considering the range of input power that the Imote2 can support (4.6~10V, up to 1400mA), the SPE-350-6 solar panel of Solarworld (9V-350mA) in Figure 6.8 was employed. The Powerizer lithium-polymer rechargeable battery (Powerizer, 2009) was selected, the voltage of which is up to 4.2V when fully charged. This system has 10,000 mAh capacity – half of that of D-cell battery; therefore, this system can supply power to the Imote2 for an extensive period without recharging.



(a) SPE-350-6 (9V-350mA, Solarworld) (b) on cable node (c) Rechargeable battery

Figure 6.7. Solar panel and rechargeable battery for Jindo Bridge SHM.

6.2.5 Software framework

The main software for the deployment is *AutoMonitor*, an autonomous SHM network management application (Rice and Spencer, 2009). The *AutoMonitor* employs *RemoteSensing*, *ThresholdSentry*, and *SnoozeAlarm*. *SnoozeAlarm* employs a strategy that allows the network to sleep most of the time, thus improving energy efficiency and allowing long-term system deployment. To wake the network for an important event, the *ThresholdSentry* application defines a specified number of the leaf nodes as sentry nodes. The sentry nodes wake up frequently at predefined times and measure a short period of acceleration or wind data. When

the measured data exceeds a pre-defined threshold, the sentry node sends an alarm to the gateway node, which subsequently wakes the entire network for synchronized data measurement. In this way, *AutoMonitor* facilitates the automatically recurring monitoring with reduced power consumption.

The *AutoMonitor* application employs multiple threshold levels for the Jindo Bridge SHM. When a single threshold level is used to define the events that are recorded, if the threshold level is too high, the data measurements would rarely if ever occur. On the other hand, if a threshold level is too small, the memory will be quickly filled with minor structural responses; hence, possible strong vibrations during remaining period cannot be captured. In this deployment, multiple threshold levels were defined, each having a separate limit to the number of events that can be recorded in a given period of time. This approach makes it possible to measure both rare but strong responses and frequent but low-level ambient vibration, which enables more effective SHM.

Another feature of the *AutoMonitor* application is a wind threshold sentry. The wind sentry node is equipped with SHM-W sensor board connected to the ultrasonic anemometer. Strong wind like typhoons induces large structural responses. Therefore, the wind sentry will trigger network sensing when the velocity exceeds the specified threshold. In this deployment, both vibration and wind-based sentry nodes have been installed for use by the *AutoMonitor* application. In summary, the *AutoMonitor* application had data measurement and on-board computing functionality, multiple threshold triggering strategy using vibration/wind sentries, and energy efficiency using *SnoozeAlarm*.

6.3 Environmental Hardening

Environmental protection of the SHM system is required for the deployment on a bridge in harsh surroundings. The site of the Jindo Bridge is often subject to high humidity due to frequent fog and harsh winds. The environmental hardening of the hardware components are discussed in this section.

6.3.1 Base station

This section describes hardening of the two base station PCs. The base station PCs are each housed in ABS enclosures. After the initial deployment, the industrial-grade PC was found to radiate significant heat, which results in failure of the PC due to high temperatures inside the enclosure. To address this problem, the enclosure was modified to include two-way ventilation, as shown in Figure 6.8. All ventilation openings have anti-bug nets and rain-protection brackets. The exhaust fan is connected to a temperature sensor inside the enclosure, which turns the fan on if the temperature in the enclosure is over 35°C. In addition, the power cable, the USB cable to the gateway node, and the LAN cable to the wired internet line pass through the enclosure wall via cable glands. This enclosure with the ventilation system has provided effective and stable operation of the base station.

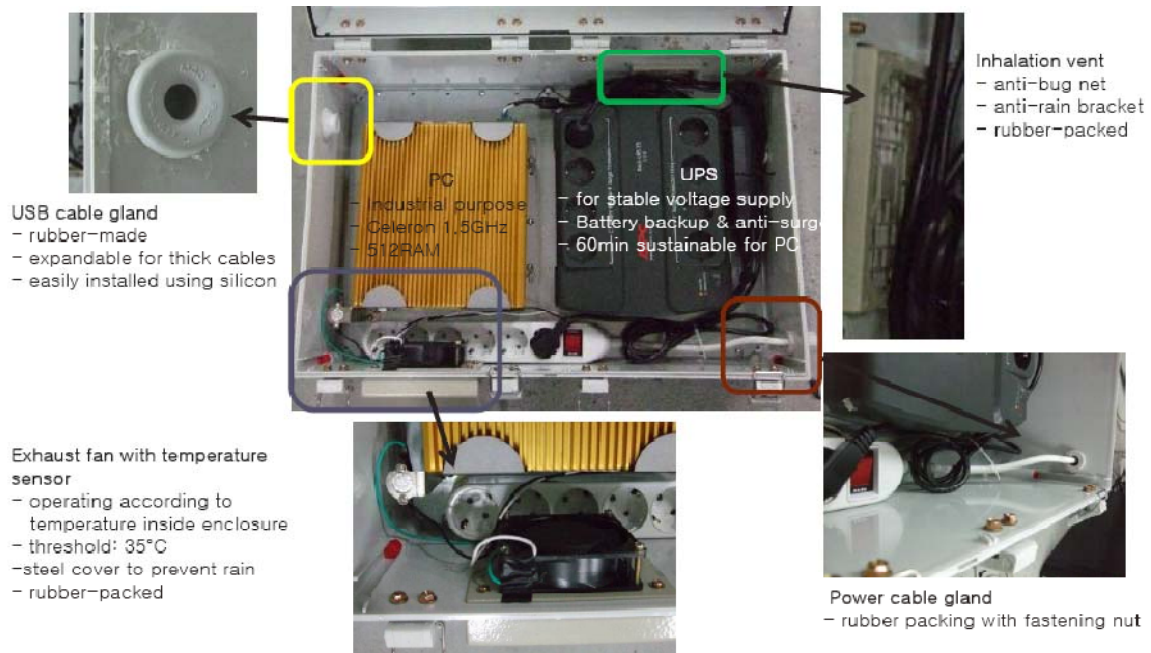


Figure 6.8. Ventilation enhancements for base station enclosure.

6.3.2 Smart sensor nodes

The leaf nodes were also placed in environmentally hardened enclosures. Water-tight PVC enclosures were employed to protect the nodes from moisture as shown in Figure 6.11. The battery board is modified to employ three D-cell batteries instead of standard AAA batteries. The nominal voltage of both a single AAA and a single D-cell battery is 1.5V, while the capacity of an alkaline D-cell battery is 20,000 mAh, versus 1,200 mAh for an AAA alkaline battery; thus, enabling significantly longer network operation. The size of the enclosure is primarily dependent on the size of the batteries.

To increase the radio communication range, the Imote2 has been modified to use an external antenna (Linderman *et al.* 2010: Antenna gigaNova Titanis 2.4 GHz external antenna – Antenna, 2009). The external antenna is mounted to the enclosure and then connected to the Imote2 with an antenna extension cable. The sensor unit is mounted separately from the battery

holder. The bottom of the battery board is attached on the enclosure using the Scotch® Exterior Mounting Tape.

6.4 Deployment of SHM System

After careful environmental hardening of the hardware components, the bridge monitoring system has been deployed. Because the SHM system includes many nodes, the whole network has been divided into two sub-networks. The prepared software has been uploaded into all sensor nodes, and the performance has been validated before installation. On the bridge, the sensor location has been fixed based on each sensor's radio communication capability, which has been determined by the field experiments. According to the fixed sensor location, the leaf nodes have been installed. The antenna orientation has been optimized for stable communication.

6.4.1 Network topology

The network topology is carefully determined to ensure reliable network sensing for the Jindo Bridge. The major factors to define the network topology are the size of network, the communication range, *etc.* The total length of the bridge is 484m, the communication range of Imote2 with an external antenna is ~200m, and the number of sensor nodes in network is 71. Considering the range and the communication time, the network was divided into two sub-networks: one on the Jindo side and the other on the Haenam side.

The Jindo sub-network consists of 33 nodes, with 22 nodes on the deck, three nodes on the pylon, and eight nodes on the cables. The Haenam sub-network consists of 37 nodes, with 26 nodes on the deck, three nodes on the pylon, and seven nodes on the cables. Each sub-network is

controlled by a base station located on the concrete piers supporting the steel pylons of the first Jindo Bridge. These locations were chosen to achieve consistent line-of-site communication with leaf nodes.

6.4.2 Software setup and verification

Two software configurations were employed on the smart sensor nodes for the deployment. The gateway nodes have been programmed with the *AutoMonitor* application to control the autonomous monitoring of the network. The remote nodes have been programmed with the *RemoteSensing*, which combined with *TestRadio* and *DecentralizedDataAggregation* (Sim and Spencer, 2009). In the *AutoMonitor* application, users can decide whether raw acceleration data or correlation functions using decentralized estimation from the local groups are returned to the base station by selecting either *RemoteSensing* or *DecentralizedDataAggregation*, respectively.

The software performances using a large network of wireless smart sensors have been previously verified both in the laboratory and field environments after programming the nodes. During the tests, basic communication parameters were modified to accommodate the large network size.

Fault tolerance features have been designed into the software to ensure robust operation. To this end, the *AutoMonitor* application provides several features, including: (1) sending the network wake-up command repeatedly, as in some cases a node can return to the sleep mode soon after waking up, (2) skipping over unresponsive nodes after a short timeout when sending commands or receiving data, and (3) rebooting the remote nodes in case of failures of component services that may leave the node in an inconsistent state and prevent further operation. Additionally, the *AutoMonitor* application coordinates with its component services

(*SnoozeAlarm*, *ThresholdSentry*, and *RemoteSensing*) to handle internal errors in those services in a consistent manner.

6.4.3 Optimal sensor location using the communication range tests

Because peer-to-peer communication was used for this deployment, radio communication tests were conducted on-sight using the *TestRadio* application, which can be used to measure the packet reception rates at various communication distances. During the communication range tests, the gateway node was located at the Haenam side pylon and the leaf nodes were gradually moved out to the mid-span. The number of sensors which were unresponsive to the *TestRadio* request from the gateway node was counted as shown in Figure 6.9. In total, 73 Imote2s were tested and five nodes were found to be unresponsive and subsequently replaced. At the mid-span (172 m), 23 Imote2s were found to communicate effectively. Based on these radio communication tests, sensors location were chosen as shown in Figure 6.10.

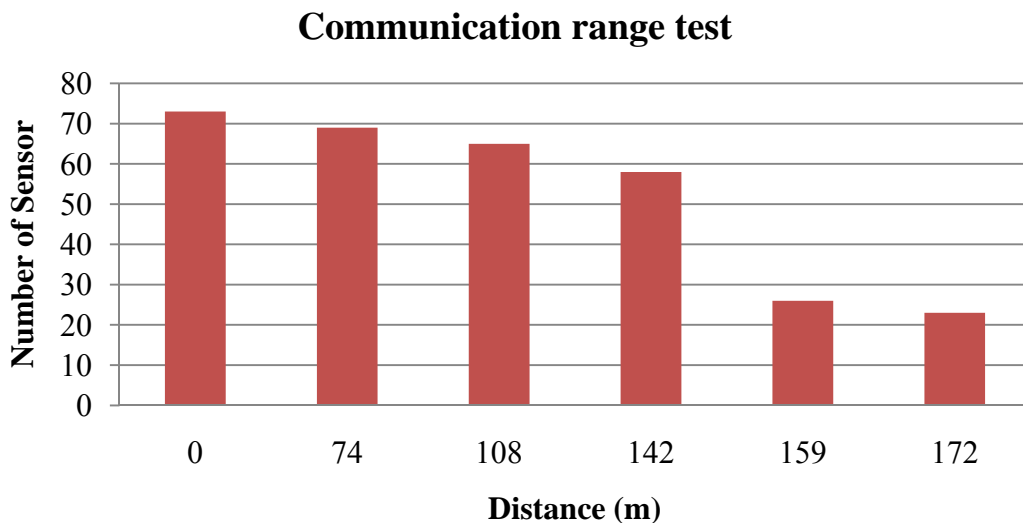


Figure 6.9. Communication range tests.

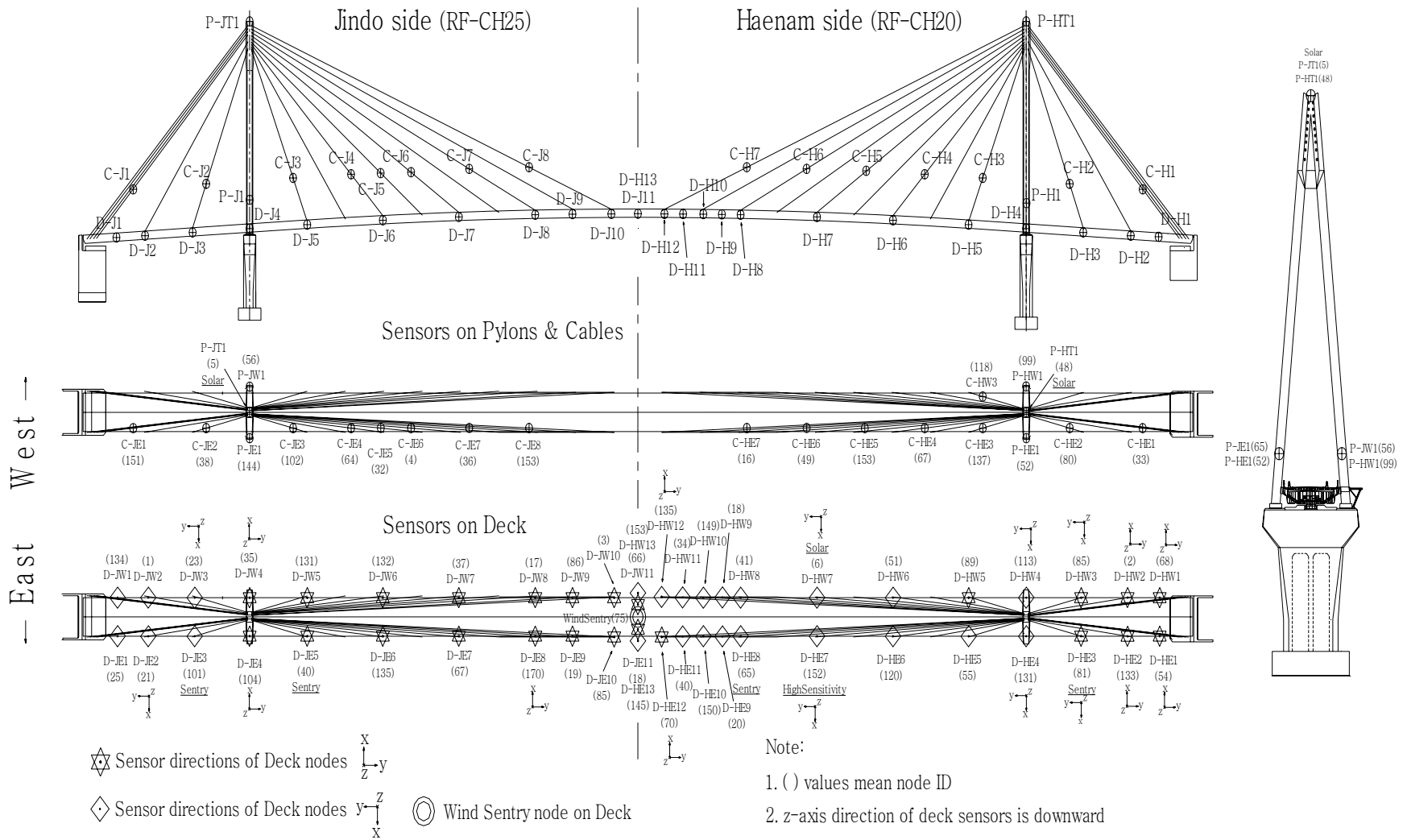


Figure 6.10. Sensor location.

6.4.4 Sensor installation

The smart sensor nodes for the deck, pylons, and cables are mounted using different methods. The deck sensors and the pylon sensors are mounted upside down on the bottom side of deck using one-directional magnets, of which holding capacity is up to 10kg (Figure 6.11 (a)). Using two magnets on the bottom of each enclosure, a secure connection between the sensor enclosure and the bridge steel surface is ensured. In addition, the magnets are surrounded by a styrofoam panel with the thickness of the magnet to prevent vibration due to vortex-shedding in the gap between the enclosure and structure surface (see Figure 6.11 (b)). This approach reduces the installation time and effort under the deck; however, the magnet-based method is not feasible for the cable sensors due to round surface. Therefore, cable sensors are mounted using two U-bars and an aluminum mounting plate, as shown in Figure 6.11 (c). Because these nodes are directly exposed to sun light, a stainless steel cover is employed to protect the PVC enclosure.



(a) Battery-powered node



(b) Solar-powered node



(c) Cable node

Figure 6.11. Hardened sensor nodes.



(a) 10 kg capacity one-directional magnet



(b) Bottom of the leaf nodes

Figure 6.12. Magnet-based sensor attachment.

6.4.5 Optimal antenna direction

The antenna orientation is optimized to obtain optimal network performance. In general, the antennas should be co-linear, to ensure effective radio communication. Optimizing the antenna orientation is not a simple problem for large WSSNs, because elevations of sensors are different for those under the deck, at the side of the pylon, on the top of the pylon and the cable nodes. The antenna direction for the gateway nodes is critical to reliable communication with all leaf nodes. Therefore, the antenna for the gateway node and all leaf nodes are oriented perpendicular to the longitudinal axis of the bridge and parallel to the ground as shown in Figure 6.13. In this manner, all sensors can communicate with the gateway node efficiently. This configuration has been verified through communication tests.

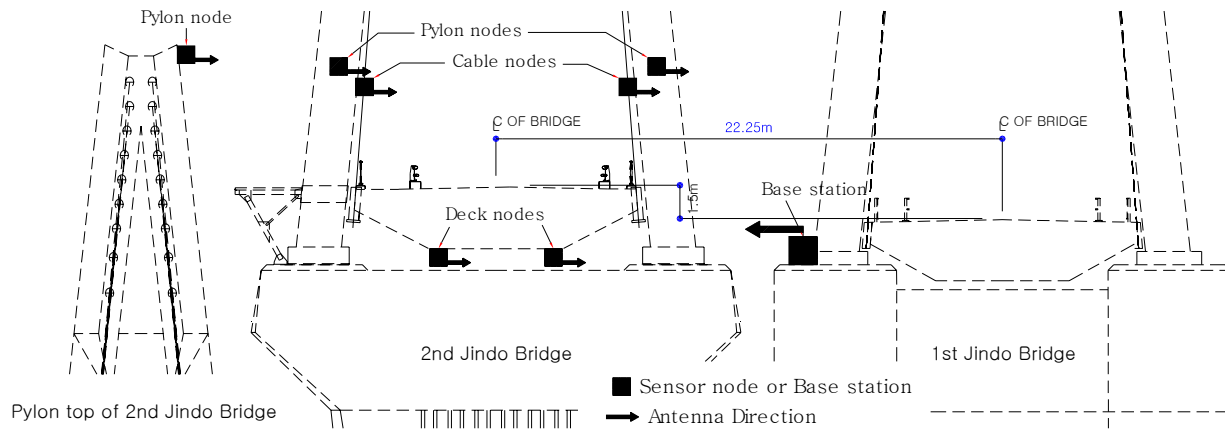


Figure 6.13. Antenna direction.

6.5 Communication Parameter Optimization

The communication parameters have been optimized to operate the large WSSN for the Jindo Bridge in terms of *RemoteSensing*, *DecentralizeDataAggregation*, *SnoozeAlarm*, *ThresholdSentry*, and *Watchdog Timer*. Table 6.2 shows the list of the initial network parameters and updated values after optimization. The number of times the *RemoteSensing* application can be invoked is updated into 4 times a day. The main issue regarding the number of measurements is the power consumption which was found to be higher for the *SnoozeAlarm* than that of the sensing.

The communication waiting times are important for successful *RemoteSensing* with large networks of smart sensors. There are four wait times associated with *RemoteSensing*: (1) network time synchronization, (2) sending measurement parameters from the gateway to leaf nodes, (3) data collection, and (4) transferring data back to the gateway node and saving it on the PC. The first communication is the wait time for time synchronization. The second wait time is

the time required to send the sensing parameters to all of the nodes in the network. This total wait time is expressed by

$$T = S_c + n \cdot S_n \quad (4.18)$$

where, S_c is a constant wait time, S_n is a wait time for each sensor which can incorporate with large network, and n is the number of sensors. These two parameters are increased considerably because the communication took longer as the distances between sensor nodes increased.

The data measurement parameters include the sampling frequency, the measurement directions, and the number of data point for each channel. 10,000 data points are measured in three directions at 10 Hz. 5,000 data points are usually measured when the network communication is not desirable.

The *SnoozeAlarm* parameters include the duration of the wake/listen time and the sleep time. The sleep time can be chosen based on the target excitation. For Jindo Bridge, loading from strong winds such as typhoons having a duration of several hours to a day is important. For such excitations, waking the network up within several minutes of a trigger event is quite reasonable. In this sense, the deep sleep interval is set to 15 seconds, and the wakeup time to listen for commands is 750ms. With this setup, the wake-up time for the entire network was in the range of 1 ~ 5 minutes based on the radio communication conditions.

The *ThresholdSentry* parameters include the number of sentry nodes used in the network. The number of sentry nodes for this deployment is three for Haenam side and two for Jindo side. The sentry checks the acceleration level frequently to catch large vibration due to strong winds. The sentries are set to wake up every 10 minutes and measure the acceleration for 10 seconds.

In this deployment, new functionalities for the threshold sentry have been added. Because the Jindo bridge is on windy environment, the wind-based sentry has been newly employed.

Multiple threshold strategy has been programmed. If the threshold value is very small, then the network will initiate the sensing frequently. While the threshold value is too high, the WSSN will rarely start sensing. By employing two threshold values with small and high value, the network can initiate network sensing for rare event, no matter how many set of data sets have been measured using the smaller threshold. In this deployment, the thresholds for the vibration sentry are 10-mg and 50-mg, the thresholds for the wind sentry are 3 m/sec and 8 m/sec. In Haenam side, three sentries are taking turns to measure the maximum vibration/wind to report the threshold exceeding event to the base station. The network sensing will be initiated 4 times for the first threshold, and 1 time for the second threshold.

Finally, a *Watchdog* timer is used to reset the nodes to ensure the network reliability in the case of a node hanging due to some unexpected error. The *Watchdog* update time is the waiting time before the processor resets the node when the node gets hung up. Using this setup, an indefinite hang-up of nodes may be avoided. The *Watchdog* period should be longer than the measurement duration so that the *Watchdog* timer does not interrupt the measurement and reset the leaf nodes. The *Watchdog* update was set to one minute, and the watchdog timer period is set to 10 minutes during the initial state, because the network sensing takes less than 10 minutes. This is updated to 60 minutes and 60 minutes respectively for the updated state to measure longer data from increased distances.

Table 6.2. Parameters for the Jindo Bridges.

Category	Parameter	Initial	Updated
RemoteSensing	Number of RemoteSensing events	1 per day	4 for 1st threshold 1 for 2nd threshold per day
	Time synchronization wait time	30 sec	30 sec
	SENSING START DELAY	15,000	50,000
	NODE SENSING START DELAY	1,000	1,500
	Sampling frequency	50 Hz	10 Hz
	Channels sampled	3	3
	Number of data points	1,000	5,000
Snooze Alarm	<i>SnoozeAlarm</i> wake/listen time	750 ms	750 ms
	<i>SnoozeAlarm</i> sleep time	15 sec	15 sec
	<i>SnoozeAlarm</i> duty cycle	4.76%	4.76%
ThresholdSentry	ThresholdSentry check interval	20 min	10 min
	ThresholdSentry sensing time	10 sec	10 sec
	Threshold value for vibration sentry	10 mg	10 ,50 mg
	Threshold value for wind sentry	N/A	3, 8 m/sec
Watchdog Timer	Period	10 min	60 min
	Update	1 min	60 min

6.6 Evaluation of the SHM System

The performance of the hardware and software framework has been evaluated in terms of basic functionality and long-term stability. The data from the deployed system have plotted in vibration, frequency-domain data, and wind velocity. The power consumption and the performance of the solar energy harvesting devices are examined.

6.6.1 Hardware performance

The hardware components, including smart sensor nodes, base stations, and the anemometer with environmental hardening devices have shown reliable performance during this deployment. The SHM-A and SHM-W sensor boards have reliably measured the vibration and wind information. However, the horizontal component of the wind direction is not measured by channel 2 of the SHM-W board because of hardware malfunction on the anemometer.

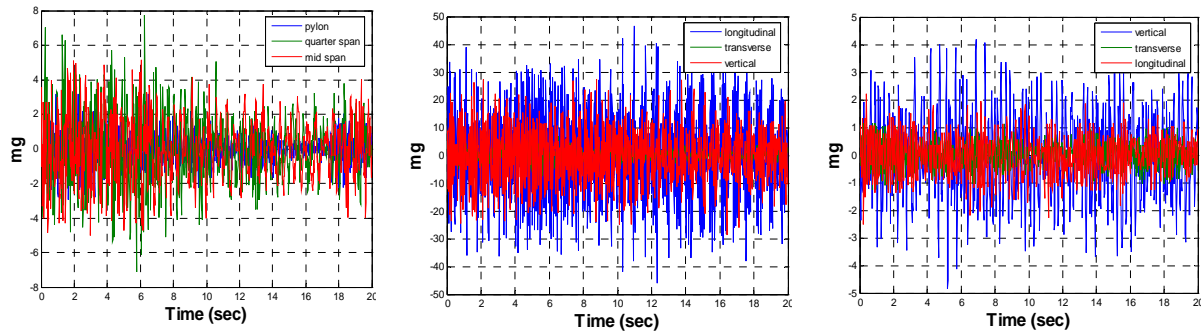
The two base stations functioned reliably for four months, enabling stable remote monitoring of the Jindo Bridge and communication with each gateway node. When checking the condition of the inside of the base station enclosure after four months of operation, it was confirmed that it has successfully protected the computer from overheating and the harsh environment.

The enclosure for the smart sensor nodes have also performed well. The inside of the sensor enclosures were dry and the temperature was acceptable when it is checked. The magnet-based attachment has proven to be an excellent solution for the Jindo Bridge, because all leaf nodes were attached firmly for four months.

6.6.2 Software performance

The *AutoMonitor* application showed stable performance after appropriate optimization of the sensing and radio communication parameters. All software was operating reliably and accessible using remote desktop via a VNC® server. *RemoteSensing* and *DecentralizedDataAggregation* worked successfully with optimized communication parameters.

The ambient vibration data at the Jindo Bridge has been acquired from the WSSN. One sample of recorded data has shown in Figure 6.14, for which the levels are ~8mg, ~40mg, ~5mg for the deck, cable, and pylon, respectively.

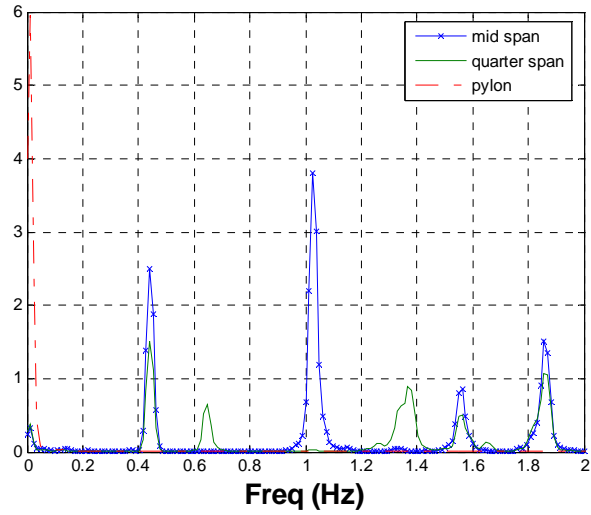


(a) Deck vibration (b) Cable vibration (node 4, Cable3) (c) Pylon vibration (node 5, top)

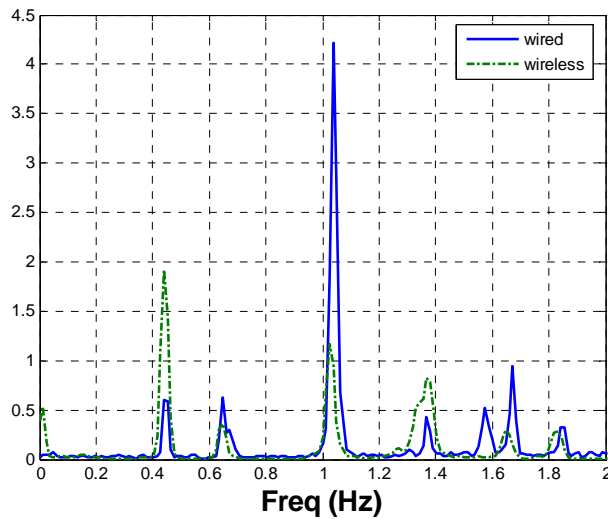
Figure 6.14. Acceleration on the Jindo side on 6/12/2009 at 04:50PM.

The power spectral densities (PSD) of the vibration data were also investigated. Figure 6.15 (a) shows the PSDs of the deck vibrations at the mid span and quarter span, as well as at the pylon. The PSD magnitude of deck sensors near the pylon is almost zero; however, the other two sensors at the mid span and the quarter span show significant energy around 0.44, 0.66, and 1.03 Hz, indicating the natural frequencies of the bridge. Figure 6.15 (b) shows a comparison between the PSD from the existing wired sensor at the quarter span and the PSD from the deployed wireless sensor at the same location. Though the wired sensor data was measured in

2007 and the wireless sensor data was measured in 2009, most natural frequencies agree well with the previous data.



(a) Deck vibration (7/18/2009)



(b) Comparison with wired data measured in 2007

Figure 6.15. Power Spectral Density comparison at the quarter span of the Jindo side.

Figure 6.16 shows the PSD from the cable and pylon sensors. Figure 6.16 (a) shows the PSD of the six cables sensors in Jindo side. For the cable sensors, the consistent peaks are shown

around 0.44, 0.66, 1.03 Hz for all sensor but other peaks in higher frequency region are not consistent. Figure 6.16 (b) shows the PSD from the pylon sensors. In the legend, 1 is the sensor on the side, and 2 is the sensor at the top of the pylon. The natural frequencies of the pylon sensor on the side and of the one at the top are different. Detailed modal analysis and detailed cable tension estimation is described in Cho *et al.* (2010).

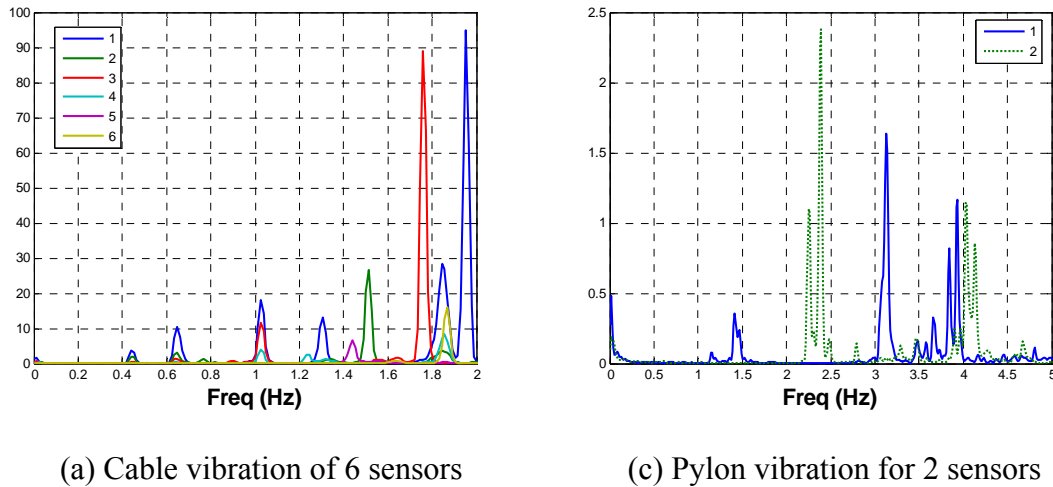


Figure 6.16. Power spectral density on 7/18/2009.

6.6.3 Wind speed and direction

The wind speed and direction has been successfully measured using the 3D ultra-sonic anemometer at the mid span. The outputs of the SHM-W sensor board are raw voltage measurements from the anemometer. The data were converted to the wind speed and voltage using the sensitivity. The data is synchronized with vibration data measured by the SHM-A sensor board. Figure 6.17 shows example data. In this sample data, the wind speed was 4-6 m/sec, and the direction is at 0 degrees to the longitudinal direction of the bridge.

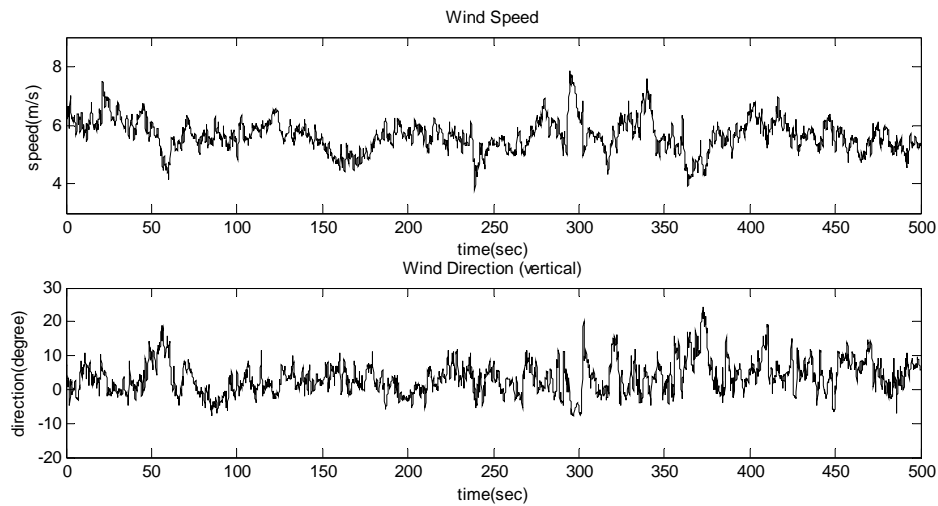


Figure 6.17. Wind data measured at 6:33 am on 9/8/2009.

Figure 6.18 shows the operating time for the *RemoteSensing* application in terms of various phases for different requested sample sizes. In total, three axes of accelerations were measured at 50 Hz from 23 sensor nodes. In this specific deployment, the communication time sending data back to the gateway node has been measured. Although the total communication time depends on various environmental and communication factors, the communication time shows a linear relationship with the number of requested data points. Based on this result, the total communication time to acquire 30,000 points from 46 sensors of two networks is about 30 minutes.

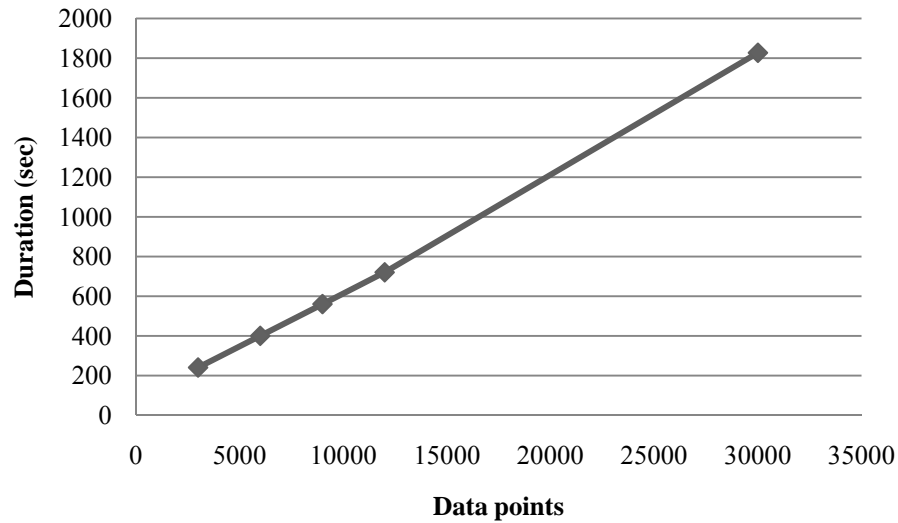


Figure 6.18. Communication time of 23 sensors based on the number of data points collected.

6.6.4 Power consumption

The battery voltage levels for all nodes on both the Jindo and the Haenam sides have been recorded for two months as shown in Figure 6.19. The average initial voltage of the three D-cell batteries on each sensor nodes was 4.6V, and the average on board voltage reading using *RemoteVbat* command was 4.2V. Recall that the measured voltage reading is 0.3~0.4V less than the actual battery voltage because of the diode drop on the battery board. From 8/27/09 to 9/8/09, the parameters stored in FLASH on each Imote2 were uploaded many times to optimize network performance, which is a power demanding procedure. After 9/8, the *AutoMonitor* application has run continuously to measure the data. During this period, the power consumption has been approximately linear. The minimum onboard voltage for sensing is 3.4V. The power consumption depends on the frequency of data measurement, data length, and sleeping parameters. Based on once a day measurement with the network parameters mentioned in Table 6.2, 3 D-cell battery can operate approximately 2 months.

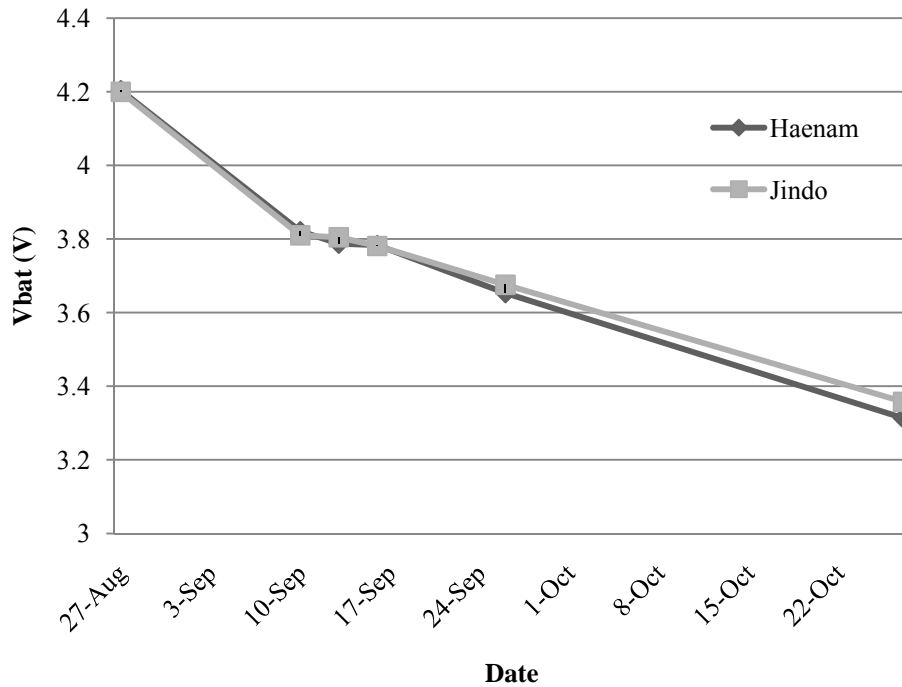


Figure 6.19. Average on-board voltage.

6.6.5 Energy harvesting strategy using solar power

In total, eight sensor nodes employ solar panels and rechargeable batteries. Five of the solar powered sensor nodes are on the cables, two on the pylons, and one on the deck. Figure 6.20 shows the voltage of the solar rechargeable batteries during monitoring. The voltage level of the rechargeable battery was maintained around 4.15V, which confirms that the charging process of the solar power system is working well. However, the solar powered node located under the deck (Haenam side, node 6) shows a continuous decrease in the voltage level. The reason for the decrease is that it only can receive indirect reflected sunlight, because its orientation is downward. a more sensitive solar panel, reorienting the panel, or another type of energy harvesting system should be considered for sensors located under the deck in the next deployment.

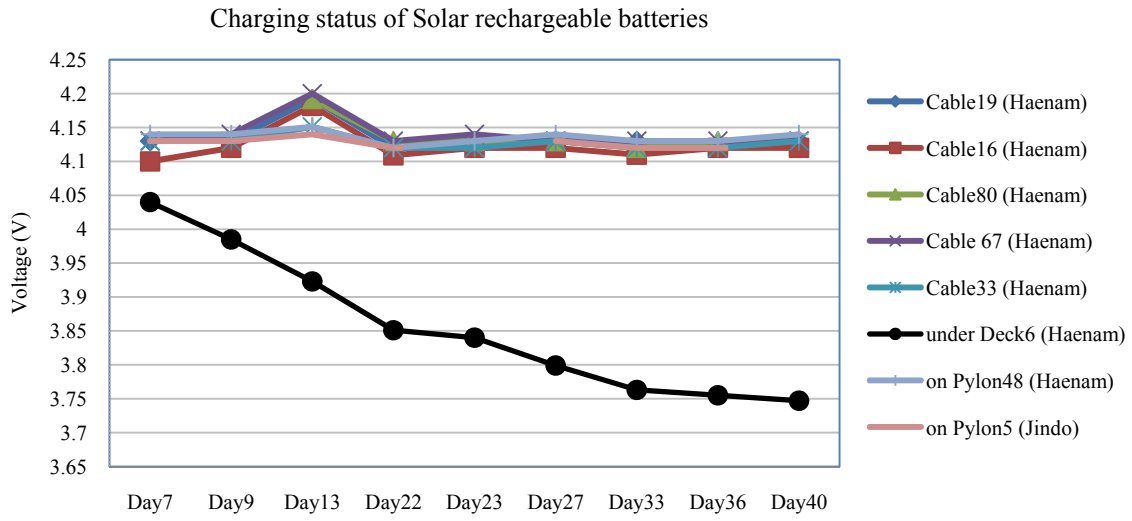


Figure 6.20. Charging status of solar rechargeable batteries.

6.7 Conclusion

A state-of-the-art SHM system using a WSSN was successfully deployed on the Jindo Bridge in South Korea to verify the performance of the system and to serve as a driver for advancement of smart sensor technology. The Imote2 was selected as the wireless sensor platform to use along with the custom-designed SHM-A and SHM-W sensor boards. An autonomous structural monitoring system was developed employing a threshold detection strategy and an energy-efficient sleeping mode to extend the network lifetime. Solar powered nodes were employed to investigate the possibility of energy harvesting to power the sensor network.

In total, 71 sensor nodes were installed, divided into two sub-networks to decrease the communication time and because of the limit of the radio communication range. All sensors are carefully located based on radio communication capability determined by extensive radio communication tests. The measured data shows a good agreement with data from the existing wired system, which verifies the data quality of the WSSN. Successful deployment of this WSSN demonstrates the suitability of the Imote2 smart sensor platform, the SHM-A sensor board, and the ISHMP software for full-scale, autonomous SHM.

CHAPTER 7 FULL-SCALE SHM OF A HISTORIC BRIDGE

The Jindo bridge deployment presented in the previous chapter has shown the potential of WSSNs for autonomous monitoring of large-scale bridge structures. The main goal of that deployment was to collect data from all nodes. However, the next step is damage detection of bridge structures using the measured data.

This chapter provides a full-scale condition assessment of a historic steel truss bridge using model updating. As a first step, the bridge has been visually investigated to estimate current structural condition. A series of short-term, full-scale forced vibration tests have been conducted to measure high fidelity acceleration data on this bridge using both wired and wireless sensor systems. During the vibration tests, the data quality of the wireless sensor system has been compared with the wired sensor system. A brief modal analysis using the peak picking method has been conducted using the measured data. A FE model is built based on field measurements. However, the natural frequencies of the initial FE model and the measured data were considerably different, mainly due to significant corrosion after 100-year of operation in a harsh environment. Therefore, the FE model has been updated using a multi-step optimization strategy to estimate the corrosion level in the bridge members, which are then correlated with the visual investigation results.

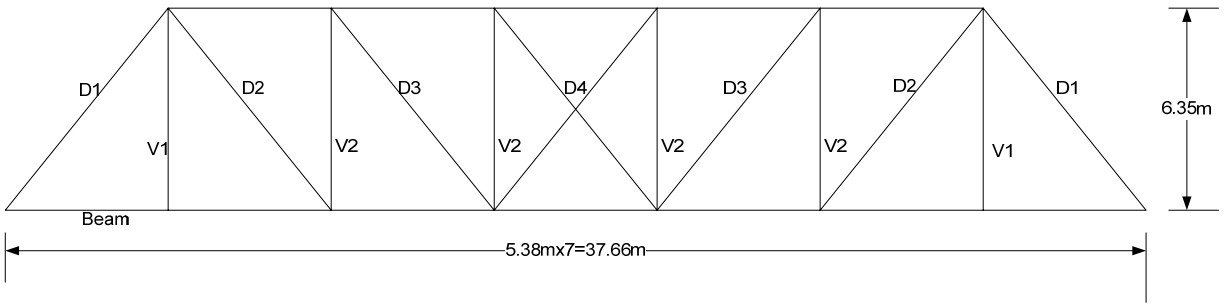
7.1 Bridge Description

The Mahomet Bridge crossing the Sangamon River is located at 106 South East Street in Mahomet, Illinois (see Figure 7.1). This bridge was constructed in 1912 by Decatur Bridge Company, as one of typical metal truss bridges of the era. The total length of the two-span steel

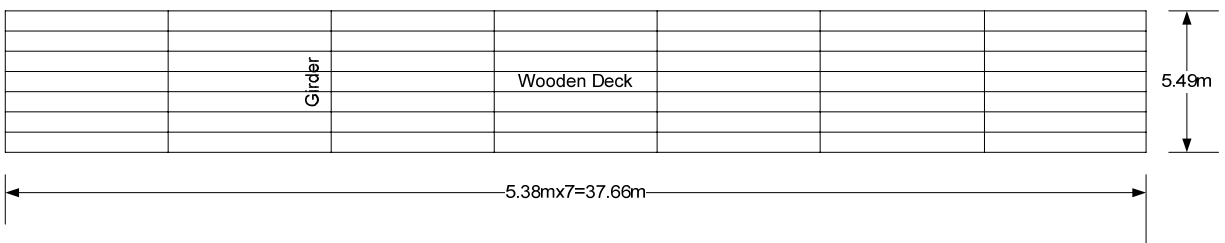
bridge is 75 meters. The dimensions of the bridge are shown in Figure 7.2. The superstructure consists of various box sections with inverted channel sections riveted to two steel plates. The timber deck is supported on a series of 8 steel girders connected to transverse I-beams. Both spans rest on a central concrete abutment and the side banks.



Figure 7.1. Mahomet Bridge, IL.



(a) Elevation view



(b) Plan view

Figure 7.2. Bridge dimension.

The boundary conditions for the girders are shown in Figure 7.3. Among 8 girders, two exterior girders are rollers, and the interior 6 girders are either completely or partially embedded into the concrete for the north side and the center. For the south side, two exterior girders are rollers, and the interior 6 girders are welded to a transverse beam.



(a) North side



(b) Center



(c) South side

Figure 7.3. Boundary conditions.

This bridge is subjected to many environmental loadings, including wind, extreme temperature, floods, *etc.* The Mahomet region has frequent tornados and wind gusts. The annual temperature fluctuation in this location is nearly 73°C, the highest of 42°C in July, the lowest of -31°C in January and February according to the recorded weather data (<http://weatherbase.com>). In addition, the bridge has frequently suffered from floods. For example, two floods occurred due to melting accumulated snow and heavy rain in 2008, as shown in Figure 7.4. When it is flooded, the debris in the Sangamon River hits the bridge pier and abutments, which may result in damage.



(a) January 11, 2008



(b) February 6, 2008

Figure 7.4. The Mahomet Bridge during flood.

The bridge has several advantages for SHM studies. First of all, because it is a pedestrian bridge, no automobile/truck traffic needs to be stopped to conduct tests. Also, this bridge is built having two nearly identical spans; however, each span may have different degrees of deterioration and repairs. Currently, the bridge has experienced extensive corrosion, resulting in various kinds of stiffness reduction damage, as shown in the brief visual investigation in section

0. Finally, this bridge is a standard steel truss bridge built in early 1900s which are widespread in the US, so that this bridge can represent many existing steel truss bridges. For all of these reasons, this bridge is an excellent Testbed for implementation of SHM.

7.2 Visual Investigation

In this section, current condition of the bridge has been investigated. Major and minor damage have been determined in visual monitoring. In this monitoring, significant corrosion has been found as major damage in this bridge. The degrees of corrosion have been estimated using the ASTM corrosion estimation chart.

7.2.1 General investigation

A brief visual investigation of the status of the bridge was conducted before dynamic tests. In general, the most noticeable damage is steel corrosion. As shown in Figure 7.5, the main truss elements, including the horizontal, diagonal, and vertical chords, supports, and connections, are considerably corroded. Miscellaneous structural damage is in sectional loss at a support, bent eye bar, and top flange of the main diagonal chord (see Figure 7.6).



(a) Vertical chord



(b) Support



(c) Connections: rivet and bolts

Figure 7.5. Corrosion of the bridge



(a) Section loss and hole.



(b) Bent elements.

Figure 7.6. Damage of the bridge.

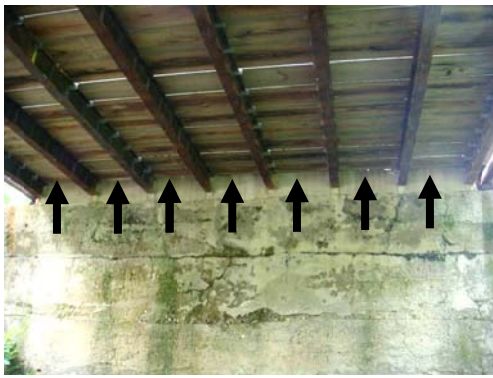
Evidence of repair has also been identified (see the arrows in Figure 7.7). The deck was originally made of reinforced concrete when the bridge was used for horses and carriages (Decatur Bridge Company, 1912). In March 2000, the deck was replaced with timbers, after which the bridge was dedicated to pedestrian and bicycle passage (see Figure 7.7 (a)). The flanges of the vertical chords at the pin connection were reinforced by new welded steel plates (see Figure 7.7 (b)) due to severe corrosion. At the center support, the space between inside girders was filled with new concrete (see Figure 7.7 (c)). Finally, the south abutment was rebuilt with new concrete (see Figure 7.7 (d)).



(a) Timber deck



(b) Retrofitted vertical chord



(c) Concrete fill



(d) New abutment

Figure 7.7. Repair of the bridge.

7.2.2 Corrosion assessment

The corrosion levels of various elements are investigated by correlating the ASTM standard corrosion chart with visual monitoring. Severe pitting corrosion was found in the end post, vertical channels, cross girders, and longitudinal beams as Figure 7.8, while the vertical and diagonal members have less severe corrosion which appears to be stable (see Figure 7.9). The detailed strength of the steel elements and exact degree of the corrosion are unknown. The detailed coring tests are intractable because the bridge is in use. Therefore, the varying degrees

of the corrosion of bridge elements are estimated by visual investigation using ASTM corrosion chart.



(a) End post



(b) Vertical channels



(c) Cross girders



(d) Longitudinal beams

Figure 7.8. Severely corroded sections



(a) Vertical rods

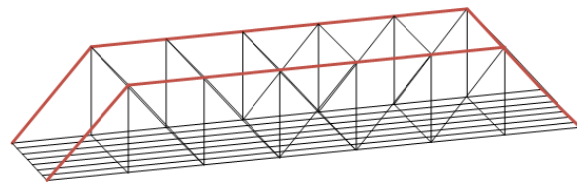


(b) Diagonal rods

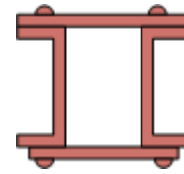
Figure 7.9. Less severely corroded sections.

Brief corrosion estimation using a standard ASTM rating chart has been conducted. Based on the visual investigation, the structure has been categorized into 6 groups in Figure 7.10. For the severely corroded sections, the thickness loss is estimated as 1.6 mm; for the less severely corroded sections, the loss is estimated as 0.8 mm. The corresponding sectional properties are calculated based on the sectional shape in Table 7.1.

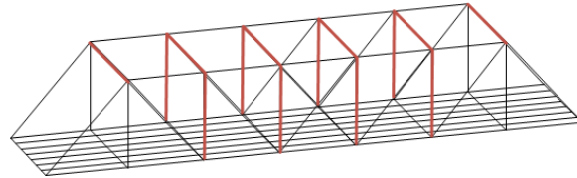
Cross sections 1, 2 are channel sections with V-lacing; cross sections 3, 4 are rectangular; cross section 5, 6 are I-beams. The corrosion of the channels and I-beams result in significant bending stiffness loss due to larger surface areas. As shown in this table, the corrosion is significant over the whole bridges, resulting in losses of stiffness up to 51%.



(a) Section 1: end post



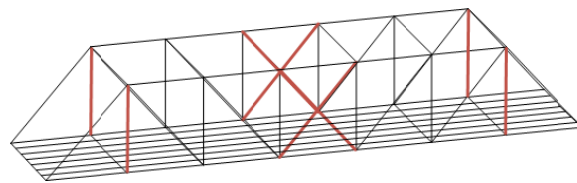
Cross section



(b) Section 2: vertical chords



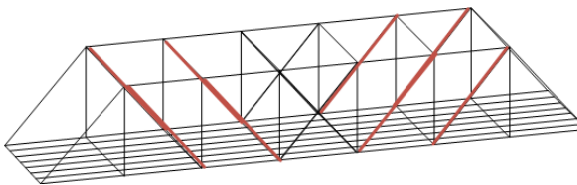
Cross section



(c) Vertical and central diagonal rods



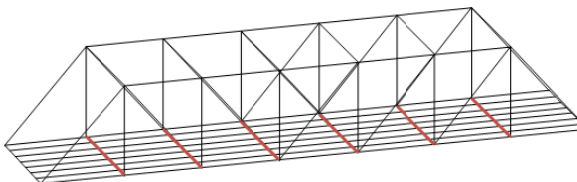
Cross section



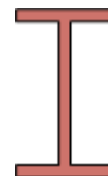
(d) Section 4: diagonal rods



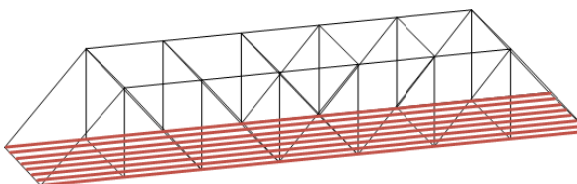
Cross section



(e) Section 5: cross girders



Cross section



(f) Section 6: longitudinal beams



Cross section

Figure 7.10. Cross sections

Table 7.1. Corrosion evaluation and corresponding sectional properties.

Cross Section	1	2	3	4	5	6
Thickness Loss (in)	0.064	0.064	0.032	0.032	0.08	0.064
Reduced A (%)	51.46	48.99	89.13	91.88	53.32	62.17

7.3 Full-scale Modal Analysis using Wired System

A campaign-type vibration test was conducted on the bridge using wired sensor system to gain an understanding of the basic dynamic properties of the bridge. Additionally, because measured data corresponding to the undamaged bridge in 1912 is not available, the state of the bridge in 2008 was taken as the baseline for subsequent testing. The equipments for the experiment and the setup are briefly described. Using the wired sensor system, bridge responses from the ambient vibration test and forced vibration tests are shown. The modal analysis has been conducted using the measured data.

7.3.1 Experimental setup

The necessary testing equipment was assembled and taken to the bridge site. The components of the wired sensing system are accelerometers, signal conditioners/amplifier units, a spectrum analyzer, National Instrument (NI) data acquisition modules, and computers. PCB 353B33 accelerometers were installed to measure a single input excitation and 10 output accelerations. The measurement range of the accelerometers is between 1-4,000 Hz. The schematic of the sensing system is shown in Figure 7.11. PCB 442B104 signal conditioners and 441A101 AC power supply units provided power to the accelerometers and amplified the analog signal up to

100 times, respectively. An NI SCXI-1141 anti-aliasing filter module is connected to the NI DAQpad 6052E data acquisition card. A Labview program was developed to control this equipment.

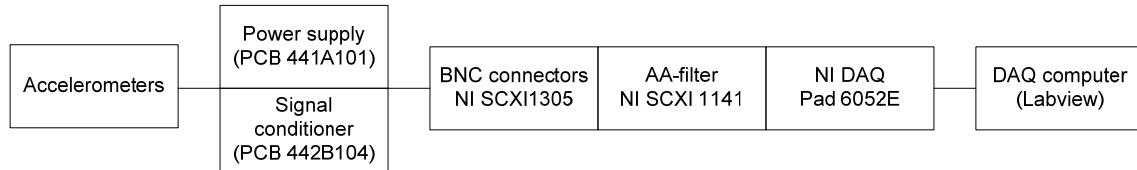


Figure 7.11. Data acquisition system for the acceleration measurement.

The input excitation for the random vibration tests is generated by a vertically-intalled shaker. A small-scale uniaxial shaking table used for lab-scale experiments was employed (see Figure 7.12). The dimension of the shaker platen is 45.72 cm square on each side. The power supply unit is custom-designed to provide power to the shaker and amplify the output signal from the shaker. This power supply unit is connected to a Quanser MultiQ-E8 board to control the shaker (Quanser, 2000). Wincon software provided by Quanser is used to connect the external command signal from Siglab SL20-42 unit (Spectral Dynamics, 2010).

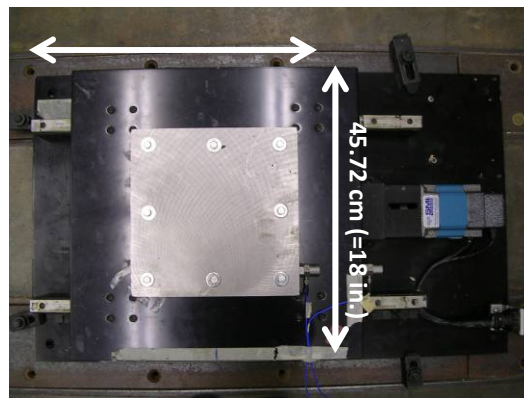
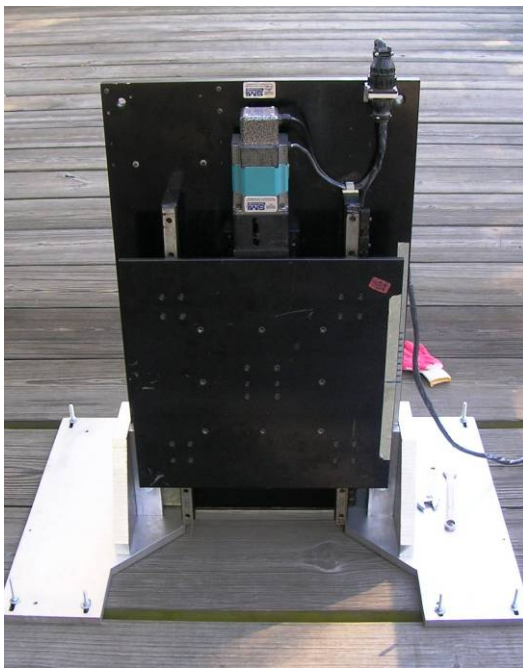


Figure 7.12. Mechanical uniaxial shaker.

This shake table is installed vertically at the bridge girder using brackets and U-bolts to ensure the force transmission to the main structure, as shown in Figure 7.13. The system is designed to generate the vertical vibration only; however, it may also generate some small amount of moment due to small offset between the bottom plate and the top plate.



(a) Shaker bracket



(b) Shaker connected to the bridge

Figure 7.13. Bridge excitation device: mechanical shaker and brackets.

The excitation method for the free vibration tests is a student jumping on the bridge. The jumping pattern was measured in the laboratory using the AMTI® Force Platform BP300500 and MiniAmp. Figure 7.14 shows the measured jumping force. Approximately 90.7 kgf (=200 lbf) of peak jumping force was induced, which was sufficient to excite this bridge generating up to 150mg of vibration in the field (see Figure 7.22).

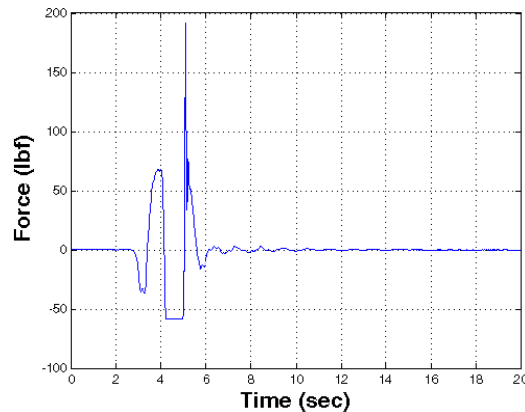
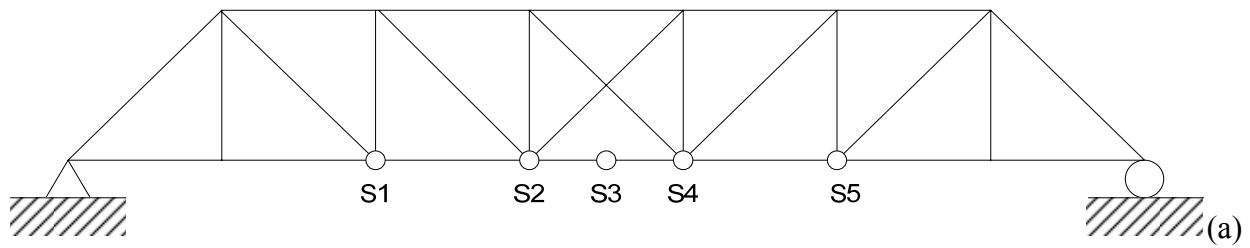
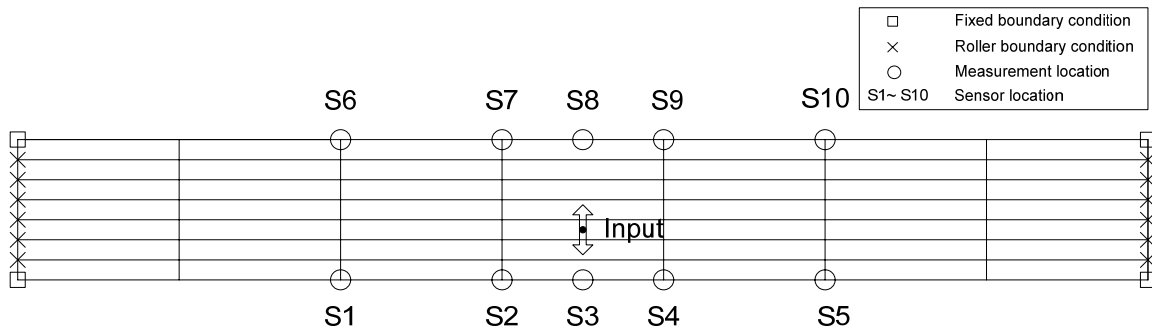


Figure 7.14. Human jumping force.

A total of 11 sensors were employed to measure both excitation and bridge responses. As shown in Figure 7.15, one accelerometer was installed on the shake table and 10 accelerometers were installed vertically along the lower exterior girders. In this test, only vertical accelerations are measured, because of the limited number of sensors.



(a) Elevation view of a testing span

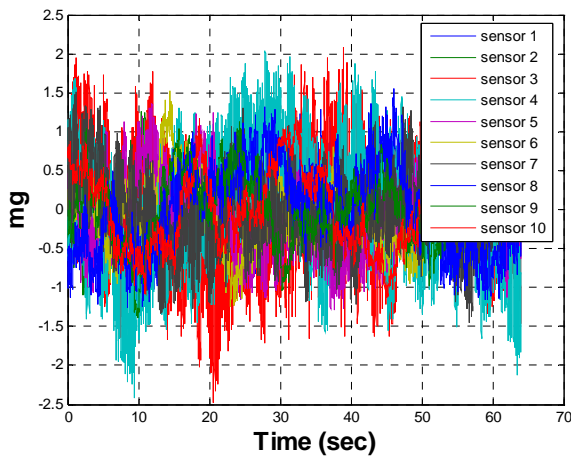


(b) Plan view of a test span

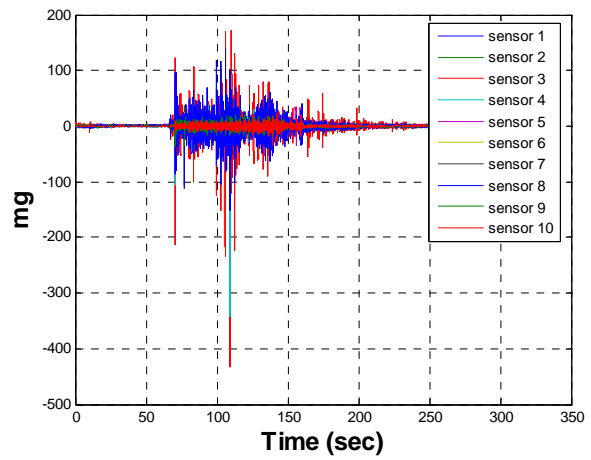
Figure 7.15. Sensor locations.

7.3.2 Ambient vibration tests

The ambient vibration of the bridge was measured to check the environmental acceleration levels for ordinary operating conditions. The acceleration levels of the ambient vibration during a normal day are less than 3 mg, which is negligible vibration compared to the vibration of a person jogging across the bridge (see Figure 7.16). Moreover, the frequency content of the ambient vibration is inadequate to yield meaningful results (see Figure 7.17). To obtain meaningful results, dynamic tests during strong wind may be feasible. However, for short term tests usually conducted for several hours, waiting for strong winds is not feasible. Therefore, external force is required to excite the bridge to obtain meaningful structural properties in short term.



(a) Ambient vibration



(b) One pedestrian jogging

Figure 7.16. Ambient vibration levels.

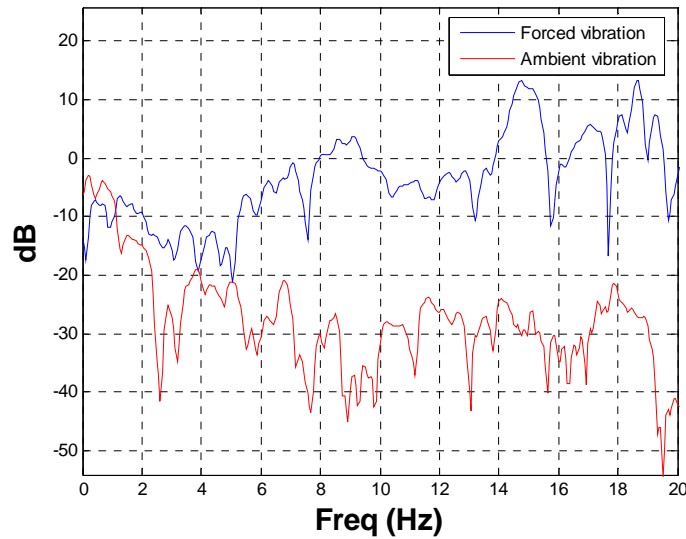


Figure 7.17. Ambient vibration vs one person jumping.

7.3.3 Random vibration tests

To obtain higher bridge responses, the forced vibration tests have been conducted using the shaker. A band-limited random white noise excitation was generated by the vertically-installed

shaker. The accelerations from all 11 sensors are measured during 320 seconds at 256 Hz (=81,920 data points). The time history of the measured acceleration is shown in Figure 7.18.

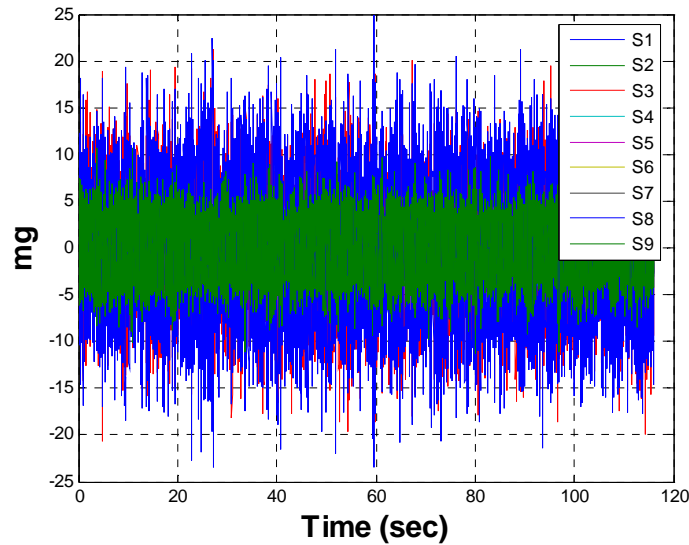


Figure 7.18. Acceleration time history: random vibration

Using the measured data, modal analysis has been conducted. The frequency response functions and coherence functions from input excitation to the measured output are shown in Figure 7.19. The natural frequencies and mode shapes are calculated by a peak picking method from the frequency response functions (see Figure 7.20). From the modal analysis, the first three mode shapes have been successfully identified.

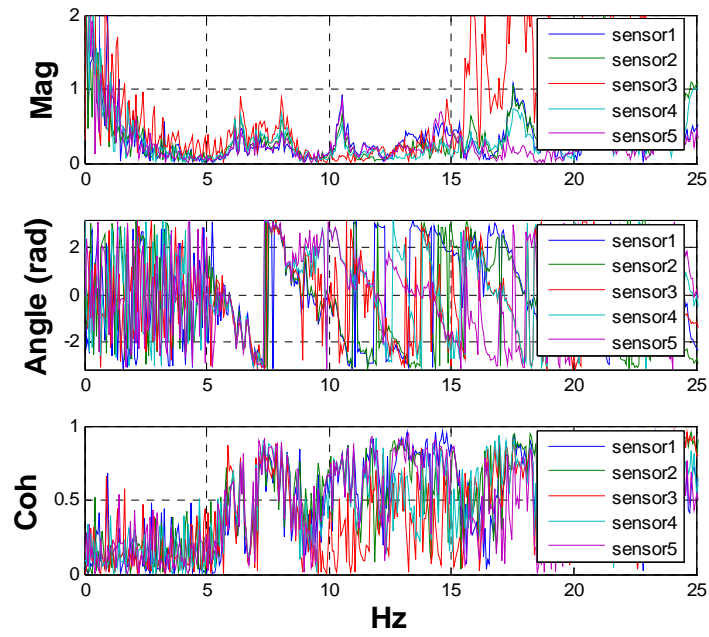
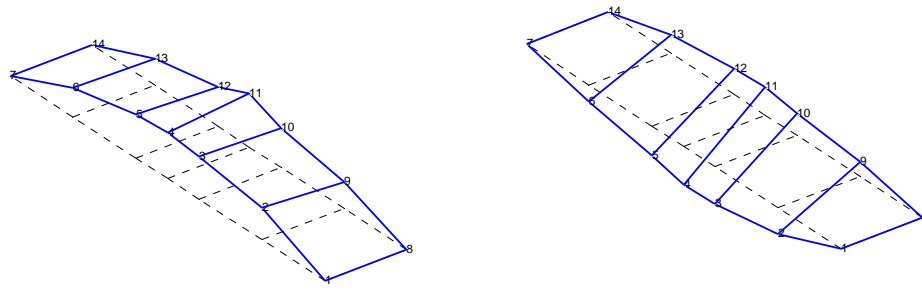
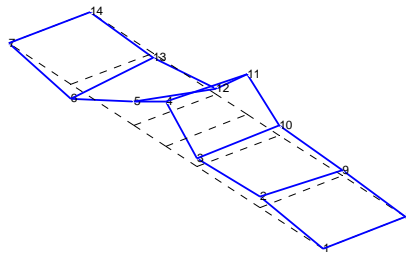


Figure 7.19. Measured frequency response functions



(a) 1st bending: 6.375 Hz

(b) 1st torsional: 8.25 Hz



(c) 3rd vertical mode: 15.6875 Hz

Figure 7.20. Mode shapes.

7.3.4 Free vibration tests

The dynamic properties of the bridge are obtained from the free vibration tests. One person jumped on the bridge, and the free vibration responses of the bridge after jumping were measured. To identify various mode shapes, jumping was at (1) the center of midspan, (2) center of quarter span, and (3) off from the mid span (see numbers in Figure 7.21).

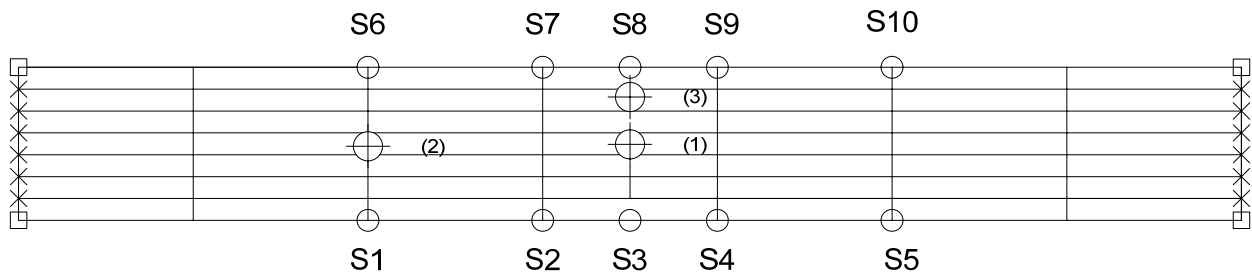


Figure 7.21. Jumping locations

The measured accelerations have been processed to determine modal properties. To ensure that the transient responses and environmental noise decay in the window, the accelerations are exponentially windowed (see Figure 7.22). The windowed free vibration responses are used to calculate the cross spectra as shown in Figure 7.24. By using peak picking method, the modal properties are obtained (see Figure 7.25). In this test, the second vibration mode has been identified with the first and the third modes.

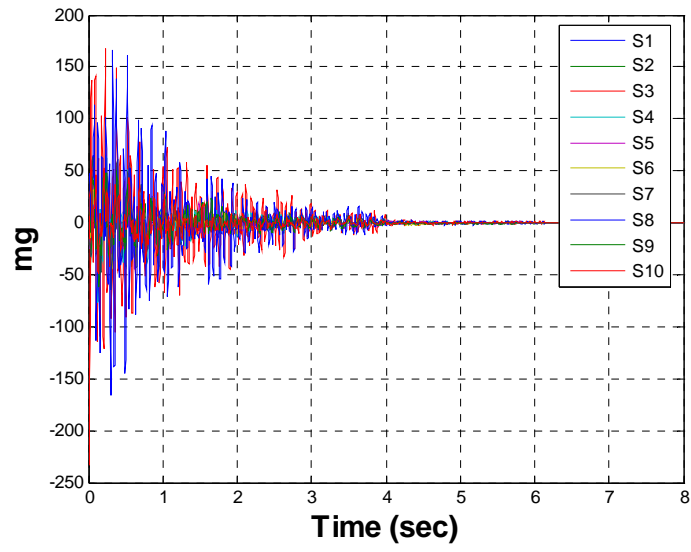
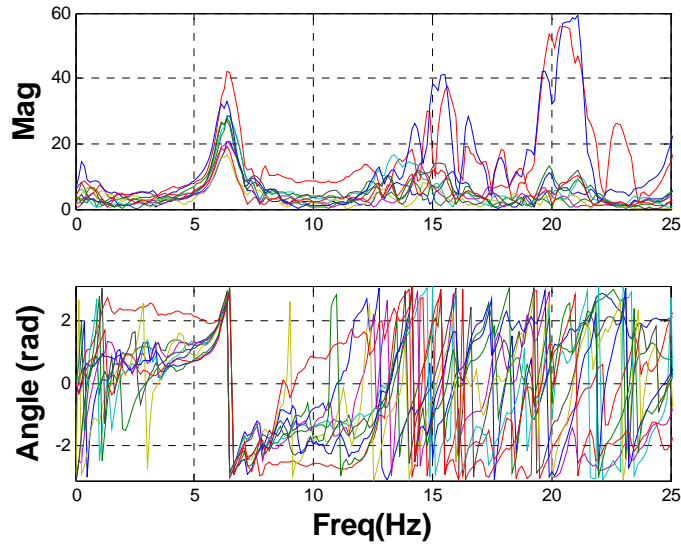
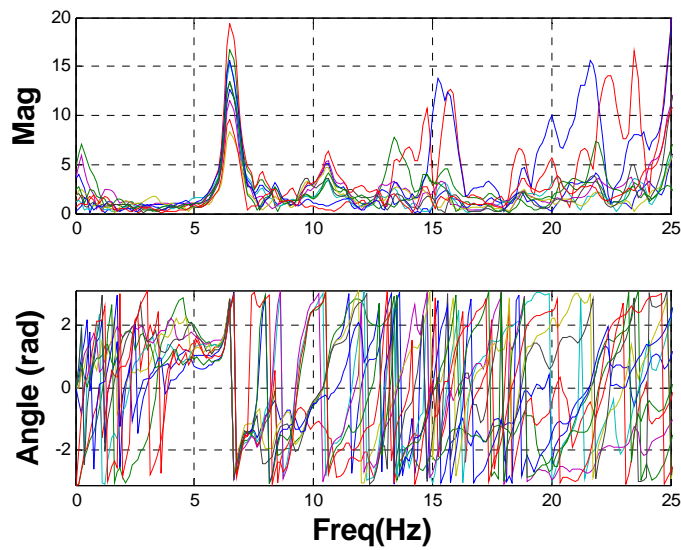


Figure 7.22. Acceleration time history: free vibration

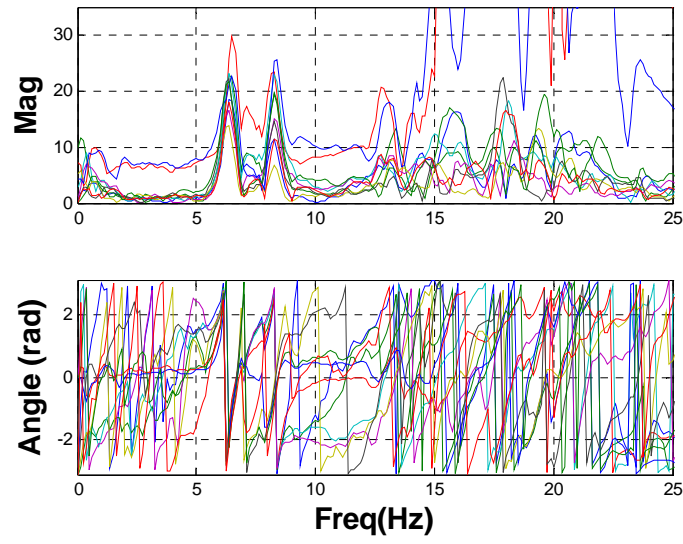


(a) Test1: Jump at center of midspan



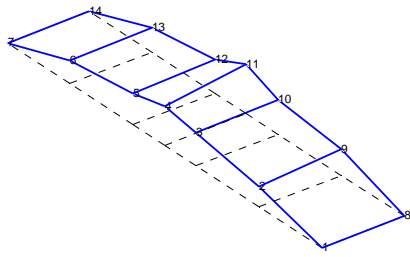
(b) Test2: Jump at quarter span

Figure 7.23. FFT of the free vibration responses: sensor 1 to 5.



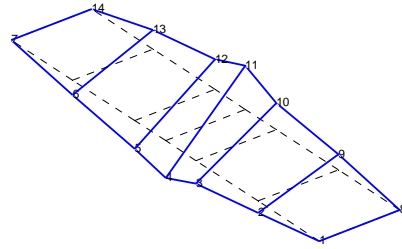
(c) Test3: Jump at side of midspan

Figure 7.24. FFT of the free vibration responses: sensor 1 to 5 (cont.).



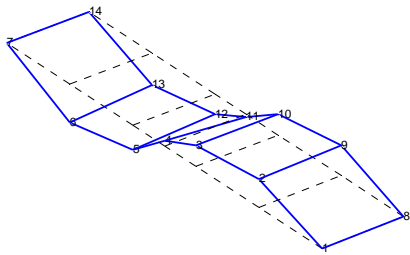
(a) 1st bending: 6.375 Hz

(Test1, 2, 3)



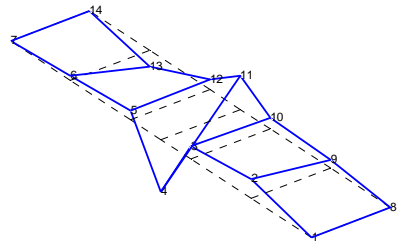
(b) 1st torsional: 8.25 Hz

(Test3)



(c) 2nd bending : 10.625 Hz

(Test2)



(d) 3rd torsional : 15.375 Hz

(Test1, 2, 3)

Figure 7.25. Mode shapes.

7.4 Modal Survey using WSSN

To confirm the data quality of the WSS-based monitoring system, a brief free vibration test has been conducted using both wired and wireless sensor system. Descriptions of wireless sensors and experimental setup are followed by vibration data and modal analysis data. The primary achievement of this test is to verify the ability of wireless sensors and the ISHMP Services Toolsuite for conducting a modal survey.

7.4.1 Wireless sensors

The wireless sensor system used in this test is similar as the system that was used in the Siebel staircase tests. The detailed setup is shown in section 5.2.1 and section 2.3. Because this test was conducted before the Siebel staircase deployment, the original battery board using 3 AAA batteries was used. The external antenna was used only for the gateway node, because the communication between the leaf nodes and the gateway node was stable without it within one span. The types of the wireless sensor systems are a gateway node and leaf nodes (see Figure 7.26).



(a) Gateway node



(b) Leaf node

Figure 7.26. Wireless sensor units.

At the time was the development of the middleware services to provide high-quality sensor data and to transfer the data reliably to the base station via the wireless network. The *RemoteSensing* application in the Toolsuite was employed and examined the functionality for measuring acceleration data adequate for modal survey on the bridge.

7.4.2 Experimental setup

A series of forced vibration tests have been conducted using the wireless sensor system. To compare the data quality for full-scale modal analysis, the brief wired sensor system has been employed along with the wireless system to eliminate potential differences due to the influence of environmental conditions. The wired sensor system employed for this test is similar to the system in section 7.3.1. Because the purpose of testing is to compare the functionality, two Siglab SL20-42 boxes are employed for simplicity.

The sensor locations are shown in Figure 7.27. At each of these six points, a wireless sensor and a wired sensor were collocated on a 20-lb steel weight, as shown in Figure 7.28. This cylindrical shaped steel weight is stable on the bridge during excitation. Between the mass and the wooden deck, some modeling clay was put to prevent rocking motion of the weight.

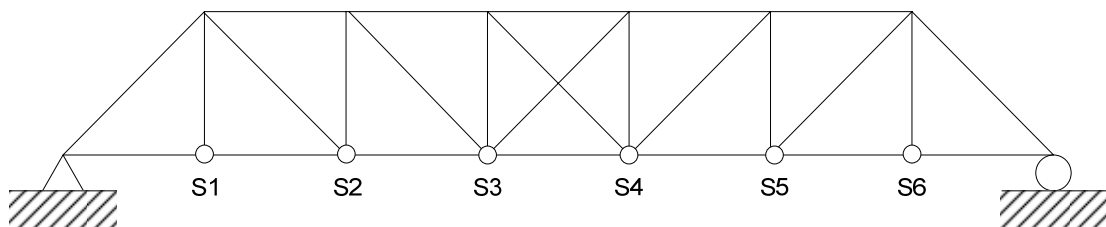


Figure 7.27. Sensor locations.

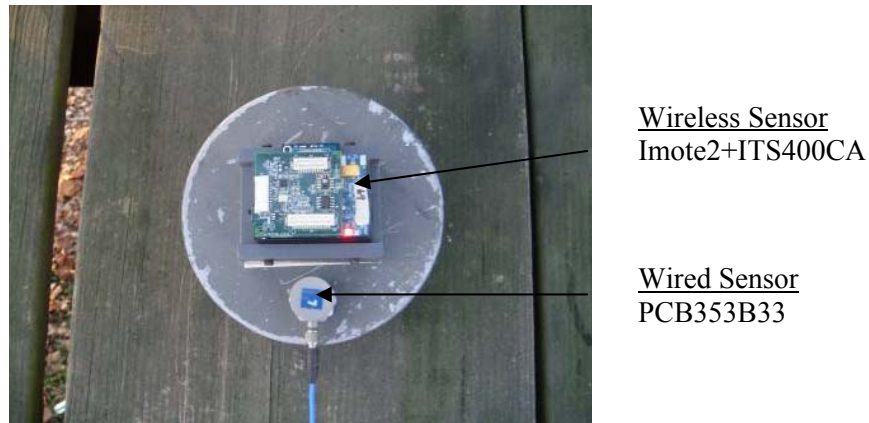


Figure 7.28. Wired and wireless sensor attachment on steel weight.

For the wireless system, one gateway node and six leaf nodes are programmed with the *RemoteSensing* application. In total, 10,000 data points are collected in each of the longitudinal, transverse, and vertical directions. The lowest sampling rate using the ITS400CA, 280 Hz, was used to ensure a 70-Hz measurement bandwidth, which cover several major natural frequencies of the bridge. For the wired system, six uniaxial accelerometers are installed using a magnet base on the weights to measure the vertical vibration. A sampling frequency of 256 Hz was used, and 8,192 data points were recorded.

7.4.3 Vibration data

The vibration responses of the bridge have been recorded using both systems during jump testing. To compare the data from the two systems, the data from wireless sensors are down-sampled from 280 Hz to 256 Hz after collection. Subsequent to down-sampling, the data for both systems is synchronized by maximizing the correlation function between records. The acceleration data from the wireless sensors are shown in Figure 7.29.

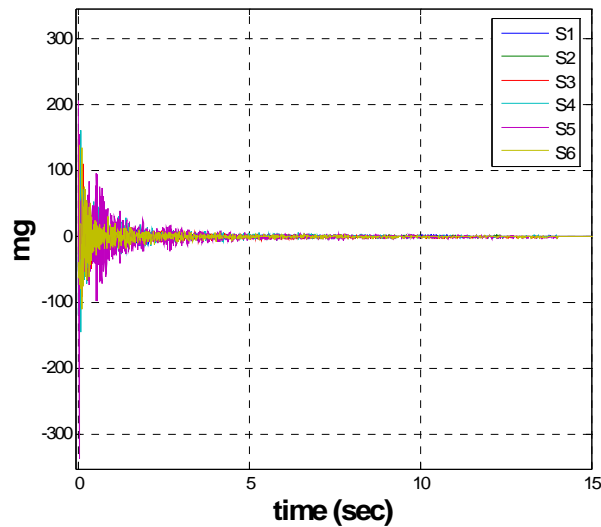


Figure 7.29. Vibration responses using the wireless sensors: S1 – S6.

The measured data for the wireless sensors has been compared with wired sensors. The accelerations from the wired and wireless sensors matched well when the magnitude is larger than 2 mg (see Figure 7.30). However, when the measured bridge response is less than 2 mg, the data from the wireless sensors becomes unreliable as shown in Figure 7.31; the primary limitation in the wireless system is due to the limited resolution of the wireless sensor is approximately 1 mg. The ambient vibration level of this bridge is near 2 mg. This confirms one of the conclusions from the Siebel staircase: the basic sensor board is inadequate to monitor low-level vibration.

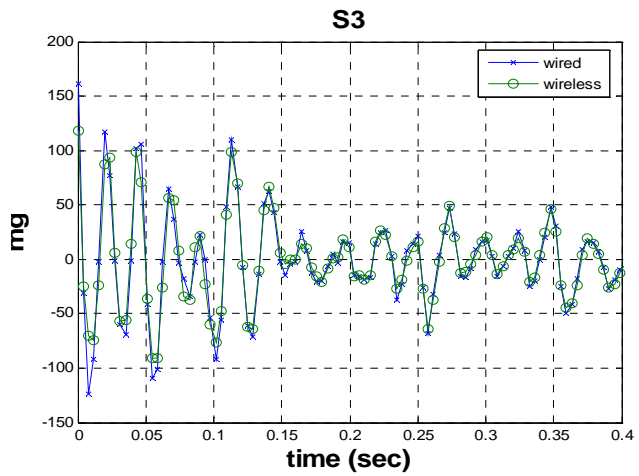
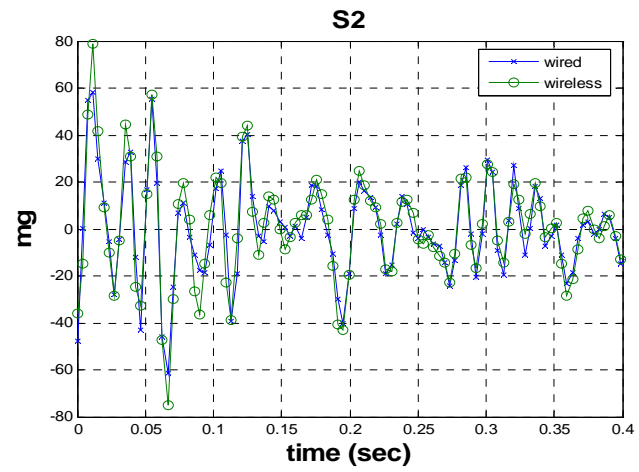
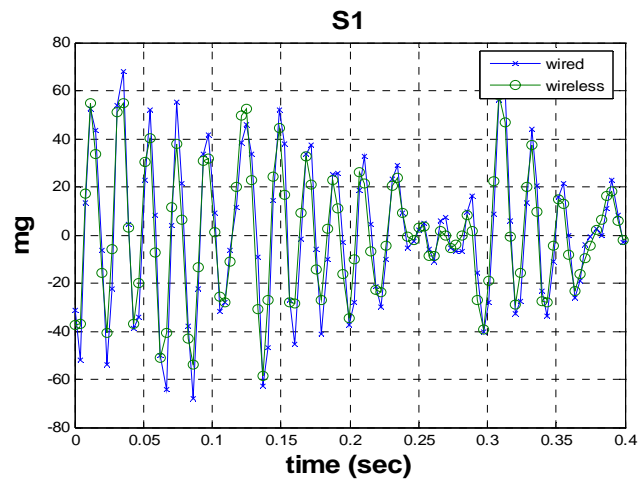


Figure 7.30. Larger vibration comparison: S1 – S3.

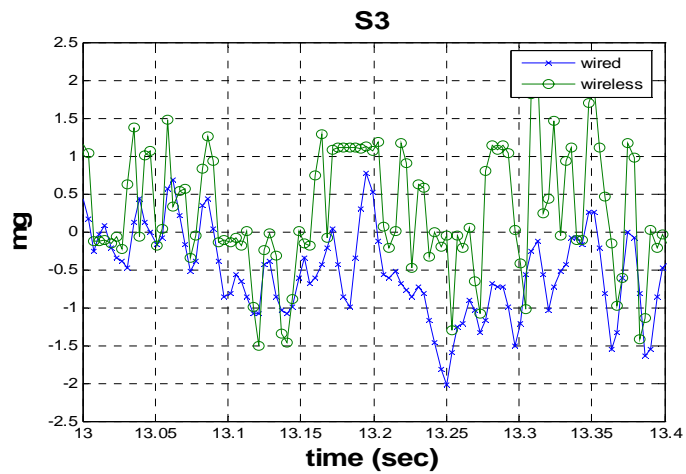
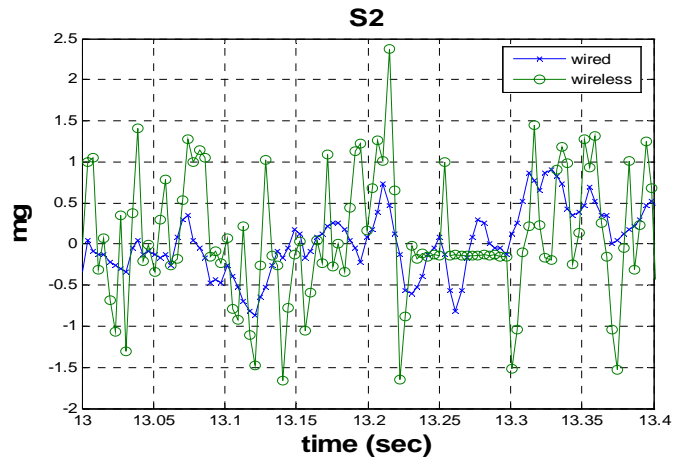
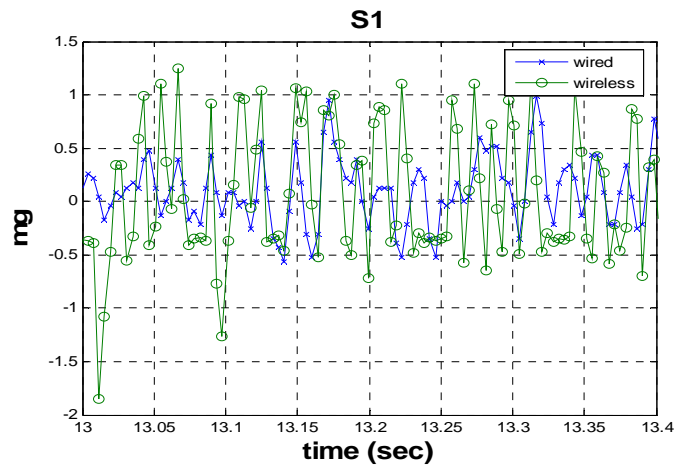


Figure 7.31. Lower vibration comparison below 2 mg: S1 – S3.

The cross spectral density (CSD) functions of the wireless sensor data have been calculated with respect to the reference sensor placed at the jumping point (S4) as shown in Figure 7.32. Comparisons of the CSD plots for the wired and wireless sensors are shown in Figure 7.33. The CSD functions match well around peaks. However, the lower amplitude responses are not properly captured, because of the low resolution of the accelerometer on the ITS400CA sensor boards.

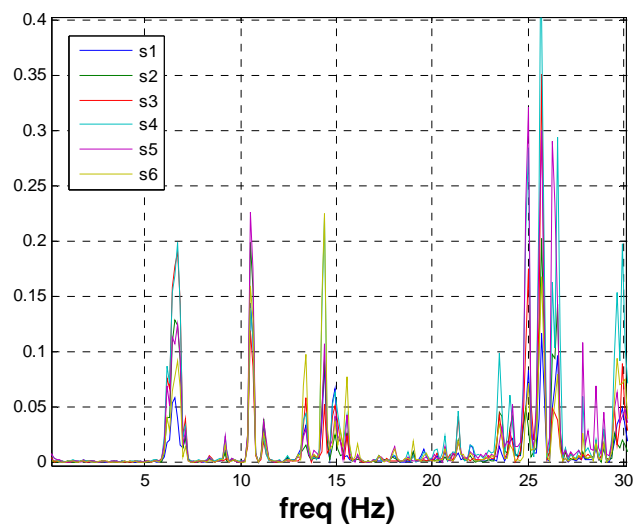


Figure 7.32. CSD from the wireless sensors: S1 ~ S6

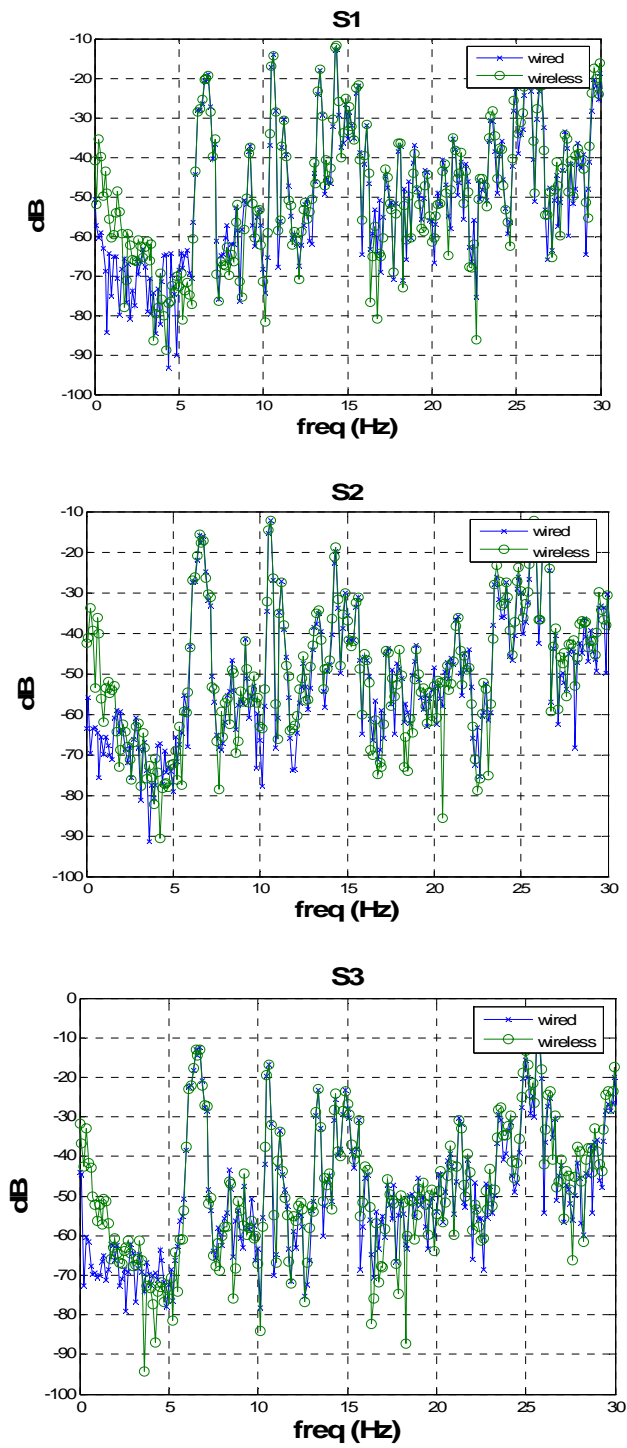
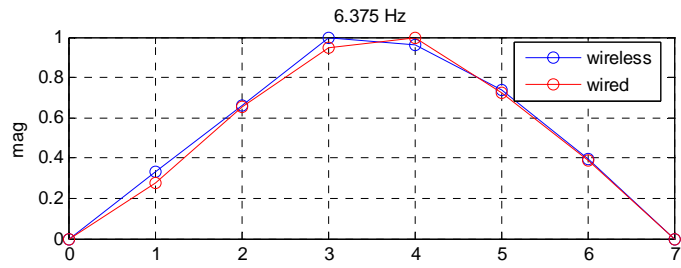


Figure 7.33. CSD comparison: S1 – S3.

7.4.4 Modal analysis

Modal properties are obtained from the measured data using the peak picking method (Silva, 2007). An exponential window was applied to reduce the low amplitude noise of the impulse. The exponent of the window function was selected so that it decays to 0.1% by the end of the window. This exponential window has been applied for both the wired and wireless data.

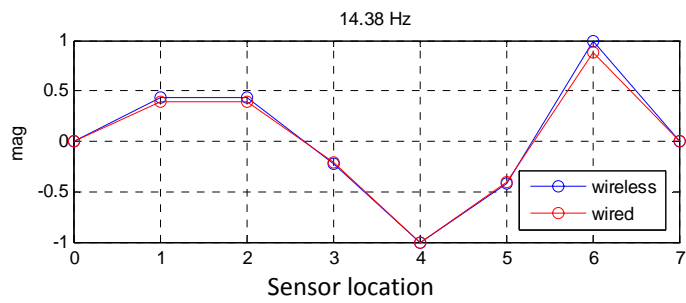
The estimated mode shapes, obtained by peak picking from the CSD, are plotted in Figure 7.34. The natural frequencies match well with the free vibration tests. In the first and third mode shapes, the motions from S5 and S6 are higher than S1 and S2. This situation is amplified in the third mode as shown in Figure 7.34 (c). Because the mode shapes from the wired and wireless sensors match closely, the wireless sensor data is considered to be synchronized accurately. Thus, high-fidelity data for structural modal analysis have been achieved using the COTS wireless sensor board and ISHMP Services Toolsuite.



(a) First mode



(b) Second mode



(c) Third mode

Figure 7.34. Deflection mode shapes.

7.5 Corrosion Assessment using Model Updating

Based on the modal properties obtained from the measured data, the degree of corrosion of the Mahomet Bridge has been estimated based on the model updating strategy. An initial FE model has been constructed and updated using a nonlinear optimization strategy. The objective function is defined based on the modal properties of the bridge. The updating parameters are selected according to the sensitivity analysis. A brief summary of the optimization methodology and the model updating results are provided.

7.5.1 Finite element modeling

An initial finite element (FE) model was developed in Matlab (Mathworks, 2006) for further damage assessment. The FE model is required to apply model-based algorithms such as the decentralized SDDL method developed in Chapter 4. The truss superstructure of the north span was modeled, as shown in Figure 7.35. The 3D model consists of 102 nodes and 172 3D frame elements. As shown in the section 0, the boundary conditions for both ends are assumed as fixed, because the supports are all embedded in concrete blocks.

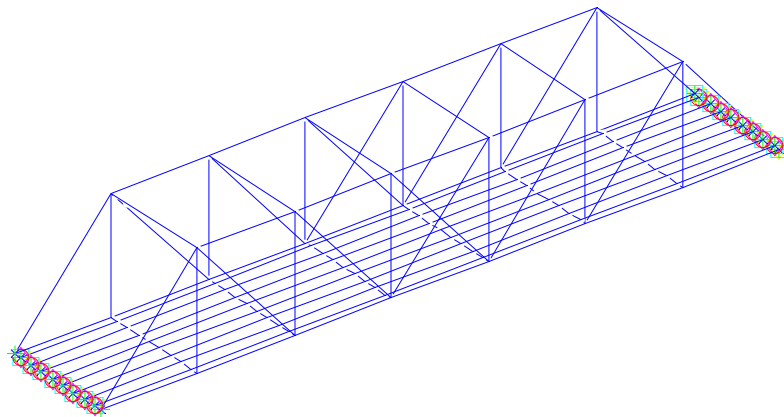


Figure 7.35. 3D FE model: Matlab®

The dynamic properties from the initial model and the measured data are compared in Table 7.2. The difference of the modal properties of the measured data and the initial FE model is considerable. The differences are mainly attributed to the degradation and corrosion of the bridge due to aging. Furthermore, the corrosion is unevenly distributed throughout the bridge. Therefore, the goal of the model updating is to adjust the structural parameters to represent the distributed corrosion to match the modal properties based on the measured data.

Table 7.2. Dynamic properties from the analytical model and measurement

Mode shape	Measured data (Hz)	Initial FE model (Hz)	Error (%)
1st vertical bending	6.375	8.0919	26.93
1st torsional	8.25	11.2368	36.20
2nd vertical bending	10.625	15.9047	49.69

7.5.2 Problem formulation with objective function

The updating process of the bridge FE model is conducted by (1) establishing an appropriate objective function, (2) selecting the updating parameters, and (3) finding the optimal solution using a robust algorithm (Mottershead, 1993).

The goal is to find the optimal combination of the selected updating parameters such that,

$$\min_p f(p) \quad (7.1)$$

The objective function chosen for this study consists of the differences of the mode shapes and natural frequencies, to match these modal frequencies from the model and the measured data.

The objective function, $f(p)$, is defined as,

$$f(p) = \eta \sum_{i=1}^{n_f} \left(\frac{\omega_{id,i} - \omega_{fe,i}(p)}{\omega_{id,i}} \right)^2 + \beta \sum_{i=1}^{n_m} \theta_i \quad (7.2)$$

where, $\omega_{id,i}$ is the i -th identified natural frequencies from the measured data, $\omega_{fe,i}(p)$ is the i -th natural frequency from the FE model, which is a function of p , the vector of updating parameters to be determined, and η and β are weighting constants, which are assumed by 1 in this study. n_f and n_m are the number of natural frequency residuals and number of mode shape residuals included in the objective function.

$\theta_i = \arccos(\sqrt{MAC_i})/(\pi/2)$ is the normalized angle between the mode shapes of the measured data and of the FE model. The MAC (Modal Assurance Criteria) is defined as (Allemang and Brown, 1982)

$$MAC_i = \frac{(\Phi_{fe,i}^T \Phi_{id,i}^T)^2}{(\Phi_{fe,i}^T \Phi_{fe,i}^T)^2 (\Phi_{id,i}^T \Phi_{id,i}^T)^2} \quad (7.3)$$

where $\Phi_{id,i}$ is the i -th identified mode shape from the measured data and $\Phi_{fe,i}(p)$ is the i -th mode shape from the FE model. Note that the MAC is actually the square of the inner product between the two mode shape vectors. Therefore, the objective function for the mode shape residual is formed as the normalized angle between the two mode shape vectors, which is much more sensitive than MAC value to the changes in the mode shapes.

7.5.3 Selection of updating parameters

The updating parameters have been chosen based on the severely corroded condition of the bridge. Corrosion occurred at the outer surface of the steel elements, which reduces the stiffness, while the change in bridge mass may not be significant due to residues of corroded steel sections.

To adjust the stiffness of the structure, the thicknesses of various sections are considered as the updating parameters. To adjust the different degrees of corrosion of various elements, the thicknesses of the six different element groups are considered. The mass density is also chosen to represent the mass of the structure. Additionally, the mass of the wooden deck is considered because it is highly variable in terms of moisture contents.

The sensitivity analysis has been conducted with respect to 8 updating parameters in terms of the thickness of six types of sections, mass density, and the lumped mass of the wooden deck. The changes in the natural frequencies of the first five vertical modes are determined in terms of a single parameter, while holding the other parameters constant. As shown in Figure 7.36, the sensitivities of the eight parameters are similar. Therefore, all 8 parameters are chosen as the updating parameters for this study.

To avoid ill-conditioning and retain the physical meaning of the structure, the following constraints are preset,

$$p_i^- \leq p_i \leq p_i^+ \quad (7.4)$$

where p_i^- and p_i^+ are the lower and upper bounds of the i -th updating parameter. The lower and upper bounds have been defined based on field investigation.

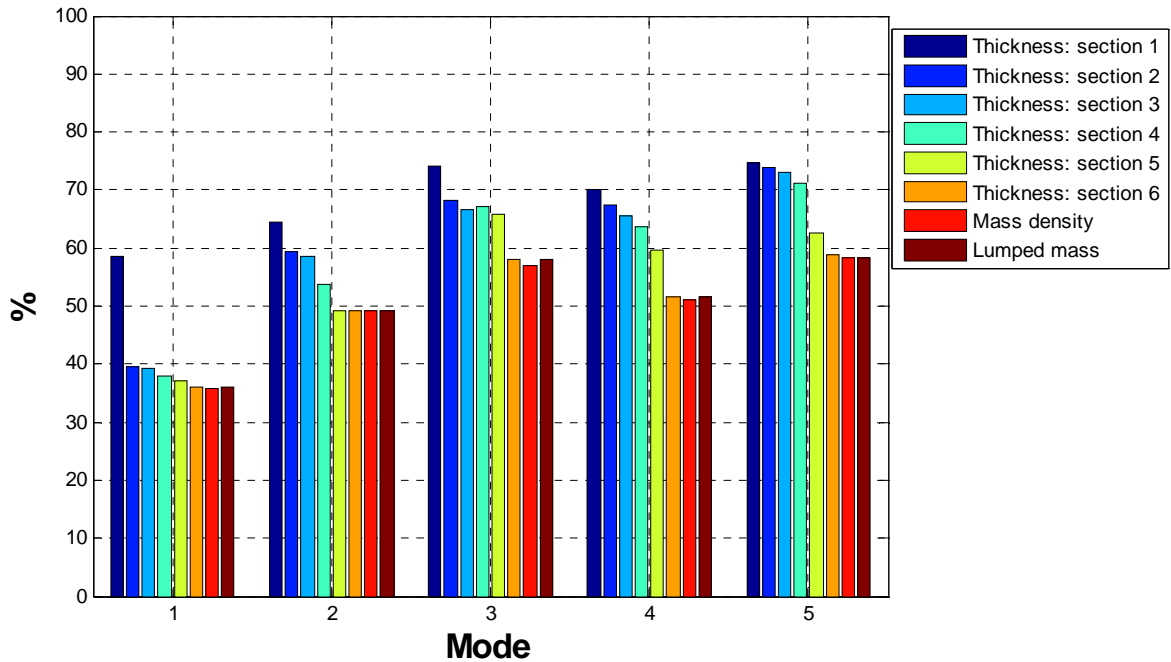


Figure 7.36. Sensitivity analysis for candidate parameters

7.5.4 Optimization strategy

Sequential Quadratic Programming (SQP) method is one of the most popular and robust algorithms for solving constrained optimization problems. For finding the solution for multi-variables with multi-constraints problem, the SQP method is selected for this study.

The brief concept of the SQP method is that the SQP forms a quadratic programming (QP) sub-problem with the quadratic approximation of the Lagrange function and the linear approximation of the constraint at the current estimation of $x^{(k)}$ of a solution x^* . The next iteration direction d is then obtained by solving this QP sub-problem, and the next estimation of $x^{(k)}$ is found by a line search. The QP sub-problem is formed as follows:

$$\min \frac{1}{2} d^T B^{(k)} d + \nabla f(x^{(k)})^T d \quad (7.5)$$

$$\text{s.t. } \nabla g_i(x^{(k)})^T d + g_i(x^{(k)}) \geq 0, \quad i = 1, 2, \dots, m_1 \quad (7.6)$$

$$\nabla h_j(x^{(k)})^T d + h_j(x^{(k)}) = 0, \quad j = m_1 + 1, \dots, m \quad (7.7)$$

$$x^l - x^{(k)} \leq d \leq x^u - x^{(k)} \quad (7.8)$$

where $B^{(k)}$ is a positive-definite matrix, usually a unit matrix for the first iteration. The solution of this sub-problem gives $d^{(k)}$. To enhance the convergence property, a appropriate line search is performed to find the iteration step-length α_k ; thus, the next estimation of $x^{(k)}$ is $x_{k+1} = x_k + \alpha_k d_k$. After each iteration, the matrix $B^{(k)}$ is updated using the BFGS (Broyden-Fletcher-Goldfarb-Shanno) algorithm (Fletcher, 1963). The SQP algorithm is available in the MATLAB optimization toolbox.

7.5.5 Results

After running the SQP algorithm, the first three natural frequencies were matched. The convergence of the objective function is shown in Figure 7.37. After 5 iterations, the results close to the experimental results were obtained. The updated modal properties are shown in Table 7.3. The first three natural frequencies of the updated model are matching with those of the measured data within 8%.

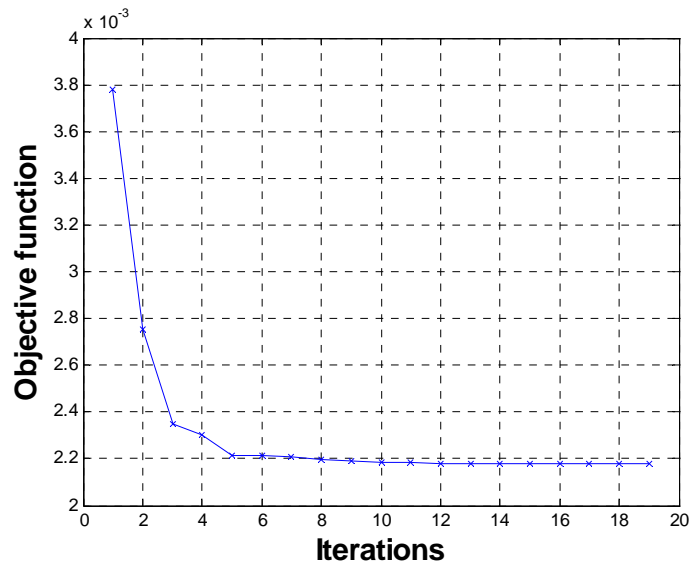


Figure 7.37. Convergence chart: SQP algorithm

Table 7.3. Model updating result

Mode shape	Measured data	FE model	MAC	Error (%)
1st vertical bending	6.375	6.2941	0.9975	-1.2697
1st torsion	8.25	8.0781	0.9825	-2.0833
2nd vertical bending	10.625	11.5405	0.9246	7.9330

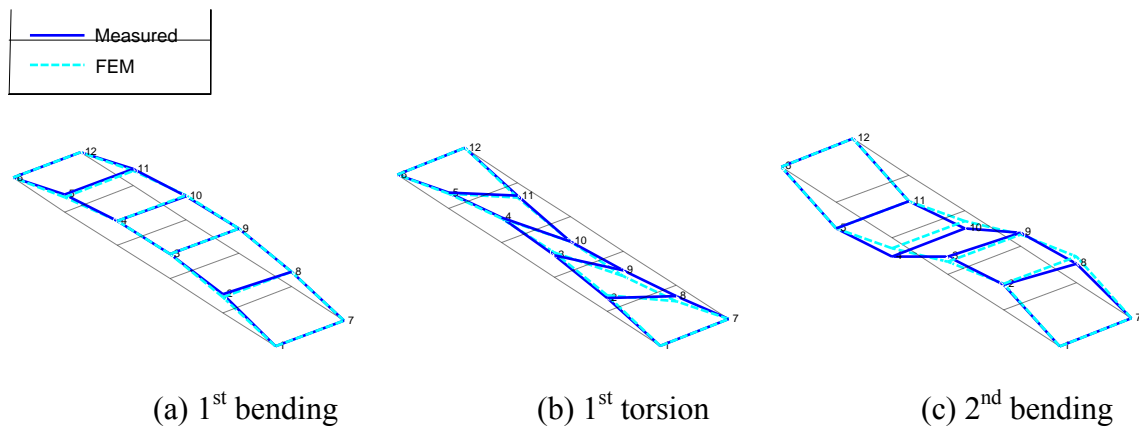


Figure 7.38. Mode shape agreement with the updated model between the measured data

The finally updated parameters are summarized in Table 7.4. The thicknesses of 6 sections are decreased up to 25%. Based on the thickness decreases, the reduction percentage of the cross sectional area is calculated in Table 7.5. As shown in Figure 7.39, the reduction rates of the visual investigation and the updated model agree well.

Table 7.4. Updated thickness

Variables	Updated value ($t_{\text{updated}} / t_{\text{original}}$)
Thickness : section 1	0.8
Thickness : section 2	0.75
Thickness : section 3	0.94
Thickness : section 4	0.95
Thickness : section 5	0.78
Thickness : section 6	0.9

Table 7.5. Updated thickness loss and corresponding sectional properties.

Section group	1	2	3	4	5	6
Reduced A (%) Visual corrosion investigation	51.46	48.99	89.13	91.88	53.32	62.17
Reduced A (%) Updated FE model	58.37	48.69	88.36	90.25	49.81	72.17
Error (%)	11.84	0.62	0.87	1.81	7.65	12.75

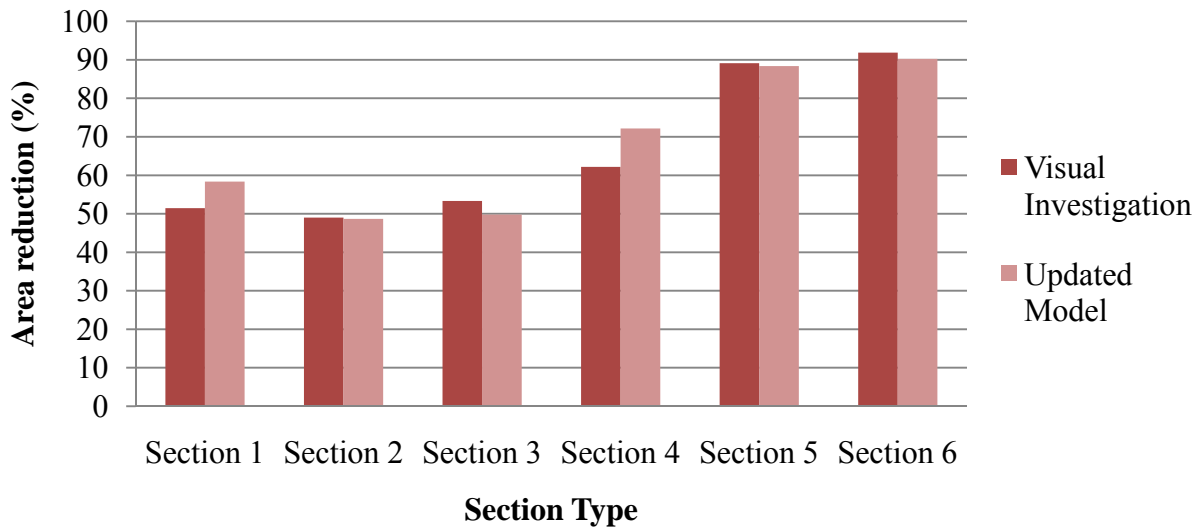


Figure 7.39. Area reduction match of updated model and visual investigation

The mass density increased by 5% of the reduced sectional area. In severely corroded sections such as section groups 1 and 2, the ratio of the volume reduction is about 50% by 0.064 inch corrosion. However, the mass of the section remains unchanged or is slightly reduced due to the corrosion. To compensate the volume reduction effect due to corrosion, the mass density of the remaining section should be increased.

The mass of the lumped mass has also increased up to 30%. The density of wood varies according to the specific gravity and the moisture contents. For same type of wood with a fixed specific gravity, the density of wood can vary up to 250% as shown in Figure 7.40 (Simpson, 1993). Therefore, the modal properties of the bridge have been successfully matched with those from the numerical model considering severe corrosion by updating the structural parameters.

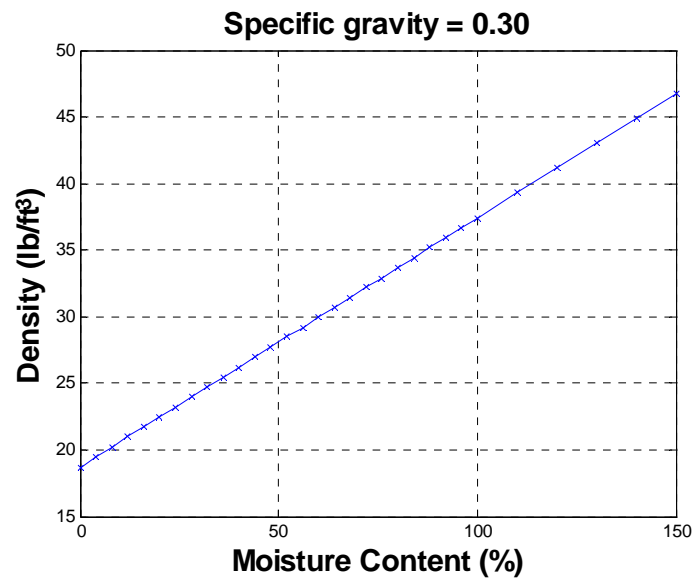


Figure 7.40. Density variation of wood (data from Simpson, 1993)

7.6 Conclusion

A historic bridge has been monitored for corrosion estimation using model updating strategy. Brief visual investigation has shown significant corrosion damage of this bridge. A series of full-scale vibration tests were conducted using a traditional wired sensor system. Using the measured data, the modal analysis has done using the peak picking to obtain natural frequencies and mode shapes. Additional vibration tests were conducted to validate the performance of the wireless sensor-based SHM system in comparison with the wired sensor system modal analysis for future full-scale experiments using the wireless sensor system. The data in the time-domain and frequency-domain of the wired and wireless sensor systems have been compared. With the acceleration measurement application, *RemoteSyncSensing* application in ISHMP Services Toolsuite, the synchronized data without any data loss were transferred to the base station.

A Matlab-based FE model has been built and updated using a model updating strategy based on the experimentally measured data, which accounts for the severe corrosion of the bridge. The modal properties of the measured data differed from those of the initial FE model. After updating 8 structural parameters including the thicknesses of 6 different groups of sections, mass density, and the lumped mass of the wooden deck, a match of the modal properties has been achieved within 8%. The updated thicknesses agreed well with the visual corrosion estimation results. Therefore, the corrosion distribution has been successfully estimated and verified using model updating, and the updated FE model can be employed for future SHM algorithm applications.

CHAPTER 8 FULL-SCALE SHM OF A HISTORIC BRIDGE USING WSSN

This chapter presents full-scale validation of the state-of-the-art WSS-based SHM system developed in Chapter 4 on the Mahomet Bridge. First, the components of the long-term bridge monitoring system are provided in terms of hardware and software. Then, various deployment issues are discussed in terms of environmental hardening and communication adjustment. The communication environment has been improved by appropriate antenna selection and orientation. Full-scale vibration tests are conducted using the deployed wireless sensor-based SHM system. The condition of the bridge is examined using the decentralized SDDL method. Also, the DDI application is tested on the bridge during the full-scale vibration test for damage detection. The damage detection results from the post processing of the measured data, and using the comprehensive on-board application will be compared. Finally, the performance of the hardware and the solar panels is evaluated.

8.1 Long-term Bridge Monitoring System

The long-term bridge monitoring system is described in this section. Similar to the Jindo bridge deployment, the hardware system is prepared aiming stable long-term performance outdoor. The software is set up to conduct on-demand damage detection application as well as autonomous vibration monitoring using ISHMP Services Toolsuite.

8.1.1 Hardware components

The hardware components for the long-term bridge monitoring system include the base station and the wireless smart sensor nodes. To ensure stable performance of the base station during the

severe temperature fluctuations at the bridge site, an industrial grade PC, the AAEON AEC-6905, is employed, which was used for the Jindo Bridge deployment. Because this PC runs Windows XP, installation of hardware components, such as the cellular model, is straightforward.

The base station is installed on north side of the bridge as shown in Figure 8.1. To prevent freezing, a heavy duty freeze-protection strip heater was installed with the thermostat set at 0°C. For internet connection, a Multitech® MultiModem® MTCBA-C using the Verizon® network was connected to the PC. Additionally, an APS Back-UPS has been installed for uninterruptible power supply.



Figure 8.1. Base station.

The base station was housed in a small fiberglass weather proof RLH-242010-F enclosure shown in Figure 8.2. The enclosure is National Electrical Manufacturers Association Type 4 enclosure, which is for either indoor or outdoor use to provide a degree of protection to personnel against access to hazardous parts, ingress of falling dirt and windblown dust, water (RLH Industries, 2008).



Figure 8.2. Base station enclosure.

The wireless sensor nodes used in the Jindo bridge deployment have been installed in new enclosures (see Figure 8.3). Each leaf node includes a battery board, an Imote2, and a SHM-A sensor board that has been attached using plastic bolts to a PVC plate so that the components can be easily removed after the deployment. The USB port is facing outside so that the software reprogramming can be done when the sensor is attached in the enclosure. An external antenna has been attached outside of the enclosure for reliable communication. The antenna extension cable is straightened to prevent excessive cable loss. To extend the network life, 3 D-cell batteries are used.

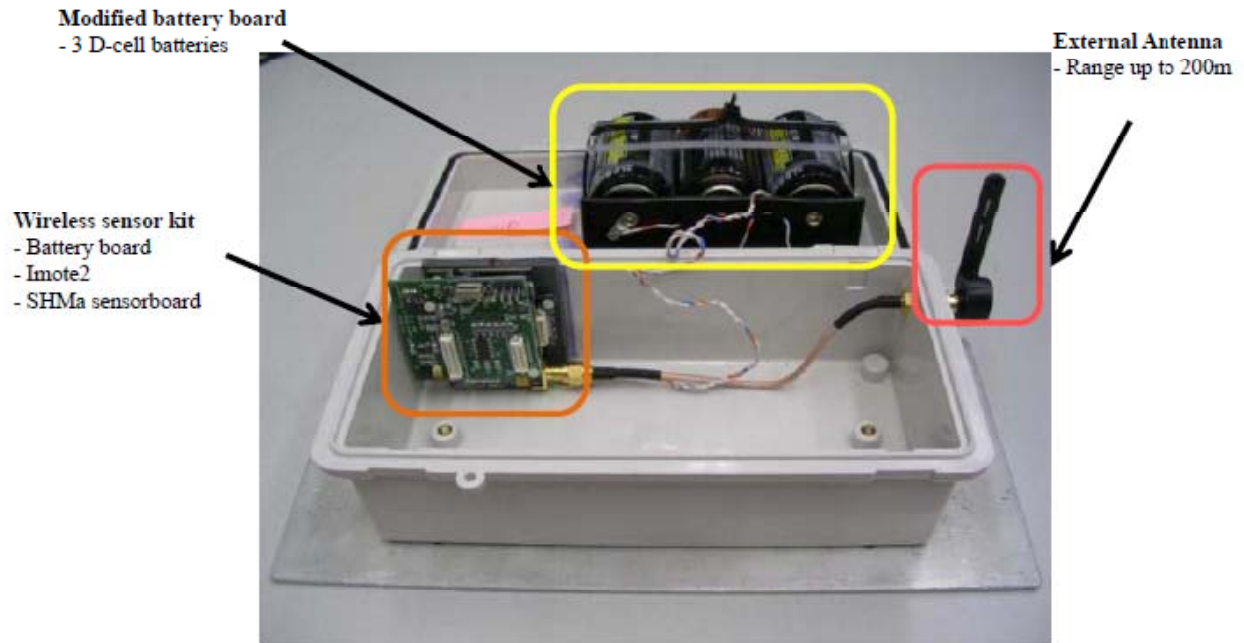


Figure 8.3. Enclosure configuration: battery powered node.

For long-term continuous monitoring, solar panels have been employed as introduced in section 6.2.3 with a new connecting block. A fiberglass/PVC triangular block with 30° angle has been attached on the cover (Figure 8.4) to install the solar panel. With the inclination, the surface of the solar panel can be cleansed by rain, and the efficiency of solar power harvesting will be increased by facing the solar panel toward sun.

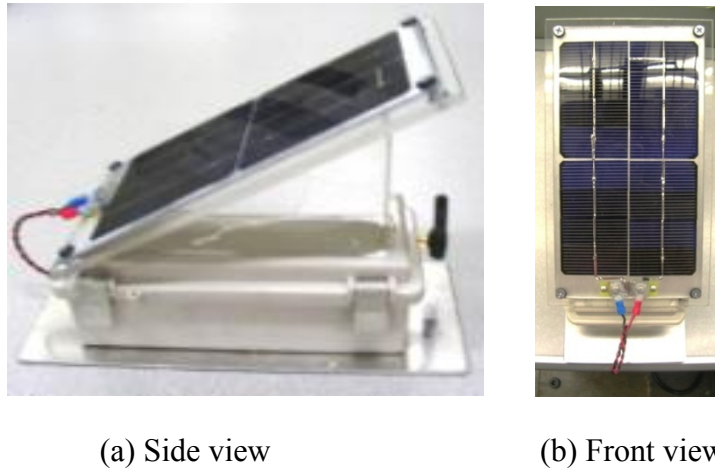


Figure 8.4. Enclosure configuration: solar powered node.

The gateway node has been housed in a smaller waterproof enclosure as shown in Figure 8.5 because power is directly supplied from the base station pc. One USB cable is connected to the IIB interface board to run the application, and the other USB cable is connected to the Imote2 for remote reprogramming.



Figure 8.5. Enclosure configuration: gateway Node.

The prepared enclosures are installed using cantilever C-clamps. The magnet-based sensor attachment is inadequate for the Mahomet Bridge, because the surface of steel elements is not smooth due to severe pitting corrosion. Instead, an aluminum plate is bolted on the bottom of the

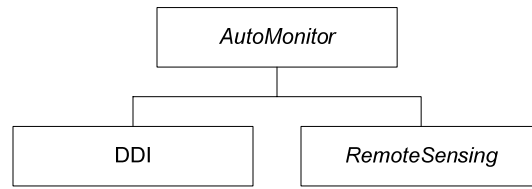
enclosure, and the plate has been connected to sensor location with two clamps, as used in the Siebel staircase deployment. The clamping method is chosen for convenient installation and retrieval without damaging target structure.



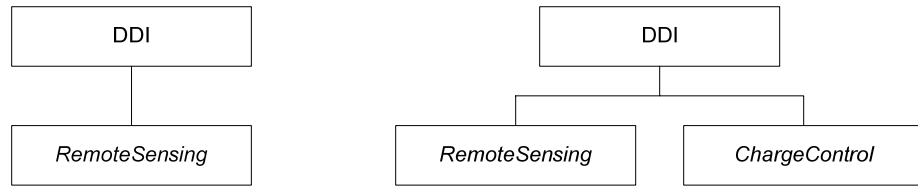
Figure 8.6. Sensor attachment.

8.1.2 Software setup

The goal of the software configuration is to run the DDI application as well as *AutoMonitor* with *RemoteSensing*, to be able to run on-demand damage identification and autonomous periodic monitoring. Because *AutoMonitor*, introduced in sections 2.4.3 and 6.2.5, and the DDI are separate software components, the DDI and *AutoMonitor* applications have been combined as shown in Figure 8.7. The software on the gateway node is *AutoMonitor*, which includes the DDI and *RemoteSensing*. The leaf nodes are loaded with DDI, which includes the *RemoteSensing*. For the leaf nodes that are equipped with solar panels, the charge control service also has been embedded in the DDI.



(a) Gateway node



(b) Leaf nodes: battery or AC powered (c) Leaf nodes: solar powered

Figure 8.7. Software Hierarchy.

The parameters for running the DDI are selected based on time to run each part of software. The measurement parameters are listed first. The sampling frequency is 100 Hz, and the cutoff frequency is 40 Hz. Using 100Hz rate, first 5 natural frequencies can be captured. The number of data points is determined by the FFT points and the number of FFT windows in system identification parameters.

The parameters for the system identification using the ERA-NExT method are listed. The number of FFT points is selected as 1024, and the number of average is 10 times. The Hanning windows with 50% overlap are selected. The order of the system is chosen to be 8, so that the first 4 modes can be used for the damage detection. The size of the Hankel matrix is 50×50. These parameters are selected because these values are tested and validated in lab-scale damage detection experiments. More data points and larger Hankel matrix size can be usable if various parameters and wait times in *DecentralizedDataAggregation* and ERA-NExT service are adjusted.

The group communication parameters are the wait times during the DDI after *DecentralizedDataAggregation*. The DDI delay is the duration from the time when the correlation function has been computed to the time the gateway node queries the cluster heads for the damage detection results. The Group query interval is the interval to send the query to the next cluster head after data transfer from one cluster head is completed. After sending the end results, the cluster head will reset after a specified reset time. The DDI delay is 110 seconds, the group query interval is 5 seconds, and the reset time after sending is 3 seconds. These network parameters were selected after running the DDI application on the bridge. All parameters are listed in Table 8.1. Using these parameters, the DDI application ran successfully on the Mahomet Bridge.

Table 8.1. Parameters for the DDI.

Measurement	Sampling frequency	100 Hz
	Cutoff frequency	40 Hz
	Measurement directions	Longitudinal & Vertical
System Identification	FFT point	1,024
	Average	10 times
	Overlap	50 %
	Window	Hanning
	System order	8
	Hankel matrix size	50×50
Group Communication	DDI delay	110 seconds
	Group query interval	5 seconds
	Reset time after sending	3 seconds

8.2 Field Deployment

The long-term remote SHM system was deployed on the Mahomet Bridge. First, the base station was installed on the north side of the bridge as shown in Figure 8.8. Two wooden posts have been installed to mount the base station. A tension cable is provided to balance the forces of the electrical cable attached to the top of the post. The base station pc is AC-powered. The gateway node is installed above the base station enclosure. Originally, the gateway node employed the Antenova® Giganet Titanus swivel antenna (see Figure 8.5). To improve the radio communication quality, a high-gain directional patch antenna, Hawking® HAO14SDP antenna has been connected to the gateway node. The discussion on comparison of the Antenova and Hawking antenna will be provided in section 8.3.



Figure 8.8. Base station.

The environmentally protected wireless sensor nodes were deployed on the north span of the bridge. The sensor locations are shown in Figure 8.9. In total, 12 solar powered nodes, 11 battery-powered nodes, and one AC-powered node have been deployed (see Figure 8.10 and Figure 8.11).

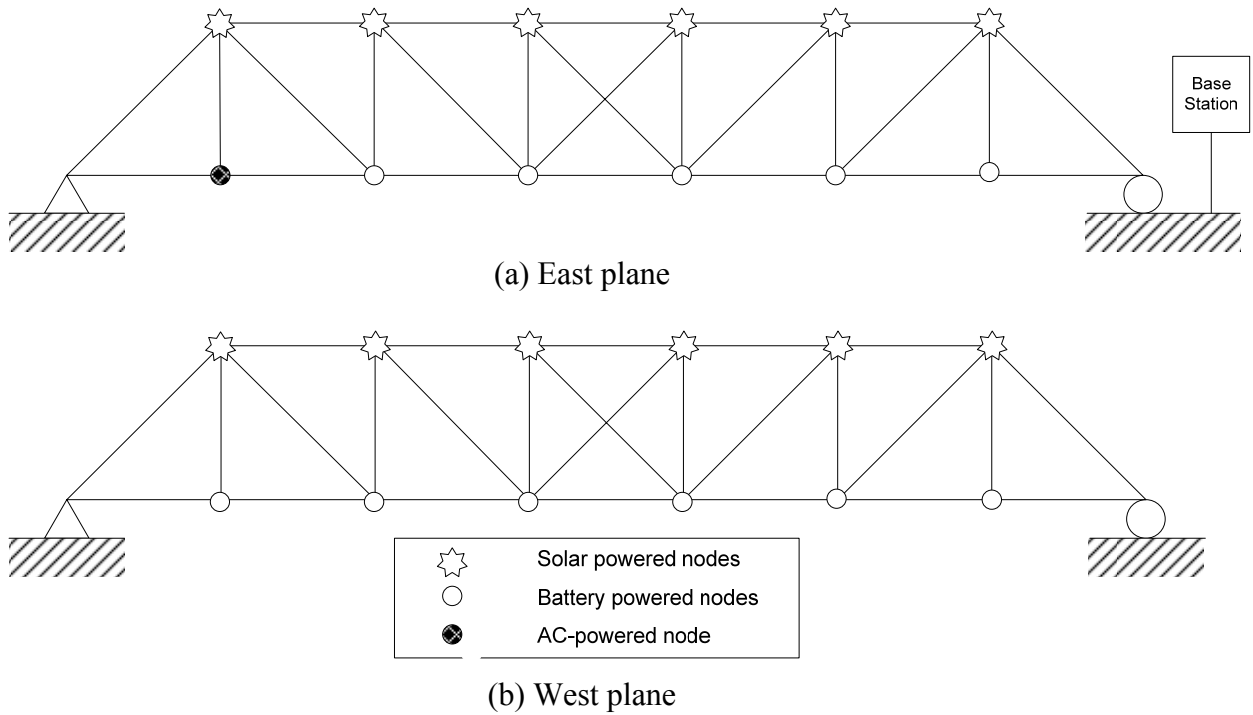


Figure 8.9. Sensor location on North span.



Figure 8.10. Sensors on the lower chords.



Figure 8.11. Sensor on the upper chords.

8.3 Communication Optimization

Stable wireless communication is essential for successful operation of an SHM system using WSSs. However, the communication of the gateway node and the leaf nodes was considerably unstable after first deployment of the system on the Mahomet Bridge in January. The biggest problem is that the nodes were neither line-of-sight nor at the same elevation due to physical interference with steel members. Furthermore, the moisture problems due to snows on the bridge in winter and the foliage in summer surrounding the bridge obstructed stable communication (see Figure 8.12 and Figure 8.13). Therefore, the communication issues were addressed using antenna technology.



(a) Mahomet bridge on January 14, 2010

Figure 8.12. Mahomet Bridge environment



(b) Mahomet Bridge on July 2, 2010



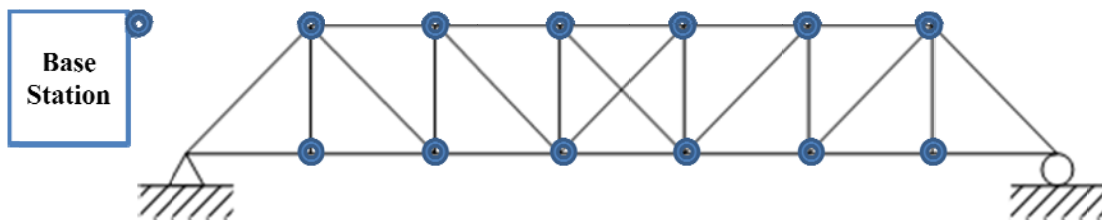
(c) Base station environment on July 2, 2010

Figure 8.13. Mahomet Bridge environment (cont.)

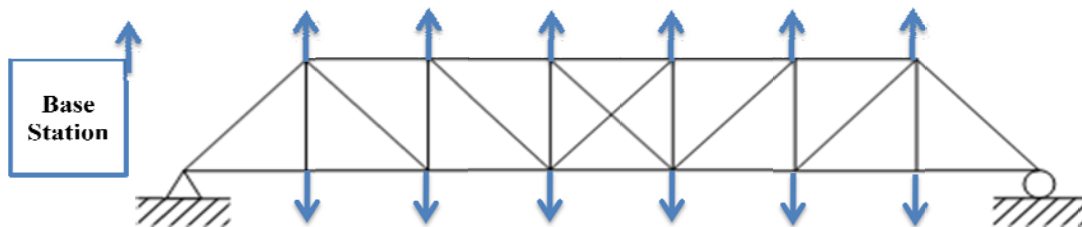
Two antenna orientations were considered for the deployment, as shown in Figure 8.14. The horizontal configuration is aligning all antennas parallel to the ground in an out-of-plane direction. The horizontal alignment was used for the Jindo bridge deployment because the leaf

nodes at different elevation can communicate each other. This orientation has used because the DDI application requires good communication between the leaf nodes to employ the distributed computing strategy. However, 32% of nodes were unresponsive after deployment. The reason is that the antenna is located in the middle of the steel member, so that the half of the signal radiation is blocked by the steel member. Therefore, the horizontal orientation is not adequate for the Mahomet bridge.

The second orientation is the vertical polarization aligning all antennas vertically. Using the vertical alignment, the leaf nodes in the upper chords can communication each other, but not with the lower chord nodes. Because the horizontal alignment is not suitable for the Mahomet Bridge, the vertical alignment is chosen for this deployment. Therefore, all antennas were aligned in vertical direction.



(a) Horizontal polarization



(b) Vertical polarization

Figure 8.14. Antenna orientation.

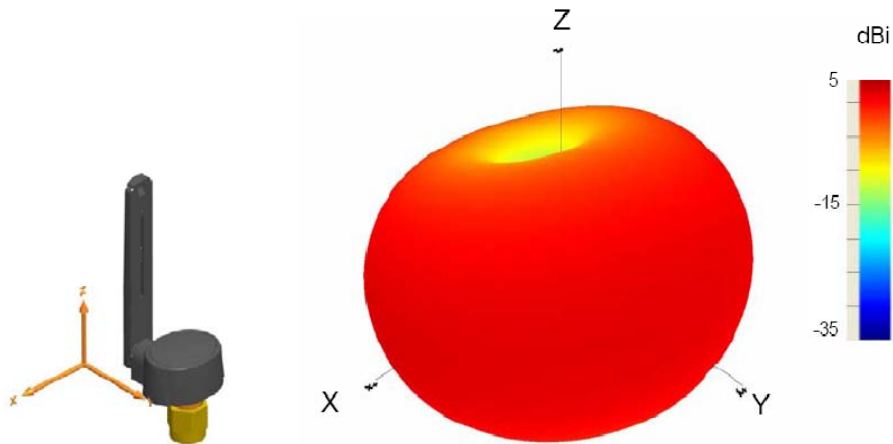


Figure 8.15. Antenna patterns (Courtesy of Antenova, 2007).

In addition, a new powered antenna for the gateway node is recommended considering gain and directionality/radiation pattern. High gain is desirable, amplifying the radio signal; the tradeoff of the high gain is a narrower radiation pattern. Directionality of the antenna should be considered based on the sensor placement. If the base station is on one side of the bridge, a directional antenna can amplify the signal in the direction of the sensors.

A Hawking high-gain outdoor directional patch antenna selected as meeting the application needs. Table 8.2 shows a comparison between the Antenova antenna and the Hawking patch antenna. Both antennas are suitable for the 2.4 GHz bands employed by the 802.15.4 protocol (*i.e.*, the upper channels from 11 through 26). The gain of the patch antenna is 14 dBi, which is 128 ($=2^7$) times higher than the Antenova antenna. The radiation is available within $\pm 30^\circ$ in both the horizontal and vertical directions. For the Mahomet deployment, this radiation pattern covers all sensors (see Figure 8.17). Therefore, the Hawking's directional antenna was deployed for the gateway node.

Table 8.2. Antenna comparison.

	Antenova Titanis (Antenova, 2009)	Hawking HAO14SDP (Hawking, 2007)
Frequency (GHz)	2.4~2.5	2.4~2.4835
Polarization	linear	linear
Impedance (Ohm)	50	50
Weight	7.1g	635 g
Antenna type	swivel external	High-gain outdoor directional antenna
Dimensions	20 × 19.5 × 62.5 mm	213.36 × 213.36 × 76.2 mm
Peak gain	2.2 dBi	14 dBi
Maximum VSWR*	1.6:1	1.8:1

*VSWR (voltage standing wave ratio)



(a) Antenova Titanus antenna
(Antenova, 2009)



(b) Hawking directional antenna
(Hawking, 2007)

Figure 8.16. Antennas

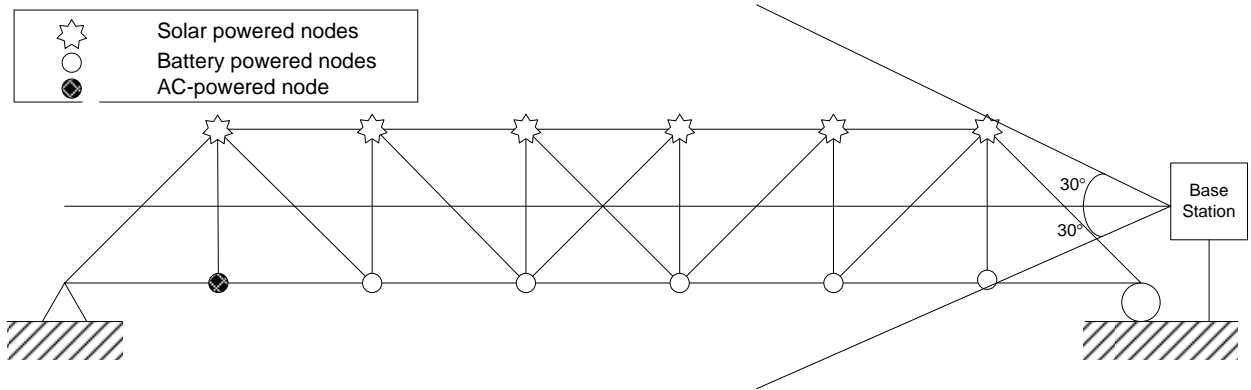


Figure 8.17. Radiation pattern using a patch antenna (east plane).

After using the Hawking antenna with the vertical alignment, the communication quality has significantly improved. The number of leaf nodes which can communicate with the gateway node is shown in Figure 8.18. As mentioned earlier, only 68% of nodes can communicate with the gateway node using the horizontal polarization. By employing the directional patch antenna, 84% of the leaf nodes can communicate with the gateway node. After the antenna directions were adjusted vertically, all leaf nodes are responsive and the reception rate of all nodes was 100%. Therefore, the network communication has been successfully adjusted using new antenna and vertical orientation.

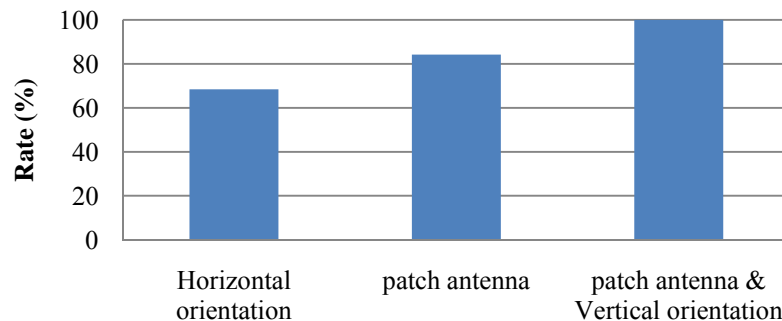


Figure 8.18. Communication success rate.

8.4 Bridge Health Monitoring

The section describes the bridge monitoring procedures and results. For this study, the undamaged state of the bridge is based on the updated model obtained from the 2008 testing (see Section 7.5). The ambient vibration level is continuously monitored using *AutoMonitor* application. The condition of the bridge has been assessed using the decentralized SDDL V method based on the measured data using the *RemoteSyncSensing* application. The DDI application is tested on the bridge to validate the damage detection capability. The results from on-board computation using the DDI application are compared with those from the post processing of the decentralized SDDL V method. In this case, damage is interpreted as significant degradation since the 2008 tests.

8.4.1 Ambient vibration monitoring

The ambient vibration of the bridge was measured as shown in Figure 8.19. 200 seconds of acceleration in three directions were measured at 100Hz. Because it is small size bridge without significant external loading, the range of vibration was within ± 3 mg. Higher resolution data than those of ITS400CA sensor board have been measured using the SHM-A sensor board. The level of ambient vibration corresponds with the level of the measured data using the ITS400CA sensor board in Chapter 7.

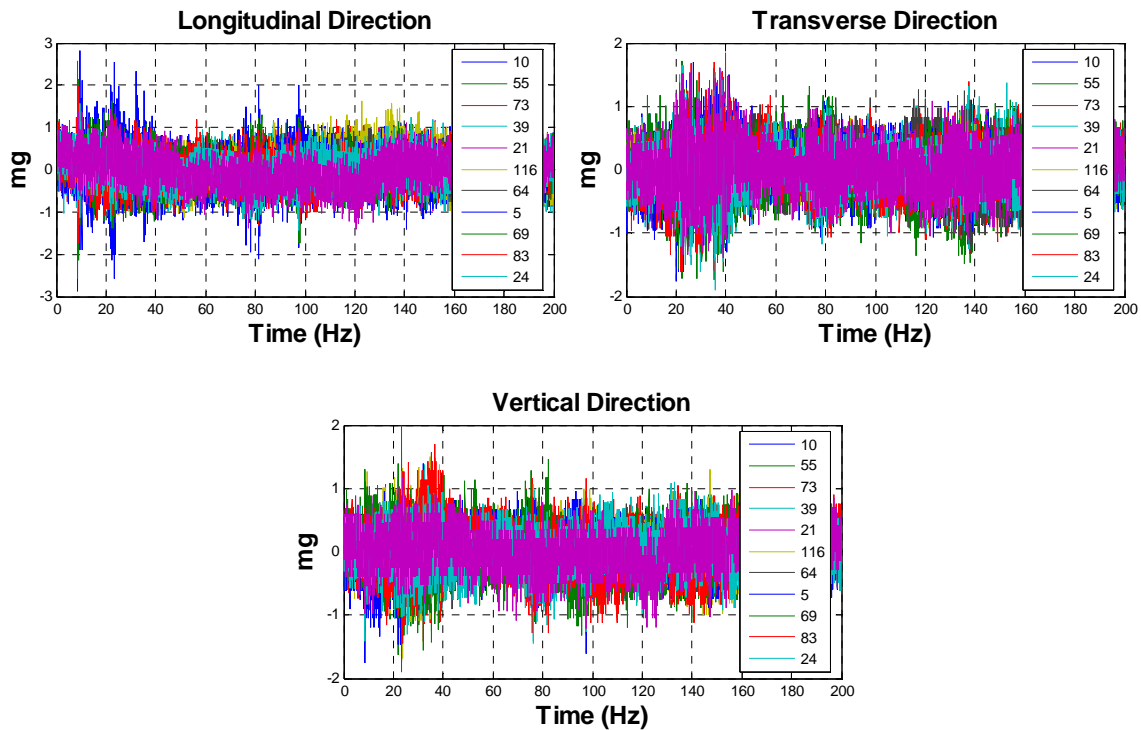
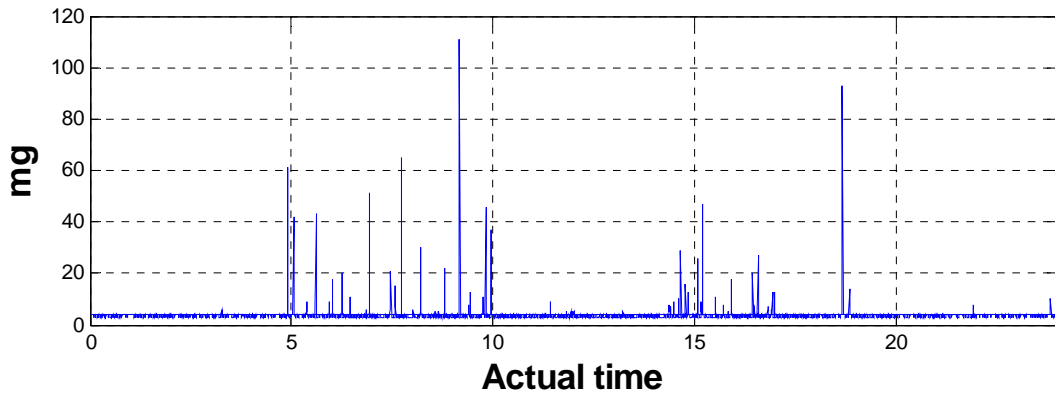
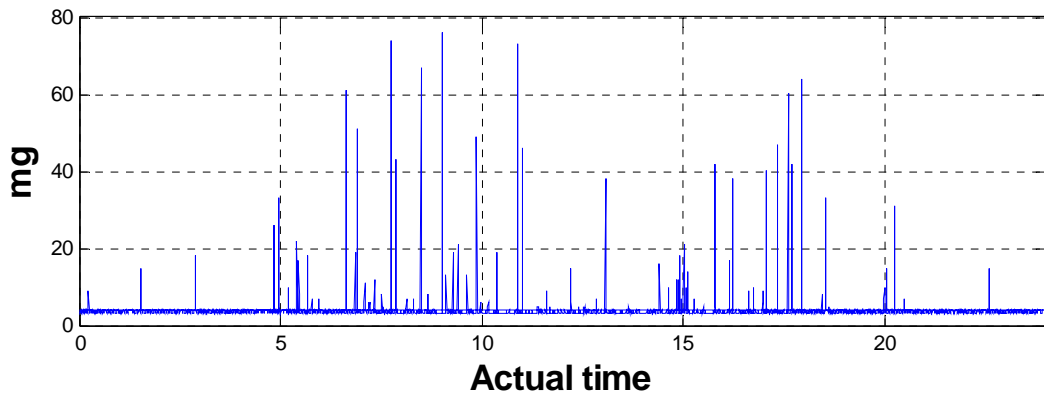


Figure 8.19. Ambient vibration.

The ambient vibration is measured continuously for 48 hours to find the possibility of high vibration by external loading. An AC-powered sentry node is used to measure the maximum vibration levels using the *AutoMonitor*. The sensor wakes up every 10 seconds, measures 10 seconds of acceleration data in all 3 directions, and outputs the maximum levels of vibration. The maximum levels were measured for 48 hours, as shown in Figure 8.20. Most of time, the maximum vibration levels are 3 or 4 mg. High peaks were recorded during 5-10AM and 2-6PM, which is likely when pedestrians (*e.g.*, joggers and school children) are passing over the bridge. Thus, the ambient vibration levels for this bridge are mostly small.



(a) 5PM May 17 – 5PM May 18



(b) 5PM May 18 – 5PM May 19

Figure 8.20. Continuous monitoring of maximum vibration.

8.4.2 Damage assessment using the decentralized SDDL V method

The structural condition of the bridge has been considered using the decentralized SDDL V method. Because the measured data from the bridge in its initial state in 1912 is currently unavailable, the bridge in 2008 is assumed as the baseline configuration. The damage detection results can then be interpreted as providing an indication of where significant degradation has occurred as compared to the 2008 state of the bridge.

The acceleration data have been measured from the deployed sensor nodes when the bridge is subjected to the external loading. The input excitation is the band-limited white noise up to 100Hz, generated using the vertically installed shaker (see Figure 7.13). The location of the shaker is shown in Figure 8.21. The accelerations in the longitudinal and the vertical directions have been measured from 24 nodes using *RemoteSyncSensing* application. The sampling frequency is 100Hz with the cutoff frequency of 40Hz. The measurement duration was 200 seconds.

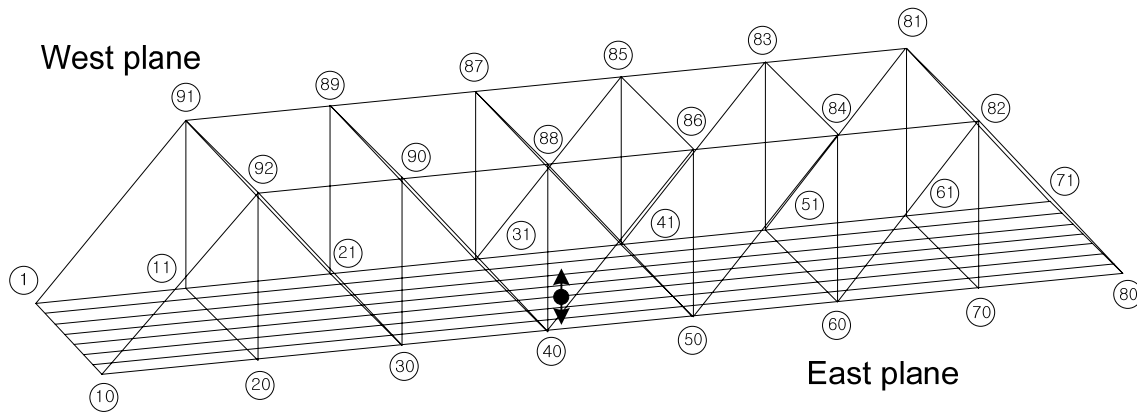


Figure 8.21. Location of shaker

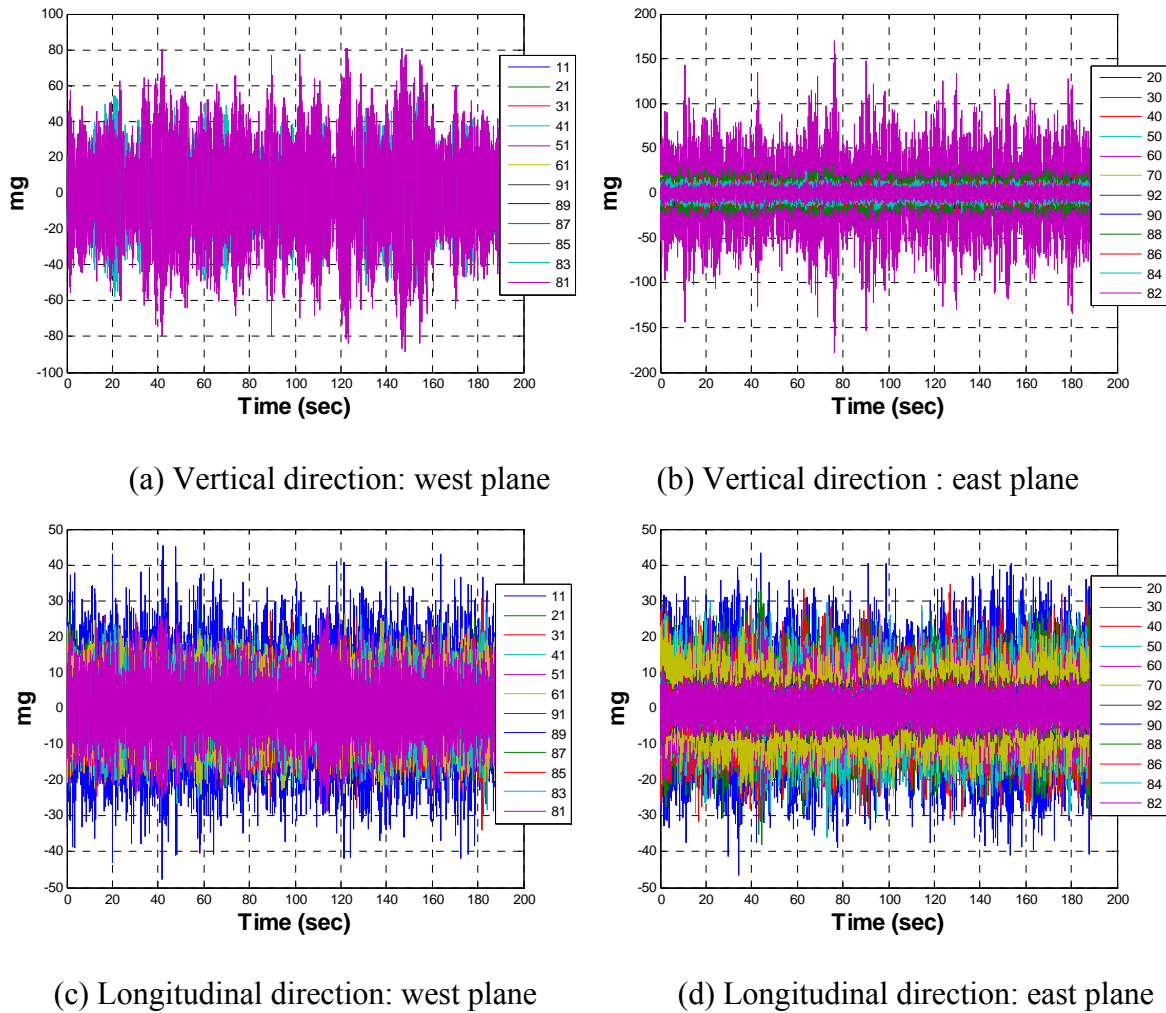


Figure 8.22. Measured acceleration data

The measured acceleration data have been processed to obtain modal properties for conducting the damage detection. The point of FFT is 1024, 50% overlap was used to run FFT of the acceleration. The size of Henkel matrix is 150×1300 . Using the ERA in conjunction with NExT, the modal properties, and system matrices, A and C are obtained.

Based on the obtained dynamic information of the bridge, the decentralized SDDL procedure has been conducted. The frequencies of interests are 0, 5, 10, 15, 20 Hz. These frequencies are selected because they are not at zeros or at poles of the structure. The

performance of the decentralized SDDL method at zeros is not reliable, and the data quality at natural frequencies is usually not good for digital measurement due to spectral leakage.

The bridge structure has been divided into 4 groups for damage identification as shown in Figure 8.23. This network topology is utilized to compare with the decentralized damage identification results in next section. Because the decentralized SDDL method has been validated with truss structure, the outer truss elements are considered for damage identification. The element numbering is shown in Figure 8.24. The node numbers and the elements included in each group are summarized in Table 8.3.

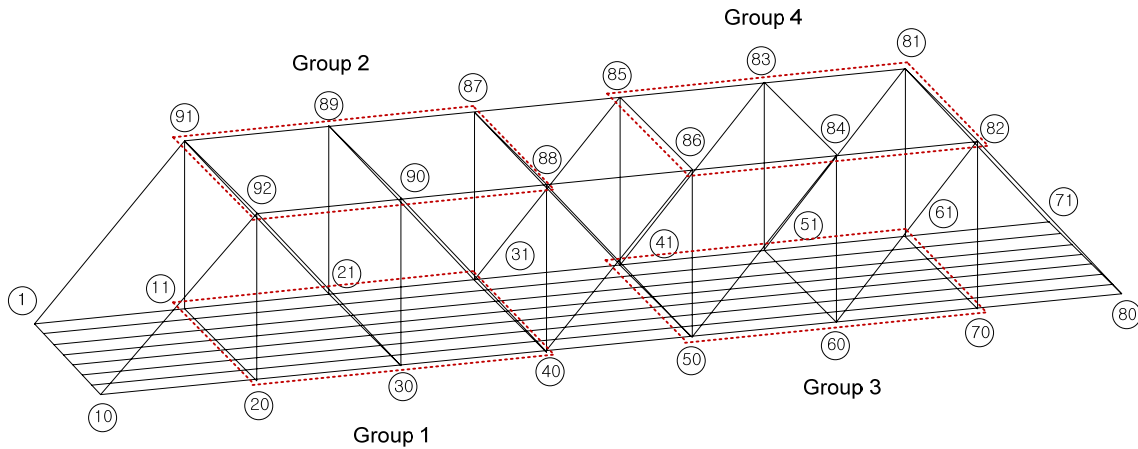
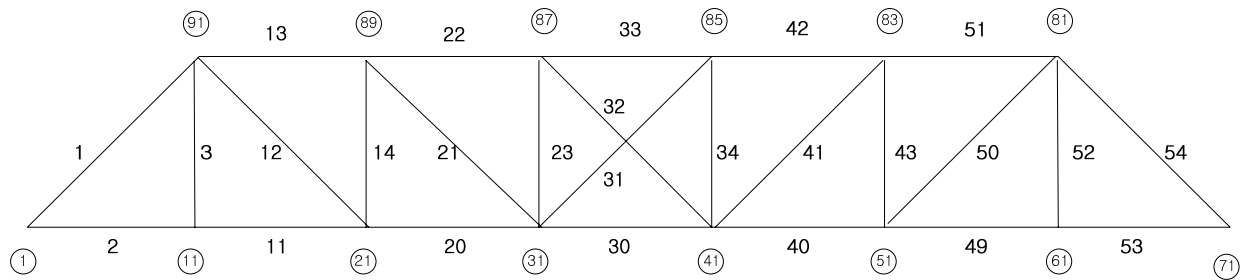


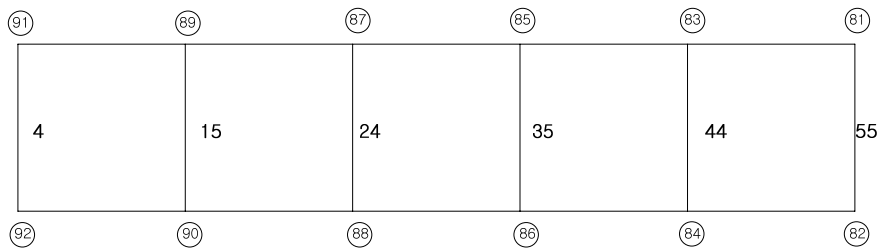
Figure 8.23. Network topology.

Table 8.3. Local communities.

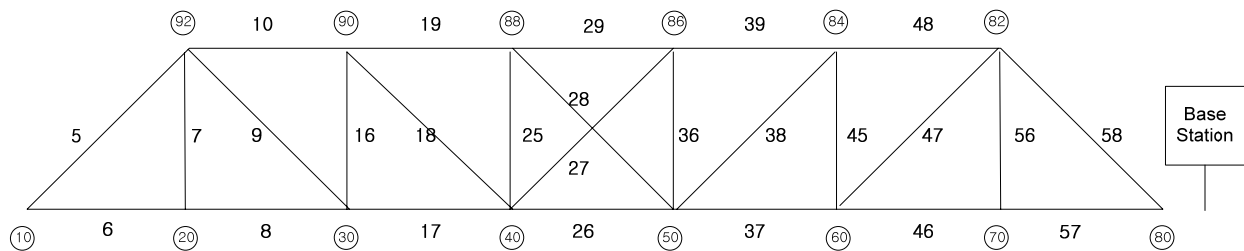
	Nodes	Elements included
Group 1	11,20,21,30,31,40	2,3,6,7,8,9,11,12,14,16,17,18,20,21,23,25,26,27,30,31
Group 2	87,88,89,90,91,92	1,3,5,7,9,10,12,13,14,16,18,19,21,22,23,25,27,29,32,33
Group 3	41,50,51,60,61,70	26,28,30,32,34,36,37,38,40,41,43,45,46,47,49,50,52,53,56,57
Group 4	81,82,83,84,85,86	28,29,33,34,36,38,39,41,42,43,45,47,48,50,51,52,54,56,58



(a) West plane



(b) Top plane



(c) East plane

Figure 8.24. Element numbering

The damage indices of 58 elements are plotted in terms of ASI and MSI in Figure 8.25. The threshold for the damage detection is set as 0.2. The damaged locations are indicated using thick lines in Figure 8.26. The possible damaged location includes the central vertical and diagonal elements, and the side vertical elements.

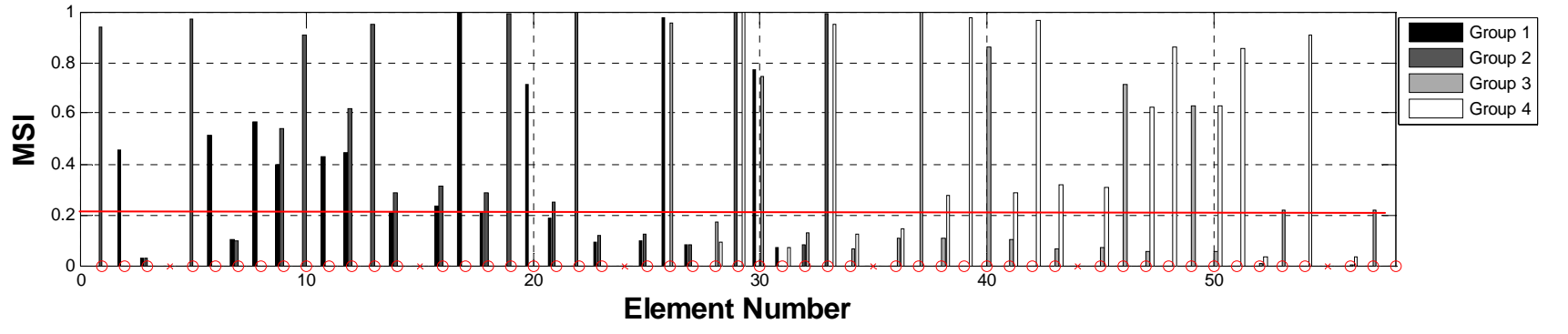
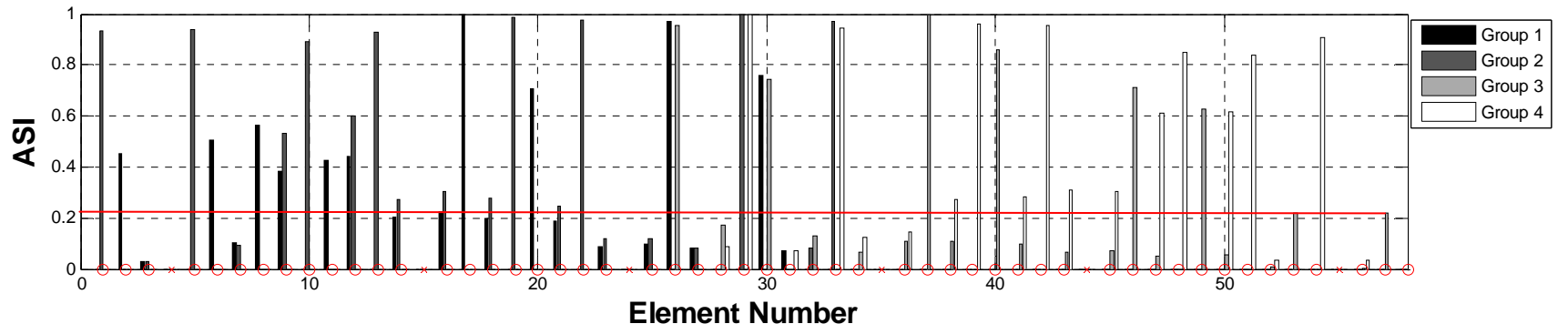
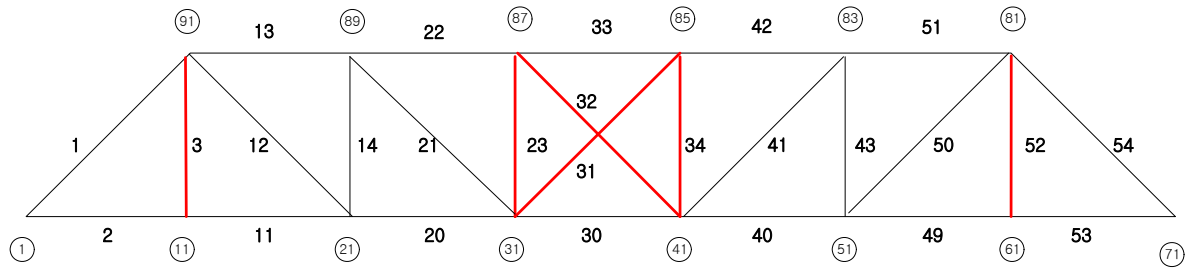
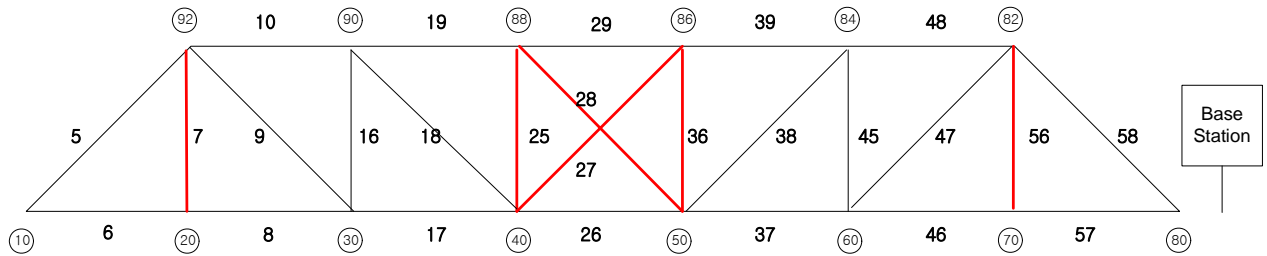


Figure 8.25. Damage indices using centralized approach



(a) West plane



(c) East plane

Figure 8.26. Potential damage locations.

8.4.3 Decentralized damage identification

The DDI application is tested on the Mahomet Bridge to check the damage detection capabilities. The DDI application is the first comprehensive SHM software for wireless smart sensors involving complex network communication and heavy on-board computation. Therefore, the purposes of the tests are confirming the performance of the network operation under harsh communication environment on the bridge, and validating damage detection capability of the application using the current parameters in comparison with the result in section 8.4.2.

With the parameters in Table 8.1, the DDI application has been successfully running on the bridge indicating that the network parameters are well suited for the Mahomet Bridge deployment. However, the application sometimes fails due to communication problems. The

main reason is an unstable communication environment in Mahomet due to interference from the steel elements and dense foliage. When the leaf nodes are on the deck and the gateway node is line of sight with the leaf nodes, the DDI application has always performed well.

The vibration tests have been conducted for damage detection using the DDI application. Similarly, the baseline is the updated FE model in Chapter 7. All 24 nodes are used for the group operation. The same network topology of the leaf nodes are used (see Figure 8.23). The antenna direction of the upper nodes is upward, and the antenna direction of the lower nodes is downward. Because the communication quality is the best if the antennas are co-linear, direct line of sight, and at the same elevation, the nodes in the same elevation were included in each group.

After running the DDI application for 4 groups, the damage indices are obtained as final results. The O and X symbols along the x -axis in the DDI plot denote that the nodes between the signed elements are measured or not: O is measured, X is not measured. The overall patterns of the damage indices in Figure 8.25 and are very similar. The identical candidate damage elements were determined using the DDI application and the post processing of the centrally measured data. Therefore, the damage detection results match well with the centralized approach and the decentralized approach using WSSN.

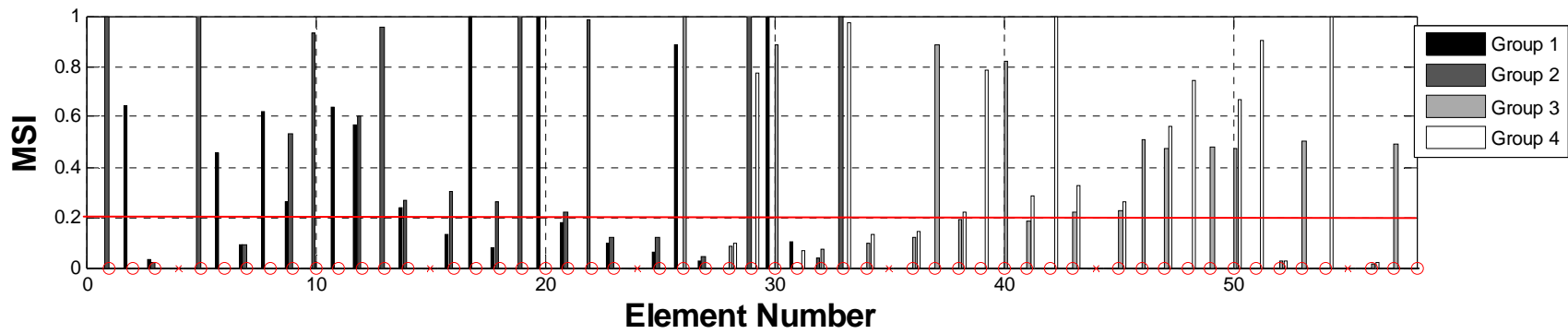
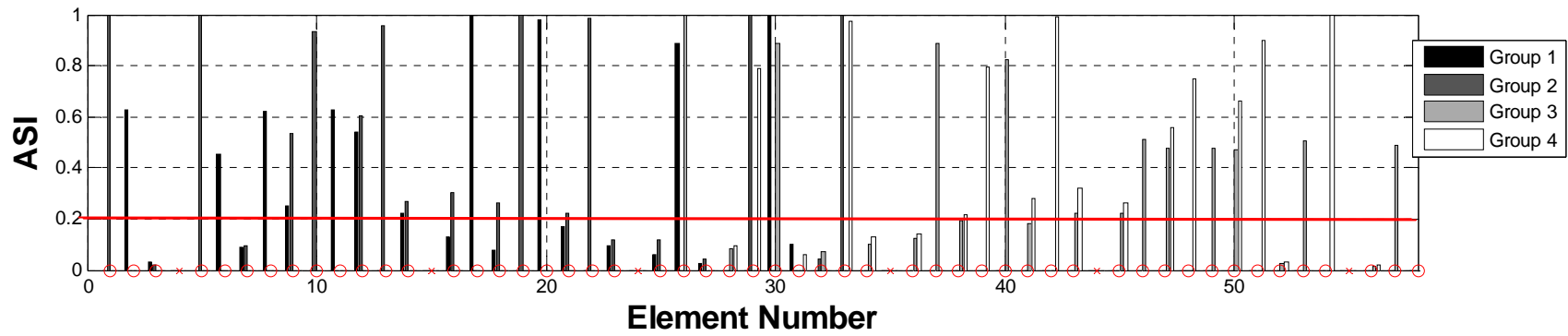


Figure 8.27. Damage indices from the DDI application.

8.4.4 2nd Visual investigation

For better understanding of the damage detection results from the DDI application, the Mahomet Bridge was subsequently investigated. The size of pitting corrosion of all sections is overall similar in 2010 than that in 2008, while the density of pitting was similar or slightly increased (see Figure 8.28 and Figure 8.29). Based on the similar degree of the pitting corrosion during 2008-2010, the reduction in structural stiffness was minor. However, severe corrosion was observed at the central vertical elements. Originally, the connections of the vertical elements were fractured and retrofitted in Figure 7.7. Two plates were welded on the fractured section of the vertical element. The heat affected zone of the welded plates is a common place for accelerated pitting corrosion and crack initiation (Eid, 1989). In 2010, the pitting corrosion was initiated at the welded plates as shown in Figure 8.30. Based on the size of holes and the density of the holes, the thickness reduction due to pitting corrosion is 0.8mm, which corresponds to 19.52% reduction of the sectional area of the welded plates. These corroded sections included the candidate damage elements determined by the DDI application. Therefore, the damage detection performance of the DDI application has been validated on a historic truss bridge.



(a) Section 1 in 2008 (left) and in 2010 (right)



(b) Section 2 in 2008 (left) and in 2010 (right)

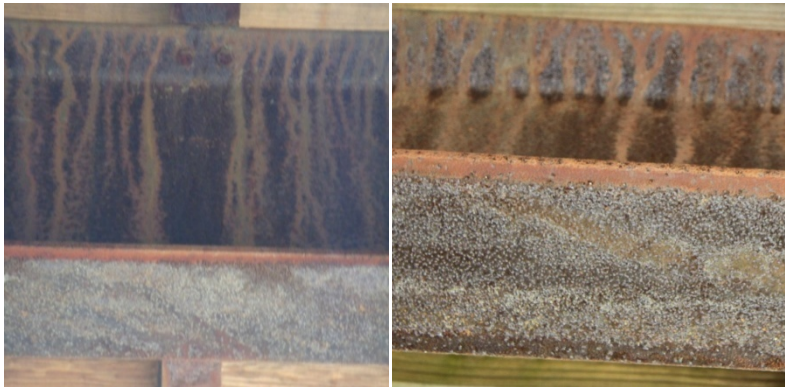


(c) Section 3 in 2008 (left) and in 2010 (right)

Figure 8.28. Comparison of degrees of corrosion



(d) Section 4 in 2008 (left) and in 2010 (right)



(e) Section 5 in 2008 (left) and in 2010 (right)



(f) Section 6 in 2008 (left) and in 2010 (right)

Figure 8.29. Comparison of degrees of corrosion (cont.)



Figure 8.30. Retrofitted plates in 2008 (left) and in 2010 (right).

8.5 Long-term Performance of SHM System

8.5.1 Base station

The base station of the SHM system has shown reliable performance in the deployed environment except the internet connection. The base station PC has been operating continuously during the last 4 months. The fiberglass enclosure protects the electric parts from temperature and humidity. The automatic reconnection function of the cell-phone modem has stopped 3 times during 4 months. In this case, the operator should press ‘reconnect’ button on the screen. Although the internet connection was off, the automatic monitoring did not stop, but the user cannot control the network monitoring. The problem can be solved using a watchdog timer on PC and running a tag to initiate the modem to connect to the internet.

8.5.2 Wireless sensor nodes

The wireless sensor nodes also have performed stably during the last 6 months. Both the AC-powered and battery-powered nodes performed well during the operation, with the enclosures protecting the electrical components. The D-cell batteries have been replaced once a month, while the solar powered nodes were continuously working during the operation. To overcome the inconvenience of the battery replacement, the solar powered nodes are recommended for long-term deployment. Therefore, the hardware components are suitable for long-term structural monitoring system.

8.5.3 Solar energy harvesting devices

In this deployment, the usability of the solar powered nodes has been validated. Before full-scale deployment, three solar powered nodes were deployed on the upper nodes of the west plane. Before the deployment, the rechargeable batteries are fully charged up to 4.1~4.2V. Using the *RemoteCommand Vbat* and *RemoteCommand ChargeStatus*, the on-board voltage level and battery charging status have been monitored in every hour from sunrise to sunset on January 20. The battery voltage is in Figure 8.31, the charging current is in Figure 8.32, and the hourly weather is recorded in Table 8.4 from <http://weather.com>.

Because the weather was mostly cloudy, the charging current was lower than 50 mA during the day. When the charging current was 0, the battery voltage was measured using the *RemoteCommand Vbat*. With small charging voltage, the on board voltage was remained high during the day.

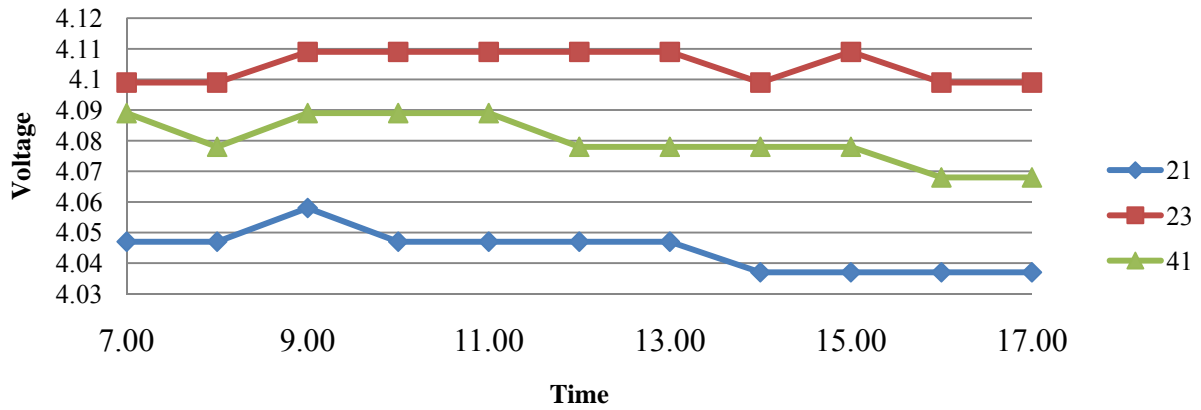


Figure 8.31. Battery voltage

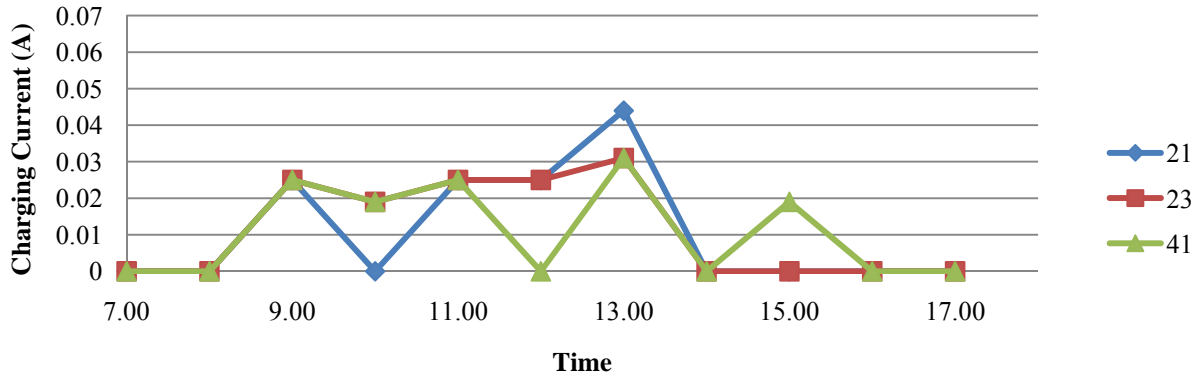


Figure 8.32. Charging current

Table 8.4. Weather condition

Time	Temperature (°C)	weather
7:00	-1.67	Cloudy, sunrise 7:12AM
8:00	-1.11	Light Snow
9:00	-0.56	Icy (Freezing rain)
10:00	-1.11	Cloudy/Windy
11:00	-0.56	Icy (Freezing rain)
12:00	-1	Icy
13:00	0	Icy
14:00	-1	cloudy
15:00	-1	cloudy
16:00	-1	cloudy
17:00	0	cloudy

From January 19 to February 17, the voltage levels of the rechargeable batteries and the charging current from the solar panel have been monitored once a day at 12:00PM – 1:00PM (see Figure 8.33 and Figure 8.34). The weather is also recorded from <http://www.weather.com> as shown in Table 8.5. The weather conditions were point measurements at the time, not the average value for the whole day. During the cloudy days from January 19 to 25, the battery voltage was decreasing because of low charging current from the solar panel. After that, the charging current was up to 0.2A according to the weather condition. The battery voltage has remained high during this one month period.

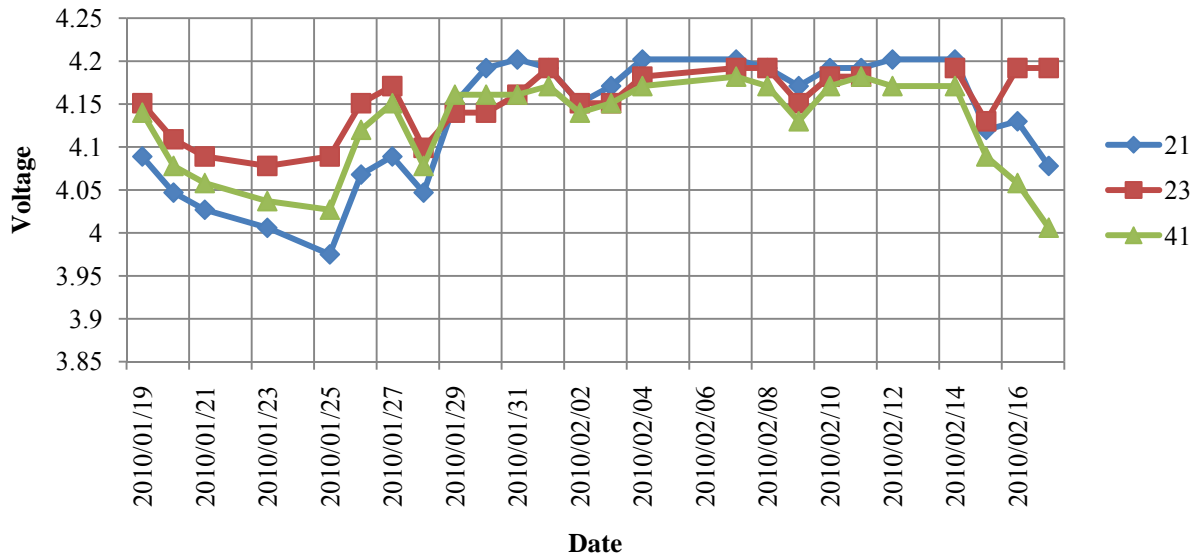


Figure 8.33. Voltage of rechargeable batteries of solar powered nodes.

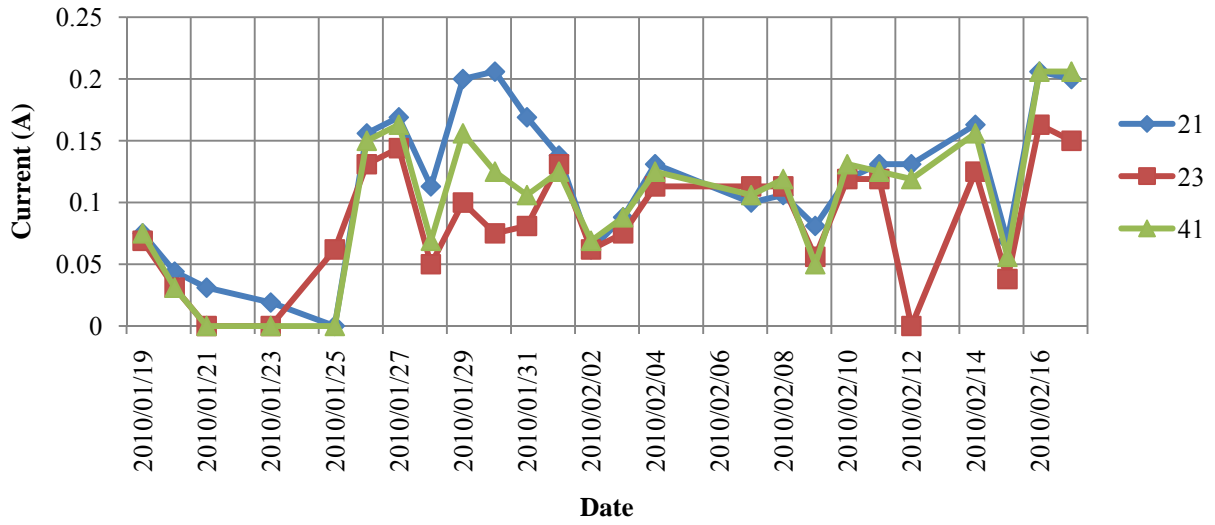


Figure 8.34. Charging current of solar powered nodes.

Table 8.5 Weather Condition

Date	Temperature (°C)	weather
1/19	-3	Fog & Cloudy
1/20	0	Icy
1/21	1	Rain shower
1/22	3	Cloudy
1/23	6	Fog
1/24	6	Cloudy
1/25	-1	Light Snow
1/26	-7	Cloudy and Windy
1/27	-4	Cloudy
1/28	-9	Sunny
1/29	-9	Most Cloudy
1/30	-6	Sunny
1/31	-3	Sunny
2/1	0	Partly Cloudy
2/2	1	Cloudy
2/3	-3	Cloudy
2/4	2	Most Cloudy
2/5	1	Snow/Windy
2/6	-3	Sunny
2/7	-4	Cloudy
2/8	-9	Cloudy/Windy
2/9	-5	Partly Cloudy
2/10	-8	Sunny
2/11	-4	Mostly Cloudy
2/12	-2	Partly Cloudy
2/13	-6	Cloudy
2/14	-3	Mostly Cloudy
2/15	-2	Cloudy

The solar powered nodes have been deployed for 5 months from January to May, and June to July. During the period of the deployment, the solar powered nodes were continuously functioning; therefore, the solar energy harvesting is the suitable power supply option of the wireless sensors for long-term deployment.

8.6 Conclusion

A state-of-the-art WSSN SHM system using the DDI application has been deployed and validated on a historic steel truss bridge. The developed DDI application was run successfully on the bridge with careful communication optimization in antenna orientation, the addition of a powerful gateway antenna, and adjustment of network parameters. A series of damage detection experiments were conducted to determine additional damage during 2008-2010 using the 2008 updated FE model as a baseline. The candidate damage elements were successfully identified using the centralized approach based on the measured data and the DDI application, and the results from both centralized and decentralized methods agreed well. The environmentally hardened hardware system showed stable performance during the deployment. The solar powered nodes have worked stably during 5 month showing the solar energy harvesting is suitable for power options for wireless sensors in long-term deployment. Therefore, the on-board modularized decentralized SHM application using WSSN has been successfully deployed on a full-scale historic bridge, and the performance has been validated.

CHAPTER 9 CONCLUSIONS AND FUTURE WORK

9.1 Conclusions

The research in this dissertation provided a comprehensive framework for long-term structural health monitoring (SHM) for full-scale bridge structures using wireless smart sensors (WSS). The research achieved the first successful data measurement from world's largest WSSN to date. The decentralized SDDL method developed in this research was shown to be robust to false positive damage detection. The DDI application based on the decentralized SDDL method was deployed and demonstrated its performance in damage detection on the Mahomet Bridge. The deployment constituted the first full-scale SHM utilizing on-board computation of WSSN on a bridge structure.

Comprehensive background was given on SHM, full-scale bridge monitoring applications, wireless smart sensors, and software development for WSSN. The development of current technology of SHM and WSSN summarized in this chapter was the foundation of the research in this dissertation.

For monitoring bridge structures to assess structural performance and conditions, a static strain-based damage detection method was developed with the goal of determining the damaged location via a simple truck passage experiment using a limited number of sensors. The performance of the method was validated based on numerical studies and lab-scale experiments. However, damage is intrinsically a local phenomenon; therefore, a dense network of wireless smart sensors is desirable.

To this end, a vibration-based damage localization method was extended using a decentralized computing strategy for WSSN. The extension includes employing the

decentralized computing strategy and a new damage index. A series of experiments on the lab-scale truss bridge showed the robust performance of this method for WSSN. The experiments were conducted using a wired sensor system to emulate the WSSN to confirm the method without considering some issues on wireless communication and network operation of WSSN.

The developed decentralized SHM strategy was implemented on the Imote2 platform to develop a comprehensive SHM application, *Decentralized Damage Identification* (DDI). The main components of the DDI application are the synchronized data measurement, correlation function estimation, system identification, and damage detection. This application is a comprehensive modularized damage detection application using Illinois SHM Project Services Toolsuite. The performance of the developed program was tested on the lab-scale truss structure, and the damage detection results was shown to be robust consistent with the previous tests using the wired sensor system.

The long-term performance of the WSSN was investigated on the Siebel Center Staircase. This deployment identified the requirements of full-scale deployment such as radio channel selection based on ambient spectrum, and network and measurement parameter optimization. Using the optimized parameters for network and measurement, the wireless monitoring system was successfully running for 52 days with a single set of 3 D-cell batteries.

With the experience in the long-term deployment on the Siebel Center Staircase, a large-scale SHM system using WSSN was deployed on the Jindo Bridge in South Korea. In total, 427 sensor channels were deployed on 71 sensor nodes located at various points on the bridge. The major enablers of the deployments were the radio communication tests to fix the sensor location, and the network parameter optimization. Using the optimized system, the vibration and wind data were transferred successfully using the ISHMP Services Toolsuite. This deployment

constituted the world's largest deployment of WSSN for central data measurement on a cable-stayed bridge to date.

The developed SHM system was deployed on a historic bridge utilizing the on-board computation capability of WSS. Before deploying WSSN-based SHM system, bridge responses were measured using wired and wireless sensor system, and an initial refined numerical model was prepared for the baseline for damage detection. An initial FE model was successfully refined by multi-variable multi-constraint model updating using SQP considering significant distributed corrosion. The modal properties matched reasonably with close agreement in the degrees of corrosion between the model and the visual corrosion estimation. A WSSN-based SHM system was deployed on the historic truss bridge and the damage detection performance was verified. The environmentally hardened base station was developed and shown to be suitable for remote monitoring using WSSN. In total, 144 sensor channels in 24 sensor nodes were deployed. The harsh communication environments by physical interferences and moisture problems were overcome by antenna orientation optimization and powerful antenna selection. With the adjustments, 100% of reception rates were achieved. The condition of the historic bridge was evaluated using the decentralized SDDL method. The candidate damaged elements were successfully identified using the DDI application, which was confirmed by comparing with the post processing of the measured data. The hardware including base station, sensor nodes, and the solar panels showed stable performance during 5 months of deployment. This deployment on the Mahomet Bridge with the DDI application was the first full-scale damage detection implementation using a comprehensive SHM software and WSSN.

In conclusion, this research provided a comprehensive foundation of long-term SHM system including robust damage detection algorithms, field applicable versatile hardware components,

software applications, and deployment strategy on full-scale bridges using WSSN. The next section describes suggested future studies to extend the developed framework to be applicable for various large-scale civil structures in a long-term manner.

9.2 Near-term Future Studies

9.2.1 Improvement of the DDI application

The constraint for successfully running the developed DDI application is fairly good radio communication. However, the quality of the radio communication is variable in terms of random uncertainties and interferences. Therefore, the software should be upgraded with fault tolerance features. After damage detection, the gateway node should wait a specific time and skip the cluster head and move on to the next cluster head, if the previous node is unresponsive during the time. With this adjustment, the DDI application will become more usable for the field deployments.

9.2.2 Decision making logic for the DDI application

The DDI application does not employ logics for decision making for damage detection. The final goal for the DDI application is to employ the decision making logic by sharing damage detection results between local communities.

9.2.3 Sensitivity analysis on damage detection

The DDI application was validated in the lab-scale experiments to identify the damaged element which has 40% stiffness reduction. However, the detailed sensitivity on damage identification

was not investigated. The sensitivity of damage detection should be determined in the lab-scale tests to investigate how small damage can be identified using the DDI application.

9.2.4 Communication issues

The basic assumption when using the WSSN is that the wireless communication between the gateway node and the leaf nodes is considerably stable. However, the quality of radio communication depends on many factors including uncertain ambient spectrum. In this research, partial solutions for improving the wireless communication have been provided such as strong antenna and antenna orientation optimization. These solutions were working well to improve the communication of the Mahomet Bridge, where the ambient wi-fi interference is negligible. For monitoring infrastructure where the wi-fi inference is significant, further investigation on improving the radio communication environment will be done using the antenna technology.

9.2.5 Graphical user interface

Cygwin has been commonly used to run WSSN. Current ISHMP applications are controlled through a command-line interface, which is not user friendly. To facilitate users in understanding and controlling the monitoring system, a web-based or Matlab-based graphical user interface will be developed for the DDI application. In the user interface, raw data, correlation function plots and final damage detection results can be viewed. Additional features including visual information using webcams or multimedia sensor boards can also be incorporated.

9.3 Broader Future Studies

9.3.1 General damage detection algorithm development

The applicability of the decentralized SDDL_V method on non-truss structures should be examined and experimentally verified. The applicability of the method has been investigated mainly for truss structures. The methodology should be examined on general structures including beams or plates. Further experimental studies need to be done on general civil infrastructure such as cable-stayed bridges.

Moreover, the decentralized damage detection strategy assumed the damage is linear. Though the linear stiffness reduction damage can be found commonly in the field such as steel corrosion and concrete cracking, an effective method for nonlinear damage should be developed for structural assessment after strong natural events or terrorist attacks.

9.3.2 Excitation-specific monitoring

Strong winds are the major environmental excitation of interest in this research such as typhoons and hurricanes. These events can be forecasted and typically last for several hours to several days. However, earthquake excitation is relatively unexpected, and will last only for several seconds. To monitor such high consequence but rare events, a continuous monitoring effort and abrupt wakeup strategy is required. In this research, continuous autonomous monitoring has been tested on the Mahomet Bridge using a powered sentry; the software and associated parameters should be optimized for much faster reaction.

9.3.3 Sensing capabilities

The sensing capabilities for SHM should be enhanced for strain and displacement measurements. Chapter 3 presented the static strain-based DLV method, which has been validated using the lab-scale tests. For application of the strain-based methodology for the full-scale bridges using wireless sensors, the high sensitivity strain sensing capability is required. The resolution of the strain sensor board may rely on strain gage or strain sensor, amplifier, A2D converter, etc. Field application higher resolution strain sensor should be developed.

Displacement is also useful measurement for damage detection because it can provide the flexibility information of structure directly without modal analysis. However, displacement sensor boards for WSSN have not been developed yet. One possible sensor is the GPS-based sensor board. The challenges for this sensor board are this board is power intensive, and the resolution for the commercial GPS sensor board is poor, meter level for commercial GPS receivers. To make the GPS sensor board feasible, the high resolution GPS chip should be used along with an estimation technology. Other high resolution displacement sensors may be developed using LASER, vision-based sensors, and traditional displacement sensors.

9.3.4 Communication improvement

The basic assumption when using the WSSN is that the wireless communication between the gateway node and the leaf nodes is considerably stable. However, the radio communication is affected by many uncertain environmental factors. In this research, partial solutions for improving the wireless communication have been provided such as appropriate antenna and antenna orientation optimization. Further investigation on new antenna technology will be done for robust application of WSSN on the wireless communication.

9.3.5 Multihop communication

The research herein used exclusively the single-hop (peer-to-peer) communication. However, the applicability of the wireless SHM system is limited by the range of the external antenna. Long civil structures such as km-length bridges or high-rise buildings require multi-hop communication, which enables long-distance data transfer. The multi-hop communication strategy is rapidly developing; still some practical problems have not been addressed in network waiting time, structure-specific route optimization, and power consumption.

The network parameters including waiting time need to be selected from the experimental study on the target structure, because the radio communication is environment-specific. The routing optimization algorithm can be developed based on the network configuration and sensor location of the target bridge.

9.3.6 Underwater structure monitoring

To date, the wireless SHM system has mainly used in the ambient radio communication using Wi-Fi frequency. The 2.4 GHz range is not transmittable under water; thus, other waves to transmit underwater can significantly increase the range of applicable structures of wireless sensing. The lowest Amateur Radio frequency, 1.8MHz, was reported to transmit under water, and ultrasound at 20kHz can transmit within fluids. For example, one of the main sources of bridge collapses is scouring of the pier. The underwater communication capability can enable the pier scour monitoring. Furthermore, underwater communication capability will enable many environmental system monitoring including water pipeline, sewage, and tank structures. The

challenges are slower speed, higher attenuation, and power consumption. The investigation on various communication ranges can be done for possibility of under water monitoring.

9.3.7 Energy harvesting

The pre-requisite of the reliable performance of the wireless smart sensor is the stable power supply. Especially, the multi-hop communication strategy requires high power consumption due to longer communication time. Therefore, reliable energy harvesting devices are required. In this research, solar panel has been employed for energy harvesting. However, in some climate, the solar power may not be the optimal power sources if the number of sunny day is small. Other energy harvesting devices can be developed using various sources based on target infrastructure and the environment. Wind energy harvesting, vibration-based harvesting, piezo-electric energy harvesting can be explored to find environment specific energy sources for wireless smart sensors. The challenges using the listed transient energy sources are the development of charging strategy. Therefore, the reliable energy harvesting capability will enable stable long-term monitoring of full-scale structures.

REFERENCES

- [1] Abe, M. (1998). "Structural monitoring of civil structures using vibration measurement – Current practice and future." Ian Smith (ed.), *Artificial Intelligence in Structural Engineering: Information Technology for Design, Collaboration, Maintenance and Monitoring*, Lecture Notes in Artificial Intelligence 1454, Springer, Germany, 1-18.
- [2] Abe, M., Fujino, Y., Yanagihara, M. and Sato, M. (2000). "Monitoring of Hacucho suspension bridge by ambient vibration measurement." *Nondestructive Evaluation of Highways, Utilities, and Pipelines*, SPIE proc. Series, 3995: 237-244.
- [3] Adler, R., Flanigan, M., Huang, J., Kling, R., Kushalnagar, N., Nachman, L., *et al.* (2005). Intel mote 2: An advanced platform for demanding sensor network applications. *Proc. of the 3rd International Conference on Embedded Networked Sensor Systems*, 298-298.
- [4] Agardh, L. (1991). "Modal analysis of two concrete bridges in Sweden." *Structural Engineering Int.*, 4: 34-39.
- [5] Akgül, F. and Frangopol, D. M. (2004). "Bridge rating and reliability correlation: comprehensive study for different bridge types." *J. Structural Engineering*, ASCE, 130(7): 1063-1074.
- [6] Allemang, R. J., Brown, D. L., 1982, "A Correction Coefficient for Modal Vector Analysis," *Proceedings, International Modal Analysis Conference*, Orlando, Florida, 110~116.
- [7] Ando, S., Nakamura, T. and Sakaguchi, T. (1997). "Ultrafast correlation image sensor; concept, design, and applications." *TRANSDUCERS 97, 1997 Int. conf. Solid-state Sensors and Actuators*, 307-310.

- [8] Ando, S., Nara, T., Ono, N. and Kurihara, T. (2007). "Real-time orientation-sensitive magneto-optic imager for leakage flux inspection." *IEEE Transactions on Magnetics*, 43(3): 1044-1051.
- [9] Antenova, 2009, <http://www.antenova.com/?id=536>.
- [10] Bernal, D. (2000). "Extracting flexibility matrices from state-space realizations", *Proc. COST F3, Madrid, Spain*, 127-135.
- [11] Bernal, D. (2002). "Load vectors for damage localization." *J. Engineering Mechanics, ASCE*, 0733-9399, 128(1):7-14.
- [12] Bernal, D. (2005). "A null space approach for damage localization in systems identified from operational or ambient vibration data", *Structural health monitoring 2005: Advantages and challenges for implementation*, Editor: Fu-Kuo Chang, 133-141.
- [13] Bernal, D. (2006). "Flexibility-based damage localization from stochastic realization results", *J. Engineering Mechanics, ASCE*, 132(6):651-658.
- [14] Bernal, D. (2006). "Damage localization from the null space of the transfer matrix." *Proc. XXIC International Modal Analysis Conference*.
- [15] Bernal, D. (2007). "Damage localization from the null space of changes in the transfer matrix." *AIAA Journal*, 45(2): 374-381.
- [16] Bridge Diagnostics, Inc., (2008). Boulder, CO. <http://www.bridgetest.com>.
- [17] Brownjohn, J.M.W., and Xia P.Q. (2000). "Dynamic assessment of curved cable-stayed bridge by model updating." *ASCE, J. Structural Engineering*, 126 (2): 252-260.
- [18] Carder, D. S. (1937). "Observed vibrations of bridges." *Bulletin, Seismological Society of America*, 27: 267-303.

- [19] Carrasco, C. J., Osegueda, R. A., Ferregut, C. M., and Grygier, M. (1997). "Localization and quantification of damage in a space truss model using modal strain energy." *Smart Structures and Materials 1997: Smart Systems for Bridges, Structures, and Highways*, SPIE, 3043: 181–192.
- [20] Cawley, P. and Adams, R. D. (1979). "The location of defects in structures from measurement natural frequencies." *J. Strain Analysis*, 14(2): 49-57.
- [21] Celebi, M. (2002). "GPS in pioneering dynamic monitoring of long-period structures." *Earthquake Spectra*, 18(1): 47 -61.
- [22] Chan, T. H. T., Li, Z. X., Ko, J. M. (2001). "Fatigue analysis and life prediction of bridges with structural health monitoring data — Part II: application." *Int. J. Fatigue*, 23: 55–64.
- [23] Chan, W. S., Xu, Y. L., Ding, X. L., Xiong, Y. L., and Dai W. J. (2005). "Dynamic displacement measurement accuracy of GPS for monitoring large civil engineering structures." *Smart Structures and Materials 2005: Sensors and Smart Structures Technologies for Civil, Mechanical, and Aerospace Systems*, 54-65.
- [24] Chance, J., Tomlinson, G. R. and Worden, K. (1994). "A simplified approach to the numerical and experimental modeling of the dynamics of a cracked beam." *Proc. 12th int. modal analysis conf.*, Hawaii.
- [25] Chang, C. C., Chang, T. Y. P. and Zhang, Q.W. (2000). "Iterative constrained optimization scheme for model updating of long-span bridges." *Nondestructive Evaluation of Highway, Utilities, and Pipelines IV*, Proc. SPIE, 3995: 334-345.
- [26] Chase, S. B. (2005). "The role of sensing and measurement in achieving FHWA's strategic vision for highway infrastructure." *Sensing issues in civil structural health monitoring*, Springer Publishing Co., Netherlands, 23-32.
- [27] Chen, H. L., Spyrakos, C. C., and Venkatesh, G. (1995). "Evaluating structural deterioration by dynamic response." *J. Structural Engineering*, 121:1197–1204.

- [28] Cho, S., Jo, H., Jang, S. A., Park, J., Jung, H.-J., Yun, C.B., Spencer, B.F. Jr., Seo, J. (2010). "Structural Health Monitoring of a Cable-Stayed Bridge Using Smart Sensor Technology: Data Analysis." *Smart Structures and Systems*, 2010 (this issue).
- [29] Cosser, E., Roberts, G. W., Meng, X. and Dodson, A. H. (2004) "Single frequency GPS for bridge deflection monitoring progress and results." 1st FIG Int. Symp. on Engineering Surveys for Construction Works and Structural Engineering, Nottingham, UK.
- [30] Crossbow Technology, Inc, "MICA2 Wireless Measurement System," San Jose, CA (2007a).
- [31] Crossbow Technology, Inc., ITS400, Imote2 Basic Sensor Board, San Jose, CA, (2007b).
- [32] Crossbow, Inc. (2007c). "Imote2 Hardware Reference Manual." Revision A, PN: 7430-0409-01,
http://www.xbow.com/Support/Support_pdf_files/Imote2_Hardware_Reference_Manual.pdf.
- [33] Crossbow, Inc. (2009). "Imote2 Data Sheet", Revision A, PN: 6020-0117-02,
http://www.xbow.com/Products/Product_pdf_files/Wireless_pdf/Imote2_Datasheet.pdf.
- [34] Decatur Bridge Company, (1912). 24 July 1912, Champaign County Historical Archives, Box 594, Folder Mahomet Township – Bridge over Sangamon, File "Metal Order Contract, " Urbana Free Library, Urbana, Illinois.
- [35] De Stefano, A. (2003). "A national Italian project: internet based monitoring of monumental buildings." AMAS Workshop on Smart Materials and Structures, SMART'03: 301-314.
- [36] D'Errico, John. (2006). *Fminsearchcon*, MATLAB Central File Exchange.

- [37] Doebling, S. W. and Farrar, C. R. (1997). "A statistical comparison of impact and ambient testing results from the Alamosa Canyon bridge." Proc. Int. Modal Analysis Conf. - IMAC, 1: 264-270.
- [38] Doebling, S. W., Peterson, L. D. and Alvin, K. F. (1998). "Experimental determination of local structural stiffness by disassembly of measured flexibility matrices." J. Vibration and Acoustics, 120: 949-957.
- [39] Duan, Z., Yan, G., Ou, J. and Spencer, B. F. Jr. (2005). "Damage localization in ambient vibration by constructing proportional flexibility matrix." J. Sound and Vibration 284: 455-466.
- [40] Eid, N.M.A. (1989). "Localized corrosion at welds in structural steel under desalination plant conditions Part I: Effect of surface roughness and type of welding electrode." Desalination, 73: 397-406.
- [41] Ember (2008). Boston, MA.
- [42] Farrar, C. R., Baker, W. E., Bell, T. M., Cone, K. M., Darling, T. W., Duffey, T. A., Eklund, A. and Migliori, A. (1994). "Dynamic characterization and damage detection in the I-40 bridge over the Rio Grande." Los Alamos National Laboratory Report LA-12767-MS.
- [43] Farrar, C. R. and Jauregui, D. A. (1998). "Comparative study of damage identification algorithms applied to a bridge: I. Experiment", Smart mater. Struct., 7: 704-719.
- [44] Farrar, C.R. and Doebling, S.W. (1999). "DAMAGE DETECTION II: Field Applications to Large Structures," in Modal Analysis and Testing, J. M. M. Silva and N. M. M. Maia, eds., Nato Science Series, Kluwer Academic Publishers, Dordrecht, Netherlands.
- [45] Farrar, C. R. and Worden, K. (2007). "An introduction to structural health monitoring." Phil. Trans. R. Soc. A365, 303–315.
- [46] FHWA, National Bridge Inventory (NBI): <http://www.fhwa.dot.gov/bridge/defbr06.htm>

- [47] Fletcher, R., Powell, M.J.D (1963), "A rapidly convergent descent method for minimization." *The Computer Journal*, 1 pp. 163-168.
- [48] Gao, Y. (2005). *Structural health monitoring strategies for smart sensor networks*, Doctoral dissertation, University of Illinois at Urbana-Champaign.
- [49] Gao, Y., Spencer, B. F. Jr., and Bernal, D. (2004). "Experimental verification of the damage locating vector method." *Proc., Int. Symp. on Smart Structure Technology*, Hawaii.
- [50] Gay D., Levis, P. Culler D., Brewer E. (2003). "nesC 1.1 Language Reference Manual", <http://nesc.sourceforge.net/papers/nesc-ref.pdf>
- [51] Ge, M. and Liu, E.M. (2005). "Structural damage identification using system dynamic properties." *Computers & Structures*, 83: 2185-2196.
- [52] Gentile, C. and Gallino, N. (2008). "Condition assessment and dynamic system identification of a historic suspension footbridge." *Structural Control and Health Monitoring*, 15:369-388.
- [53] Giacosa, L. M., De Stegano, A., Civera, P. and Ansari, F. (2008). "Long-term structural health monitoring of the 2006 Torino's Olympic pedestrian cabled-stayed bridge." *Proc. World Forum on Smart Materials and Smart Structures Technology*. In CD-ROM.
- [54] Gunes, B. and Bernal, D. (2004). "A data-driven approach for earthquake damage detection." *Proc. 6th International Conference on Advances in Civil Engineering*, İstanbul, Turkey, 1: 364-373.
- [55] Historic Bridges, <http://www.historicbridges.org>
- [56] Hjelmstad, K.D. and Shin, S. (2007). "Damage detection and assessment of structures from static response." *J. Engineering Mechanics*, ASCE, 123(6):568-576.

- [57] Huth, O., Feltrin, G., Maeck, J., Kilic, N. and Motavalli, M. (2005). "Damage identification using modal data: experiences on a prestressed concrete bridge." *J. Structural Engineering*, ASCE, 131(12):1898–1910.
- [58] Jaishi, B. and Ren, W. X. (2005). "Structural finite element model updating using ambient vibration test results." *J. Structural Engineering*, ASCE, 131(5): 617-628.
- [59] Jaishi, B. and Ren, W. X. (2007). "Finite element model updating based on eigenvalue and strain energy residuals using multiobjective optimization technique." *Mechanical Systems and Signal Processing*, 21: 2295-2317.
- [60] Jang, S.A., Sim, S.H. and Spencer, B.F. Jr. (2008). "Structural damage detection using static strain data." *Proc. World Forum on Smart Materials and Smart Structures Technology*. In CD-ROM.
- [61] Jang, S.A., Spencer, B.F. Jr., Rice, J.A., and Wang, Z. (2010). "Full-scale experimental validation of high-fidelity wireless measurement on a historic truss bridge." *Advances in Structural Engineering*. (in press).
- [62] Jang, S., Jo, H., Cho, S., Mechitov, K., Rice, J.A., Sim, S.H., Jung, H.J., Yun, C.B., Spencer, Jr., B.F., and Agha, G. (2010) "Structural health monitoring of a cable-stayed bridge using smart sensor technology: deployment and evaluation." *Journal of Smart Structures and Systems*. (in press).
- [63] Jang, S. and Spencer, Jr., B.F. (2009) "Receptance-based Structural Health Monitoring Approach for Bridge Structures." *Health Monitoring of Structural and Biological Systems III*, 16th International Symposium on: Smart Structures and Materials & Nondestructive Evaluation and Health Monitoring, SPIE. (to appear)
- [64] Juang, J.N. and Pappa, R.S. (1984). "An eigensystem realization algorithm for modal parameter identification and model reduction." *AIAA Journal*, *J. Guidance, Control, and Dynamics*, 8(5): 620-627.

- [65] Jones, D. A. (1996). Principles and prevention of corrosion, 2nd ed., Prentice Hall.
- [66] Kijewski-Correa, T., Su, S., Abittan, E., and Antsaklis, P. (2006) "On the use of heterogeneous, wireless sensor networks for damage assessment in bridges under unknown excitations," Fourth World Conference on Structural Control and Monitoring (4WCSCM), 183, July 11-13, San Diego, CA.
- [67] Kim, J.T., Rye, Y.S., Cho, H.M., and Stubbs, N. (2003). "Damage identification in beam-type structures: frequency-based method vs mode-shape-based method." *Engineering Structures*, 25: 57-67.
- [68] Kim S., Pakzad, S., Culler, D., Demmel, D., Fennes, G., Glaser, S., and Turon, M. (2007). "Health Monitoring of Civil Infrastructures using Wireless Sensor Networks". Proc. 6th Int. Conf. on Information Processing in Sensor Networks, pp. 254-263.
- [69] Kling, R. M. (2003). Intel mote: An enhanced sensor network node. Proc. of the International Workshop on Advanced Sensors, Structural Health Monitoring, and Smart Structures.
- [70] Kling, R., Adler, R., Huang, J., Hummel, V., and Nachman, L. (2005). Intel mote-based sensor networks. *Structural Control and Health Monitoring*, 12, 469-479.
- [71] Law, S. S., Ward, H. S., Shi, G. B., Chen, R. Z., Waldron, P. and Taylor, C. (1995). "Dynamics assessment of bridge load-carrying capacities" *J. Structural Engineering*, ASCE , 121(3): 488-495.
- [72] Lee, J.J. and Yun, C.B. (2006). "Damage diagnosis of steel girder bridges using ambient vibration data." *Engineering Structures*, 28: 912-925.
- [73] Lee, J.J. and Shinozuka, M. (2006). "A vision-based system for remote sensing of bridge displacement." *NDT&E International*, 39: 425-431.

- [74] Lee, J. J., Fukuda, Y., Shinozuka, M., Cho, S. and Yun, C. B. (2007). "Development and application of a vision-based displacement measurement system for structural health monitoring of civil structures." *Smart Structures and Systems*, 3(3): 373-384.
- [75] Lee, J. W., Kim, J. D., Yun, C. B., Yi, J. H. and Shim, J. M. (2002). "Health-monitoring method for bridge under ordinary traffic loadings." *J. Sound and Vibration*, 257 (2): 247-264.
- [76] Lemaitre, J. and Desmorat, R. (2005). *Engineering damage mechanics*, Springer.
- [77] Levis, P., Madden, S., Polastre, J., Szewczyk, R., Whitehouse, K., Woo, A., Gay, D., Hill, J., Welsh, M., Brewer, E., and Culler, D. (2005), *TinyOS: An Operating System for Sensor Networks*. *Ambient Intelligence*, Weber, W., Rabaey, J.M., Aarts, E., Eds. 115-148, Springer, Berlin, Heidelberg.
- [78] Li, Z. X., Chan, T. H. T. and Ko, J. M. (2001). "Fatigue analysis and life prediction of bridges with structural health monitoring data - Part I: methodology and strategy." *Int. J. Fatigue*, 23: 45-53.
- [79] Linderman, L.E., Rice, J.A., Barot, S., Spencer, B.F.Jr., and Bernhard, J.T. (2010). "Characterization of Wireless Smart Sensor Performance." *Newmark Civil Engineering Laboratory Report 21* <http://hdl.handle.net/2142/15101>.
- [80] Lynch, J. P., and Loh, K. J. (2006). A summary review of wireless sensors and sensor networks for structural health monitoring. *The Shock and Vibration Digest*, 38(2), 91-28.
- [81] Lynch, J. P., Wang, Y., Loh, K. J., Yi, J. H., and Yun, C. B. (2006). "Performance Monitoring of the Geumdang Bridge using a Dense Network of High-resolution Wireless Sensors", *Smart Materials and Structures*, Vol. 15, pp. 1561-1575.
- [82] Macdonald, J. H. G., Taylor, C. A., Thomas, B. T. and Dagless, E. L. (1998). "Real-time remote monitoring of dynamics displacements by computer vision." *Seismic Design Practice into the Next Century, Research and Application*, 389-396.

- [83] Maeck, J. and De Roeck, G. (1999). “Dynamic Bending and torsion stiffness derivation from modal curvatures and torsion rates.” *J. Sound and Vibration*, 225(1): 153-170.
- [84] Mechitov, K.A., Kim, W., Agha, G.A., and Nagayama, T. (2004). “High-frequency distributed sensing for structure monitoring.” *Proc., 1st Int. Workshop on Networked Sensing Systems*, Tokyo, Japan, 101–105.
- [85] Mainwaring, A., Culler, D., Polastre, J., Szewczyk, R., and Anderson, J. (2002). *Wireless sensor networks for habitat monitoring. Proceedings of the 1st ACM International Workshop on Wireless Sensor Networks and Applications*, 88-97.
- [86] Nelder, J. A. and Mead, R. (1965). “A simplex method for function minimization.” *Computer Journal*, 7: 308-313.
- [87] MEMSIC, Inc. (2010). “ITS400, Imote2 Basic Sensor Board”, Andover, MA.
- [88] MicroStrain (2008). Williston, VT, <http://www.microstrain.com>.
- [89] Millennial Net, Inc. (2008). Chelmsford, MA, <http://millennial.net>.
- [90] Miller, T., Spencer Jr., B.F., Li, J., Jo, H. (2010). “Solar Energy Harvesting and Software Enhancements for Autonomous Wireless Smart Sensor Networks.” NSEL Report Series, University of Illinois at Urbana-Champaign. <http://hdl.handle.net/2142/16300>
- [91] Minnesota Department of Transportation. (2001). “Fatigue evaluation of the deck truss of bridge 9340.” Report #MN/RC-2001-10.
- [92] Mottershead, J. E. and Friswell, M. I. (1993). “Model updating in structural dynamics: A survey.” *J. Sound and Vibration*, 167(2): 347-375.
- [93] Nagayama, T., Spencer, B. F. Jr., Agha, G. A., and Mechitov, K. A. (2006). “Model-based data aggregation for structural monitoring employing smart sensors.” *Proc. of 2nd Int. Workshop on Networked Sensing System (INSS 2006)*, 203-210.

- [94] Nagayama, T. and Spencer Jr., B.F., (2007). "Structural Health Monitoring using Smart Sensors", NSEL Report Series, No. 1, University of Illinois at Urbana-Champaign. <http://hdl.handle.net/2142/3521>.
- [95] Nagayama, T., Moizadeh, P., Mechtov, K., Ushita, M., Makihata, N., Ieiri, S., Agha, G., Spencer, Jr., B.F., Fujino, Y., and Seo, J. (2010) "Reliable multi-hop communication for structural health monitoring." *Journal of Smart Structures and Systems*. (in press).
- [96] Orszag, P.R., (2008). "Investing in Infrastructure." Testimony for Congressional Budget Office. <http://www.cbo.gov/ftpdocs/95xx/doc9534/7-10-Infrastructure.pdf>
- [97] Pakzad, S. (2008). "Statistical Approach to Structural Monitoring Using Scalable Wireless Sensor Networks", Ph.D. Dissertation. University of California, Berkeley.
- [98] Pandey, A. K., Biswas, M. and Samman, M. M. (1991). "Damage detection from changes in curvature mode shapes." *J. Sound and Vibration*, 145(2): 321-332.
- [99] Patil, D.P., Maiti, S.K. (2003). "Detection of multiple cracks using frequency measurements." *Engineering Fracture Mechanics*, 70: 1553-1572.
- [100] Patjawit, A. and Kanok-Nukulchai, W. (2005). "Health monitoring of highway bridges based on a global flexibility index." *Engineering Structures*, 27:1385-1391.
- [101] Peil, U. (2005). "Assessment of bridges via monitoring." *Structure and Infrastructure Engineering: Maintenance, Management, Life-cycle Design and Performance*, 1(2): 101-117.
- [102] Polastre, J., Szewczyk, R., and Culler, D. (2005). *Telos: Enabling Ultra-Low Power Wireless Research*. Proc. Fourth Int. Symposium on Information Processing in Sensor Networks. Los Angeles, California.
- [103] Posenato, D., Lanata, F., Inaudi, D., Smith, F. C. (2006). "Model free interpretation of monitoring data." *Intelligent Computing in Engineering and Architecture*, 4200: 529-533.

- [104] Pothisiri, T. and Hjelmstad, K. D. (2003). "Structural damage detection and assessment from modal response." *J. Engineering Mechanics, ASCE*, 129(2): 135-145.
- [105] Powerizer, 2009,

<http://www.batteryspace.com/polymerli-ionmodule37v10000mah37wh85arate-prewiredwithpcbpl9059156.aspx>
- [106] Rahai, A., Bakhtiari-Nejad, F., and Esfandiari, A. (2007). "Damage assessment of structure using incomplete measured mode shapes." *Structural Control and Health Monitoring*, 14: 808-829.
- [107] Ren, W.X., Blandford, G.E., and Harik, I. E. (2004a). "Roebing suspension bridge. I: finite-element model and free vibration response." *Journal of Bridge Engineering, ASCE*, 9(2): 110-118.
- [108] Ren, W.X., Harik, *I.E.*, Blandford, G.E., Lenett, M., and Baseheart T.M. (2004b). "Roebing suspension bridge. II: ambient testing and live-load response." *Journal of Bridge Engineering, ASCE*, 9(2): 119-126.
- [109] Rene Motes (1999). Harvard Sensor Networks Lab. <http://fiji.eecs.harvard.edu/node/6>
- [110] Rice, J.A., Mechitov, K.A., Spencer Jr., B.F. and Agha, G. (2008). "A Service-Oriented Architecture for Structural Health Monitoring using Smart Sensors," Proc. 14th World Conference on Earthquake Engineering, Beijing, China.
- [111] Rice, J.A. and Spencer Jr., B.F. (2009). "Flexible Smart Sensor Framework for Autonomous Full-scale Structural Health Monitoring," NSEL Report Series, No. 18, University of Illinois at Urbana-Champaign. <http://hdl.handle.net/2142/13635>.
- [112] Rice, J.A., Mechitov, K., Sim, S.-H., Nagayama, T., Jang, S.A., Kim, R., Spencer, B.F. Jr., Agha, G., Fujino, Y. (2010). "Flexible smart sensor framework for autonomous structural health monitoring." *Smart Structures and Systems* (this issue).

- [113]RLH Industries (2008). "2008 Product guide."
http://www.fiberopticlink.com/Tech_Info/pdf/2008_Product_Guide-online.pdf
- [114]Roundy, S., Wright, P. K., & Rabacy, J. M. (2004). Energy Scavenging for Wireless Sensor Networks. Norwell: Kluwer Academic Publishers.
- [115]Sensicast Systems, Inc. (2008). Needham, MA. <http://www.sensicast.com>.
- [116]Silva, C. W. (2007). Vibration. 2nd Ed. Taylor & Francis. pp. 738-742.
- [117]Sim, S.H., Jang, S.A., Spencer, Jr., B.F. (2008). "Reliability-based evaluation of the performance of the damage locating vector method." Probabilistic Engineering Mechanics, Vol 23, pp. 489-495.
- [118]Sim, S.H. and Spencer, Jr., B.F. (2009), "Decentralized Strategies for Monitoring Structures using Smart Sensor Networks," NSEL Report Series, No. 19, University of Illinois at Urbana-Champaign
- [119]Sim, S. H. and Spencer, B.F. (2008). "Multi-scale sensing for structural health monitoring." Proc. World Forum on Smart Materials and Smart Structures Technology. In CD-ROM.
- [120]Shade, D. (2010). "Practical antenna choices for 802.15.4 enabled consumer electronics." RF Globalnet newsletter, March 30.

<http://www.wirelessdesignonline.com/article.mvc/Practical-Antenna-Choices-For-802154-Enabled-0002?VNETCOOKIE=NO>
- [121]Shankar P.M. (2002). Introduction to Wireless Systems. Wiley and Sons, New York.
- [122]Shepherd, R. and Charleson, A. W. (1971). "Experimental determination of the dynamic properties of a bridge substructure," Bulletin of the Seismological Society of America, 61: 1529-1548.

- [123] Shi, Z. Y., Law, S. S. and Zhang, L. M. (2000). "Structural damage detection from modal strain energy change." *J. Engineering Mechanics, ASCE*, 126(12):1216-1223.
- [124] Shi, Z. Y., Law, S. S., and Zhang, L. M. (2002). "Improved Damage Quantification from Elemental Modal Strain Energy Change." *J. of Engineering Mechanics, ASCE*, 128(5):521–529.
- [125] Simpson, W. T. (1993). "Specific gravity, moisture content, and density relationship for wood." General Technical Report FPL-GRT-76, U.S. Forest Service, Dept of Agriculture.
- [126] Shin, S., and Hjelmstad, K. D. (1994). "Damage detection and assessment of structural systems from measured response." *Civil Engrg. Studies, SRS 593, UILUENG-94-2013*, Univ. of Illinois at Urbana-Champaign.
- [127] Sohn, H., Farrar, C. R., Hemez, F. M., Shunk, D. D., Stinemates, D. W., and Nadler, B. R. (2003). "A review of structural health monitoring literature: 1996-2001.", Los Alamos national laboratory report, LA-13976-MS.
- [128] Sohn, H. (2006). "Effects of environmental and operational variability on structural health monitoring." A Special Issue of *Philosophical Transactions of the Royal Society on Structural Health Monitoring*.
- [129] Spectral Dynamics, (2010), Technical papers on Siglab, http://www.sd-star.com/index.php?option=com_content&view=category&layout=blog&id=26&Itemid=36
- [130] Spencer Jr., B.F., Ruiz-Sandoval, M and Kurata, N. (2004), *Smart Sensing Technology: Opportunities and Challenges, Structural Control and Health Monitoring* 11, 349–368.
- [131] Spencer, B. F. Jr. and Nagayama, T. (2006). "Smart sensor technology: a new paradigm for structural health monitoring." *Proc. Asia-Pacific Workshop on Structural Health Monitoring*, keynote lecture, Yokohama, Japan.

- [132] Standard rating chart for pitting corrosion (actual size), Standard Practice G 46-76, Annual Book of ASTM Standards, Vol 3.02, ASTM, Philadelphia, P. 197, 1988, Reprinted by permission, American Society for Testing and Materials.)
- [133] Straser, E. and Kiremidjian, A.S. (1996). "A Modular, Visual Approach to Damage Monitoring for Civil Structures," Proc. 2nd International Workshop on Structural Control, Hong Kong.
- [134] Todd, M., Johnson, G., Vohra, S., Chen-Chang, C., Danver, B. and Malsawma, L. (1999). "Civil infrastructure monitoring with fiber Bragg grating sensor arrays." Structural Health Monitoring, 359-368.
- [135] US Census Bureau. (2008). "Statistical abstract of the United States.": Table 422. <http://www.census.gov/prod/2007pubs/08statab/energy.pdf>
- [136] Vincent, G. S. (1958). "Golden Gate Bridge Vibration Study," J. Structural Division, ASCE, 84(ST6).
- [137] Wahab, M. M. A., Roeck, G. D. and Peeters, B. (1999). "Parameterization of damage in reinforced concrete structures using modal updating" J. of Sound and Vibration, 228(4): 717-730.
- [138] Wang, T. L. and Zong, Z. (2002). "Improvement of evaluation method for existing highway bridges." Research report no. FL/DOT/RMC/6672-818, Contract No. BC-818
- [139] Wang, S., Ren, Q. and Qiao, P. (2006). "Structural damage detection using local damage factor." J. Vibration and Control, 12(9):955-973.
- [140] Wang, M. L. (2008). "Long term health monitoring of post-tensioning box girder bridges." Proc. World Forum on Smart Materials and Smart Structures Technology. In CD-ROM.

- [141] Wong, K. Y., Man, K. L. and Chan, W. Y. (2001). "Application of Global Positioning System to structural health monitoring of cable-supported bridges." Health Monitoring and Management of Civil Infrastructure Systems, Proc. of SPIE, 4337: 390-401.
- [142] Wong, K. Y. (2004). "Instrumentation and health monitoring of cable-supported bridges." Structural Control and Health Monitoring, 11(2): 91-124.
- [143] Zapico, J. K., Ganzalez, M. O., Friswell, M. I., Taylor, C. A. and Crewe, A. J. (2003). "Finite element model updating of a small scale bridge." J. Sound and Vibration, 268: 993-1012.
- [144] Zhang, Y. X, Sim, S. H, Spencer, B. F. (2007). "Finite element model updating of a truss model using incomplete modal data." The World Forum on Smart Materials and Smart Structures Technology (SMSST'07), Chongqing, China, In CD-ROM.
- [145] Zhang, Q. W., Chang, T. Y. P. and Chang, C. C. (2001). "Finite-element model updating for the Kap Shui Mun cable-stayed bridge." J. bridge engineering, ASCE, 6(4): 285-293.

APPENDIX A: DECENTRALIZED DAMAGE IDENTIFICATION

This appendix summarizes the procedure of the DDI application.

A.1. Parameter setting

The first step of the DDI application is waking up the nodes from *SnoozeAlarm* mode. After all nodes are awake, the parameters for the DDI application have set. The parameters are as follows:

- number of FFT points
- number of averaging windows
- number of overlapping points between two consecutive spectral windows
- spectral windows
 - o 1 = Welch window
 - o 2 = Hamming window
 - o 3 = Hanning window
- Filter option
 - o 1= apply filter
 - o 0= do not apply filter
- Detrend option
 - o 1= detrend signal (AC)
 - o 0= do not detrend signal (DC)
- sampling frequency in Hz
- cutoff frequency for the low pass filter in Hz
- reference channel to estimating correlation functions

- sensing channels
 - o single digit among 1,2,3: the specific channel (e.g. 1= channel 1)
 - o two digit among 1,2,3: two specific channels (e.g. 12= channel 1 and 2)
 - o 123: all three channels
- raw data saving option
 - o 1= save raw sensor data in a text file at the base station
 - o 0= do not save the raw sensor data
- correlation function saving option
 - o 1= save correlation functions in the text file at the base station
 - o 0= do not save the correlation functions
- System order
- number of rows and columns of Hankel matrix for ERA

After setting all the parameters, the confirmation message of parameters is printed on the screen.

The image shows a terminal window in UltraEdit-32. The window title is "UltraEdit-32 - [E:\W21 Work-MyCurrent\W8. Mahomet long-term\W2nd deployment - debugged\WDCSsuccess2\WDCS...". The menu bar includes File, Edit, Search, Project, View, Format, Column, Macro, Advanced, Window, and Help. The toolbar contains various icons for file operations and editing. The active file is "DCS_20100408-234023.txt". The terminal content is as follows:

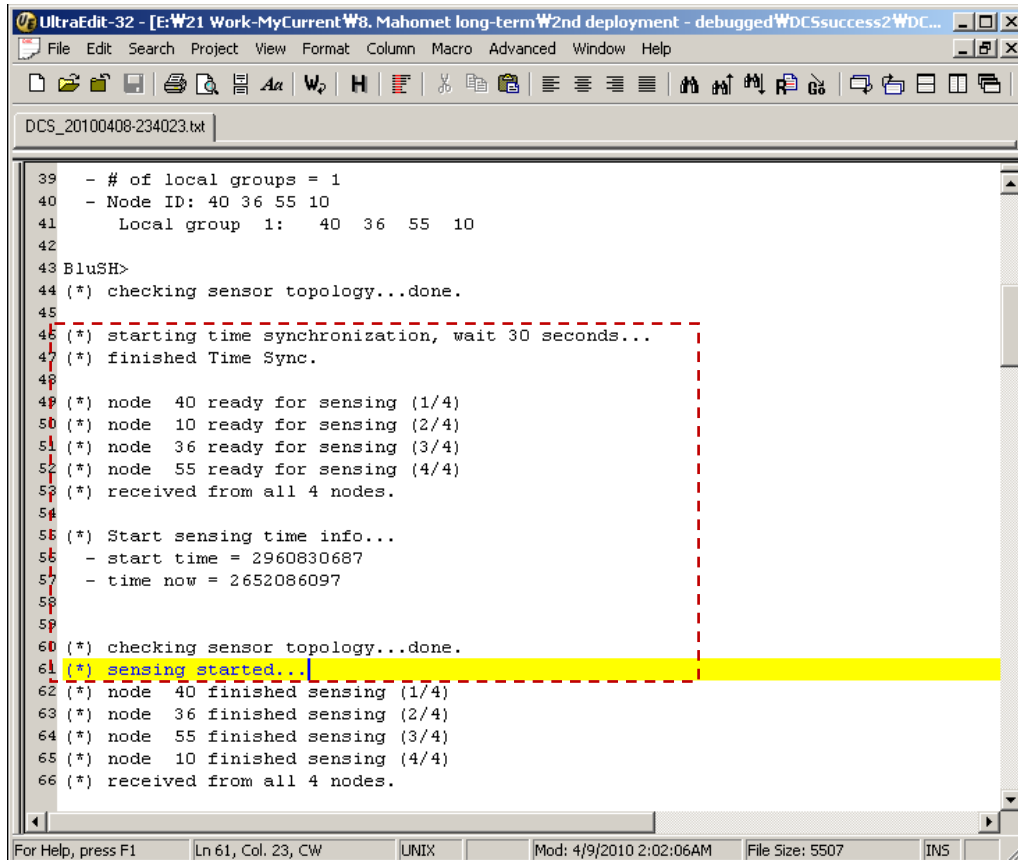
```
2 BluSH>
3 BluSH>
4 BluSH>
5 BluSH>
6 BluSH>WakeUp 10 55 36 40
7 Waking up 4 nodes: 10 55 36 40
8
9 Waiting 26 seconds
10 BluSH>All nodes awake
11 DCSParameters 1024 5 512 3 0 1 100 40 3 123 1 1 8 50 50
12 (*) User-defined parameters are set.
13 BluSH>DCSSensorTopology 40 36 55 10
14 nnodes = 4, nodes= 40
15 group 1: 40 36 55 10
16 maddr = 40
17 (*) Sensor Topology is set
18 (*) waking up sensor nodes... wait.
19
20 Waiting 26 seconds
21 BluSH>(*) Sensor nodes are awake: 40 36 55 10
22 (*) checking sensor topology...done.
23 (*) Ready for start
24 SensorTopology is set. DD& is ready to start.
25 All nodes awake
26 DCSStart
27 (*) Parameters...
28 - # of averages = 5
29 - # of FFT = 1024
30 - Sampling Rate = 100
31 - Spectral window (1->Boxcar, 2->Hamming, 3->Hanning): 3
32 - Normalize? = 1
33 - Low pass filter?: 0 (fc = 40 Hz)
34 - # of samples = 3579
35 - Addr of gateway node = 7
36 - Reference channel = 3
37 - Sensing channel info: 3 channel(s) - Mask: 123
38 - # of overlap points = 512
```

The status bar at the bottom shows "Select open file (The TAB E |Ln 2, Col. 1, CW |LINUX |Mod: 4/9/2010 2:02:06AM |File Size: 5507 |INS |".

Figure A.1. Step 1: parameter setting

A. 2. Synchronized sensing

After setting parameters, the leaf nodes start synchronized sensing based on the parameter setting in the previous step.

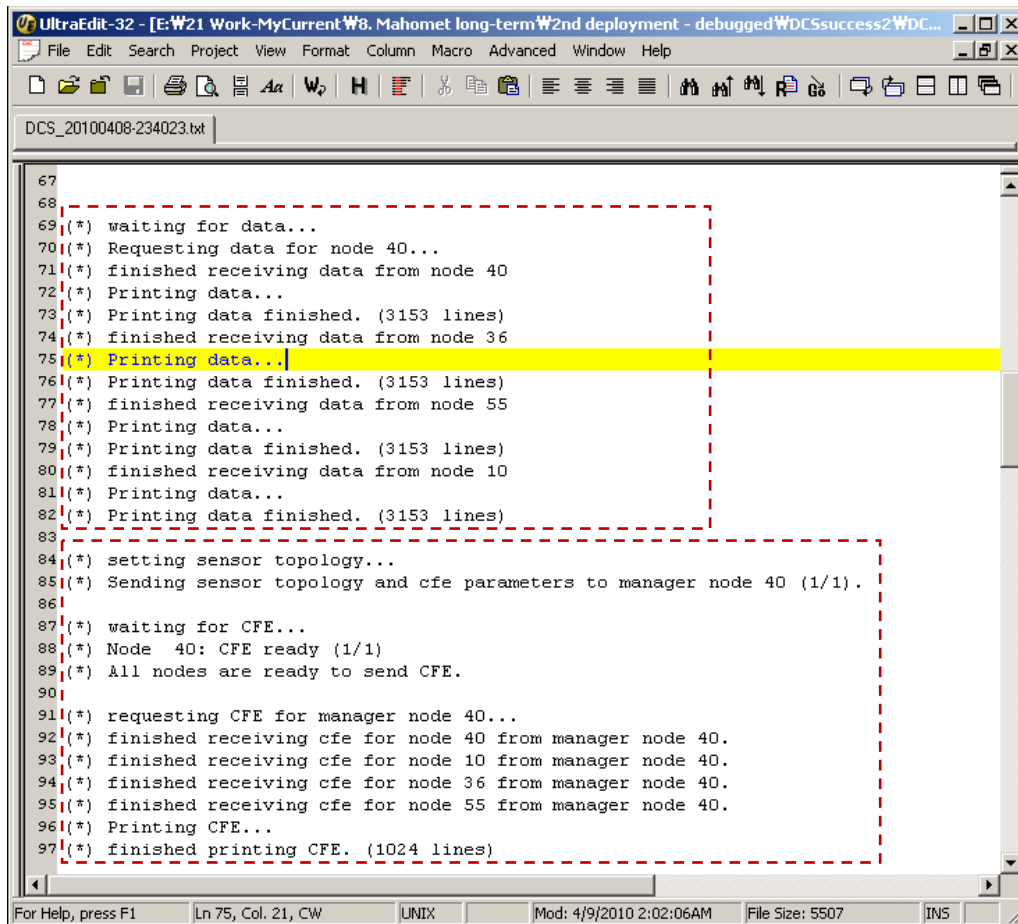


```
UltraEdit-32 - [E:\W21 Work-MyCurrent W8. Mahomet long-term W2nd deployment - debugged WDC5success2 WDC...
File Edit Search Project View Format Column Macro Advanced Window Help
DCS_20100408-234023.txt
39 - # of local groups = 1
40 - Node ID: 40 36 55 10
41   Local group 1:  40 36 55 10
42
43 BluSH>
44 (*) checking sensor topology...done.
45
46 (*) starting time synchronization, wait 30 seconds...
47 (*) finished Time Sync.
48
49 (*) node 40 ready for sensing (1/4)
50 (*) node 10 ready for sensing (2/4)
51 (*) node 36 ready for sensing (3/4)
52 (*) node 55 ready for sensing (4/4)
53 (*) received from all 4 nodes.
54
55 (*) Start sensing time info...
56   - start time = 2960830687
57   - time now = 2652086097
58
59
60 (*) checking sensor topology...done.
61 (*) sensing started..
62 (*) node 40 finished sensing (1/4)
63 (*) node 36 finished sensing (2/4)
64 (*) node 55 finished sensing (3/4)
65 (*) node 10 finished sensing (4/4)
66 (*) received from all 4 nodes.
For Help, press F1   Ln 61, Col. 23, CW   UNIX   Mod: 4/9/2010 2:02:06AM   File Size: 5507   INS
```

Figure A.2. Step 2: raw data measurement

A.3. Correlation function estimation

After sensing, the cluster head asks the measured data to leaf nodes. The leaf nodes in a group send data to the cluster head for calculating the correlation functions.

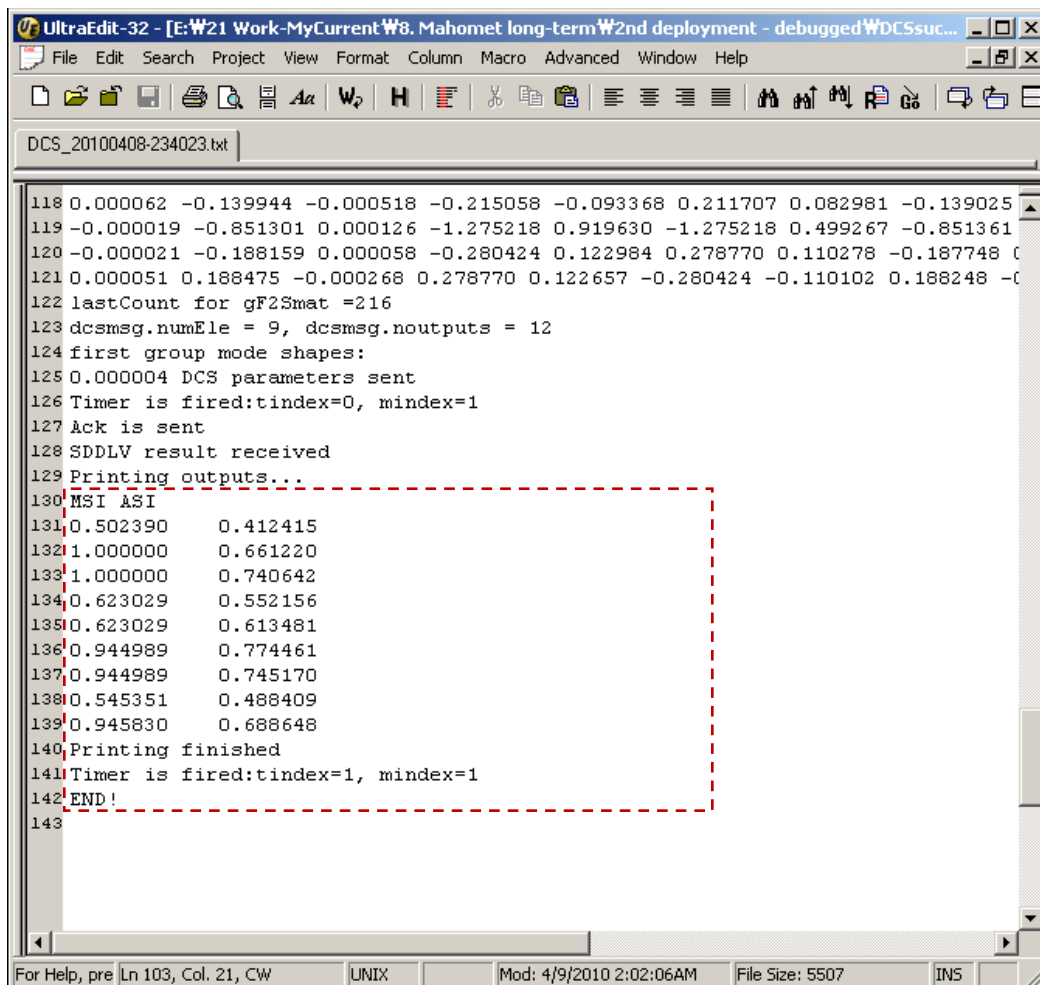


```
UltraEdit-32 - [E:\W21 Work-MyCurrent\W8. Mahomet long-term\W2nd deployment - debugged\WDCsuccess2\WDC...
File Edit Search Project View Format Column Macro Advanced Window Help
DCS_20100408-234023.txt
67
68
69 (*) waiting for data...
70 (*) Requesting data for node 40...
71 (*) finished receiving data from node 40
72 (*) Printing data...
73 (*) Printing data finished. (3153 lines)
74 (*) finished receiving data from node 36
75 (*) Printing data...
76 (*) Printing data finished. (3153 lines)
77 (*) finished receiving data from node 55
78 (*) Printing data...
79 (*) Printing data finished. (3153 lines)
80 (*) finished receiving data from node 10
81 (*) Printing data...
82 (*) Printing data finished. (3153 lines)
83
84 (*) setting sensor topology...
85 (*) Sending sensor topology and cfe parameters to manager node 40 (1/1).
86
87 (*) waiting for CFE...
88 (*) Node 40: CFE ready (1/1)
89 (*) All nodes are ready to send CFE.
90
91 (*) requesting CFE for manager node 40...
92 (*) finished receiving cfe for node 40 from manager node 40.
93 (*) finished receiving cfe for node 10 from manager node 40.
94 (*) finished receiving cfe for node 36 from manager node 40.
95 (*) finished receiving cfe for node 55 from manager node 40.
96 (*) Printing CFE...
97 (*) finished printing CFE. (1024 lines)
For Help, press F1 Ln 75, Col. 21, CW UNIX Mod: 4/9/2010 2:02:06AM File Size: 5507 INS
```

Figure A.3. Step 3: correlation function estimation

A. 4. Damage detection

The computed correlation functions are fed into ERA-NExT for system identification. ERA-NExT component outputs the natural frequencies, mode shapes, and A, C matrices. Based on the system information, the damage indices, MSI and ASI, are printed on screen and saved in the text file.



```
UltraEdit-32 - [E:\W21 Work-MyCurrent\W8. Mahomet long-term\W2nd deployment - debugged\WDCSsuc...
File Edit Search Project View Format Column Macro Advanced Window Help
DCS_20100408-234023.txt
118 0.000062 -0.139944 -0.000518 -0.215058 -0.093368 0.211707 0.082981 -0.139025
119 -0.000019 -0.851301 0.000126 -1.275218 0.919630 -1.275218 0.499267 -0.851361
120 -0.000021 -0.188159 0.000058 -0.280424 0.122984 0.278770 0.110278 -0.187748
121 0.000051 0.188475 -0.000268 0.278770 0.122657 -0.280424 -0.110102 0.188248
122 lastCount for gF2Smat =216
123 dcsmsg.numEle = 9, dcsmsg.noutputs = 12
124 first group mode shapes:
125 0.000004 DCS parameters sent
126 Timer is fired:tindex=0, mindex=1
127 Ack is sent
128 SDDLW result received
129 Printing outputs...
130 MSI ASI
131 0.502390 0.412415
132 1.000000 0.661220
133 1.000000 0.740642
134 0.623029 0.552156
135 0.623029 0.613481
136 0.944989 0.774461
137 0.944989 0.745170
138 0.545351 0.488409
139 0.945830 0.688648
140 Printing finished
141 Timer is fired:tindex=1, mindex=1
142 END!
143
For Help, pre Ln 103, Col. 21, CW UNIX Mod: 4/9/2010 2:02:06AM File Size: 5507 INS
```

Figure A.4. Step 4: damage detection